

# Ultrafast Laser Spectroscopy of Vibrational Energy Transport in Conjugated Chains and Metal Complexes

AN ABSTRACT

SUBMITTED ON THE NINETEENTH DAY OF APRIL 2023

TO THE DEPARTMENT OF CHEMISTRY

OF THE SCHOOL OF SCIENCE AND ENGINEERING

OF TULANE UNIVERSITY

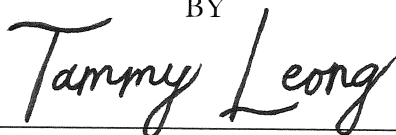
IN PARTIAL FULFILLMENT OF THE REQUIREMENTS

FOR THE DEGREE

OF

DOCTOR OF PHILOSOPHY

BY



TAMMY XIU WEN LEONG

APPROVED:



IGOR V. RUBTSOV, PH.D.

CHAIR OF DISSERTATION COMMITTEE



BRENT KOPLITZ, PH.D.



MARK SULKES, PH.D.



RUSSELL SCHMEHL, PH.D.

# Abstract

Obtaining a full understanding of the temporal and spatial resolution of vibrational energy flow in molecules is one of the main goals in Physical Chemistry. The transfer of vibrational energy within molecular systems plays a crucial role in various fields, including biochemistry, chemistry, molecular electronics, as well as novel materials and technology. Vibrational energy is necessary to achieve the transition state in chemical reactions, while eliminating excess energy from the products renders the reaction irreversible. Presently, there is significant attention being given to the thermal transport characteristics of molecular layers, interfaces, and junctions, as part of the wider examination of thermal transport at the nanoscale. Having a complete understanding of every aspect of the process is essential to control the rate and efficiency of energy transport through molecular chains.

Previous studies have identified two classes of regimes for vibrational energy transport in molecules- namely diffusive and ballistic. The first is diffusive energy transport, where vibrational energy hops between localized states in a Brownian-like motion. The second is ballistic energy transport, where a vibrational wave packet moves freely through delocalized vibrational modes. Previous research has shown rapid vibrational energy transport in various oligomer chains, with speeds of 3.9 Å/ps in perfluoroalkanes, 5.5 Å/ps in PEGs, and 14.4 Å/ps in polyethylene oligomers, indicating a ballistic transport regime over significant distances. However, there was a lack of comprehensive research on the effect of conjugated chains on vibrational energy transport, as well as the energy transfer mechanism in complex molecules, such as those that consist of transition metals.

The objective of the dissertation at hand is to comprehend the fundamental causes of the variation in speeds of vibrational energy transport within such chains. To experimentally study energy transport in different molecular chains, relaxation-assisted two-dimensional infrared (RA 2DIR) spectroscopy is used. In this experimental technique, an IR-active group (tag) is excited to initiate transport, and the effect of the excess energy on the frequency of another mode in the molecule (reporter) is measured. The energy transport time between the tag and reporter can be measured, and the speed of transport through the molecule can be determined. Experiments on a series of poly(*p*-phenylene) chains with carbonyl and nitro end groups showed that the excess energy from m-IR excitation provided a way to funnel high-frequency vibrational quanta rapidly and unidirectionally over large distances. A comprehensive examination of the chain states of vibrational chains and

intramolecular vibrational relaxation pathways of the tag modes was carried out to comprehend the reasons behind varying speeds of transport. Based on the analysis, it was determined that the efficiencies of energy injection into the chain and transport along the chain are found to be very high and dependent on the extent of conjugation across the structure.

Similar experiments were conducted on complex compounds that featured a platinum center, triazole-terminated alkyne ligand of two or six carbons, a perfluorophenyl ligand, and two tri(*p*-tolyl)phosphine ligands. Comprehending the rules governing the relaxation and transfer of energy across the metal center in such compounds could optimize their switching properties for electron transfer. The energy transport dynamics of several diagonal and cross peaks were analyzed extensively, with a focus on parameters related to coherent oscillation, energy transfer, and cooling. The requirements for high-frequency mode energy transport across the metal centers have been formulated and demonstrated, which necessitate the coupling and delocalization of local modes located on both sides of the metal center. Additionally, the presence of many coherent oscillations (quantum beating) in the cross peaks in the fingerprint region indicates strongly coupled modes, often belonging to the same moiety. This discovery suggests the possibility of utilizing oscillations as structural reporters, enhancing the recognition capability of two-dimensional infrared spectroscopy.

The second topic in this dissertation aims to comprehend the effect of gold nanoantenna arrays' plasmonic fields on molecular samples through nanofabrication of such arrays. Surface-enhanced infrared absorption (SEIRA) spectroscopy incorporates plasmonic surfaces into measurements, enhancing traditional infrared techniques. Previous studies indicate that the placement of molecules with resonant vibrational transitions within the plasmonic field leads to the coupling between the plasmon and the vibrational mode, leading to a significant signal enhancement. The nanofabrication of periodic gold arrays on CaF<sub>2</sub> wafers using various micro-engineering technologies is described in detail. Fourier-transform infrared (FTIR) spectroscopy was used to measure the plasmonic arrays, showing that the tuning of the resonant frequency is achievable by adjusting the length of each individual array. The dimensions of an individual nanorod could be tuned to match the vibrational frequency of a selected molecule, to be further studied using multidimensional infrared spectroscopy (eg. 2DIR). A straightforward, high-output approach for producing large area packed connected gold nanoarrays for electrochemical experiments is also proposed, opening avenues for control of transport speed and efficiency of chains by altering the electronic doping extent, or through electronic excitation of electronically enriched chains.

# Ultrafast Laser Spectroscopy of Vibrational Energy Transport in Conjugated Chains and Metal Complexes

A DISSERTATION

SUBMITTED ON THE NINETEENTH DAY OF APRIL 2023

TO THE DEPARTMENT OF CHEMISTRY

OF THE SCHOOL OF SCIENCE AND ENGINEERING

OF TULANE UNIVERSITY

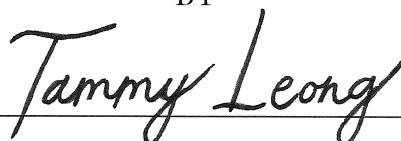
IN PARTIAL FULFILLMENT OF THE REQUIREMENTS

FOR THE DEGREE

OF

DOCTOR OF PHILOSOPHY

BY



TAMMY XIU WEN LEONG

APPROVED:



IGOR V. RUBTSOV, PH.D.

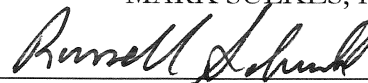
CHAIR OF DISSERTATION COMMITTEE



BRENT KOPLITZ, PH.D.



MARK SULKES, PH.D.



RUSSELL SCHMEHL, PH.D.

© Copyright by Tammy Xiu Wen Leong, 2023

All Rights Reserved

# Acknowledgements

The journey of graduate school is a challenging yet fulfilling one, with its fair share of highs and lows. Over the past five years, my time at Tulane has been nothing short of a self-discovery journey, revealing my true potential and ability to achieve goals that once seemed unattainable. I would like to express my heartfelt gratitude to the numerous individuals who have played a pivotal role in helping me achieve one of the greatest achievements of my life. The successful completion of this dissertation would not have been possible without their unwavering support and guidance.

I am especially indebted to my advisor, Professor Igor Rubtsov, whose expertise, encouragement, and mentorship have been invaluable throughout this journey. His extensive expertise, unwavering encouragement, and effective mentorship have been invaluable in shaping me into the scientist I am today. When I joined his group, I had no prior experience in nonlinear optics, let alone two-dimensional infrared spectroscopy, but with his guidance, I was able to learn quickly and make significant progress in my research. Dr. Rubtsov's unwavering support was a constant source of motivation, and he never hesitated to assist me when I faced challenges in the lab. Dr. Rubtsov, thank you for accepting me into your group, if given the chance to do it all over again, I would make the same decision.

I would also like to extend my sincere appreciation to the members of my dissertation committee: Professors Brent Koplitz, Mark Sulkes, and Russell Schmehl, for graciously accepting to serve on my committee, and for their invaluable time and effort in meticulously reviewing my dissertation, providing constructive feedback, and engaging in insightful discussions.

I would also like to extend my gratitude to the members of the Rubtsov Group. I am especially grateful to Dr. Robert Mackin, who patiently mentored me through the intricacies of the lab when I first joined the group. His guidance and support were instrumental in helping me lay a solid foundation for my research projects. Working together for long 16-hour days to conduct cryostat measurements during my first summer here was the start of our friendship and remains one of my most cherished memories from graduate school. I would also like to thank Dr. Michael Johnson for his guidance in the cleanroom. His extensive knowledge and valuable insights were instrumental in my research work on nanofabrication. The knowledge gained through our interactions has been incredibly enlightening and will undoubtedly prove valuable in my future pursuits.

## II

Thank you to all the friends I have made while at Tulane, both in the chemistry department and others. All of you have made the past five years here in New Orleans an unforgettable experience, from barbeques in the park to late night card games. Although it saddens me that we will have to part ways, I trust that we will all keep in touch. I would like to thank Amin Zarandi for being an invaluable friend who has put up with my antics for the past five years. I am truly grateful to have a wonderful friend (dost) like you. I also want to express my gratitude to Artem Sribnyi for supporting me through both the highs and the deep, dark lows that are an inevitable part of graduate school. Thank you for always believing in me and being there for me, no matter what.

Leaving Singapore to start my undergraduate degree in Michigan was a daunting experience. It was the first time I had been so far away from my parents, and I felt anxious about what the future held. However, I was fortunate to have Uncle Michael and Aunty Rita step in as parental figures in Berrien. They welcomed me into their home and prepared homemade meals for me every week. Even when I moved to New Orleans, they made the long journey from Michigan to Louisiana to help me with the transition. I am forever grateful to them for their kindness and support, and I cannot imagine what my life in America would have been like without them.

Lastly, I would like to express my gratitude to my family, who have been my constant source of support and encouragement. I am particularly thankful to my siblings, Fiona and Kevin, who have been my lifelong steadfast supporters. I would also like to extend my heartfelt appreciation to my parents, Joachim and Melissa, whose unwavering love and guidance have been the cornerstone of my success. I will always remember the sacrifices you made to provide me with the opportunities I have today. I cannot thank you enough for everything you have done for me, and I promise to make you proud in all my future endeavors.

# Contents

<b>Acknowledgements</b> .....	I
<b>List of Tables</b> .....	VII
<b>List of Figures</b> .....	VIII
<b>1 Theory of Vibrational Energy Transport</b> .....	<b>1</b>
1.1. Measuring Vibrational Energy Transport: An Overview.....	1
1.2. Diffusive Energy Transport in Molecules.....	5
1.3. Ballistic Energy Transport in Molecules.....	8
1.4. Infrared Spectral Signal Enhancement by Plasmonic Nanoarrays .....	11
1.5. Dissertation Outline .....	14
<b>2 Non-Linear Spectroscopy: Concepts of Two-Dimensional Infrared Spectroscopy</b> .....	<b>16</b>
2.1. Introduction.....	16
2.2. Nonlinear Optical Spectroscopy.....	18
2.3. Linear Infrared Spectroscopy.....	20
2.4. Two-dimensional Infrared (2DIR) Spectroscopy .....	22
2.4.1. 2DIR Spectrum of a Single Vibrational Mode.....	26
2.4.2. 2DIR Spectrum of Two Coupled Vibrational Modes .....	28
2.5. Frequency Domain 2DIR Spectroscopy .....	31
2.6. Time-domain Dual-Frequency 2DIR Spectroscopy.....	31
2.7. Relaxation-assisted 2DIR Spectroscopy .....	34
2.8. Fully automated 2DIR Spectrometer.....	37
2.9. Measurement Details .....	40

### 3 Unidirectional coherent energy transport via conjugated oligo(*p*-phenylene) chains 41

3.1. Introduction.....	42
3.2. Experimental Details .....	43
3.2.1. Experimental Method.....	43
3.2.2. Sample Preparation .....	43
3.2.3. DFT Calculations .....	43
3.3. Results.....	44
3.3.1 Energy Transport Initiated by $\nu_{C=O}$ .....	44
3.3.1 Energy Transport Initiated by $\nu_{NO_2}$ .....	45
3.4. Discussion.....	46
3.4.1. Chain Band Analysis .....	46
3.4.2. Tag Relaxation Channels.....	49
3.4.3. Torsion Angles .....	53
3.4.4. Modeling of the Transport Initiated with $\nu_{C=O}$ .....	55
3.4.5. Nature of the Coupling in Selected Chain Bands.....	56
3.4.6. Transport Initiated by $\nu_{NO_2}$ .....	57
3.4.7. Cross-peak Amplitude Decay with Distance.....	58
3.4.8. Harmonic Mixing of End-group and Chain-states .....	59
3.4.9. Energy Injection Efficiency.....	60
3.4.10. Energy Transport Efficiency.....	62
3.4.11. Computations and Experiments with Polythiophene .....	64
3.4.12. Novel Research Avenues .....	65

<b>4 Tracking Energy Transfer across a Platinum Center</b>	<b>67</b>
4.1. Introduction.....	68
4.2. Experimental Details .....	70
4.2.1. Experimental Method.....	70
4.2.2. Sample Preparation .....	70
4.2.3. DFT Calculations and Vibrational Relaxation Modeling.....	70
4.3. Results.....	71
4.3.1. Linear FTIR Spectroscopy Measurements .....	71
4.3.2. DFT-based Modeling of FTIR Spectra .....	72
4.3.3. Energy Transfer Initiated by $\nu_{C=C}$ .....	76
4.3.4. Energy Transfer Towards $\nu_{C=C}$ .....	77
4.3.5. Diagonal and Cross-peaks in the Fingerprint Region.....	79
4.3.6. Cross-peak and Diagonal-peak Decay Times .....	82
4.3.7. Coherent Oscillations in Cross-peaks .....	84
4.4. Discussion.....	86
4.4.1. Computing Vibrational Relaxation Pathways .....	86
4.4.2. Electric Dipole-dipole Coupling across Pt Center .....	89
4.4.3. Origin of Mode Coupling across the Pt Center.....	89
4.5. Conclusions.....	95
<b>5 Coherent Oscillations as Structural Reporters</b>	<b>97</b>
5.1. Introduction .....	98
5.2. Experimental Details.....	99
5.2.1. Experimental Method .....	99
5.2.2. Sample Preparation.....	99
5.3. Results .....	100
5.3.1. Linear FTIR Measurements .....	100

5.3.2. Multiple Oscillations in Cross-peaks in the Fingerprint Region.....	100
5.3.3. Diagonal Peaks in the Fingerprint Region.....	103
5.3.4. Non-Rephasing Measurements.....	103
5.4. Discussion.....	104
5.4.1. Isolating Frequency Components .....	105
5.4.2. Rephasing vs. Non-rephasing Sequences.....	106
5.4.3. Origin of Coherent Oscillations .....	108
5.4.4. Analyzing Diagonal Peaks in the Fingerprint Region .....	109
5.4.5. Suppressing Quantum Beat Oscillations.....	110
5.5. Conclusion.....	112
<b>6 Nanofabrication of Gold arrays</b>	<b>113</b>
6.1. Introduction .....	114
6.2. Experimental Details.....	116
6.2.1. Nanoarray Fabrication .....	116
6.3. Results and Discussion .....	119
6.3.1. Linear Spectroscopy of Gold Arrays .....	119
6.3.2. Electron Scattering in the Resist Layer Affects PMMA Dose.....	120
6.3.3. Tuning Frequency Selectivity of Antennas .....	123
6.3.4. Design and Fabrication of Nanoarrays for Electrochemical Measurements.....	126
6.4. Conclusions .....	129
<b>Summary .....</b>	<b>130</b>
<b>Bibliography.....</b>	<b>134</b>

# List of Tables

## 3 Unidirectional Coherent Energy Transport via Conjugated Oligo(*p*-phenylene) Chains

**Table 3.1.** Values of  $\beta$  and  $\gamma$  obtained from a fit of the DFT-computed energy states using Eq. 3.1.

**Table 3.2.** Dominant relaxation pathways calculated for the  $\nu_{C=O}$  and  $\nu_{NO_2}$  tags in P4. The rates into all four states of a single band are summed and divided by the overall relaxation rate (shown as footnotes) for the rate percent. Maximum speeds in Å/ps supported by these bands are shown, involving only the nearest-neighbor interaction ( $\gamma=0$ ) and both nearest-neighbor and next-nearest-neighbor interactions

**Table 3.3.** Band parameters,  $\omega_0$ ,  $\beta$  and  $\gamma$ , maximum speed supported,  $V_{max}$ , band rate contribution,  $\eta_{inj}$ , to the  $\nu_{NO_2}$  tag relaxation, and percent of tag energy injected into each band,  $\eta_{inj}$ , in P4.

## 4 Tracking Energy Transfer across a Platinum Center

**Table 4.1.** Main experimental absorption peaks and DFT computed, scaled normal modes of  $\nu_{C=C}$  for C2 and C6.

**Table 4.2.** Main experimental absorption peaks and DFT computed, scaled normal modes of C2 and C6.

**Table 4.3.**  $T_{max}$  values from the waiting-time dependences of several cross-peaks of C2 and C6.

**Table 4.4.** Fit parameters for several diagonal peaks.

**Table 4.5.** Fit parameters for several cross peaks for C6.

**Table 4.6.** Exponential decay parameters for cross peaks for C6.

## CHAPTER 5. Coherent Oscillations as Structural Reporters

**Table 5.1.** Fit Parameters for C6 Cross Peaks (Rephasing)

# List of Figures

## 1 Introduction

**Figure 1.1.** Structure of PBN and the energy transport time between various modes. The transport time from  $\nu_{C\equiv N}$  to  $\nu_{C=O}$  and from  $\nu_{C\equiv N}$  to Am-I are shown in red and blue respectively.

**Figure 1.2.** Structure of **(a)** ortho, **(b)** meta, and **(c)** para isomers of acetylbenzonitrile (AcPhCN). The transport time from  $\nu_{C\equiv N}$  to  $\nu_{C=O}$  for each isomer is shown inset.

**Figure 1.3.** Process of ballistic energy transport in oligomeric chains

**Figure 1.4.** Structures of the azPEG0, 4, 8, and 12 compounds

**Figure 1.5.** Different types of surface plasmons: **(a)** surface plasmon polaritons at a metal-dielectric interface and **(b)** localized surface plasmons on a metal nanoparticle excited by free-space light

## 2 Non-Linear Spectroscopy: Concepts of Two-Dimensional Infrared Spectroscopy

**Figure 2.1.** **(a)** Energy level and **(b)** double-sided Feynman diagrams of the IR absorption. The arrows represent the interactions with the laser field, where the solid arrow represent excitation and the dash arrow represents de-excitation.  $\tau_1$  and  $\tau_2$  are the times when the applied field interacts with the system.

**Figure 2.2.** Energy level split for two acetone molecules, with an unperturbed frequency of  $1710\text{ cm}^{-1}$ . The split represents  $2\beta_{ij}$ , where  $\beta_{ij}$  is the coupling strength.

**Figure 2.3.** **(a)** Simulated 2DIR spectrum, depicting the  $\nu_{C=O}$  stretches of two acetone molecules coupled with fundamental frequencies at  $1610\text{ cm}^{-1}$  and  $1640\text{ cm}^{-1}$ , with a relative transition dipole coupling of **(a)**  $10\text{ cm}^{-1}$  and **(b)**  $4\text{ cm}^{-1}$ . The diagonal peak pairs represent the excitation/stimulated emission of individual molecules, while the cross peaks represent the coupling between their CO modes. **(c)** The coupling strength depends on the distance,  $d$ , and orientation,  $\theta$ . The carbonyl stretches are represented with transition dipoles (blue arrows).

**Figure 2.4.** **(a)** Spring model representing a diatomic molecule, separated by distance,  $r$  **(b)** Energy level scheme of a harmonic oscillator (green line) and an anharmonic oscillator (black line) with the dipole-allowed transitions depicted. The red arrow represents the pump process, while the blue arrows represent the probe process. **(c)** The resulting 2DIR spectrum. The red contour represents negative response (GSB, SE) and the blue contour represents positive response (ESA).

**Figure 2.5.** Types of vibrational couplings of the H-O-H molecule. **(a)** Bending-bending mode **(b)** stretching-stretching mode **(c)** bending-stretching mode, known as a combination band.

**Figure 2.6.** (a) Level scheme of two coupled oscillators before coupling (local modes) and after coupling (eigenstates). The dipole-allowed transitions are depicted. The solid arrows represent the pump process, the dotted arrows the probe process. (b) Resulting 2D IR spectrum. Red represents negative response (bleach and stimulated emission), blue represents positive response (excited state absorption).

**Figure 2.7.** (a) An energy diagram for vibrational modes  $\omega_1$  and  $\omega_2$  showing coherence and population states accessed by the pulse sequence. The spectra of the IR pulses are shown on the left. (b) Delays between the pulses are shown in dual-frequency 2DIR measurements.  $\tau$  is the delay between  $k_1$  and  $k_2$ ,  $T$  is the delay between  $k_2$  and  $k_3$ , and  $t$  is the delay between the local oscillator and the 3rd-order signal. (c) Schematic of the three-pulse dual-frequency 2DIR experiment.

**Figure 2.8.** (a) Cartoon describing the direct coupling and relaxation-assisted coupling, respectively, between vibrational modes  $\omega_1$ ,  $\omega_2$ , and  $\omega_x$ . (b) and (e) reflect the cross peaks generated in the direct coupling and relaxation-assisted coupling cases, respectively. (c, d) An energy diagram of the energy transport process is illustrated. (f) Waiting-time kinetics curve obtained from the intensity of the cross peak plotted as a function of  $T$ .

**Figure 2.8.** Optical schematic of the dual-frequency 2DIR instrument. Here, Q is an MCT quad detector, D is an optical delay stage, T is a translation stage, PR is a parabolic reflector, Pr is a right-angled prism reflector, PZ is a gold mirror equipped with a piezo actuator, BS is a beam splitter, WP is a waveplate – wire-grid polarizer or two wire-grid polarizers assembly, GP is a wire-grid polarizer, W is a phase modulator (wobbler), F is a mechanical flipper, OM is an optical mask, PD is a Si photodiode, SC is a sample cell, IS is an image spectrometer, and MCD is a MCT array detector. BS1 is a 50/50 beam splitter with separate regions for m-IR and HeNe beams. Standard mirrors are omitted to increase legibility.

### 3 Unidirectional Coherent Energy Transport via Conjugated Oligo(*p*-phenylene) Chains

**Figure 3.1.** (a) Structure of compounds P1 – P3 featuring oligo(*p*-phenylene) backbones. Vibrational modes at the end groups,  $\nu_{C=O}$  and  $\nu_{NO_2}$  (asymmetric stretch) served as tags and reporters in the RA 2DIR study. (b) Solvent subtracted linear absorbance spectra of P1 – P3 in DMSO, normalized at  $\nu_{C=O}$ .

**Figure 3.2.** (a) 2DIR magnitude spectrum of P1 at  $T = 2.2$  ps, showing  $\nu_{C=O}/\nu_{NO_2}$ . The integration window used for analysis is shown. (b) Waiting-time dependences of the  $\nu_{C=O}/\nu_{NO_2}$  cross-peak amplitude for P1 (black line), P2 (blue line), and P3 (green line) and their fits with an asymmetric double sigmoidal function (red lines).

**Figure 3.3.** (a) 2DIR magnitude spectrum of P1 at  $T = 2.5$  ps, featuring  $\nu_{NO_2}/\nu_{C=O}$  and several other cross peaks. (b) Waiting-time dependences of the  $\nu_{NO_2}/\nu_{C=O}$  cross-peak amplitude for P1 (black line), P2 (blue line), and P3 (green line) and their fits with an asymmetric double sigmoidal function (red lines).

**Figure 3.4.**  $T_{\max}$  (circles) and  $T_{0.8}$  (squares) values plotted as a function of tag-reporter distance for the P1-P3 compounds for the transports initiated by  $\nu_{\text{C=O}}$  (blue symbols) and  $\nu_{\text{NO}_2}$  (green symbols). The linear fits and the transport speeds obtained from the fit are shown with the matching colors.

**Figure 3.5.** DFT-computed state energies of A-(Ph)<sub>5</sub>-B for **(a,b)** in-plane and **(c)** out-of-plane optical bands lower than 2000  $\text{cm}^{-1}$  (see atomic displacements in Fig. 3.8). The conformation with the  $\theta$  angle between neighboring phenyl rings in the chain alternating as  $+38^\circ$ ,  $-38^\circ$ ,  $+38^\circ$ ,  $-38^\circ$  was used. Fits to Eq. 3.1 are shown with solid lines; the  $\omega_0$  values are shown with squares in the left margin; the resulting  $\beta$  and  $\gamma$  values are given in Table 3.1.

**Figure 3.6.** Rates of dominant relaxation channels into optical chain states for the **(a)**  $\nu_{\text{C=O}}$  and **(b)**  $\nu_{\text{NO}_2}$  tags computed for P4.

**Figure 3.7.** DFT-computed normal-mode displacements for  $q = 0$  optical **(a)** in-plane and **(b)** out-of-plane bands of poly(*p*-phenylene). Modes that contribute the most to the  $\nu_{\text{C=O}}$  initiated transport are circled in yellow.

**Figure 3.8. (a-e)** DFT calculated normal-mode frequencies for selected modes of (Ph)<sub>2</sub> as a function of a torsion angle. **(f)** Energy of the molecule relative to that at equilibrium as a function of the torsion angle.

**Figure 3.9. (a)** Experimental (blue symbols) and modeled with two participating wavepackets (green symbols)  $T_{\max}$  and  $T_{0.8}$  values plotted as a function of tag-reporter distance in the P1-P3 compounds for the transport initiated by  $\nu_{\text{C=O}}$ .  $T_{\max}$  values for the individual wavepackets (WP), fast and slow, are shown with red symbols; their transport speeds are shown as inset. **(b)** Waiting-time dependences of the  $\nu_{\text{C=O}} / \nu_{\text{NO}_2}$  experimental cross-peak amplitude for P1 (blue), P2 (green), and P3 (gray). The modeled waiting-time traces, obtained by the summation of the fast and slow wavepackets, are shown with red lines.

**Figure 3.10.** Structures used for calculating the coupling of nearest neighbor C=C stretching local modes. Carbon atoms assigned with normal atomic masses are highlighted in cyan.

**Figure 3.11.** Waiting-time traces for P1 of the diagonal  $\nu_{\text{C=O}}$  amplitude (blue) and diagonal  $\nu_{\text{NO}_2}$  amplitude (green) and for P2 of the diagonal  $\nu_{\text{C=O}}$  amplitude (purple) and diagonal  $\nu_{\text{NO}_2}$  amplitude (cyan). All four peaks were fit with a triple exponential function (red lines).

**Figure 3.12.** DFT-computed third-order reduced force constants,  $V_{ijk}$ , as a function of the B-state frequency. Indices  $i$  and  $j$  denote the  $\nu_{\text{C=O}}$  mode and each of K states, respectively. Index  $k$  is selected for the pathway with the highest rate of  $\nu_{\text{C=O}}$  relaxation populating the respective K mode.

**Fig. 3.13.** Influence of the end-group-state location with respect to the chain band **(a-c vs. d-f)** and their coupling strength (green oval) on the end-group state delocalization.

**Figure 3.13.** Normalized  $\nu_{\text{NO}_2}/\nu_{\text{C=O}}$  cross-peak amplitude of as a function of the tag-reporter distance for P1, P2 and P3. The fit with an exponential function (red line) result in a decay factor,  $R_0$ , of  $9.5 \pm 1 \text{ \AA}$ .

**Figure 3.14.** Structure of poly(2,5 pyridine), polythiophene, polyfuran and polypyrrole

**Figure 3.15. (a)** 5-nitro-2-thiophene carboxylic acid **(b)** In-plane optical chain bands lower than  $2000\text{ cm}^{-1}$  DFT-computed for (Th)<sub>5</sub> chain.

**Figure 3.16.** 2DIR magnitude spectra of 5-nitro-2-thiophene carboxylic acid showing  $1700\text{ cm}^{-1}$  diagonal region at **(a)** 1.2 ps and **(b)** 3.6 ps.

**Figure 3.17.** Quinoidal Structure of polyphenylene.

**Figure 3.18.** A polyphenylene derivative, with COOH and NO<sub>2</sub> end groups, attached to a single AuNR, by Au-S bond

## CHAPTER 4. Tracking Energy Transfer across a Platinum Center

**Figure 4.1.** Structures of C2 ( $n=1$ ) and C6 ( $n=3$ ).

**Fig. 4.2.** Solvent-subtracted infrared absorption spectra of compounds C2 and C6 in CDCl<sub>3</sub>. The spectrum of C6 was scaled by a factor of ca. 1.2 to match that of C2.

**Figure 4.3.** DFT-computed uncorrected line spectra for C6 **(a)** and frequency corrected line spectra for C6 **(b)** and C2 **(c)**. The modes associated with F<sub>5</sub>Ph-, C $n$ - Tri, and Tol moieties are shown with red, blue, and green, respectively. Experimental linear absorption spectra for C6 **(a,b)** and C2 **(c)** in CDCl<sub>3</sub> are shown with gray lines. Theoretical spectra of C2 **(c)** and C6 **(b)** obtained from applying Lorentzian line shape with a full width at half maximum of  $8.1\text{ cm}^{-1}$  are shown with orange lines. The y-axes report the DFT-computed IR intensities (km/mole) for the line spectra. The experimental FTIR spectra in panels B and C (gray lines) were normalized to visually match the theoretical spectra.

**Figure 4.4.** DFT-computed and experimental line spectra for the modes associated with the  $\nu_{C=C}$  motion. Experimental linear spectra for **(a)** C2, blue line and **(b)** C6, navy blue line.

**Figure. 4.5. (a).** 2DIR magnitude spectrum of C2 at  $T = 2.7\text{ ps}$ . The magenta boxes show the integration windows for obtaining the waiting-time traces in panels b-f. **(b-f)**. Waiting-time traces for indicated cross peaks for C2 (blue lines) and C6 (green lines). The traces were fitted with an asymmetric double sigmoidal function.  $T_{\text{max}}$  values are shown in the graphs with matching colors.

**Figure. 4.6.** Scaled waiting-time traces for indicated diagonal and cross peaks for C2. **(a)**. All peaks ( $1530, 1500, 1455$  and  $1430\text{ cm}^{-1}$ ) were fitted globally with a double-exponential decay function (red lines). **(b)**. Cross peaks in the fingerprint region for C2 were analyzed and fitted with a double-exponential decay function (red lines) The insets in A and B show 2DIR spectra measured at  $3.5\text{ ps}$  with color-matching boxes indicating the cross-peak integration regions.

**Fig. 4.7 (a)** 2DIR magnitude spectrum of C6 at  $T = 2.0\text{ ps}$ . The magenta boxes show the integration windows for obtaining the waiting-time traces in panels b-d. **(b-d)** Waiting-time traces for indicated cross peaks for C2 (blue lines) and C6 (green lines). The traces were fitted with an asymmetric

double sigmoidal function (cyan lines for C2 and red lines for C6).  $T_{\max}$  values are shown in the graphs with matching colors.

**Figure 4.8.** Scaled waiting-time traces for indicated diagonal and cross peaks for C6. **(a)** The 1600/1600 and 1600/1570 peaks were fitted globally with a double-exponential decay function (red lines) resulting in  $t_1 = 1.06 \pm 0.06$  ps and  $t_2 = 27 \pm 2$  ps and amplitudes of the fast component of 55% for 1600/1600 and 45% 1600/1570. **(b)** The results of individual fits of  $T$ -traces of diagonal peaks (red lines) are shown in Table 4.4. The insets in (a) and (b) show 2DIR spectra measured at 2.3 ps with color-matching boxes indicating the cross-peak integration regions.

**Figure 4.9. (a)** Scaled waiting-time traces for indicated cross peaks for C6. The traces were fitted globally with an exponential decay function (red lines), see results in Table 4.6. The 1435/1500 cross peak was also fitted with an asymmetric double sigmoidal function (cyan, see Table 4.5). **(b)** Exponential decay times measured are summarized for each diagonal and cross peak. The vertical and horizontal lines are color coded to indicate FTIR contributions originated from different ligands, F<sub>5</sub>Ph (red), Tri (blue), and Tol (green).

**Fig. 4.10.** Waiting-time dependence of the indicated cross peaks for C6. The inset shows 2DIR spectrum measured at 4.3 ps with color-matching boxes indicating the cross-peak integration regions. Thin red lines show fits of the traces with a function  $y = y_0 + A_1 \times \exp(-T/T_1) + A_2 \times \exp(-T/T_2) \times \cos(2\pi T/T_0 + j)$ . The fit resulted in the oscillation period,  $T_0$ , of  $0.78 \pm 0.02$  ps for both cross peaks involving 1460 and 1500 cm<sup>-1</sup> peak and of  $1.6 \pm 0.1$  ps for the peak at 1435/1460. The oscillation damping time,  $T_2$ , was  $0.8 \pm 0.1$  ps for 1460/1500 and 1500/1460 peaks and  $1.2 \pm 0.3$  ps for the peak at 1435/1460. The overall decay time,  $T_1$ , is about 10 ps for all three cross peaks. Complete list of fit parameters is given in Table 4.5.

**Figure 4.11.** Rates of dominant relaxation channels of  $\nu_{C=C}$  computed for **(a)** C2F and **(b)** C6F. The displacements of the strongly contributing normal modes (labeled with stars) are shown as insets. Delocalization factors,  $\chi$ , are shown for each normal mode to the right of its rate bar. Note that  $\chi(\nu_{C=C}) < 10^{-4}$ .

**Figure 4.12.** Delocalization factor,  $\chi$ , for all normal modes below 1650 cm<sup>-1</sup> in **(a)** C2F and **(b)** C6F. Three pairs of significantly delocalized high-frequency modes are shown with red circles. Most high-frequency modes ( $>400$  cm<sup>-1</sup>) are localized at either F<sub>5</sub>Ph ( $\chi \sim 1$ ) or C<sub>2</sub>-Tri ( $\chi \sim 0$ ) ligands. Low frequency modes ( $<400$  cm<sup>-1</sup>) are mostly delocalized across the Pt center.

**Figure 4.13.** Mode frequency of delocalized pairs **(a)** 1354 and 1362 cm<sup>-1</sup>, **(b)** 729 and 790 cm<sup>-1</sup>, and **(c)** frequencies around 360 cm<sup>-1</sup> as a function of the mass scaling factor for the C and F atoms of the F<sub>5</sub>Ph moiety. Vertical red lines show the frequency jump ( $2\beta$ ) of the observed modes.

**Figure 4.14.** Displacements for normal modes at **(a)** 1355 cm<sup>-1</sup>, **(b)** 1362 cm<sup>-1</sup>, **(c)** 394 cm<sup>-1</sup>, **(d)** 359 cm<sup>-1</sup>, **(e)** 790 cm<sup>-1</sup>, and **(f)** 575.5 cm<sup>-1</sup>.

**Figure 4.15.** Rates of dominant relaxation channels in C<sub>2</sub>F for two delocalized modes **(a)** 1361 cm<sup>-1</sup> and **(b)** 1354 cm<sup>-1</sup> and one mode localized at C<sub>2</sub>-Tri ligand, **(c)** 1256 cm<sup>-1</sup>. The values on the right of each bar represent the mode delocalization factor,  $\chi$ .

**Figure 4.16. (a)** Contributions of different groups of modes to the  $\nu_{C\equiv C}/1500(F_5Ph)$  cross peak computed for C<sub>2</sub>F. The groups are formed based on the frequency (>15, >400, 220-400, or 15-220 cm<sup>-1</sup>) and delocalization factor,  $\chi$  (all, >0.96, or <0.1). **(b)** Waiting-time population traces for high-frequency modes of F<sub>5</sub>Ph ( $\chi>0.96$ ) and the mode at 575.5 cm<sup>-1</sup> ( $\chi=0.51$ ). 10-fold normalized population trace for 1362 mode is also shown by black dashed line. **(c)** Cross-peak contributions of the modes shown in panel B. The overall contributions of all F<sub>5</sub>Ph modes ( $\chi>0.96$ ) of frequencies >700 cm<sup>-1</sup> (green) and >400 cm<sup>-1</sup> (black) are shown with dashed lines.

**Figure 4.17. (a)** Contributions of different groups of modes to the  $\nu_{C\equiv C}/1500(F_5Ph)$  cross peak computed for C<sub>6</sub>F. The groups are formed based on the frequency (>15, >400, 220-400, or 15-220 cm<sup>-1</sup>) and delocalization factor,  $\chi$  (all or >0.94). **(b)** Waiting-time population traces for high-frequency modes of F<sub>5</sub>Ph ( $\chi>0.94$ ) contributing the most to the cross peak.

## CHAPTER 5. Coherent Oscillations as Structural Reporters

**Figure 5.1.** Structure of C<sub>6</sub>. Notation for the main functional groups is shown in colors that are used throughout the chapter.

**Figure 5.2.** Solvent-subtracted infrared absorption spectra of C<sub>6</sub> in CDCl<sub>3</sub>.

**Figure 5.3.** 2DIR spectrum of C<sub>6</sub> measured at T= 0.6 ps. The boxes indicate the integration area of various diagonals and cross peaks, where the color of the box indicates the main contributors for each peak in reference to colors in Figure 5.1. Cross-peaks that indicate the presence of oscillations are denoted by the letter “O”. The spectrum was combined from two parts with  $\omega_t$  smaller and larger than 1500 cm<sup>-1</sup>. The FTIR spectrum of C<sub>6</sub> is attached as top panel.

**Figure 5.4.** Waiting-time dependences of the indicated cross peaks for C<sub>6</sub>. The inset shows the 2DIR spectrum measured at 4.3 ps with red boxes indicating the cross-peak integration regions. Red lines show fits of the oscillations with Equation 5.1.

**Figure 5.5.** Scaled waiting-time traces for the **(a)** 1455 cm<sup>-1</sup> and **(b)** 1500 cm<sup>-1</sup> diagonal peaks for C<sub>6</sub>. The insets in both show 2DIR spectra measured at 1.6 ps, with the integration region indicated by the red box. The peaks were fitted globally with a double-exponential decay function (red lines) and the results of the fit are shown in Table 4.4.

**Figure 5.6.** Scaled waiting-time traces for indicated non-rephasing **(a)** diagonal and **(b)** cross peaks for C<sub>6</sub>. The insets show 2DIR spectra measured at 1.6 ps, with the integration regions shown with the red box. The waiting time trace for the 1500 cm<sup>-1</sup> diagonal was fit with Eq. 5.1 (red line).

**Figure 5.7. (a)** Waiting-time dependence of the 1500/1360 cm<sup>-1</sup> rephasing cross-peak. The fit with Eq. 5.1 is shown with the red line, and the non-oscillations component of the fit is shown in green. **(b)** Waiting-time dependence of the same cross-peak, after the subtraction of the non-osc. fit from the data **(c)** Fourier transform of the oscillatory component shown in panel (b), fitted with a Lorentzian function (red line).

**Figure 5.8.** Phase of the signal as a function of time. Blue dotted line represents non-rephasing signal while the red line represents the rephasing signal.

**Figure 5.9.** Double-sided Feynman diagrams associated with the **(a)** rephasing ( $k_R = -k_1 + k_2 + k_3$ ) and **(b)** the non-rephasing ( $k_{NR} = k_1 - k_2 + k_3$ ) 2DIR peaks. The pathways are categorized as ground state bleach (GSB), stimulated emission (SE), or excited state absorption (ESA). In the rephasing sequence, the cross-peaks showcase coherent oscillations, while in the non-rephasing sequence, the diagonal peaks demonstrate coherent oscillations. Furthermore, there is an excited state absorption pathway that demonstrates coherent oscillations in both cases. The signal in such cases is emitted at the frequency difference between a combination band and an excited fundamental. The yellow boxes represent a population state, while the red boxes represent the presence of coherent states which oscillate during  $T$ .

**Figure 5.10.** Double-sided rephasing Feynman diagrams associated with the labeled pathways: **(a)** population transfer and **(b)** relaxation-assisted. The yellow boxes represent a population state. Note that none of these diagrams exhibit oscillations during the waiting time.

**Figure 5.11.** Beam profile of the **(a,b)** pump laser pulses used in 3-beam 2DIR instrument, centered at 1358 and 1610  $\text{cm}^{-1}$  in separate experiments, while the **(c)** probe laser pulse centered at 1431  $\text{cm}^{-1}$  is the same for both experiments.

**Figure 5.12.** 2DIR magnitude spectrum of C6 at  $T = 1.38$  ps for **(a)** 1350/1450  $\text{cm}^{-1}$  pump/probe and **(b)** 1600/1450  $\text{cm}^{-1}$  pump/probe.

**Figure 5.13.** Feynman diagram for double-CT pathway.

## CHAPTER 6: Nanofabrication of Gold array

**Figure 6.1.** Schematic representation of the nanofabrication process sequence

**Figure 6.2.** **(a)** AFM amplitude image of the cross section of PMMA resist and  $\text{CaF}_2$  substrate. **(b)** The resulting cross section of the PMMA.

**Figure 6.3.** Size of the array unit cell (1)

**Figure 6.4.** Optical Microscopy images of the stitching error (red boxes) between two writefields, when unit cell spacing is not taken into consideration.

**Figure 6.5.** Optical setup for FTIR measurement with nanoarrays. A wire grid polarizer selects the polarization of mid-IR radiating parallel (or perpendicular) to the direction of the individual bars of the array. Because of the small size of the nanoarray, an aperture is used to eliminate the radiation passing around the array. The aperture should be placed close to the array, typically within 1 cm distance.

**Figure 6.6.** Linear spectrum of the plasmonic antenna array, where an individual array was  $1.95 \times 0.26 \mu\text{m}^2$  (see Fig. 6.3)

**Figure 6.7.** A representation of the interactions of an electron beam with a resist layer on a substrate. The scattering of electrons causes unintentional exposure of resist (proximity effect)

**Figure 6.8.** SEM images of nanoarrays exposed at (A)  $300 \mu\text{C}/\text{cm}^2$  (B)  $500 \mu\text{C}/\text{cm}^2$  (C)  $650 \mu\text{C}/\text{cm}^2$  and (D)  $1550 \mu\text{C}/\text{cm}^2$ .

**Figure 6.9.** SEM image of deformed arrays due to high dose ( $1330 \mu\text{C}/\text{cm}^2$ )

**Figure. 6.10. (a)** Size of the nanoarray unit cell, designed to have its m-IR peak in the carbonyl region. The edited lengths are marked in bold. **(b)** Linear FTIR extinction of the plasmonic antenna array manufactured to the dimensions in panel (a).

**Figure 6.11.** SEM images of antennas fabricated on a  $\text{CaF}_2$  substrate. The size of an individual array is  $2.10 \times 0.26 \mu\text{m}^2$ .

**Figure 6.12 (a)** Simplified setup of the connected arrays, where orange represents the bars connected to the positively charged terminal and brown represents the bars connected to the negatively charged terminal. **(b)** The LSPR field expected from the setup, purple cloud represents a positive charge while blue represents a negative charge.

**Figure 6.13.** Photomask printed on a transparency, used for photolithography with a positive resist. The terminals are the T-bars on the side and four alignment markers are equally spaced around the circumference of design.

**Figure 6.14.** Schematic representation of the UV lithography process sequence used to fabricate the side terminals.

**Fig. 6.15 (a)** Size of the array unit cell of the electrochemical fabrication. **(b)** Linear spectrum of the plasmonic antenna array of electrochemical cell.

**Figure 6.16.** SEM images of connected antennas fabricated on a  $\text{CaF}_2$  substrate. The size of an individual array is  $2.15 \times 0.26 \mu\text{m}^2$  and the width of the connecting wires are  $\sim 50$  nm thick

**Figure 6.17. (a)** Cartoon diagram shows a schematic representation of a single array and a connected array on a  $\text{CaF}_2$  wafer, providing a clear idea of the geometry and size of the structures. The diagram is made to scale, providing a realistic sense of the dimensions of the arrays. **(b)** An actual image of the fabricated arrays is shown, providing a visual verification of the successful fabrication of the structures.

# CHAPTER 1

## Theory of Vibrational Energy Transport

The work detailed in this dissertation encompasses two topics. The first topic focuses on the study of vibrational energy transport through electronically conjugated systems (Chapter 3) as well as large platinum complexes (Chapter 4). The second study discusses the nanofabrication of gold nanoarrays and their renditions for spectroelectrochemical studies (Chapter 6).

### 1.1. Measuring Vibrational Energy Transport: An Overview

Energy transport in molecules is important for a wide range of fields, spanning from biochemistry<sup>1-9</sup>, chemistry<sup>10-16</sup>, molecular electronics<sup>17-21</sup> to novel materials<sup>22-26</sup> and technology<sup>27-31</sup>. For a long time, it has been recognized that the transfer of vibrational energy within molecules is a ubiquitous driving force behind most chemical processes. However, a comprehensive understanding of the complex mechanisms underlying vibrational energy transfer remains to be unknown. Improved knowledge of how vibrational energy propagates can enable us to customize or enhance these systems for specific requirements, leading to the ability to manipulate chemical reactions and to discover novel reaction pathways that can lead to more efficient chemical systems. For instance, when a peptide undergoes a conformational alteration, additional vibrational energy is required to overcome the barrier. Once the new conformation is obtained, the surplus vibrational energy should be eliminated to make the process irreversible.<sup>32,33</sup> In contrast to the addition of a catalyst, vibrational energy does not lower the activation energy needed for a reaction, but rather supplies enough energy to overcome the conformational barrier of the system.

Efficient vibrational energy transport is also essential for the advancement of emerging technologies like molecular junctions<sup>34</sup> and molecular electronic devices,<sup>35,36</sup> which depend on the rapid and effective transfer of energy for optimal performance.<sup>17,37-39</sup> In order to optimize molecular electronic devices, it is important to study the impact of excess heat on their performance, since these devices are analogous to modern electrical circuits. It is well known that high levels of heat in electrical conduits, due to large resistance or impedance in a wire, can impede the flow of electrons or result in short circuits. Therefore, to develop the most effective materials for molecular electronics, it is

important to gain a complete understanding of not only how energy is transported within the material, but also how it is dissipated or conducted away from the material.<sup>40-42</sup>

There are several experimental methods to study vibrational energy transport in molecules. One such method is surface-enhanced Raman scattering (SERS), a highly sensitive technique that enhances the Raman scattering of molecules supported by some nanostructured materials.<sup>43</sup> For example, Dlott and co-workers utilized SERS to study Raman scattering of benzenethiolate molecules on silver-coated nanosphere lattices.<sup>44</sup> The flash heating of a gold wafer with attached densely packed self-assembled monolayers (SAMs) of long-chain hydrocarbon molecules, combined with sum frequency generation (SFG) was another method used to study energy transport in molecules.<sup>45</sup> Another method is the vibrational excitation of end groups with relaxation-assisted two dimensional infrared spectroscopy, which is discussed in detail in Chapter 2.8.

The  $3\omega$  modulation and time-domain thermoreflectance methods are the most commonly employed techniques for studying energy transport and thermal conductivity in materials. By inducing a temperature gradient in the sample through resistive heating or a laser pulse, these methods enable the measurement of physical changes in the material,<sup>46-48</sup> from which the thermal conductance can be determined. Different energy transport regimes have been detected in such materials, including ballistic and diffusive regimes. Furthermore, as the sample thickness decreases, there is a transition between transport mechanisms, such as from diffusive to ballistic, which can be observed experimentally by a variation in the thermal conductivity coefficient.

The strong covalent bonds in the backbones of molecules present promising prospects for efficient energy transfer. At the molecular level, various techniques using ultrafast laser spectroscopy have been employed to measure the transport of vibrational energy. In such instances, molecular systems are constructed to feature a tag that is excited. Following relaxation, the tag injects excess energy into the molecule, initiating energy transport. The transport can be investigated using a range of reporters, which are sensitive to the arrival of excess energy. Numerous tag moieties are used for this purpose, such as those that necessitate vibrational<sup>15, 49</sup> or electronic excitation,<sup>50-53</sup> as well as the flash-heating of a metal surface to which the molecules are attached.<sup>54</sup> The last two methods generate a significant amount of energy that is either released into the molecule or nearby it, resulting in the initiation of multiple transport pathways. However, isolating the individual contributions of these pathways to the overall transport is challenging. To provide further clarification on this topic, Fourier's law is examined in detail.

Joseph Fourier formulated Fourier's law in the 19<sup>th</sup> century, which provided the initial general understanding of heat transport in materials. According to this law, the heat current density  $\vec{j}$  is directly proportional to the negative gradient of temperature,  $T$ .

$$\vec{j}(\vec{r}, t) = -\kappa \nabla T(\vec{r}, t) \quad (1.1)$$

Where  $\kappa$  is the thermal conductivity of the material ( $\text{Wm}^{-1}\text{K}^{-1}$ ), and  $\nabla T$  is the temperature gradient ( $\text{Km}^{-1}$ ). The minus sign for  $\kappa$  signifies that the direction of heat flow opposes the temperature difference. The volumetric heat capacity, which is the outcome of multiplying the mass density  $\rho$  by the specific heat capacity  $c$ , is defined as:

$$\frac{\partial q}{\partial T} = \rho c \quad (1.2)$$

And the continuity equation for the heat density,  $q$  can be formulated as

$$\nabla \cdot \vec{j} = -\frac{\partial q}{\partial t} = -\rho c \frac{\partial T}{\partial t} \quad (1.3)$$

The general heat diffusion equation can be obtained as follows:

$$\begin{aligned} \frac{\partial T(\vec{r}, t)}{\partial t} &= -\frac{1}{\rho c} \nabla \cdot \vec{j}(\vec{r}, t) \\ &= -\frac{1}{\rho c} \nabla \cdot (-\kappa \nabla T(\vec{r}, t)) \\ &= \frac{\kappa}{\rho c} \nabla^2 T(\vec{r}, t) \\ &= D \Delta T(\vec{r}, t) \end{aligned} \quad (1.4)$$

Hence, Fourier's Law directly implies that heat transport occurs from regions of high temperature to regions of lower temperature, with a thermal diffusion constant,  $D$ :

$$D = \frac{\kappa}{\rho c} \quad (1.5)$$

Fourier's Law is the basis for explaining heat transfer in various scientific fields. This law states that the rate of heat transfer in a material is directly proportional to the negative gradient in the temperature, and the system can be described by its local temperature  $T(\vec{r}, t)$ . It has been widely used to describe heat transport in microscopic to nanoscopic systems at quasi-equilibrium<sup>55, 56</sup>, wherein localized parts of the system along the heat transfer path can be characterized by temperature. However, the quasi-equilibrium conditions required for the application of Fourier's law are not always

met. In situations such as chemical reactions, excess energy is often rapidly released, resulting in a system that lacks a high degree of thermal equilibration, making it difficult to use Equation 1.1 as local temperature is not well-defined.

Aside from heat transport through materials according to Fourier's law, another mechanism for energy transport is through acoustic phonons, which can propagate ballistically. This is further elaborated on in the following section, but in summary, acoustic phonons are low-frequency vibrational modes that are often greatly spatially delocalized forming acoustic bands of states featuring different frequencies. This allows for the creation of vibrational wavepackets that can transport energy at a faster rate and over greater distances than heat redistribution through thermal equilibration.<sup>57</sup>

A method for assessing vibrational energy transfer at the molecular level in non-equilibrium situations is two-dimensional infrared (2DIR) spectroscopy.<sup>58</sup> This approach, which will be elaborated in Chapter 2, employs several laser pulses to stimulate and investigate specific vibrational modes. An advantage of 2DIR is that these modes are frequently confined to a molecule, which enhances comprehension of how vibrational energy can propagate from the excited portion of the molecule (vibrational tag) to the investigated portion (vibrational reporter). These measurements can reveal a range of molecular properties, such as the relaxation rates of individual vibrational modes, the strength of coupling between vibrational modes, the speed of vibrational energy transport within a molecule, the molecule's ability to equilibrate thermally within an environment, and the effects of the environment on molecular characteristics. By adjusting the molecular structure, such as adding or removing functional groups, changing the length of oligomers, or bridging groups, altering the physical properties of the oligomer, and exploring various tag/reporter combinations, it is possible to identify the key parameters that have the most significant impact on the energy redistribution and transport.

## 1.2. Diffusive Energy Transport in Molecules

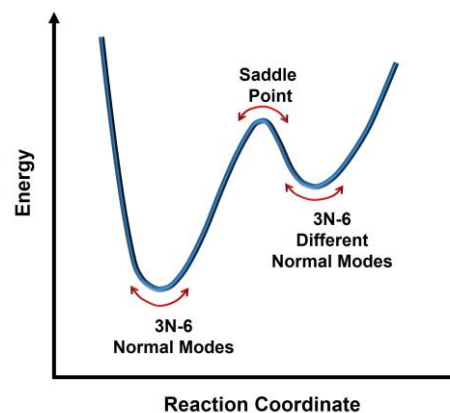
The progress made in investigating thermal conductivity in materials has led to the identification of two main energy transport regimes: diffusive and ballistic. In the diffusive regime, energy is transmitted by randomly hopping between spatially separated and localized vibrational modes.<sup>59, 60</sup> This transport regime has been observed not only in bulk materials but also at the molecular level in various systems, including ionic liquids,<sup>61, 62</sup> peptides,<sup>6, 63, 64</sup> DNA<sup>65, 66</sup> and amino acids.<sup>67</sup>

The diffusive characteristic of heat transport can be comprehended at a microscopic level through the movement of heat carriers, such as electrons or lattice vibrations. These carriers experience random collisions, causing them to move diffusively. Due to the stochastic nature of heat transport, the energy's mean square displacement,  $\langle r^2 \rangle$ , grows linearly with time.

$$\langle r^2 \rangle(t) \propto Dt \quad (1.6)$$

Within molecules, diffusive energy transport is achieved through a process known as intramolecular vibrational energy redistribution (IVR). IVR is a crucial mechanism for thermalizing a molecule by redistributing the vibrational energy among different quantum states of the molecule. Scheme 1 illustrates the reaction coordinate diagram depicting the conversion of reactants into products, highlighting the close relationship between IVR and chemistry. Initially, the vibrational energy is confined to a specific normal mode in one or more oscillators. However, as we progress towards higher energy levels, the harmonic behavior of the system collapses, resulting in an anharmonic breakdown of the normal mode concept. The study of IVR is challenging in highly excited molecules due to this breakdown.<sup>68</sup> Theoretical and experimental studies have shown that by considering the finite rate of energy flow, scientists can better understand how energy is transferred between reactants and products, and this can lead to more precise predictions of reaction outcomes.

IVR involves the redistribution of the population of a polyatomic molecule's initially excited vibrational state among various quantum states of the molecule. Additionally, the states that receive secondary population may further relax into other vibrational modes, and so on. IVR has a significant



**Scheme 1.** Potential Energy of near-harmonic vibrational motion for standard chemical transformation

impact on the reaction dynamics.<sup>69</sup> This necessitates a thorough comprehension of the effects and interactions of different anharmonic (Fermi) resonances that cause the vibrational modes to couple. The anharmonicity between the modes drives the IVR process, whereby well-coupled vibrational states experience faster IVR rates. The diffusive mechanism is common in most molecular systems, especially ones which are large in size, such as peptides and DNA or molecules which lack delocalized vibrational states.<sup>49, 70, 71</sup> Note that delocalized vibrational states are commonly found in oligomeric chains or molecules with repeating units.

In a 3<sup>rd</sup> order IVR process that involves an exchange between an initially excited vibrational mode  $i$ , and lower-frequency modes  $j$  and  $k$ . This leads to energy being dissipated from  $i$  into the combination bands of  $j$  and  $k$ , resulting in transitions that alter the mode population numbers:  $n_i, n_j, n_k \leftrightarrow n_i - 1, n_j + 1, n_k + 1$ . During the IVR process, the total energy must be conserved, meaning that the energy of the initial vibrational mode ( $\omega_i$ ) must be equal to the sum of the energies of the lower-frequency modes ( $\omega_j$  and  $\omega_k$ ). However, if there is a discrepancy in energy, the surrounding environment can compensate for it within the thermal energy scale  $k_B T$ . If the relaxation daughter modes  $j$  and  $k$  are spatially distant from mode  $i$  or delocalized, the single IVR step results in significant increase of the excess energy distribution. A sequence of IVR steps results in diffusive mechanism of excess energy transport.

In an effort to characterize diffusive energy transport and illustrate the extent of diffusive transport in molecules, Naraharisetty et al. conducted an energy transport measurement in a bulk solution of 4-(4-oxopiperidine-1-carbonyl)-benzotrile (PBN)<sup>72</sup> (Fig. 1.1) The concept of IVR can be shown well using the PBN molecule, which features multiple IR-active vibrational modes that are spatially and energetically separated, allowing for selective excitation and probing. This study demonstrated that the energy arrival time when exciting one vibrational mode and probing another can be used to determine bond connectivity. The largest through-bond distance in this compound is ca. 11 Å, which is the distance between the cyano and remote carbonyl groups. The characteristic energy transport time between these groups,  $T_{\max}$ , was found to be ca. 10.6 ps resulting in an average

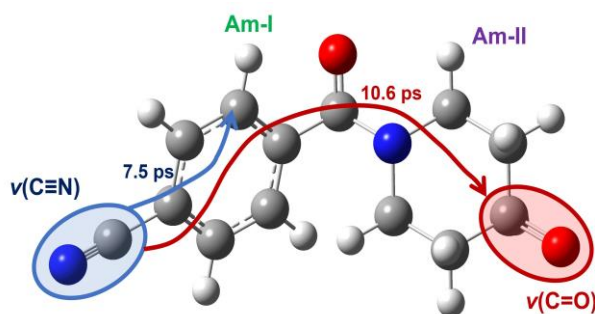


**Figure 1.1.** Structure of PBN and the energy transport time between various modes. The transport time from  $\nu_{\text{C}\equiv\text{N}}$  to  $\nu_{\text{C}=\text{O}}$  and from  $\nu_{\text{C}\equiv\text{N}}$  to Am-I are shown in red and blue respectively.

energy transport rate of 1-1.5 Å/ps (Fig. 1.1). Note that this speed is significantly slower than the speed of sound through water. It was observed that the energy transport time correlates with the effective distance between the respective groups.

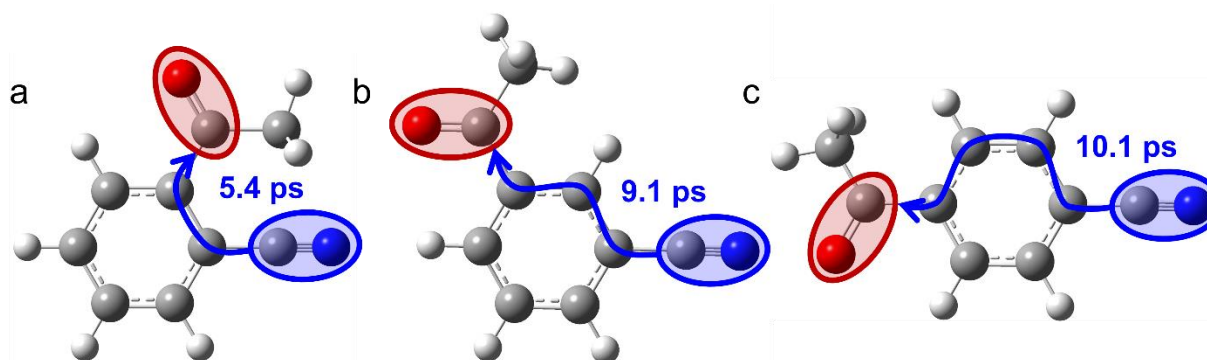


**Figure 1.2.** Energy transport times from  $\nu_{\text{C}\equiv\text{N}}$  to  $\nu_{\text{C}=\text{O}}$  for three acetylbenzotrile (AcPhCN) isomers: (a) ortho, (b) meta, and (c) para.

In a similar experiment, Kasyanenko et al. measured and compared the energy transport times in the ortho, meta, and para isomers of acetylbenzotrile (AcPhCN) (Fig. 1.2)<sup>16, 73</sup>. The findings demonstrated that the energy transport time could serve as a means of determining the through-bond distance between functional groups, including those at very small distances. Furthermore, upon pumping the  $\text{C}\equiv\text{N}$  and probing the  $\text{C}=\text{O}$  modes, the meta and para isomers exhibited an identical transport rate of 2.6 Å/ps. The accompanying modeling<sup>16, 74</sup> depicted how this slow transport rate could be explained as a result of the IVR process.

In both systems, a diffusive mechanism for energy transport was observed. It was determined that the duration of energy transport was directly proportional to the intermodal distance, resulting in an estimated velocity of 1.2 Å/ps.<sup>73, 75, 76</sup> It is worth noting that diffusive transport typically does not lead to a constant speed regime, and instead, it follows a quadratic correlation with inter-site distance.<sup>77, 78</sup> However, under certain conditions, a diffusive energy transfer can display a steady speed regime, which occurs when a significant amount of energy is lost from the molecule into the solvent. In such a scenario, only the IVR steps in the forward direction contribute energy to the reporter, requiring the fewest number of IVR steps possible and resulting in a constant speed.<sup>79</sup> This phenomenon is referred to as directed diffusion.

### 1.3. Ballistic Energy Transport in Molecules

Ballistic transport, in contrast to the diffusive transport regime, is characterized by high speeds and wave packet propagation through extensively delocalized states, rather than slow transport through IVR jumps (or steps) between states. A principle for discriminating between diffusive and ballistic transportation is based on the relative sizes of the mean free path (MFP) of a wavepacket and the transport distance. Specifically, when the MFP is considerably smaller than the transport length, diffusive transport takes place, whereas when the MFP exceeds the transport length, ballistic transport occurs. Internal and phonon boundary scattering can affect energy transport in a material by introducing additional resistance to the flow of phonons, reducing the MFP of phonons and increasing the scattering rate. Hence, in the ballistic regime, Fourier's law is inapplicable, as the energy transport is influenced by both internal and phonon-boundary scattering, and the heat flux is no longer proportional to the temperature gradient<sup>56, 80</sup>.

The ballistic energy transport must occur through delocalized states, therefore molecular structures that support such transport must possess a highly periodic nature. Hence, highly ordered systems like crystals are advantageous for facilitating ballistic transport. Although ballistic transport can also occur in molecules, it requires oligomeric chains with delocalized vibrational modes.<sup>76</sup> The existence of bands in these structures, represented by dispersion curves, arises from their translational symmetry. These bands are composed of delocalized vibrational modes that are defined by their wavevector and energy. For ballistic transport to take place, a wave packet (WP) must be formed as a superimposition of the delocalized vibrational states in one or more bands, and the free time evolution of the WP results in the ballistic energy transport through the substance. The speed of the WP is determined by the width of the vibrational band, which in turn relies on the coupling of the adjacent sites - greater coupling leads to broader bands and faster transport speeds. In the context of the ballistic regime, it is essential that the vibrational modes that constitute the band be dispersed across the entirety of the length of the molecule as the WP can only travel within the range of delocalization of its modes.

Multiple ultrafast spectroscopic studies have demonstrated instances of ballistic energy transport in molecules. In 2004, Schwarzer et al. reported the initial observation of ballistic transport in molecules, which entailed linking azulene and anthracene moieties with alkyl bridges of different lengths.<sup>81</sup> By utilizing a short laser pulse in the visible region, the azulene moiety, which has a notably

short relaxation time, was electronically excited. Through analyzing the rate of cooling of the azulene group in relation to the length of the chain, the researchers determined that the transport through the chain occurs in a ballistic manner.

In another study, Dlott and co-workers utilized sum frequency generation (SFG) spectroscopy to study self-assembled thiolated alkane monolayers chemisorbed onto a gold surface, demonstrating intramolecular transport.<sup>54</sup> This energy transport within the alkyl chain was initiated by the flash heating of gold to ca. 800K. The experiment indicated that the first energy arrival to the CH<sub>3</sub> end group (signaling) occurs ballistically with the transport speed of 9.5 Å/ps, although the overall transport is diffusive.



**Figure 1.3.** Cartoon of an oligomeric chain with two IR active end groups. The RA2DIR experiment is depicted, where the tag (purple) is excited, and the reporter (green) is probed. Energy propagates through the chain (blue) through the ballistic energy transport regime.

Further studies of ballistic transport in oligomers were conducted by employing the dual-frequency two-dimensional infrared (2DIR) technique (Fig. 1.3). In this investigation, oligomer chains were capped with end groups that possessed high-energy vibrational states, which could be selectively excited by mid-infrared (m-IR) laser pulses in order to initiate or detect energy transport. Through these studies, the energy transport speed was determined for different chain types of different energy transport initiators. The relaxation-assisted two-dimensional infrared spectroscopy (RA 2DIR) technique, which is capable of measuring vibrational energy transport between spatially separated groups, was utilized to obtain this information.<sup>70</sup> Further detailed information on this technique will be presented in Chapter 2 of the dissertation.

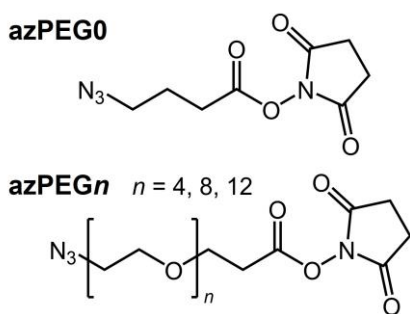


**Figure 1.4.** Structures of the azPEG0, 4, 8, and 12 compounds

Lin et al. reported fast vibrational energy transport in PEG oligomers, determined through the utilization of RA 2DIR spectroscopy,<sup>82</sup> the same method used in the study of energy transport in PBN above. In the study, PEG chains of different lengths (0, 4, 8, and 12 PEG units, Fig. 1.4) were capped with an azido and succinimide ester (NHS ester) groups. Upon initiating energy transport via excitation of  $\nu_{(\text{N}\equiv\text{N})}$  of the azide, a constant speed of 5.5 Å/ps was observed. The initially assumed transport regime was ballistic, due to the high transport speed. The constant speed in PEGs was observed extending up to 12 PEG units, which corresponds to a through-bond distance of more than 60 Å and lasting over 9 ps. In order to determine the mode of the transport, calculations were conducted on the dispersion relations of the PEG chain.<sup>83</sup> These calculations revealed that although numerous chain bands have the potential to aid in the transport, the majority of them have short lifetimes (1-2 ps). As a result, they are unable to sustain a ballistic regime over distances greater than that of PEG8. However, under the conditions of directed diffusion, it is possible for a transition to occur between the regimes of ballistic and diffusive transport, without any sudden alterations to the speed of the transport.<sup>57</sup>

During the past decade, RA 2DIR spectroscopy was used to study vibrational energy transport in a range of oligomeric chain types featuring various end groups. For example, energy transport experiments were performed on perfluoroalkane chains that had been capped with carboxylic acid and CHF<sub>2</sub> groups.<sup>84</sup> The energy transport initiated by the excitation of the carbonyl stretching in the carboxylic acid was determined to be 3.9 Å/ps. Energy transport experiments were also conducted on alkyl chains of varying lengths (CH)<sub>*n*</sub>-s, *n* = 3, 5, 10, 15 methylene units, capped with an azide and NHS ester moieties.<sup>85</sup> The energy transport initiated by the excitation of  $\nu_{(\text{N}\equiv\text{N})}$  was determined to be 14.4 Å/ps. However, energy transport studies in electronically conjugated chains had yet to be studied. The question to be answered is: In what way do electronic conjugated chains impact the mechanism of the energy transport? This question is addressed in Chapter 3 of the present dissertation.

It is interesting to design compounds that possess the capability to support high energy vibrational energy transport. The goal is to develop materials that can efficiently transport vibrational energy over long distances, which is important for applications such as molecular electronics. One approach is to engineer materials with specific vibrational modes that have high energy and long

coherence times, by designing molecules with specific chemical structures. Hence, the detection of high-speed vibrational energy transfer in molecular chains, along with their impressive transport efficiency is of high interest. Notably, the variation in both speed and efficiency across different types of chains presented a compelling opportunity for further investigation. Building upon these observations could enable the creation of molecular systems with specific thermal conductivity properties. However, these findings also led to numerous questions:

1. Does the conjugation of oligomeric chains dictate the maximum speed each chain band can support?
2. How does the end group type affect the efficiency of energy injection into the chain?
3. Under the conditions of direct diffusion, does a transition occur between the regimes of ballistic and diffusive transport in large complex molecules with metal centers?
4. How do we effectively characterize the requirements for efficient energy transfer across transition metal ligands?

The present dissertation aims to tackle these fundamental questions by conducting dual-frequency 2DIR experiments on diverse molecular chains with varying energy-transport initiators. To complement the experimental approach, computational methods, including density functional theory (DFT) computations and various theoretical models, were employed to address these queries. By integrating the experimental findings with the modeling outcomes, a comprehensive mechanistic description of energy transport in conjugated oligomers and large inorganic molecules was obtained.

#### **1.4. Infrared Spectral Signal Enhancement by Plasmonic Nanoarrays**

Surface plasmon resonance (SPR) techniques utilize the optical phenomenon of a resonance at a fixed wavelength that involves the free electrons on the surface of a metal- when electromagnetic radiation excites the conduction band electrons present on a metal surface, they collectively oscillate and produce a localized electric field. This optical phenomenon is particularly evident in the coloring of metallic nanoparticles (NPs). The spectral resonance between the strong electric field and molecular modes that are located in close proximity to the surface of the metal has been shown to amplify the spectroscopic signal of the molecules. In the field of vibrational spectroscopy, researchers have utilized surface-enhanced infrared absorption (SEIRA) spectroscopy and discovered that metallic nanoantennas can significantly enhance IR signal by utilizing the plasmonically-generated near field

enhancement to improve the limit of detection for a given measurement regime. This enhancement can increase the IR signal by several orders of magnitude.<sup>86-92</sup>

Nanodevices that employ plasmon resonances as crucial functional components have surfaced in numerous fields, including but not limited to sensors,<sup>93-98</sup> molecular machines,<sup>99-101</sup> plasmon-assisted chemistry,<sup>102-104</sup> and medicine.<sup>105-109</sup> More recently, these nanodevices have also been commercialized into surface plasmon resonance instruments, which are capable of tracking binding of biological and chemical analytes such as polymers, proteins, and DNA during molecular binding events.<sup>110-112</sup>

During the 1980s and 90s, Osawa et al. were the first to propose the notion of plasmonic effects of metal island films.<sup>113</sup> They subsequently confirmed their findings by utilizing FTIR spectroscopy to measure small amounts of *p*-nitrobenzoic acid deposited on silver metal islands. They detected an amplified spectroscopic signal, which was attributed to the existence of a plasmonic field generated around the metal and the interaction with it.<sup>114</sup> The research following Osawa's work in the field identified two distinct categories of plasmons- surface plasmon polaritons (SPP) and localized surface plasmons (LSP).

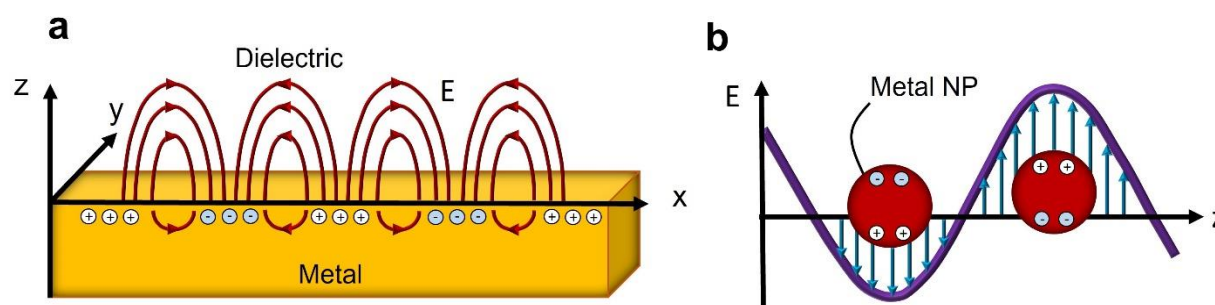


**Figure 1.5.** Different types of surface plasmons: **(a)** surface plasmon polaritons at a metal-dielectric interface and **(b)** localized surface plasmons on a metal nanoparticle excited by free-space light

SPP involves the coating of a whole metal surface with a few nanometers of metal, where the electrons oscillate on the surface, creating an electric field that is perpendicular to the surface (Fig. 1.5a). In LSPs, the electrons that are excited oscillate inside the nanostructure, causing localized plasmonic fields to emerge at various locations within the structure (Fig. 1.5b). Studies have shown that this localized electric field is considerably stronger in areas proximal to the nanostructures, in comparison to the electric field intensity generated by SPPs. This characteristic is crucial for increasing the sensitivity of surface-enhanced spectroscopy. The Pucci group contributed to the existing knowledge by demonstrating the magnitude of the enhanced near-field of the nanostructures, which

was accomplished by mapping it through a combination of experimental and modeling approaches.<sup>87, 89</sup> This study revealed that the most intense regions of the plasmonic field are in close proximity to the surface of the metal nanostructure, and the enhanced near-field rapidly diminishes as one moves away from the surface. Vibrational near-field mapping conducted by Dregely et al. revealed that the ends of specifically designed nanoantennas have the strongest regions of the plasmonic field, whereas the center of these structures shows much smaller enhanced fields.<sup>115</sup>

The LSP resonances exhibit a high degree of sensitivity to the metal particle's size,<sup>116</sup> shape,<sup>117</sup> and dielectric surroundings, and can be adjusted to wavelengths ranging from ultraviolet (UV) to near-infrared (n-IR).<sup>118</sup> LSP resonances that are dipolar in character can be supported by spherical particles (< 50 nm)<sup>119</sup>, while larger metallic particles (> 100 nm) with different shapes have the ability to exhibit multiple LSP resonances<sup>120, 121</sup> that correspond to high-order plasmon modes.<sup>122</sup> For example, Henzie et al. studied the plasmon resonances of Au pyramids with diameters of 100 nm and 250 nm. Additionally, the direction of the wave vector and polarization vectors determine the multipolar excitations of such nanostructures.<sup>123</sup> Hence, some excitation angles result in more pronounced plasmon resonances.<sup>124</sup> Research has shown that both transverse and longitudinal modes can be supported by rod-shaped Au nanoparticles, depending on polarization.<sup>125, 126</sup>

For decades, chemical synthesis was the primary way to synthesize different metal nanoparticle shapes (i.e. stars, rods, wires, boxes), due to the ability to control reaction conditions and chemical precursors.<sup>127</sup> However, the advancement in nanofabrication methods offers an alternative way of designing plasmonic structures into periodic arrays. Direct-write techniques such as Electron Beam Lithography (EBL) and photolithography can be used to fabricate linear and 2D arrays. EBL creates nanoscale patterns by directly writing on resists with a focused electron beam.

The foundation of future advanced technologies lies in fundamental plasmonic research, ranging from its applicability in optics, to electronics and imaging. To achieve this, simplification of fabrication methods by which plasmonic nanostructures are fabricated have to be established, as well as a methodology for lithographic patterning. In this dissertation, the approach toward the development of Au plasmonic nanoarrays with potential electronic applicability is described in detail. Electron beam lithography, photolithography, electron beam physical vapor deposition, and oxygen plasma cleaning are among the techniques used for nanofabrication of Au nanoarrays. The availability of these techniques provides researchers with powerful tools to create arrays with nanometer precision, to enhance different vibrational modes in molecules.

## 1.5. Dissertation Outline

Chapter 2 of the dissertation explains the spectroscopic techniques utilized to conduct the experiments discussed in this work. It covers the underlying principles of non-linear spectroscopy, provides an overview of the RA 2DIR spectroscopic method, and outlines the specifications of the 2DIR spectrometer employed to examine the molecular systems mentioned earlier.

Chapter 3 describes the RA 2DIR study of energy transport via oligo(*p*-phenylene) chains, initiated by both carbonyl and nitro end groups. It was found that oligo(*p*-phenylene) chains had the ability to funnel high-frequency vibrational quanta rapidly and unidirectionally over large distances due to its conjugated property. Chain band structures for an oligo(*p*-phenylene) chains were computed, to determine which chain states were capable of supporting high transport speeds. The IVR pathway rates for energy transport initiation process by C=O and NO<sub>2</sub> stretching modes were evaluated to determine the dominant relaxation channels of both processes. The study identified two distinct groups of wavepackets that had vastly different speeds. The modeling of C=O and NO<sub>2</sub> initiations indicated that the fast wavepackets played a significant role in the overall energy transport speed for C=O initiation, while the slower moving wavepackets determined the energy transport speed for NO<sub>2</sub> initiation. This finding corroborates the observation that there was a substantial difference in the energy transport speeds between C=O and NO<sub>2</sub> initiation. Efficiencies of energy injection into the chain and transport along the chain are found to be very high and dependent on the extent of conjugation across the structure, specifically the conjugation supporting the interaction between the vibrational modes of the end group and the chain states.

Chapter 4 describes the utilization of RA 2DIR spectroscopy to track vibrational energy transport in across metal centers in two platinum complexes featuring a triazole-terminated alkyne ligand of two or six carbons, a perfluorophenyl ligand, and two tri(*p*-tolyl)phosphine ligands. Comprehensive analyses of waiting-time dynamics for numerous cross and diagonal peaks were performed, focusing on coherent oscillation, energy transfer, and cooling parameters. These observables, along with density functional theory computations of vibrational frequencies and anharmonic force constants, enabled the identification of characteristic features of different functional groups of the compounds. Computations of vibrational relaxation pathways and mode couplings were performed, and two regimes of intramolecular energy redistribution are described. One involves energy transfer between ligands via high-frequency modes; the transfer is efficient only if the modes

involved are delocalized over both ligands. The energy transport pathways between the ligands are identified. Another regime involves redistribution via low-frequency delocalized modes, which does not lead to inter-ligand energy transport.

Chapter 5 describes in detail how quantum beats (QB) oscillations in kinetic traces can identify strongly coupled states that typically belong to the same functional group, leading to the accurate identification of such peaks in both linear FTIR and 2DIR spectra of multiple overlapping peaks. Fully resolved vibrational state coherences were analyzed in detail, revealing QB oscillations in the waiting-time dependences of cross peaks and diagonals in the fingerprint region. The quantum beat oscillatory pattern observed provided a direct signature of excited vibrational coherences resulting from coherence. The requirements for oscillations were categorized, and it was determined that highly degenerate local modes in high symmetry cases (such as metal carbonyls) and compact functional groups with many similar local modes (like perfluorophenyl) can result in the formation of normal modes featuring large cross anharmonicities, resulting in quantum beat oscillations. The QB oscillations enhance the potential of 2DIR spectroscopy as an analytical tool.

Chapter 6 describes the nanofabrication process for the fabrication of periodic gold plasmonic nanoantenna arrays on a CaF<sub>2</sub> wafer. A comprehensive description of the nanofabrication of well-ordered gold nanoarrays using electron-beam lithography is provided. These arrays consist of nanorods of various lengths and widths, and have been characterized using several techniques, including scanning electron microscopy, atomic force microscopy, and infrared spectroscopy. Building on the work of previous researchers, we investigated the tuning of surface plasmon resonances in these structures across m-IR wavelengths. To achieve this, we examined various parameters, including nanorod length, width, and spacing. By altering these parameters, we were able to tune the surface plasmon resonances in our structures. The development of an electrochemical cell that can be utilized for molecular adsorption to modify electronic properties is discussed in detail. Such nano creations have the potential to revolutionize the development of nanoscale devices, including sensors, optical switches, and electronic devices.

## CHAPTER 2

# Non-Linear Spectroscopy: Concepts of Two-Dimensional Infrared Spectroscopy

### 2.1. Introduction

Spectroscopy is the study of the interaction of light with matter. It is a technique used to measure and analyze the electromagnetic radiation absorbed, emitted, or scattered by a material. The goal of spectroscopy is to provide information about the composition, structure, and properties of a substance. For instance, analyzing the absorption spectrum of a molecule yields valuable data, such as the wavelength of the absorption peak(s) and the corresponding absorbance. The Golden Rule<sup>128</sup> states that the peak wavelengths provide information regarding the energy levels of the molecule in its excited state, while the absorbance associated with it is directly proportional to the oscillator strength of the transition. The basic principles of the interaction between light and matter can be derived from the quantum Liouville equation, which describes the behavior of a quantum system governed by the Hamiltonian operator  $\hat{H}$  and the density operator  $\hat{\rho}$

$$\frac{\partial \hat{\rho}(t)}{\partial t} = -\frac{i}{\hbar} [\hat{H}(t), \hat{\rho}(t)] \quad (2.1)$$

where Maxwell's equations, which define the behavior of electromagnetic radiation, are utilized to derive the field description in the quantum Liouville equation.

$$\nabla \cdot E(r, t) = 4\pi\sigma \quad (2.2)$$

$$\nabla \cdot B(r, t) = 0 \quad (2.3)$$

$$\nabla \times E(r, t) = -\frac{1}{c} \frac{\partial B(r, t)}{\partial t} \quad (2.4)$$

$$\nabla \times B(r, t) = \frac{4\pi}{c} J(r, t) + \frac{1}{c} \frac{\partial E(r, t)}{\partial t} \quad (2.5)$$

Equations (2.2) through (2.5) relate the electric field,  $E(t)$ , and the magnetic field,  $B(t)$ , to the position vector,  $r$ , and time,  $t$ . These fields are connected to density variables, such as charge density,  $\sigma$ , and current density,  $J$ . The symbol " $c$ " represents the speed of light.

Spectroscopy is used in a wide range of applications, including in analytical chemistry to identify the composition of a sample, in materials science to investigate the properties of materials, in medical diagnostics to analyze biological samples, and in astronomy to study the composition of stars and galaxies. Spectroscopy is a fundamental tool in many areas of science and technology, including chemistry, physics, astronomy, and material science. There are many different types of spectroscopies, each with its own principles and applications. Some common examples of optical spectroscopy include transient absorption spectroscopy, emission spectroscopy, photon-echo spectroscopy, Raman spectroscopy and infrared (IR) Spectroscopy. The work in this dissertation focuses on mid-IR spectroscopy.

Mid-infrared (m-IR) absorption spectroscopy is a form of spectroscopy that operates in the mid-infrared region of the electromagnetic spectrum, typically from 4000 to 400  $\text{cm}^{-1}$ . It is a powerful analytical tool that enables the assessment of a molecule's vibrational modes. Vibrational modes are the different ways in which atoms in a molecule can vibrate relative to one another, and they can be classified as stretching or bending modes depending on the nature of the motion. The absorption spectrum produced by exposing a molecule to m-IR radiation provides valuable information about its vibrational modes.

The advancement of ultrashort pulse lasers has opened up significant opportunities for the development of nonlinear vibrational spectroscopies that can provide real-time information about molecular vibrations. These lasers, made possible by the development of mode locking techniques as well as Kerr-optics, can generate laser pulses with temporal widths shorter than a femtosecond. Ti:Sapphire lasers, which were first developed in 1982, have become the standard light source for ultrafast spectroscopy.<sup>129</sup> Since then, various ultrafast laser spectroscopy methods have been developed.

The studies presented in this dissertation primarily rely on 2DIR spectroscopy as the main experimental technique. 2DIR spectroscopy is a third-order, non-linear spectroscopic method. In the subsequent section of this chapter, the fundamental concepts of linear and non-linear spectroscopy

are explained, based on the principles outlined in the third edition of "Nonlinear Optics, 2<sup>nd</sup> Ed." by Robert Boyd.

## 2.2. Nonlinear Optical Spectroscopy

The measurement of optical spectroscopy is dependent on the interactions between the material under investigation and an applied electric field,  $E(t)$ , which results in the generation of a dipole moment or polarization within the sample. In the case of linear spectroscopy techniques like FTIR, the polarization is directly proportional to the strength of the electric field, as defined by:

$$\tilde{P}(t) = \chi^{(1)}\tilde{E}(t) \quad (2.6)$$

Where  $\chi^{(1)}$  is the linear susceptibility of the material which includes all details of the material response. In microscopic systems, the first-order polarization can be represented as:

$$\mu = \alpha E \quad (2.7)$$

Where  $\mu$  is the induced dipole moment,  $\alpha$  is the linear polarizability, and  $E$  is the interacting electric field. In the presence of a strong electric field, a non-linear behavior can be observed. In the case of non-linear measurements, the optical response can be modeled in a similar manner as linear measurements, by expanding equation 2.6 as a power series of the electric field strength, where

$$\tilde{P}(t) = \chi^{(1)}\tilde{E}(t) + \chi^{(2)}\tilde{E}^2(t) + \chi^{(3)}\tilde{E}^3(t) + \dots \quad (2.8)$$

where  $\chi^{(2)}$  and  $\chi^{(3)}$  are the second- and third-order non-linear susceptibilities, respectively, and each term constitutes part of the optical response, linear and non-linear, of the sample being studied. One instance where this applies is in the representation of the second-order non-linear response of a laser system in terms of the strength of its electric field, which can be given by:

$$\tilde{P}^2(t) = \chi^{(2)}\tilde{E}^2 \quad (2.9)$$

$$\tilde{E}(t) = E_1 e^{-i\omega_1 t} + c. c. \quad (2.10)$$

Where c.c. stands for the complex conjugate. Substituting Eqn. 2.10 into Eqn. 2.9, results in:

$$\tilde{P}^2(t) = 2\chi^{(2)}EE^* + (\chi^{(2)}E^2 e^{-2i\omega t} + c. c.) \quad (2.11)$$

The second-order polarization is comprised of two distinct components. The first component is the contribution at zero frequency, which generates a static electric field via a process called optical rectification and does not produce any electromagnetic radiation. The second component, however, can produce radiation at the second-harmonic frequency of  $2\omega$ .

Analogous explanations can be provided for systems where the interacting electric field comprises two distinct frequency components. In such cases, the electric fields can be characterized as:

$$\tilde{E}(t) = E_1 e^{-i\omega_1 t} + E_2 e^{-i\omega_2 t} + c. c. \quad (2.12)$$

When equation 2.12 is replaced into equation 2.10, the resulting expression provides the non-linear polarization that is expressed as:  $\tilde{P}^2(t) = \chi^{(2)}[E_1^2 e^{-2i\omega_1 t} + E_2^2 e^{-2i\omega_2 t} + 2E_1 E_2 e^{-i(\omega_1 + \omega_2)t} + 2E_1 E_2 e^{-i(\omega_1 - \omega_2)t} + c. c. + 2\chi^{(2)}[E_1 E_1^* + E_2 E_2^*]$ . Where each frequency component in this equation represents a distinct optical signal, such that:

$$P(2\omega_1) = \chi^{(2)} E_1^2 \quad (\text{Second Harmonic Generation})$$

$$P(2\omega_2) = \chi^{(2)} E_2^2 \quad (\text{Second Harmonic Generation})$$

$$P(\omega_1 + \omega_2) = 2\chi^{(2)} E_1 E_2 \quad (\text{Sum Frequency Generation})$$

$$P(\omega_1 - \omega_2) = 2\chi^{(2)} E_1 E_2^* \quad (\text{Difference Frequency Generation})$$

$$P(0) = 2\chi^{(2)} (E_1 E_1^* + E_2 E_2^*) \quad (\text{Optical Rectification})$$

In typical measurements, only one of these frequency components can be detected with a substantial amount of radiation, owing to the phase-matching requirements. As a result, when conducting measurements, it is necessary to choose a specific frequency component.

It is worth mentioning that second-order non-linear optical interactions can only occur in a medium that lacks central symmetry (i.e., non-centrosymmetric). As a result, second-order spectroscopy methods are typically employed to investigate molecular interactions at interfaces rather than in bulk materials, where the even-ordered signals are nullified.

Conversely, third-order signals can be detected in centrosymmetric materials. By expanding equation 2.12 to include three frequency components and placing it into Equation 2.9, a comprehensive third-order contribution to the non-linear polarization can be derived. This outcome

can be divided into its individual frequency components, much like the second-order polarization. However, the third-order component involves a multitude of additional contributions, which comprise:  $\omega_1$ ,  $\omega_2$ ,  $\omega_3$ ,  $3\omega_1$ ,  $3\omega_2$ ,  $3\omega_3$ ,  $(\omega_1 + \omega_2 + \omega_3)$ ,  $(\omega_1 + \omega_2 - \omega_3)$ ,  $(\omega_1 - \omega_2 + \omega_3)$ ,  $(-\omega_1 + \omega_2 + \omega_3)$ ,  $(2\omega_1 \pm \omega_2)$ ,  $(2\omega_1 \pm \omega_3)$ ,  $(2\omega_2 \pm \omega_1)$ ,  $(2\omega_2 \pm \omega_3)$ ,  $(2\omega_3 \pm \omega_1)$ ,  $(2\omega_3 \pm \omega_2)$ .

Due to the vast array of non-linear frequency components generated, several non-linear spectroscopy techniques have been developed. In non-linear spectroscopy, lasers are adjusted to specific frequencies and focused/overlapped onto the sample, prompting a non-linear response. The polarization is measured using an appropriate detector, and diverse structural and dynamical characteristics of the studied molecules can be determined. These measurement techniques include, but are not limited to, sum- and difference-frequency generation (SFG, DFG), transient absorption (TA), 2D pump-probe (PP) spectroscopy, and two-dimensional spectroscopies including 2D infrared (2DIR) spectroscopy. The primary focus of the rest of this chapter will be on 2DIR, which is a powerful tool for studying the dynamics and vibrational properties of molecules and materials. However, to fully appreciate the capabilities of 2DIR, it is important to first understand linear infrared spectroscopy and its limitations.

### 2.3. Linear Infrared Spectroscopy

Linear infrared spectroscopy is a technique that measures the absorption or transmission of infrared light by a sample. The infrared radiation that is absorbed by the sample corresponds to the energy needed to excite the vibrational and rotational motions of the molecules within the sample. The energy levels involved in linear infrared spectroscopy are primarily associated with vibrational modes. For linear absorption, only the two lowest levels in the fundamental transition are considered (Fig. 2.1a).

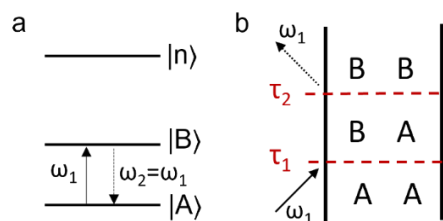


**Figure 2.1.** (a) Energy level and (b) double-sided Feynman diagram of the IR absorption. The arrows represent the interactions with the laser field, where the solid arrow represents excitation, and the dash arrow represents de-excitation.  $\tau_1$  and  $\tau_2$  are the times when the applied field interacts with the system.

When a short laser pulse interacts with a system, causing it to transition from its ground state to an excited state, creating a superposition of the two states. The strength of this transition is determined by the transition dipole. As time passes, the system returns to its ground state and releases a photon. By using perturbation theory, we can study how the system changes over time and calculate how it responds to the laser beam. This response can be represented using a Feynman diagram (Fig. 2.1b), which shows how the system evolves over time.

The linear response function is given by:

$$S^{1D}(t_1) = -\left(\frac{i}{\hbar}\right) \langle A | \mu^{AB}(\tau_2) U^{BB}(\tau_{12}) \mu^{BA}(\tau_1) | A \rangle \quad (2.13)$$

where the time evolution operator  $U^{BB}$  and transition dipoles  $\mu$  are involved, along with the times  $\tau_1$  and  $\tau_2$  at which the system interacts with the electric field, to determine the response function. The response function is then converted from the time domain to the frequency domain using Fourier transformation:

$$I(\omega) = \int_0^\infty S^{1D} e^{-i\omega t_1} \Gamma^{1D}(t_1) dt_1 \quad (2.14)$$

where  $I(\omega)$  is the linear absorption spectrum,  $\Gamma^{1D} = e^{\frac{-t_1}{2T_1}}$  is the relaxation factor, which includes a vibrational lifetime  $T_1$ , and  $\hat{t} = \tau_2 - \tau_1$ .

While linear infrared spectroscopy can provide valuable information about the vibrational modes of a molecule or material, the broadening of spectral lines can obscure important transitions that may contain information about equilibrium fluctuations. Two-dimensional infrared (2DIR) spectroscopy overcomes this limitation by spreading the vibrational spectrum over two frequency axes and providing sensitivity to vibrational couplings. This technique is particularly useful for accessing higher excited states and for studying the dynamics of molecules or materials. 2DIR spectroscopy offers a powerful tool for investigating the dynamics and vibrational properties of molecules and materials in greater detail and as discussed in the following section.

## 2.4. Two-dimensional Infrared (2DIR) Spectroscopy

The principles of 2DIR spectroscopy presented in this chapter section are derived from the book "Concepts and Methods of 2D Infrared Spectroscopy" by Hamm and Zanni.<sup>58</sup>

Unlike linear IR spectroscopies such as Fourier-transform infrared (FTIR) spectroscopy, two-dimensional infrared spectroscopy is an ultrafast laser spectroscopy technique that provides information about molecular structures and dynamics with high temporal and spectral resolution. In 2DIR spectroscopy, a sample is excited by a sequence of precisely timed ultrashort infrared laser pulses. These pulses stimulate molecular vibrations in the sample, producing an oscillating dipole moment. The resulting signals are detected by an infrared detector, which measures the amplitude and phase of the oscillating dipole moments. This enables the examination of molecular vibrational modes and furnishes bond-specific structural details across a range of timescales with resolution as fine as femtoseconds. These measurements are versatile and can be utilized for a wide range of chemical systems spanning from gas to condensed phases.

The fundamental principle of 2DIR technique is based on the coupling of vibrational modes, which allows for the measurement of pair-wise interactions between functional groups within a molecule or between molecules. For example, let us consider the coupling of carbonyl modes on adjacent acetone molecules (Fig. 2.2c). When isolated, each CO group oscillates at a resonant frequency, but when placed near one another, they interact, causing a change in one of the modes to affect the other, resulting in a shift in the fundamental frequency of each. Such vibrational modes are referred to as being coupled. 2DIR spectroscopy enables the measurement of coupling between vibrational modes by recording vibrational cross peaks. To measure a cross peak between two modes, one vibrational mode (vibrational tag) is excited with a short laser pulse, and another mode (vibrational reporter) is probed using another laser pulse.

The interaction energy in the point-dipole approximation resulting from the proximity of two molecular dipoles,  $i$  and  $j$ , indicates the strength of their coupling and can be expressed as:

$$\beta_{ij} = \frac{1}{4\pi\epsilon_0} \left[ \frac{\vec{\mu}_i \vec{\mu}_j}{r_{ij}^3} - 3 \frac{(\vec{r}_{ij} \cdot \vec{\mu}_i)(\vec{r}_{ij} \cdot \vec{\mu}_j)}{r_{ij}^5} \right] \quad (2.15)$$

Where  $\beta_{ij}$  is the coupling between the two modes  $i$  and  $j$ ,  $\vec{\mu}_i$  is the transition dipole of mode  $i$ , and  $\vec{r}_{ij}$  is the vector connecting the centers of transition dipoles  $i$  and  $j$ , and  $\epsilon_0$  is the vacuum permittivity. It

should be noted that this equation is not applicable if the transition dipoles are in very close proximity to each other.

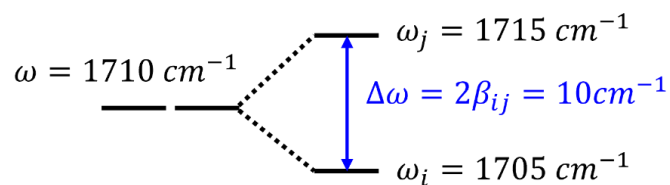


**Figure 2.2.** Energy level split for two acetone molecules, with an unperturbed frequency of  $1710 \text{ cm}^{-1}$ . The split represents  $2\beta_{ij}$ , where  $\beta_{ij}$  is the coupling strength.

For instance, consider two acetone molecules, each with an unperturbed frequency of  $1710 \text{ cm}^{-1}$ . If the dimer pair interacts strongly, with a coupling strength of, say,  $\beta_{ij} = 5 \text{ cm}^{-1}$ , the resulting states would split, causing a  $\Delta\omega = 2\beta_{ij} = 10 \text{ cm}^{-1}$  energy difference (Fig. 2.2, blue arrow) between the new coupled states (at  $1705 \text{ cm}^{-1}$  and  $1715 \text{ cm}^{-1}$ ). These states would be detected in 2DIR spectroscopy as signals on and off the diagonal, representing the signal originating from each mode (diagonal) and the interaction between the two (coupled) modes, respectively.

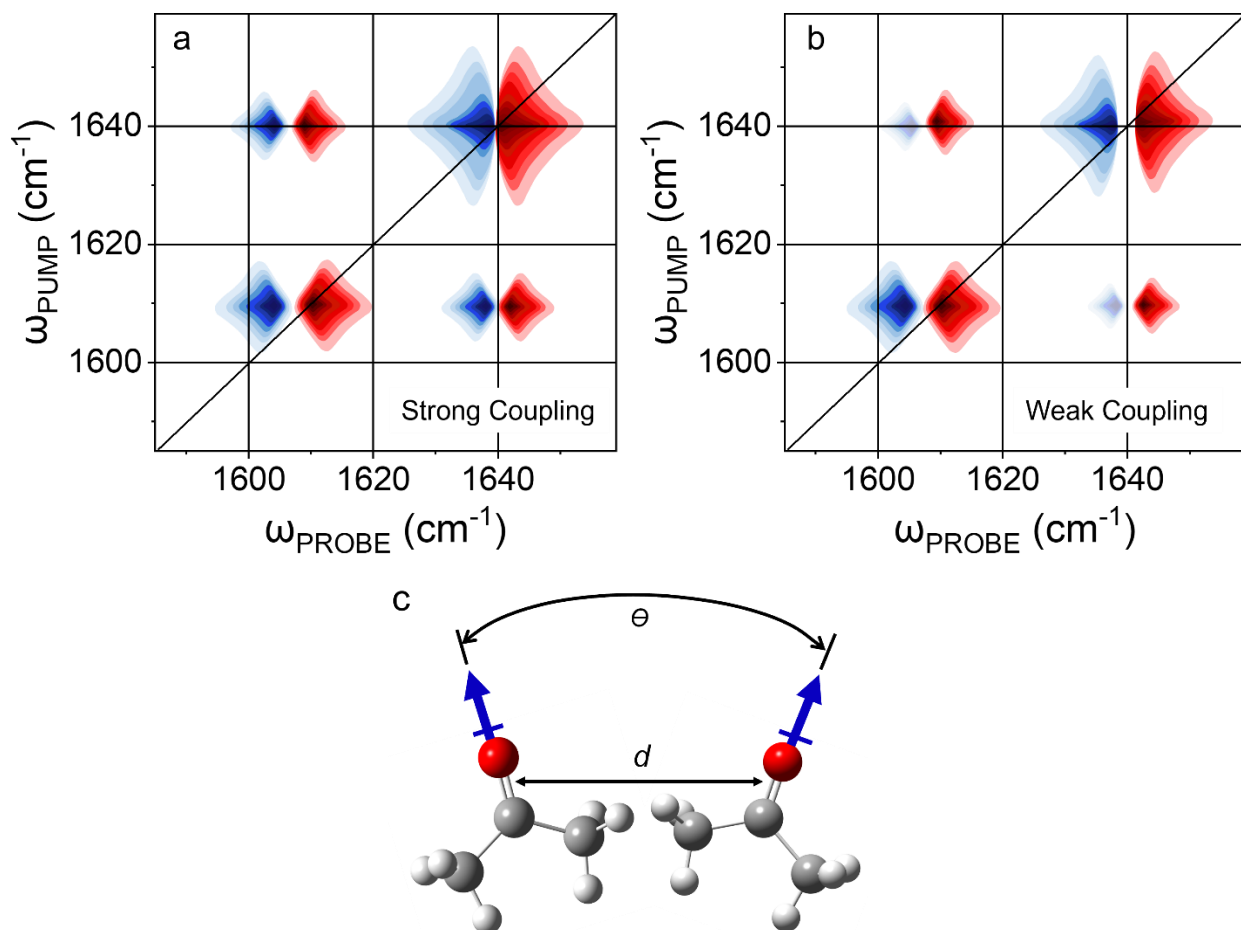


**Figure 2.3.** (a) Simulated 2DIR spectrum, depicting the  $\nu_{\text{C=O}}$  stretches of two acetone molecules coupled with fundamental frequencies at 1610  $\text{cm}^{-1}$  and 1640  $\text{cm}^{-1}$ , with a relative transition dipole coupling of (a) 10  $\text{cm}^{-1}$  and (b) 4  $\text{cm}^{-1}$ . The diagonal peak pairs represent the excitation/stimulated emission of individual molecules, while the cross peaks represent the coupling between their CO modes. (c) The coupling strength depends on the distance,  $d$ , and orientation,  $\theta$ . The carbonyl stretches are represented with transition dipoles (blue arrows).

This concept is depicted in Figure 2.3(a,b), which shows simulated 2D IR spectra for two coupled acetone molecules oriented at  $\theta = 45^\circ$  with respect to one another. In the first spectrum (Fig. 2.2a), the acetone molecules are separated by a few angstroms, resulting in a strong coupling of 10  $\text{cm}^{-1}$ . In the second spectrum (Fig. 2.3b), the acetone molecules are further apart (larger  $d$  value, Fig. 2.3c), so the coupling is weaker (4  $\text{cm}^{-1}$ ). The pump and probe frequencies are represented by the y- and x-axes, respectively. Each acetone molecule creates a pair of peaks near the diagonal of the spectrum, which we collectively refer to as *diagonal peaks*. One peak is positioned exactly on the diagonal while the other is shifted to a different  $\omega_{\text{PROBE}}$  frequency. The peak on the diagonal corresponds to the fundamental frequency,  $\omega_{01}$ , along both axes ( $\omega_{\text{PUMP}} = \omega_{\text{PROBE}} = \omega_{01}$ ), and is regarded as a negative peak. Generally, the negative amplitude peak on the diagonal is associated with the absorption

change in molecules in the vibrational ground state when the excitation laser pulse triggers a  $0 \rightarrow 1$  transition, and the stimulated emission of the excited population back to the ground state ( $1 \rightarrow 0$  transition) through the probe laser pulse. This will be discussed in more detail later in the next section. Due to the anharmonicity of the carbonyl stretch, the other peak is shifted, resulting in a frequency difference between the two peaks known as the *diagonal anharmonic shift*. As the two acetone molecules are coupled to each other, a cross peak emerges. The cross peak also appears in  $180^\circ$  phase shifted pairs. The second cross peak within the pair displays opposite polarity and a different  $\omega_{\text{PROBE}}$  frequency. The *off-diagonal anharmonic shift*, which is connected to the coupling, represents the difference in frequency between the two peaks. Another set of cross-peaks can be observed in the lower portion of the 2D IR spectrum. It is important to note that the anharmonic shifts introduce inherent asymmetry in 2D IR spectra. Therefore, cross-peaks located in the upper and lower portions of the spectrum may appear dissimilar in congested spectra with broad line shapes or cross-peaks that are partially concealed by diagonal peaks. However, they should appear identical in well-resolved spectra.

In Figure 2.1b, the coupling of the two acetone molecules is weak, resulting in a smaller off-diagonal anharmonic shift and smaller cross peak separation. In strongly coupled systems, the pair of peaks in the cross peaks are separated based on the strength of the coupling. However, when no coupling between the two molecules is present (anharmonic shift  $\approx 0$ ), the positive cross peak and negative cross peak will sit on top of one another, canceling one another out. The coupling between molecules creates cross peaks and alters the diagonal peaks too. Due to the formation of a multidimensional potential energy surface resulting from the coupling, the frequencies, anharmonic shifts, and intensities of the diagonal peaks undergo changes, displaying a slightly different curvature than in isolated molecules. The coupling strength and orientation of the molecules can be determined without utilizing 2D spectroscopy by measuring the frequency shifts and intensity changes of fundamental transitions with standard linear (FTIR) spectroscopy and isotope labeling. Nevertheless, 2DIR spectroscopy is a more effective means of measuring the coupling, requiring considerably less effort.

The example of coupled acetone molecules offers a qualitative depiction of the influence of coupling on the vibrational frequencies of these molecules, as well as how coupling can lead to the formation of cross-peaks. The next section will provide a more comprehensive explanation of how 2DIR can be utilized to describe the potential energy surface of such oscillators.

### 2.4.1. 2DIR Spectrum of a Single Vibrational Mode

Within this section, we will examine the most straightforward scenario of how a 2DIR spectrum appears for a single vibrational mode, using the carbonyl stretch of an acetone molecule as an example. To construct the 2DIR spectrum, the eigenstates and transition dipoles for the vibrational mode of the studied molecule are needed. The Morse oscillator can be utilized to depict the potential energy surfaces of molecular vibrations, as follows:

$$V(r) = D(1 - e^{-ar})^2 \quad (2.16)$$

Where  $D$  is the depth of the well,  $r$  is the interatomic distance, and  $a$  is the curvature of the potential well. When the Schrodinger equation is solved perturbatively for the anharmonic oscillator, the vibrational eigenstates obtained are:

$$E_n = \hbar\omega \left(n + \frac{1}{2}\right) - x \left(n + \frac{1}{2}\right)^2 \quad (2.17)$$

where  $\omega$  is the harmonic frequency,  $n$  is the quantized eigenstate of the oscillator, and  $x$  is the anharmonicity.

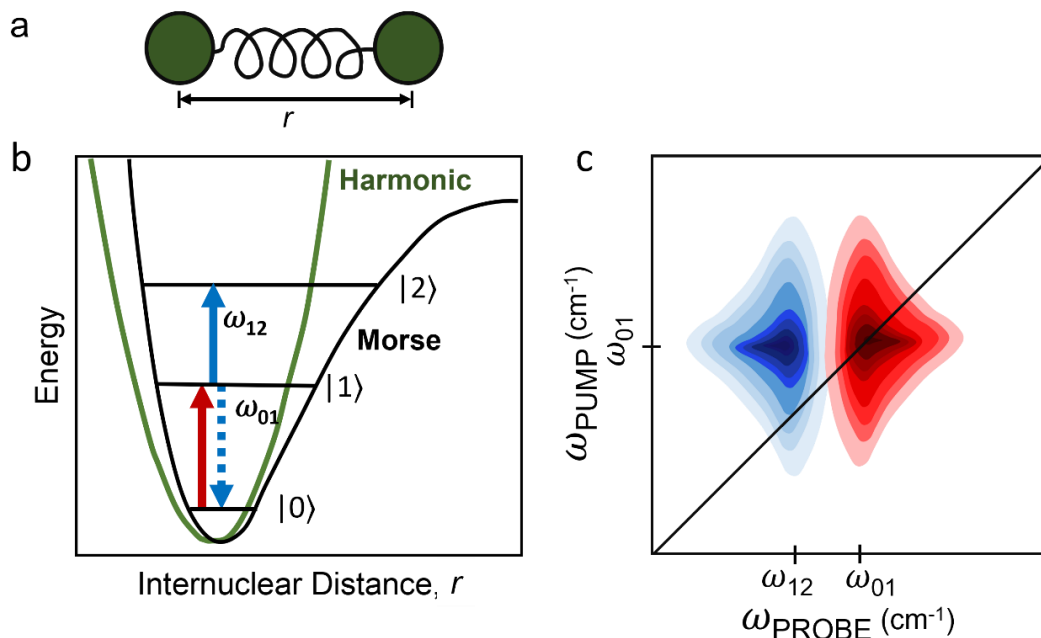


**Figure 2.4.** (a) Spring model representing a diatomic molecule, separated by distance,  $r$  (b) Energy level scheme of a harmonic oscillator (green line) and an anharmonic oscillator (black line) with the dipole-allowed transitions depicted. The red arrow represents the pump process, while the blue arrows represent the probe process. (c) The resulting 2DIR spectrum. The red contour represents negative response (GSB, SE) and the blue contour represents positive response (ESA).

The 2DIR spectrum can be measured either in the time or frequency domain. In this discussion, we will start with the frequency domain measurements, in which a basic pump-probe experiment can be utilized to generate the 2DIR spectrum. The pump-probe method is the most straightforward 2DIR technique, and hence, the correlation spectrum depicted in Figure 2.4b will be explained in the context of a pump-probe experiment. Here, we scan the frequency of a pump pulse over the resonance frequency of the oscillator and graphing its absorption as the y-axis on a 2D plot. In such an experiment, the sample is subjected to two laser pulses. The first pulse (known as the pump pulse) is a narrow-band pulse tuned to frequency  $\omega_{01}$  ( $\omega_{01} = \hbar\omega - 2x$ , where  $\hbar$  is the reduced Planck constant,  $\omega$  is the vibrational frequency of the oscillator and  $2x$  is the energy of the excited state relative to the ground state), which excites some molecules from their vibrational ground state  $|0\rangle$  to the first vibrationally excited vibrational state  $|1\rangle$  (Fig 2.4b, solid red arrow).

After the pump pulse, we proceed to scan the frequency of a probe pulse for the x-axis. The second pulse (probe), which is often spectrally broad, follows the pump and induces a fraction of molecules in the vibrationally excited state to undergo stimulated emission back to the ground state (Fig 2.4b, dotted blue arrow.) or to be promoted to the second vibrational excited state  $|2\rangle$  by excited state absorption (Fig 2.4b, blue solid arrow). Moreover, due to the reduced number of molecules in the ground state, the probe pulse is expected to experience less absorption compared to the scenario where no pump pulse is applied. The third-order signal aligns with the probe beam and is always in phase with it. Difference spectra are normally measured to contrast of absorption between the pump on and off spectra. The resulting spectrum for a three-level system will feature a SE and GSB peaks at  $\omega_{01}$  and ESA peak positive at  $\omega_{12}$ , which is red-shifted  $\omega_{01}$  due to the anharmonicity of the potential, (Fig. 2.4c, blue contour lines)  $\omega_{12} - \omega_{01} = 2x \equiv \Delta$ , known as the *diagonal anharmonic shift*.

Hence, when we plot the absorption based on the frequencies of the pump and probe, we will observe a dual set of peaks in the 2DIR spectrum with opposite polarities. Meanwhile, the signal for excited state absorption will manifest at  $\omega_{\text{PUMP}} = \omega_{01}$  and  $\omega_{\text{PROBE}} = \omega_{12}$  (Fig 2.4c, blue contours). Note that even though the negative peak results from two processes and the positive peak results from only one, the amplitudes of the positive and negative peaks will have similar intensities as the  $1 \rightarrow 2$  excited state absorption is twice as strong as a  $0 \rightarrow 1$  transition as  $\mu_{12}^2 = 2\mu_{01}^2$  according to the harmonic oscillator dipole transition moment scale. The anharmonic shift of the oscillator can be directly obtained from a 2DIR spectrum if the GSB and ESA peaks are distinctly isolated. However,

this is applicable only if the anharmonic shift is greater than the bandwidth of the transition. In the next section, the 2DIR spectrum of two coupled vibrational modes will be discussed.

### 2.4.2. 2DIR Spectrum of Two Coupled Vibrational Modes

The 2DIR spectrum of coupled oscillators encompasses significant information regarding the interaction strength of two vibrational states based on their transition dipoles, which includes information related to the distance between the two modes. Consider two transition dipoles, labeled 1 and 2, which are adequately distant from each other. The potential describing these two coupled oscillators is calculated as:

$$V(r_1, r_2) = V_1(r_1) + V_2(r_2) + \beta_{12}r_1r_2 \quad (2.18)$$

Where  $V_n(r_n)$  are the 1D potentials of each vibrational mode, and  $\beta_{12}$  is the coupling if transition dipole-dipole coupling is adequate. In the case of two coupled oscillators, such as two atoms in a molecule, the vibrational modes of each atom can combine to create a new, higher-frequency mode- a combination band. For example, we consider a water molecule, H<sub>2</sub>O which has several vibrational modes, such as O-H stretching and bending (Fig 2.5 a,b). In addition to these fundamental modes, the bending mode can combine with the stretching mode to form a combination band known as the bending-stretching combination band (Fig. 2.4c).<sup>130</sup> Combination bands are observed when more than two or more fundamental vibrations are excited simultaneously. The energy of the combination band is the sum of the two fundamental band energies.

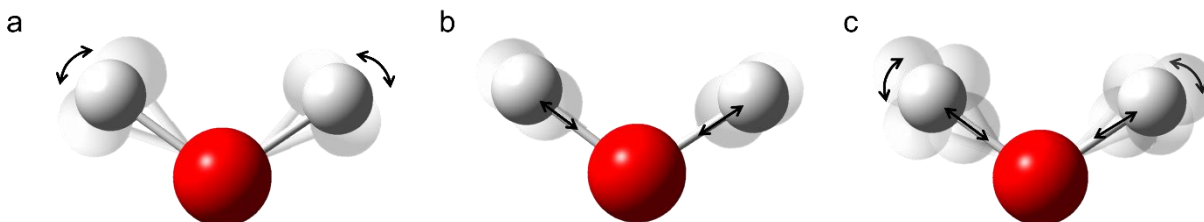


**Figure 2.5.** Types of vibrational couplings of the H-O-H molecule. **(a)** Bending-bending mode **(b)** stretching-stretching mode **(c)** bending-stretching mode, known as a combination band.

Now we consider two coupled oscillators, due to the coupling and interaction between them, they do not act as independent oscillators anymore, and instead form combination bands, where their combination band shifts from the value of  $\omega_1 + \omega_2$ , where  $\omega_1$  and  $\omega_2$  represent the fundamental frequencies of vibrational modes 1 and 2, correspondingly. Thus, besides observing anharmonic shifts

in the diagonal peaks ( $\Delta_{11}$  and  $\Delta_{22}$  represent the diagonal anharmonicity terms for transitions 1 and 2, respectively), the combination band experiences a shift due to the off-diagonal anharmonicity  $\Delta_{12}$ , as shown in Figure 2.6b. Consequently, transition dipoles that have a strong interaction will exhibit significant off-diagonal anharmonicities, which leads to a more substantial frequency shift off the cross peak compared to a pair of dipoles with a weaker interaction. In cases where anharmonicity is small, which is often the scenario, the selection rules of harmonic oscillators continue to apply. This implies that only one oscillator can experience a single-quantum change at any given time, and the intensity of the transition is determined by the transition dipole of that oscillator. Here,  $|kj\rangle$  represents a state with  $k$  quanta of excitation in the first mode and  $j$  quanta in the second mode. For example, transitions  $|10\rangle \rightarrow |20\rangle$  and  $|10\rangle \rightarrow |11\rangle$  are dipole allowed, but  $|10\rangle \rightarrow |02\rangle$  is forbidden. The arrows in Fig 2.6(a) show all the possible allowed transitions for two coupled oscillators.

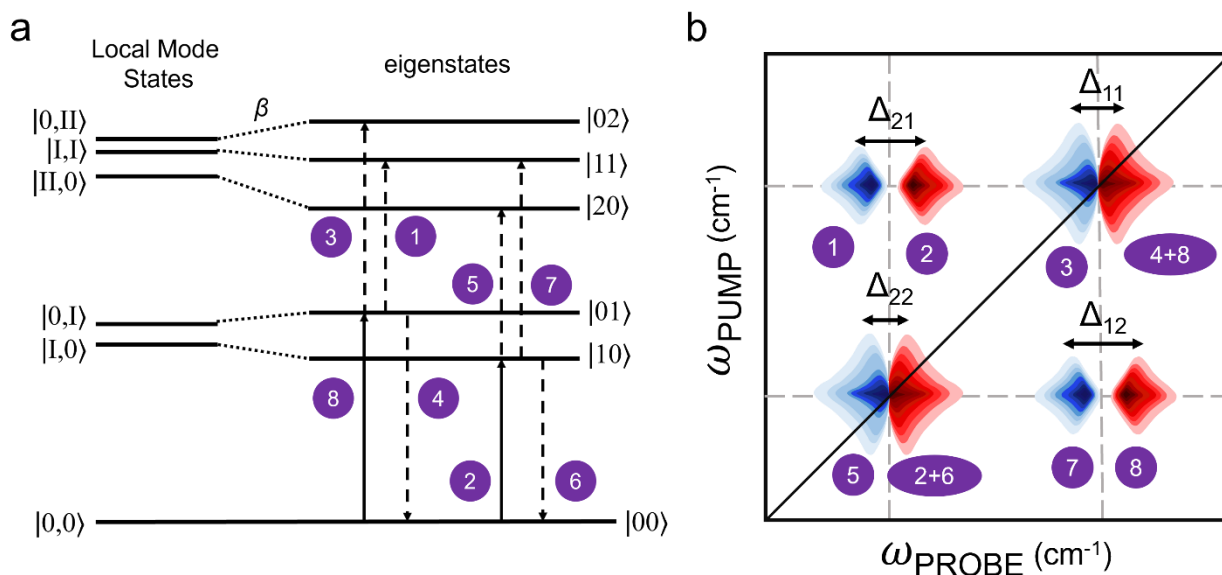


**Figure 2.6.** (a) Energy level scheme of two coupled oscillators before coupling (left, local modes) and after coupling (right, eigenstates). The dipole-allowed transitions are depicted. The solid arrows represent the pump process, the dotted arrows the probe process. (b) Resulting 2D IR spectrum. Red peaks represent GSB (and SE for diagonal peaks), shown as negative, while blue peaks represent ESA, shown as positive peaks.

Figure 2.6b shows a constructed 2DIR spectrum of two coupled oscillators. When the pump frequency matches the frequency of one of the fundamental transitions of eigen states, a transition from the ground state to an excited state is induced. To achieve this, we scan the pump frequency across the resonances of both oscillators. When the pump frequency becomes resonant with an

eigenstate, we note that frequency along the y-axis. Figure 2.6a gives our nomenclature for labeling the eigenstates of two coupled oscillators, denoted as 1 and 2.

If the pump is in resonance with the oscillator with the higher frequency, we will excite state  $|01\rangle$ . The probe pulse that follows can now induce one of three distinct transitions denoted as ①, ③, and ④ (Fig. 2.6a, purple circles). Furthermore, since the number of molecules in the shared ground state  $|00\rangle$  decreases, the probe pulse records it as a sample bleach on both oscillators, resulting in the emergence of transitions ⑧ and ②. Among the transitions, ⑧, ④, and ③ are identical to those observed for a single oscillator (Fig. 2.4b), corresponding to bleach, stimulated emission, and excited state absorption, respectively, of the higher-frequency oscillator, resulting in the diagonal peak at the higher frequency, with a diagonal anharmonicity of  $\Delta_{11}$ . Similarly, the second diagonal peak of the lower-frequency oscillator forms as a result of transitions ②, ⑤, and ⑥ (GSB, ESA, SE, respectively), with a diagonal anharmonicity of  $\Delta_{22}$ .

Transitions ① and ⑦ are new in the case of coupled oscillators. Transition ① involves the excitation of the lower oscillator by one quantum from its ground state to the first excited state, where the higher-frequency oscillator already has one quantum of excitation:  $|0,1\rangle \rightarrow |1,1\rangle$ . If the two oscillators were not coupled, the excitation frequency of the second oscillator would remain unaffected by the number of quanta present in the first oscillator, resulting in identical frequencies for the  $|00\rangle \rightarrow |1,0\rangle$  ② and the  $|0,1\rangle \rightarrow |1,1\rangle$  transitions ①. Consequently, the GSB (red peak) and ESA (blue peak) would coincide perfectly and cancel each other due to their identical transition strength but opposite sign. However, since two cross-peaks are present in the 2DIR spectra of two coupled oscillators,  $\Delta_{21}$  and  $\Delta_{12} \neq 0$ .

The presence of a cross-peak in a 2D IR spectrum indicates significant coupling between the two oscillators, where the transition frequency of one oscillator is influenced by the excitation level of the other oscillator. It should be noted that transition dipoles that exhibit strong interaction will display significant off-diagonal anharmonicities, leading to a higher off-diagonal frequency shift as compared to dipoles that have weak interaction. Therefore, the presence and absence of cross-peaks in 2DIR spectra provides insights on the coupling strength of modes in a molecule which can be linked to its structure.

## 2.5. Frequency-Domain 2DIR Spectroscopy

There are two general ways to collect 2DIR spectra: in the frequency domain or in the time domain. The frequency-domain single-frequency pump-probe method is the most straightforward 2DIR spectroscopy technique, first demonstrated by the Hochstrasser group in 1998.<sup>131</sup> To perform these measurements, a spectrally narrow IR pulse is scanned over a range of m-IR frequencies. A broad-band probe pulse is then tuned to the same or a different spectral region, which generates a 3rd-order response, as described in the previous section. The homodyned detection technique involves the co-propagation of the non-linear signal with the probe pulse towards the detector so that the probe pulse is serving as a local oscillator.

Although these measurements are relatively simple, they have several disadvantages. Firstly, the signal-to-noise ratio is low since the probe pulse is much stronger than the signal. Secondly, the pump pulse is spectrally narrow, which makes it broad in time, resulting in a reduced time resolution for the experiment.

## 2.6. Time-domain Dual-frequency 2DIR Spectroscopy

Although more complex, time-domain 2DIR spectroscopy offers greater sensitivity and higher signal-to-noise ratio than frequency-domain 2DIR spectroscopy. There are two ways of doing time-domain 2DIR measurements- using two beams or three beams.

In two-beam 2DIR IR-pump IR-probe measurements, two excitation beams are typically derived from a single source and split into two beams, which are independently delayed, recombined into a single beam (pump beam), and directed at the sample. The time delay between the two pulses of the pump beam is scanned during the measurements. The detection beam, containing a single pulse, overlaps with the pump beam in the sample and is directed to a spectrometer and a detector; as for the frequency-domain 2DIR, it also serves as a local oscillator, which is known as homodyned detection. By varying the delay time of probe beam, the waiting time, the vibrational dynamics can be tracked. Fourier transformation is used to deconvolute the frequency components in the obtained signal. As no separate LO beam is required, the measurements are fairly straightforward and often feature higher sensitivity than frequency-domain measurements. A benefit of utilizing two-beam 2DIR pump-probe measurements is that it guarantees accurate phase detection in the results obtained.

Another two-beam 2DIR method used is pulse-shaping, where the temporal profiles of the pump and probe pulses are used to excite and detect the sample respectively.

In three-beam 2DIR measurements, all three incoming beams at the sample feature single, broad-band pulses but have different directions (Fig. 2.7c). As a result, the 3<sup>rd</sup>-order signal is emitted in the direction not overlapping with the directions of the three beams and separate LO beam is required for heterodyning. Such arrangement, while significantly more involved to execute, offers an opportunity to change the LO intensity independently of that of beam 3, resulting in background-free measurements and significantly higher sensitivity. The pulse sequence for dual-frequency 2DIR measurements is shown in Fig. 2.7b. The probe pulse arrives at time delay  $T$  after the 2<sup>nd</sup> pulse, and the second femtosecond pump pulse is separated in both time and space, and the delay between the two pulses ( $\tau$ ) is varied during the measurements. After a delay time of  $T$  following the second pulse, the probe pulse arrives, and the third-order signal is emitted in a different direction, separate from the directions of the three beams. The electric field of the third-order signal is recorded using heterodyned detection. The technique of heterodyned detection is utilized for the measurement of the third-order signal of a molecular system.<sup>132</sup> To extract information from an optical signal, a local oscillator (LO) laser pulse with higher intensity is combined with the signal at the detector, producing an interference pattern that reveals details about the signal. By altering the delay of the LO, the signal can be scanned, and the detector returns a value that is proportional to the square of the total electric field it receives. To isolate the LO field, an optical chopper is often employed, and its value can be subtracted from the total received value:

$$S(\tau, t, T) = (E_{LO} + E_{FID})^2 - (E_{LO})^2 = 2E_{LO}E_{FID} + E_{FID}^2 \approx 2E_{LO}E_{FID} \sim E_{FID} \quad (2.19)$$

where  $S(\tau, t, T)$  is the resulting signal,  $E_{LO}$  is the electric field of the local oscillator,  $E_{FID}$  is the electric field of the emitted 3<sup>rd</sup>-order signal.

Since the signal is amplified with the use of the LO, the advantage of heterodyned detection is that it reduces noise and improves the signal-to-noise ratio, resulting in higher sensitivity and better detection limits. While both techniques provide information on the vibrational dynamics and couplings in the sample, three-beam 2DIR generally offers better sensitivity and resolution. However, it also requires more complex instrumentation and experimental setup, as described below.

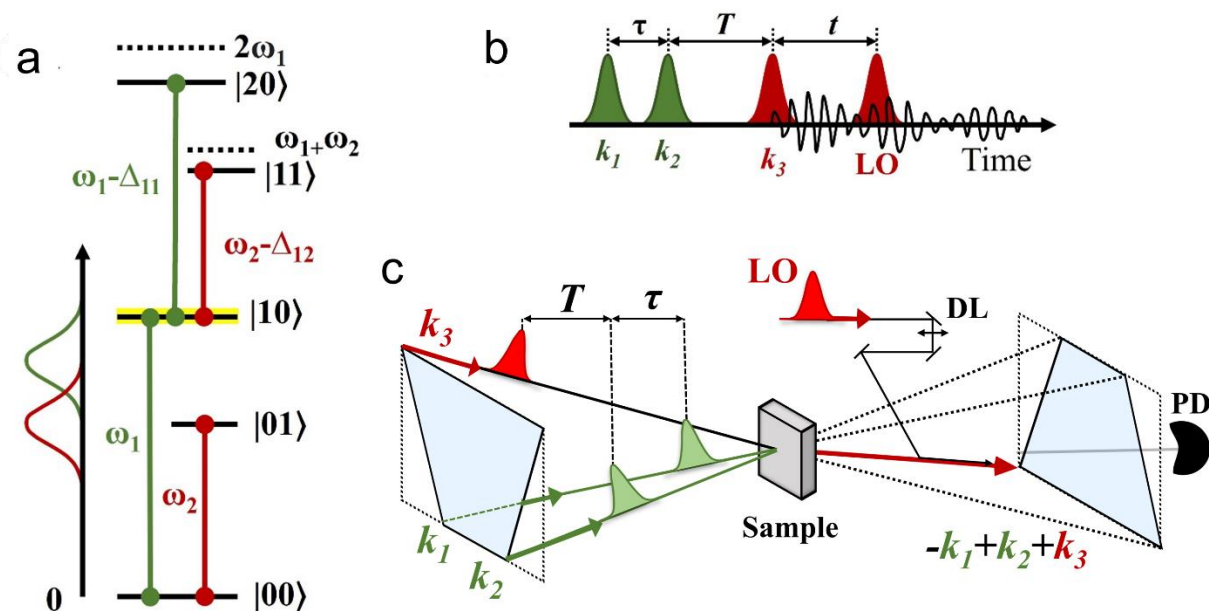


**Figure 2.7.** (a) Energy diagram for vibrational modes  $\omega_1$  and  $\omega_2$  showing coherence and population states accessed by the pulse sequence. The spectra of the IR pulses are shown on the left. (b) Delays between the pulses in dual-frequency 2DIR measurements.  $\tau$  is the delay between  $k_1$  and  $k_2$ ,  $T$  is the delay between  $k_2$  and  $k_3$ , and  $t$  is the delay between the local oscillator and the 3<sup>rd</sup>-order signal. (c) Schematic of the beam directions in a three-pulse dual-frequency 2DIR experiment.

The sample is interrogated by three ultrashort laser pulses arranged in a boxcar geometry, with each pulse being one of the corners of the "box". The first two pump pulses, associated with wavevectors  $\vec{k}_1$  and  $\vec{k}_2$  and frequency  $\omega_1$ , are adjusted to the frequency of the vibrational tag, while the  $\vec{k}_3$  probe ( $\omega_3$ ) and LO pulses are adjusted to the frequency of the vibrational reporter, which may be the same as the pump when measuring diagonal signals or different when measuring cross peaks. Depending on the type of measurement being conducted, the directionality of the laser pulses used to interrogate the sample must be altered to satisfy the phase-matching conditions (*vide infra*).

Having explained the application of the heterodyned detection technique, let us now delve into how this method can be employed to investigate energy transport in a molecular system. By observing the effects of laser pulses on the local states, we can gain insights into how energy is transferred within the system. Consider a molecular system with two closely spaced and strongly interacting vibrational modes, denoted as  $|01\rangle$  and  $|10\rangle$ . To induce a specific vibrational coherence state, the system is initially excited by a pump pulse,  $k_1$ , placing it in the state  $|01\rangle\langle 00|$ . Following the first interaction with the field ( $k_1$ ), the molecular system undergoes oscillation during  $\tau$ . The second

pulse,  $k_2$ , interacts with the sample and produces a population state  $|01\rangle\langle 01|$ . During the waiting time  $T$ , (already introduced) the system undergoes population relaxation. The third pulse,  $k_3$ , prepares another coherence state, for example,  $|11\rangle\langle 01|$  for the excited-state absorption signal, which emits radiation. This radiation is then combined with the local oscillator, spectrally dispersed by a spectrograph, and  $\omega_t$ , producing the frequency axis. The 2DIR spectrum is obtained by scanning the delay between the first and second pump pulses,  $\tau$ , at fixed waiting time,  $T$ , and Fourier transform  $\omega_\tau$  data to generate  $\omega_\tau$  axis.

When measuring diagonal signals (pump and probe have similar central frequencies), the laser pulses are arranged in what is typically referred to as "boxcar geometry," with each pulse occupying a distinct corner of the box. However, when measuring cross peaks, the separation between the directions of the pump pulses has to be adjusted resulting in trapezoid geometry in the beam cross section (Fig. 2.7c). The geometry, the  $\vec{k}_1$ ,  $\vec{k}_2$ , and  $\vec{k}_3$  wavevector directions, has to be set so that  $\vec{k}_S = -\vec{k}_1 + \vec{k}_2 + \vec{k}_3$  and  $\omega_S = -\omega_1 + \omega_2 + \omega_3$ , which are called phase-matching conditions. Here,  $\vec{k}_S$  and  $\omega_S$  represent the wavevector and frequency of the 3<sup>rd</sup>-order signal, respectively. By meeting these phase-matching conditions, the non-linear signal appears in the direction of the fourth corner of the box or trapezoid, depending on the measurement, such that it is isolated from pump and probe beams, enabling background-free conditions that provide ultimate sensitivity of the 2DIR measurement.

## 2.7. Relaxation Assisted 2DIR Spectroscopy

The studies conducted in this dissertation employ a technique known as relaxation assisted 2DIR (RA 2DIR) spectroscopy, which is a variant of time-domain dual-frequency 2DIR. RA 2DIR is based on the principle that when the excited mode (tag) relaxes, a significant amount of energy is residing inside the molecule.<sup>70</sup>

The sample is excited at frequency  $\omega_1$  by the first two m-IR pulses (Fig 2.8b, red line), resulting in an excited population state. This excess energy propagates in all directions, including towards the reporter. When the excited state is probed at the frequency of the reporter ( $\omega_2$ ), a cross-peak appears at approximately  $(\omega_\tau, \omega_t) \approx (\omega_1, \omega_2)$ . The energy of the combination state appears at  $\omega_1 + \omega_2 - \Delta_{12}$ , due to a non-zero off-diagonal anharmonicity  $\Delta_{12}$ . If the two modes are spatially far and interact weakly (small  $\Delta_{12}$ ), the excited state absorption peak at  $(\omega_1, \omega_2 - \Delta_{12})$  and the GSB peak at

( $\omega_1, \sim\omega_2$ ) will experience strong mutual cancellation. This is because excitation at  $\omega_1$  leads to the bleach of the ground state bleach at  $\omega_2$  (Fig. 2.8d, green circle) and a new absorption at  $\omega_2 - \Delta_{12}$  (Fig. 2.8d, orange circle). No cross-peak will result if the anharmonicity  $\Delta_{12}$  is smaller than the transition width at  $\omega_2$ , due to strong mutual cancellation of the two signals (Fig. 2.8d). However, a small cross-peak may occur for spatially remote tag and reporter, owing to their small anharmonicity.

As the waiting time increases, the IVR process gradually increases the spatial location of the excited region in the molecule. When the excess energy reaches the reporter mode, it excites low-frequency vibrational modes ( $\omega_X$ ) (Fig. 2.8a, blue circle). Since the mode(s) with frequency  $\omega_X$  have significant spatial overlap with the reporter mode, they are often well coupled to the reporter resulting in two transitions when probed at approximately  $\omega_2$  (Fig. 2.8b, green line): the ground state bleach, giving a negative signal at  $\omega_2$  (Fig. 2.8f, green circle), and new absorption from the  $\omega_X$  state to the combination state of mode X and the reporter (Fig. 2.8b, right orange line), producing a positive peak at ( $\omega_1, \omega_2 - \Delta_{X2}$ ) (Fig. 2.8f, orange circle). The larger  $\Delta_{X2}$  anharmonicity reduces the cancellation in the peak pair, resulting in a stronger RA 2DIR cross-peak.

To extract the waiting-time kinetic trace, the cross-peak area is integrated for each waiting time  $T$ , resulting in a curve that depicts how the cross-peak intensity changes as a function of  $T$  (Fig. 2.8e). The rise in the amplitude of the cross-peak is a result of the excess energy being transported from the initially excited mode towards the localized region of the probed vibrational mode. As  $T$  increases, the energy propagates towards the reporter site, culminating in a maximum at a specific waiting time,  $T_{\max}$ . As  $T$  surpasses  $T_{\max}$ , the cross-peak amplitude starts to decay due to cooling of the molecule to the surrounding medium. At  $T_{\max}$ , the cross-peak amplitude reaches a plateau, which is caused by an overall increase in sample temperature.  $T_{\max}$  represents the time required to transport the highest amount of energy from the tag to the reporter site, and it is referred to as the energy transport time. It should be noted that cooling times for different molecules and reporters were found to be highly dependent on the solvent type.<sup>133</sup>

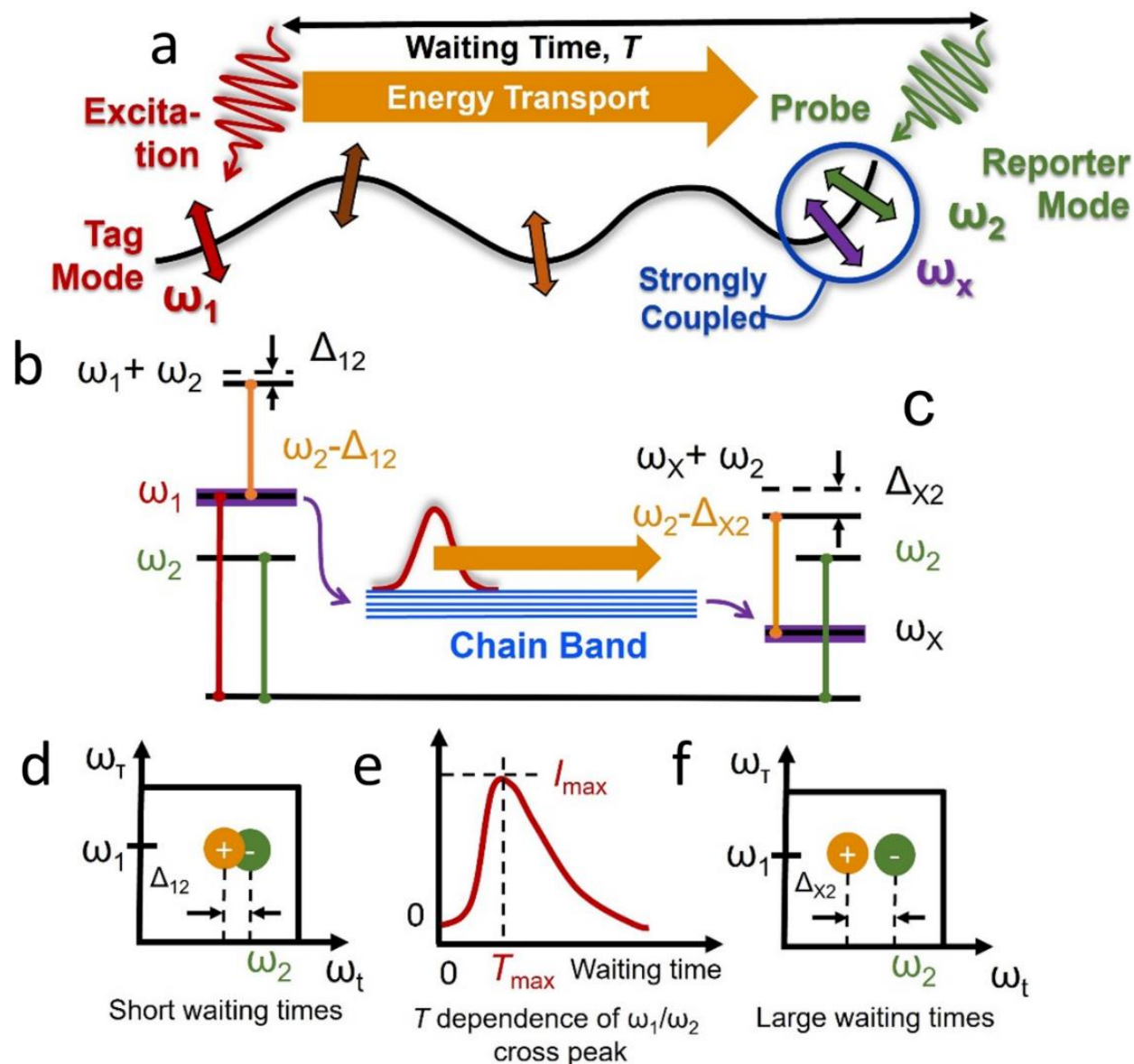


**Figure 2.8.** (a) Cartoon describing the direct coupling and relaxation-assisted coupling, respectively, between vibrational modes  $\omega_1$ ,  $\omega_2$ , and  $\omega_x$ . (b) and (e) reflect the cross peaks generated in the direct coupling and relaxation-assisted coupling cases, respectively. (c, d) Energy diagram illustrating the origin of the RA 2DIR signals. (f) Waiting-time kinetics curve obtained from the intensity of the cross peak plotted as a function of  $T$ .

In the past, a significant amount of effort was focused on improving a method known as the "single-color" approach, which involves dividing a single mid-infrared (m-IR) beam into multiple parts for conducting 2D infrared (2DIR) measurements. The "single-color" approach allows for the measurement of structural constraints based only on modes that are close in frequency because m-IR laser pulses typically have a width of around  $200 \text{ cm}^{-1}$ . The dual-frequency 2DIR method, which involves the use of two independently tunable mid-infrared (m-IR) pulses, does not impose any

restrictions on the frequencies of the modes being studied. Based on this, a novel dual-frequency 2DIR instrument was designed and built and is discussed in detail in the following section.

## 2.8. Fully-automated 2DIR Spectrometer

In 2014, the Rubtsov group designed and built the first fully-automated dual-frequency three-pulse 2DIR instrument used in the research projects discussed in this dissertation. The in-depth description of the instrument was reported by Leger et al.<sup>134-136</sup> The instrument enables the performance of three-pulse heterodyned echo measurements on any cross-peak within a spectral range spanning from 800 to 4000  $\text{cm}^{-1}$ . The instrument achieves exceptional sensitivity through a combination of closed-loop phase stabilization, spectral interferometry, and phase cycling techniques. All essential components of the 2DIR spectrometer are shown in Figure 2.9. The unique design of the phase stabilization scheme enables the polarization tuning of mid-infrared (m-IR) pulses, facilitating the measurement of angles between vibrational transition dipoles. Automatic frequency tuning is accomplished through beam direction stabilization schemes for each m-IR beam, which offers beam stability of better than 50  $\mu\text{rad}$ , and a novel scheme for setting the phase-matching geometry for the m-IR beams at the sample.

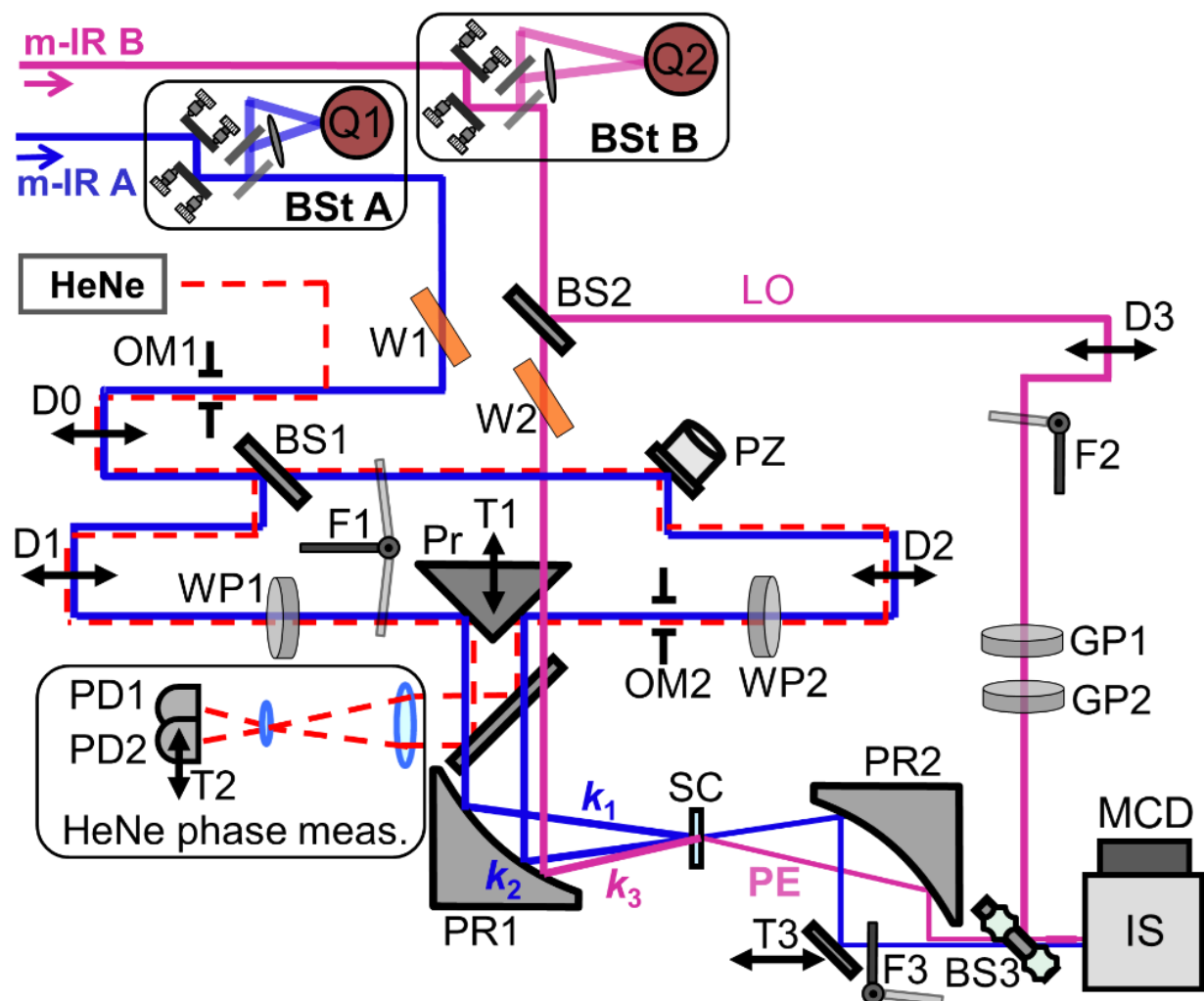


**Figure 2.9.** Optical schematic of the dual-frequency 2DIR instrument. Here, Q is an MCT quad detector, D is an optical delay stage, T is a translation stage, PR is a parabolic reflector, Pr is a right-angled prism reflector, PZ is a gold mirror equipped with a piezo actuator, BS is a beam splitter, WP is a waveplate – wire-grid polarizer or two wire-grid polarizers assembly, GP is a wire-grid polarizer, W is a phase modulator (wobbler), F is a mechanical flipper, OM is an optical mask, PD is a Si photodiode, SC is a sample cell, IS is an image spectrometer, and MCD is a mercury cadmium telluride (MCT) array detector. BS1 is a 50/50 beam splitter with separate regions for m-IR and HeNe beams. Standard mirrors are omitted to increase legibility.

A computer-controlled dual optical parametric amplifier (OPA, Palitra-duo Quantronix) is powered by a Ti:sapphire laser (Libra, Coherent) with a 1 kHz repetition rate, 1.5 W power output, and a 80 fs pulse duration. Computer-controlled non-collinear difference-frequency generation (DFG nIR-A and nIR-B, Quantronix) units receive two near-IR signal-idler pairs that were produced by the dual optical parametric amplifier (OPA). These OPA/DFG units can produce m-IR pulses with a duration of approximately 140 fs, can be tuned over a range of 500-4000  $\text{cm}^{-1}$ , and have pulse energies between 1.5-10  $\mu\text{J}$ , depending on the chosen wavelength.

The m-IR pulses generated are each guided through an individual beam stabilization scheme, which serves to position the beams in a manner that maintains their overlap at the sample. The beam stabilization design is capable of achieving a stabilization accuracy of better than 50  $\mu\text{rad}$  across the entire spectral range, which was achieved by a pair of quad detectors and a pair of computer-controlled mirrors. Following the direction stabilization, beam A is divided into two equal parts (beams 1 and 2), which act as pump pulses. A small portion of beam B is taken for use as the local oscillator (LO), while the remaining part is directed to the sample as a probe beam (beam 3). Additionally, each of the pump pulses ( $k_1$  and  $k_2$ ) is fitted with a short delay stage that can set  $\tau$  delay. The temporal overlap between the photon echo and the LO is regulated by a final translation stage for the LO ( $t$ ).

A parabolic mirror is utilized to guide and focus the three pulses onto the sample. Prior to this, the pump pulses are reflected by a computer-controlled prism reflector (Figure 2.9, Pr) to enable the choice of beam geometry to satisfy the phase-matching conditions at the sample for selected frequency region in the 2DIR spectrum.

The measurement of diagonal signals is carried out in the "boxcar geometry," where beam 3 (probe) is located directly above beam 2 (pump) (Fig. 2.7c) For cross-peak measurements, the separation between the pump beams is either widened or narrowed to change the geometry from a boxcar to a trapezoidal shape. When pumping a mode with higher energy than the reporter mode, the separation between the pump beams is reduced, enabling the phase-matching conditions to maintain the photon echo directionality. Conversely, when the vibrational tag is lower in energy than the reporter, the separation is increased. The generated photon echo from the sample is amplified by the LO and sent to a monochromator before being directed into a 64-channel MCT detector. Additionally, the system comprises a Helium Neon (HeNe) tracking system that accurately measures the translation stage movement and corrects any deviation via a mirror with a piezo-electric actuator.

## 2.9. Measurement Details

2D IR spectra usually consist of 300-500 points along  $\tau$ , depending on the vibrational lifetime of the mode and its spectral separation from other transitions. In cases where the vibrational modes have long lifetimes and are located close to other IR active modes, longer scans are needed to fully resolve the peaks. However, even with these longer scans, the single  $\tau$  scans only require 2-5 minutes of acquisition time when 400 accumulations are taken for every tau delay value.

For RA 2DIR measurements, 2DIR spectra were obtained at different waiting times ranging from -1 ps to 400 ps, resulting in spectral data with 30-40 points along  $T$ . The acquisition time for such measurements can range from 1.5-3 hours, depending on the number of  $\tau$  points. Waiting-time kinetics for individual peaks were obtained by integrating each 2DIR spectrum within a region centered on the peak.

## CHAPTER 3

# Unidirectional Coherent Energy Transport via Conjugated Oligo(*p*-phenylene) Chains

In this chapter we investigate the potential of oligo(*p*-phenylene) chains to transfer energy ballistically via its high-frequency modes through the utilization of RA 2DIR. We found that by vibrationally exciting an end-group at either side, vibrational wavepackets that can move freely along the chain were created. This transport mechanism facilitates the delivery of high-energy vibrational quanta at an impressive speed of up to 8.6 km/s, which surpasses the speed of sound in common metals (~5 km/s) and polymers (~2 km/s). The efficiency of energy injection and transport along the chain depends heavily on the extent of conjugation within the structure. The research shows that by modifying the degree of conjugation through electronic doping of the chain, it's possible to control the transport speed and efficiency. This finding opens new possibilities for developing materials with customizable energy transport properties for heat regulation, efficient energy delivery to remote areas, including transport against thermal gradients, and initiating chemical reactions from a distance, and could pave the way for the development of materials with tailored energy transport properties, leading to innovative applications in diverse fields such as energy, chemistry, and photonics.

The work detailed in this chapter has been published in the following paper: Leong, T.X.; Qasim, L. N.; Mackin, R.T.; Du, Y.; Pascal, R.A. and Rubtsov, I.V. Unidirectional coherent energy transport via conjugated oligo(*p*-phenylene) chains. *J. Chem. Phys.* **2021**, 154, 134304.

### 3.1. Introduction

In molecules with repeating units, oligomers, the formation of delocalized chain bands can support ballistic energy transport. The ballistic mechanism relies on the generation of a vibrational wavepacket – a superposition of delocalized chain band states. Ballistic transport via several saturated linear chains, such as alkyl,<sup>137</sup> perfluoroalkyl,<sup>138</sup> and polyethylene glycol (PEG),<sup>82, 83, 139, 140</sup> was reported. However, no vibrational energy transport studies were conducted on conjugated oligomeric chains. Conjugation often arises in organic molecules that contain multiple double bonds in a row or in cyclic structures (i.e. benzene). In this study, we wanted to determine how energy transfer pathways are affected by the delocalization of electrons along an electronically conjugated chain.

Conjugated oligomeric chains, such as polythiophene, polyacetylene, poly(*p*-phenylene), poly(*p*-phenylene vinylene), poly(*p*-phenylene) and polypyrrole, form rigid, rod-like structures.  $\pi$ -conjugated polymers have attracted considerable attention for photonic and electronic applications, such as organic light-emitting diodes, photovoltaics, organic lasers and organic field-effect transistors, as well as other organic devices.<sup>141, 142</sup> Compounds with poly(*p*-phenylene) chains are promising for the field of material science to serve as electrically-conductive materials and even for electroluminescence.

In this chapter, vibrational energy transport was studied in compounds featuring oligo(*p*-phenylene) chains of various lengths, forming a molecular wire, terminated with carboxylic acid and nitro end groups (Fig. 3.1a), and dissolved in DMSO. Dual-frequency relaxation-assisted two-dimensional infrared (RA 2DIR) spectroscopy measurements, quantum DFT calculations and modeling were used to investigate the energy transport.

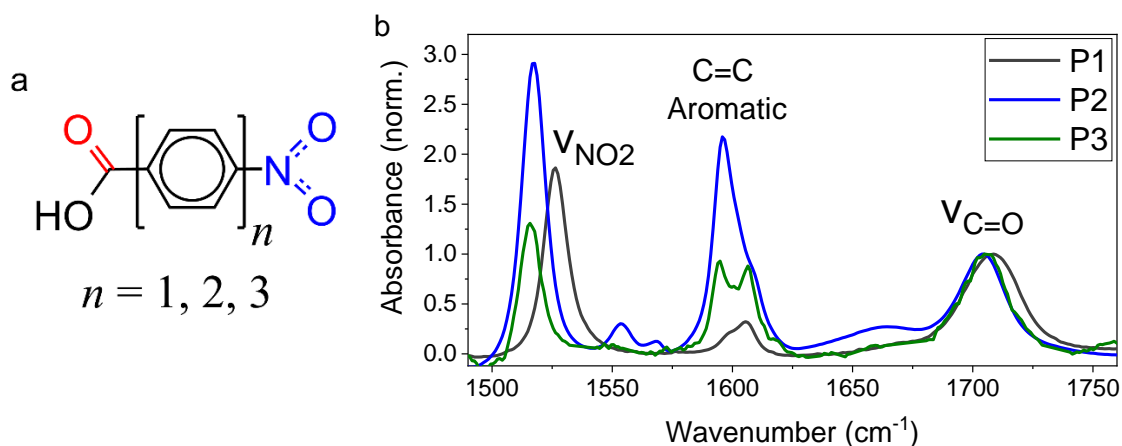


**Figure 3.1.** (a) Structure of compounds P1 – P3 featuring oligo(*p*-phenylene) backbones. Vibrational modes at the end groups,  $\nu_{\text{C=O}}$  (red) and  $\nu_{\text{NO}_2}$  (blue, asymmetric stretch), served as tags and reporters in the RA 2DIR study. (b) Solvent subtracted linear absorbance spectra of P1 – P3 in DMSO, normalized at  $\nu_{\text{C=O}}$ .

Intramolecular vibrational energy transport via poly(*p*-phenylene) chain is studied using relaxation-assisted two-dimensional infrared spectroscopy. Compounds were prepared, featuring poly(*p*-phenylene) chain of different lengths,  $(\text{Ph})_n$  with  $n = 1, 2,$  and  $3,$  functionalized with COOH and NO<sub>2</sub> end-groups, denoted as P1 – P3. The transport was initiated by exciting either the C=O stretching mode,  $\nu_{\text{C=O}}$ , or antisymmetric NO<sub>2</sub> stretching mode,  $\nu_{\text{NO}_2}$ , with a short m-IR pulse and observing the energy arrival to the opposite end of the chain.

## 3.2. Experimental Details

### 3.2.1. Experimental Method

A detailed accounting of the fully-automated 2DIR spectrometer is presented in Chapter 2.8. of this dissertation.

### 3.2.2. Sample Preparation

The polyphenylene compound 4-Nitrobenzoic Acid denoted as P1 was purchased from Tokyo Chemical Industry (N0156) and 4'-Nitro[1,1'-biphenyl]-4-carboxylic acid denoted as P2 was purchased from Matrix Scientific (044317). The polyphenylene compound denoted as P3 was synthesized by Yuchen Du and Dr. Robert Pascal Jr. at Tulane University. The solvent-subtracted linear absorption spectra of all compounds used in this study are shown in Figure 3.1b. For the spectroscopic measurements, compounds P1, P2 and P3 were dissolved in DMSO at concentrations of 30 mM. The measurements were performed in a 100  $\mu\text{m}$  thick sample cell with 1 mm thick CaF<sub>2</sub> windows at room temperature (22.5 °C). The linear absorption spectra of the samples were measured with the Nexus 870 (Thermo Nicolet) FTIR spectrometer.

### 3.2.3. DFT Calculations

Geometry optimization, normal-mode analysis, and third-order anharmonicity calculations were performed using the Gaussian 09 suite using the B3LYP functional and 6-311G(d,p) basis sets. The calculated through bond distance was taken from the carbon atom of the carboxylic acid (COOH) to the nitrogen atom of the nitro group (NO<sub>2</sub>). Theoretical methodology established by Burin and co-workers<sup>74, 143</sup> was employed to calculate the vibrational relaxation pathways of the end-group states. This approach utilizes anharmonic force constants, which are computed through Density Functional

Theory (DFT), to determine third-order relaxation pathways. The low frequency modes of the molecule act as a bath in this method

### 3.3 Results

#### 3.3.1 Energy Transport Initiated by $\nu_{C=O}$

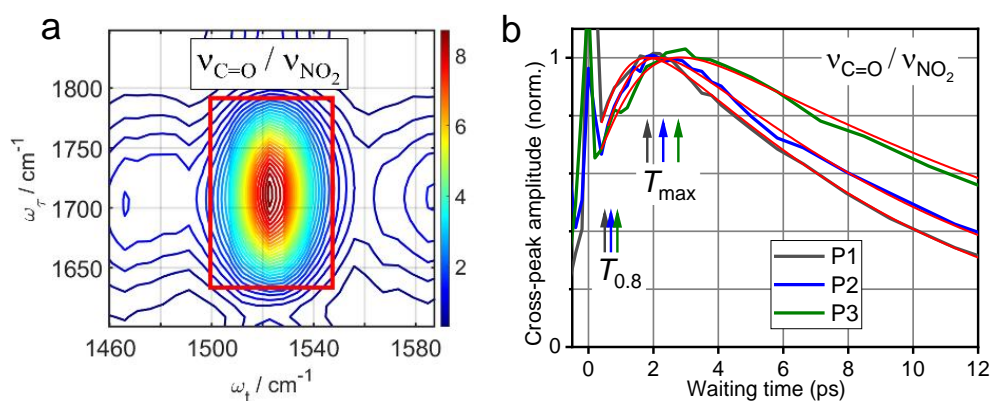


**Figure 3.2.** (a) 2DIR magnitude spectrum of P1 at  $T = 2.2$  ps, showing  $\nu_{C=O} / \nu_{NO_2}$ . The integration window used for analysis is shown. (b) Waiting-time dependences of the  $\nu_{C=O} / \nu_{NO_2}$  cross-peak amplitude for P1 (black line), P2 (blue line), and P3 (green line) and their fits with an asymmetric double sigmoidal function (red lines).

The energy transport initiated by the  $\nu_{C=O}$  tag excitation was recorded by the  $\nu_{NO_2}$  reporter for each  $(Ph)_n$  length. Figure 3.2a shows the 2DIR magnitude spectrum of P1  $\nu_{C=O} / \nu_{NO_2}$  cross peak, measured at the waiting time of 3.4 ps. An example of the one-dimensional waiting time kinetics, constructed by integrating over the cross-peak area (Fig. 3.2a, red box) as a function of the waiting time, is shown in Figure 3.2b for the  $\nu_{C=O} / \nu_{NO_2}$  cross peak. The waiting time at which the cross-peak amplitude reaches its maximum, denoted as  $T_{max}$ , corresponds to the arrival of the maximum amount of excess energy from the tag to the reporter site. The  $T_{max}$  values were evaluated from a fit of the waiting time kinetics with an asymmetric double sigmoidal function (Fig. 3.2b, red lines). The  $T_{max}$  increases with chain length (Fig. 3.2b). After the maximum occurs, each trace decays due to dissipation of the excess energy into the solvent. Each experiment was repeated at least five times for each compound and the average  $T_{max}$  values were plotted as a function of the tag-reporter distance (Fig. 3.4, blue circles). The dependence can be fit well with a linear function where the inverse slope of  $10.2 \pm 0.8 \text{ \AA/ps}$  reports on the transport speed for the transport initiated by  $\nu_{C=O}$ .

### 3.3.2 Energy Transport Initiated by $\nu_{\text{NO}_2}$

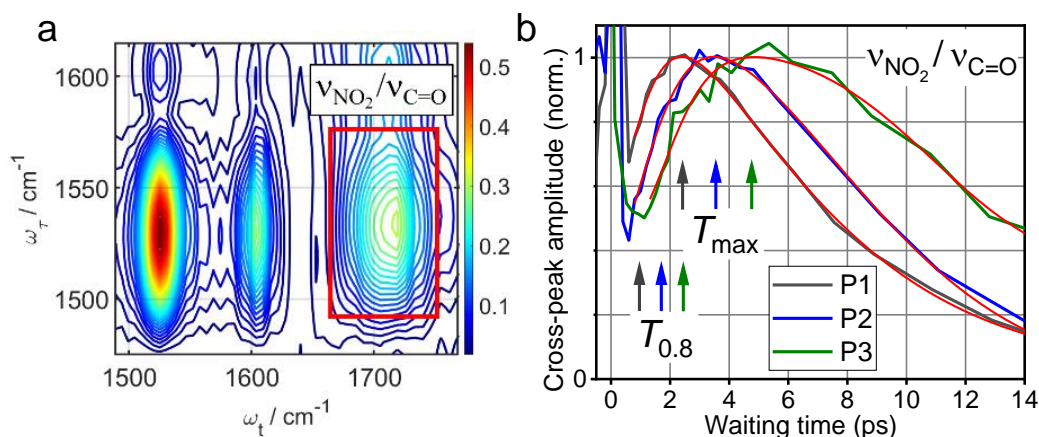


**Figure 3.3.** (a) 2DIR magnitude spectrum of P1 at  $T = 2.5$  ps, featuring  $\nu_{\text{NO}_2} / \nu_{\text{C}=\text{O}}$  and several other cross peaks. (b) Waiting-time dependences of the  $\nu_{\text{NO}_2} / \nu_{\text{C}=\text{O}}$  cross-peak amplitude for P1 (black line), P2 (blue line), and P3 (green line) and their fits with an asymmetric double sigmoidal function (red lines).

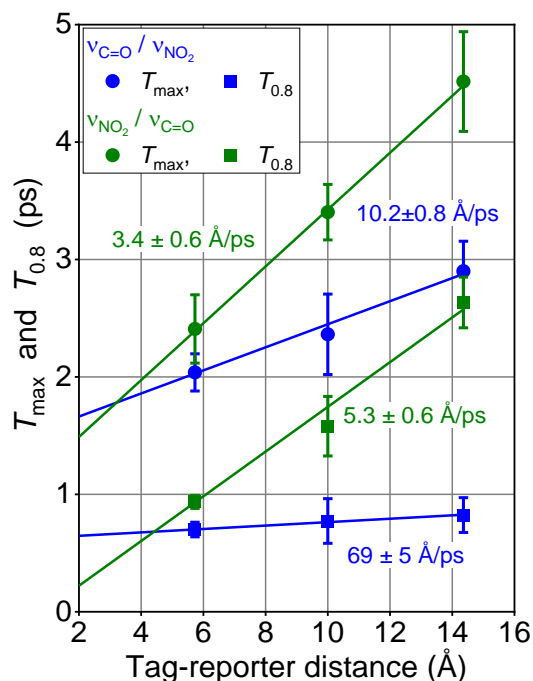


**Figure 3.4.**  $T_{\text{max}}$  (circles) and  $T_{0.8}$  (squares) values plotted as a function of tag-reporter distance for the P1-P3 compounds for the transports initiated by  $\nu_{\text{C}=\text{O}}$  (blue symbols) and  $\nu_{\text{NO}_2}$  (green symbols). The linear fits and the transport speeds obtained from the fit are shown with the matching colors.

While the ballistic transport regime induced by excitation of  $\nu_{\text{C}=\text{O}}$  of the carboxylic acid end group was studied recently in alkane and PEG chains,<sup>82, 83, 85, 140</sup> the transport initiation by exciting the fundamental  $\nu_{\text{NO}_2}$  mode of  $\text{NO}_2$  has not been tested. The energy transport was initiated by exciting

the  $\nu_{\text{NO}_2}$  tag and recording the energy arrival to the carboxylic acid end group with the  $\nu_{\text{C=O}}$  reporter. Figure 3.3a shows the 2DIR spectrum of the P1  $\nu_{\text{NO}_2}/\nu_{\text{C=O}}$  cross peak, measured at the waiting time of 2.5 ps. Several other cross and diagonal peaks are seen in the graph, involving  $\nu_{\text{NO}_2}$ ,  $\nu_{\text{C=C}}$  and  $\nu_{\text{C=O}}$  modes. The one-dimensional waiting-time kinetics, constructed by integrating over the  $\nu_{\text{NO}_2}/\nu_{\text{C=O}}$  cross peak area (Fig. 3.3a, red box), are shown in Figure 3.3b as a function of the waiting time. The average  $T_{\text{max}}$  values are plotted as a function of the tag-reporter distance (Figure 3.4, green circles). A fit with a linear function results in the energy transport speed of  $3.4 \pm 0.3 \text{ \AA/ps}$ . Interestingly, the transport speed for  $\nu_{\text{NO}_2}$  initiation is significantly slower compared to that for the  $\nu_{\text{C=O}}$  initiation.

The linear fit functions in Figure 3.4, extrapolated to the bridge length without phenyl rings (imaginary  $\text{P}_0$  compound), resulted in the transport times of 1.44 and 0.73 ps for the C=O and  $\text{NO}_2$  initiation, respectively. These times are comparable to the lifetimes of  $\nu_{\text{C=O}}$  and  $\nu_{\text{NO}_2}$ , measured at  $0.84 \pm 0.05 \text{ ps}$  and  $1.4 \pm 0.1 \text{ ps}$ , respectively. Note that within the error bars, the lifetimes were found to be independent of the chain length.

## 3.4. Discussion

### 3.4.1. Chain Band Analysis

As previously stated, the energy transport speeds in the P1-P3 compounds differ greatly when the transport is initiated by  $\nu_{\text{C=O}}$  ( $10.2 \pm 0.8 \text{ \AA/ps}$ ) and  $\nu_{\text{NO}_2}$  ( $3.4 \pm 0.4 \text{ \AA/ps}$ ). The difference in speed suggests that different chain bands are involved in the transport in each case. Chain bands refer to a series of absorption bands that arise due to the vibrational modes present in the molecule. To identify the chain bands involved in the transport, we characterized the chain states and performed theoretical analysis of the vibrational relaxation channels for both tags. Chain states were characterized according to the individual band motion of the phenyl group.

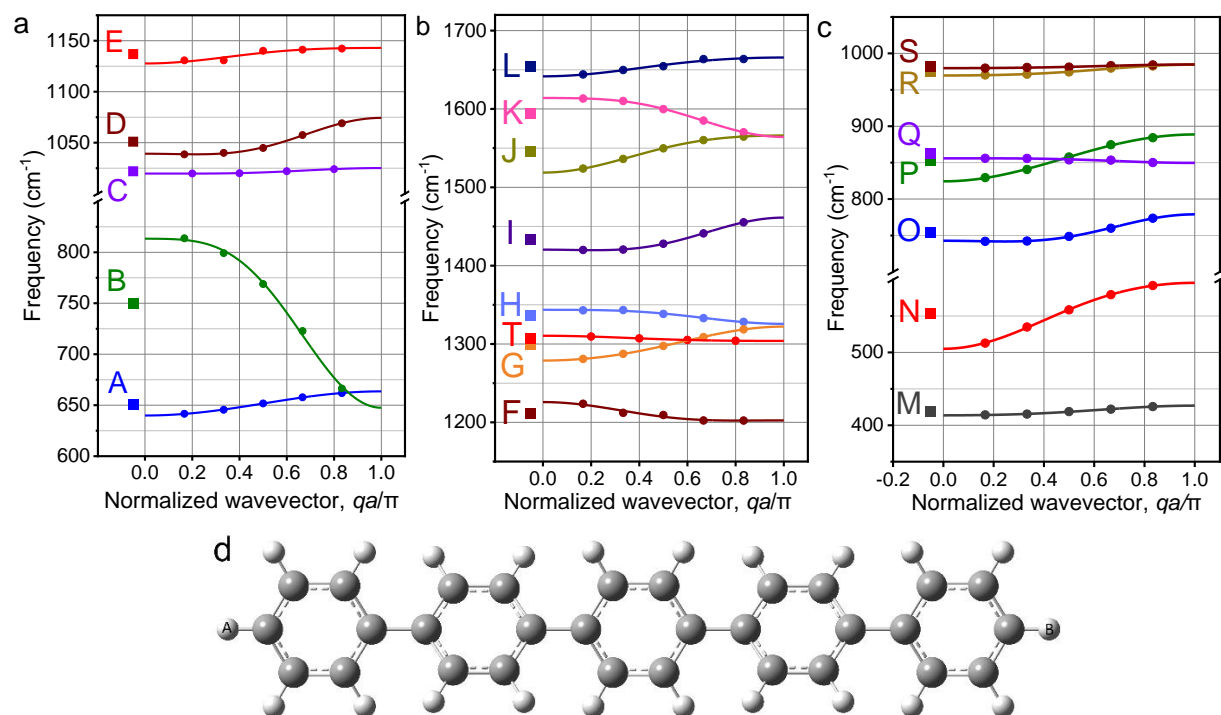


**Figure 3.5.** DFT-computed state energies of A-(Ph)<sub>5</sub>-B for (a,b) in-plane and (c) out-of-plane optical bands lower than 2000 cm<sup>-1</sup> (see atomic displacements in Fig. 3.8). The conformation with the  $\theta$  angle between neighboring phenyl rings in the chain alternating as +38°, -38°, +38°, -38° was used. Fits to Eq. 3.1 are shown with solid lines; the  $\omega_0$  values are shown with squares in the left margin; the resulting  $\beta$ ,  $\lambda$  and  $\omega_0$  values are given in Table 3.1. (d) DFT-computed structure of A-(Ph)<sub>5</sub>-B used in chain band computations.

To identify which chain states are populated upon relaxation of the end groups, the dispersion relations (chain bands) of poly(*p*-phenylene) oligomers are needed. Such dispersion relations were reported previously targeting crystalline (Ph)<sub>*n*</sub> samples.<sup>144</sup> It was determined that in solid polymeric samples the torsion angle between the neighboring phenyl groups,  $q$ , approaches zero, enforced by the crystal packing. Therefore, the reported dispersion relations were computed for  $q = 0$ .<sup>144</sup> However, in solution, the torsion angle is far from zero,<sup>144</sup> with the DFT computed angle in this study of ca. 38°. As the dispersion relations are expected to be affected significantly by the torsion angle, we have constructed the dispersion relations directly from the DFT harmonic calculations for the A-(Ph)<sub>5</sub>-B compound (Figure 3.5d), where atoms A and B were hydrogen atoms, with arbitrarily assigned masses of 1000 and 2000 amu, respectively. Such chain termination helps to avoid mixing of the CH bending modes with the high-frequency chain states, bringing the CH stretching frequencies below 400 cm<sup>-1</sup>. Chain modes showing the same motion type were grouped into bands. A wavevector for each chain state was identified by the number of the nodes for the delocalized chain-state wavefunction. The

wavevector for mode  $i$  was computed as  $q_i = \frac{\pi}{(n+1)a}(N_i + 1)$ , where  $n$  is the number of phenyl groups in the chain,  $a$  is the unit-cell length, computed at 4.32 Å, and  $N_i$  is the number of nodes. The computed chain bands are shown in Figure 3.5, separated into in-plane (a,b) and out-of-plane (c) motions. The comparison of the chain bands, computed in this study for  $q \sim 38^\circ$ , with the bands reported previously for  $q = 0$  using the molecular mechanics approach<sup>144</sup> showed significant differences in band widths and band frequencies. It is also important for this study to have the end-group mode frequencies computed at the same level of theory as the chain states to know more precisely their mutual location.

All optical bands above 400 cm<sup>-1</sup>, except those associated with CH stretching motion ( $\sim 3000$  cm<sup>-1</sup>), are presented, and labeled in Figures 3.5a-c. All the bands can be well approximated by the dispersion equation for a linear chain model involving nearest neighbor ( $\beta$ ) and next-nearest neighbor ( $\gamma$ ) interactions:<sup>145</sup>

$$\omega(q) = \omega_0 + 2\beta \cos(qa) + 2\gamma \cos(2qa) \quad (3.1)$$

Here  $\omega_0$  is the site frequency of a monomer. Lines in Figures 3.5 show the results of the fit to Equation. 3.1 for each band; the extracted parameters,  $\beta$  and  $\gamma$ , are shown in Tables 3.1. The mode splitting in the P2 dimer is indicated for each band in the captions as  $\Delta$ . Note that for a linear chain of states the splitting in a dimer equals twice the interaction energy of the two neighboring states,  $\Delta = 2\beta$ . The group velocity supported by a band is given by:

$$V_{\text{gr}}(q) = \frac{d\omega(q)}{dq} = -2\beta a \sin(qa) - 4\gamma a \sin(2qa). \quad (3.2)$$

The transport speed changes with the wavevector. Under conditions of  $\beta \gg \gamma$ , the maximum speed supported by the band of  $V_{\text{gr}}^{\text{max}}(\gamma = 0) = -2\beta a$ , occurs at  $q = \pi/(2a)$  (Table 3.2, last column). To achieve the speed of ca. 10 Å/ps, the coupling  $\beta$  should exceed ca. 6 cm<sup>-1</sup> or  $\Delta > 12$  cm<sup>-1</sup>. There are several broad in-plane bands for (Ph)<sub>n</sub>, such as K, J, I, and G, all featuring  $\Delta \sim 22$  cm<sup>-1</sup> and also a very broad band B with  $\Delta = 74$  cm<sup>-1</sup>. In addition, there are also three broad lower frequency bands corresponding to the out-of-plane motion: P, O, and N (Fig. 3.5c). Each of these bands can support a ballistic transport speed of 10.2 Å/ps, observed for the  $\nu_{\text{C=O}}$  initiation. The maximum velocity supported by a band was calculated by solving Equation. 3.2 for extremum ( $dV_{\text{gr}}(q)/dq = 0$ ).

**Table 3.1.** Values of  $\beta$  and  $\gamma$  obtained from a fit of the DFT-computed energy states using Equation. 3.1.

Optical Band	$\beta$ , $\text{cm}^{-1}$	$\gamma$ , $\text{cm}^{-1}$
A	-5.9	0.02
B	41.5	-9.9
C	-1.2	0.4
D	-9.4	2.8
E	-4.11	0.20
F	5.9	1.8
G	-10.8	0.78
H	4.5	-1.1
I	-10.2	3.3
J	-11.8	-1.9
K	12.4	-2.8
L	-6.0	-0.61
M	-3.3	0.4
N	-22.6	-2.2
O	-9.1	3.2
P	-16.1	-0.32
Q	1.6	-0.4
R	-3.7	0.6
S	-1.3	0.2
T	1.7	0.3

### 3.4.2. Tag Relaxation Channels

For computing intramolecular vibrational energy redistribution (IVR) pathway rates we used a theoretical approach developed by Burin et al.<sup>79, 143</sup> The method uses anharmonic coupling constants of an isolated molecule computed with DFT methods, while the low-frequency modes of the molecule serve as a bath. Each IVR step involves 3<sup>rd</sup>-order transition between the tag and a combination band of other two modes (or overtone),  $\omega_{\text{tag}} \rightarrow \omega_1 + \omega_2$  ( $\omega_{\text{tag}} \rightarrow 2\omega_1$ ), where  $\omega_{1,2}$  is the frequencies of the  $\nu_{\text{C=O}}$  relaxation daughter modes. Figure 3.6 shows dominant relaxation channels of (a)  $\nu_{\text{C=O}}$  and (b)  $\nu_{\text{NO}_2}$  tags represented as a total rate populating indicated states in P4. If a particular relaxation daughter state appears in multiple IVR pathways, the shown rate is the sum of all rates populating this state. Numerous pathways, populating a wide range of daughter modes were found for both tags (Fig. 3.6). Note that similar rate distributions among the bands were found for tag relaxation in P1-P3. In addition, a rate contribution was calculated for each chain band by summing the rates populating all the states of the band and dividing by the overall relaxation rate of the tag, expressed in percent. These

values provide a measure of participation of each band in the tag relaxation. The bands with an overall relaxation rate contribution exceeding ca. 2% are shown in Table 3.2.

For the  $\nu_{C=O}$  tag, we found that the states of bands K, J, F, B, A and P (Fig. 3.7) are involved strongly in the relaxation, featuring 19.3, 11, 10.7, 18.2, 12.1 and 14.8% rate contributions, respectively (Table 3.2). Two speed groups of bands can be identified: one group includes a single band B, featuring an exceptionally high speed of 86 Å/ps. Another group includes all other bands shown in Table 3.2 for  $\nu_{C=O}$  initiation, where the speed changes from 9.6 to 26 Å/ps with the rate-contribution-averaged speed of 19 Å/ps.

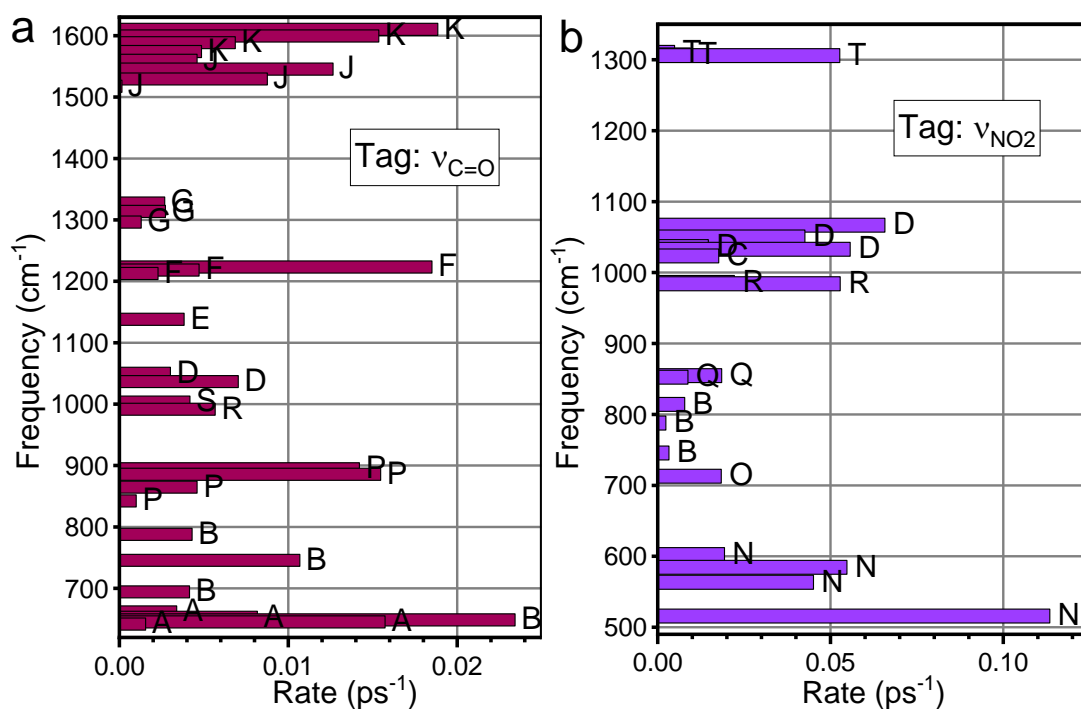


**Figure 3.6.** Rates of dominant relaxation channels into optical chain states for the (a)  $\nu_{C=O}$  and (b)  $\nu_{NO_2}$  tags computed for P4.

**Table 3.2.** Dominant relaxation pathways calculated for the  $\nu_{C=O}$  and  $\nu_{NO_2}$  tags in P4. The rates into all four states of a single band are summed and divided by the overall relaxation rate (shown as footnotes) for the rate percent. Maximum speeds in  $\text{\AA}/\text{ps}$  supported by these bands are shown, involving only the nearest-neighbor interaction ( $\gamma=0$ ) and both nearest-neighbor and next-nearest-neighbor interactions

Tag	Relaxation daughters	$\omega_0$ , $\text{cm}^{-1}$	$\beta$ , $\text{cm}^{-1}$	$\gamma$ , $\text{cm}^{-1}$	Maximum speed, $\text{\AA}/\text{ps}$	Rate contribution, %
$\nu_{C=O}^{\&}$	K	1594	12.4	-2.8	25.2	19.3
	J	1546	-11.8	-1.9	22.0	11.0
	G	1299	-10.8	0.78	18.2	1.9
	F	1211	5.9	1.8	13.2	10.7
	D	1051	-9.4	2.8	19.9	4.7
	B	750	41.5	-9.9	86.0	18.2
	A	651	-5.9	0.02	9.6	12.1
	P	853	-16.1	-0.32	26.1	14.8
	End-gr. modes					33
$\nu_{NO_2}^{\#}$	T	1307	1.7	0.3	3.2	5.7
	D	1051	-9.4	2.8	19.9	15.3
	C	1022	-1.2	0.4	3.0	2.5
	R	975	-3.7	0.6	6.9	6.4
	Q	862	1.6	-0.4	3.4	3.4
	O	754	-9.1	3.2	21.6	3.3
	N	554	-22.6	-2.2	39.0	20.0
		End-gr. modes				

The overall computed rates are  $^{\&} 0.24 \text{ ps}^{-1}$  and  $^{\#} 1.2 \text{ ps}^{-1}$ .

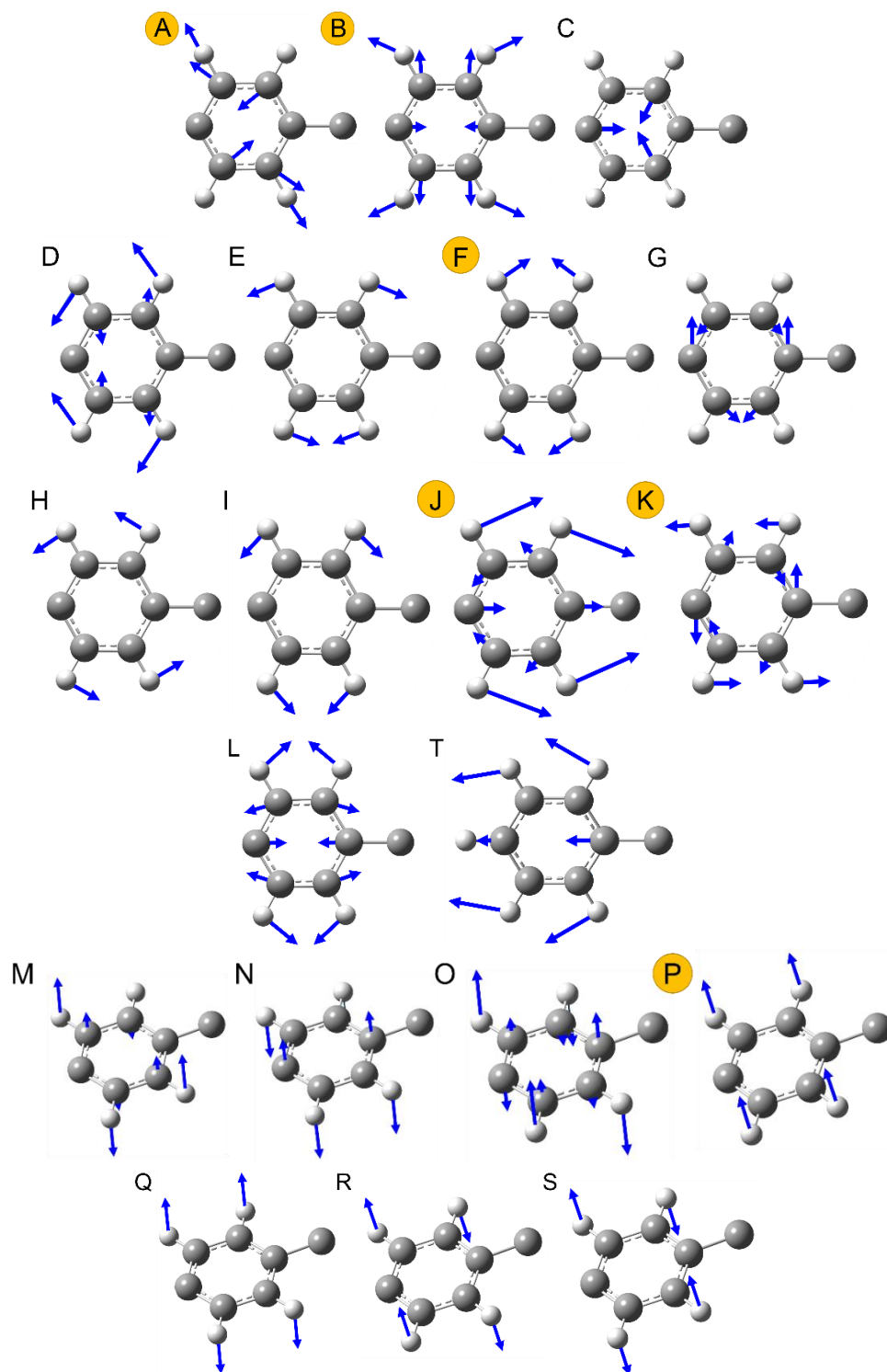


**Figure 3.7.** DFT-computed normal-mode displacements for  $q = 0$  optical (a) in-plane and (b) out-of-plane bands of poly(*p*-phenylene). Modes that contribute the most to the  $\nu_{C=O}$  initiated transport are circled in yellow.

### 3.4.3. Torsion Angle

All dispersion curves are expected to describe well the chains with a high extent of regularity and low inhomogeneity. Molecules dissolved in a solvent experience inhomogeneity associated with the thermal motion of the chain and inhomogeneity due to interaction with the solvent. The contribution involving conformational inhomogeneity of the chain for  $(\text{Ph})_n$  chains is mostly associated with variations of the torsion angle between the neighboring phenyl rings. Both inhomogeneity contributions are expected to change the site energies for vibrational states of each phenyl perturbing the band structure. The extent to which the inhomogeneity can disturb the band structure depends on the width of the inhomogeneous distribution of site energies compared to the chain band width. The chain inhomogeneity can more readily disturb narrow bands featuring weak interaction and low transport speed, causing state localization and inability to form a wavepacket over the whole chain length using such bands. The bands featuring stronger site interactions are much less sensitive to the inhomogeneity of the chains, as long as the chain width is much smaller than the site energy variations.

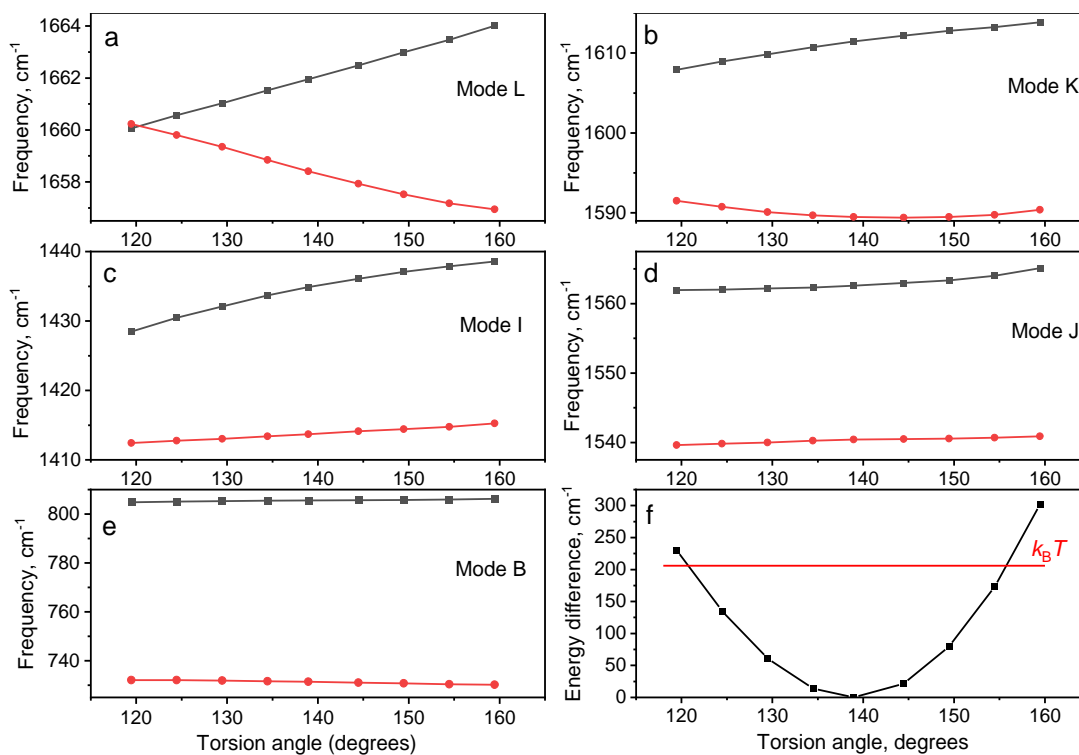


**Figure 3.8.** (a-e) DFT calculated normal-mode frequencies for selected modes of  $(\text{Ph})_2$  as a function of a torsion angle. (f) Energy of the molecule relative to that at equilibrium as a function of the torsion angle.

DFT calculations with normal mode analysis were performed for  $(\text{Ph})_2$  with different fixed torsion angles. The torsion angle represents the softest degree of freedom in  $(\text{Ph})_n$ , allowing ca.  $\pm 18^\circ$  angle variations from the equilibrium angle, while the energy stays within the  $k_B T$  level (red line in Fig. 3.8f). The normal-mode frequencies of selected modes of  $(\text{Ph})_2$  are shown in Figure 3.8a-e as a function of the torsion angle.

While different chain modes show different sensitivity to the torsion angle, a typical frequency variation extent is ca.  $4 \text{ cm}^{-1}$  within the  $k_B T$  energy window, which is much smaller than the width of the broad bands involved in the fast energy transport (Fig. 3.8 b-e). Narrow chain bands, such as mode L (Fig. 3.5b), are affected significantly by the conformational inhomogeneity, which will result in their inability to support ballistic transport. To identify which of these bands contribute to the energy transport, we studied relaxation pathways for both vibrational tags.

### 3.4.4. Modeling of the Transport Initiated with $v_{C=O}$

To illustrate that two wavepackets, featuring different speeds, can reproduce the waiting time dependences and the two experimental speeds obtained from  $T_{\max}$  and  $T_{0.8}$ , we performed a modeling in which each wavepacket resulted in a fixed shape of the waiting time dependence, while the speed was incorporated as a shift of the waiting-time dependences for longer chains by a constant time increment along the waiting time. By introducing two wavepackets with the speeds of 14 and 83 Å/ps (red symbols and lines in Fig. 3.9a), motivated by the speed analysis (Table 3.1), the shapes of the waiting time dependences were reproduced reasonably well (Fig. 3.9b, red lines), while the two experimental speed values were reproduced precisely (Fig. 3.9b, green symbols). Note that the only free parameters in the modeling were the relative decay factors with the chain length for the two wavepacket amplitudes and the waiting-time shapes for the individual wavepackets. A reasonably good fit can be obtained for a range of speeds of the individual wavepackets:  $V_{\text{slow}}$  of 12 - 20 Å/ps and  $V_{\text{fast}} = 70$  - 85 Å/ps. The modeling confirmed that the rising front of the waiting time trace is largely dependent on the speed of the fast wavepacket, while  $T_{\max}$  is affected mostly by the slower wavepackets.

For the  $v_{C=O}/v_{NO_2}$  cross-peak, the rising portion of the traces corresponds to about 30-

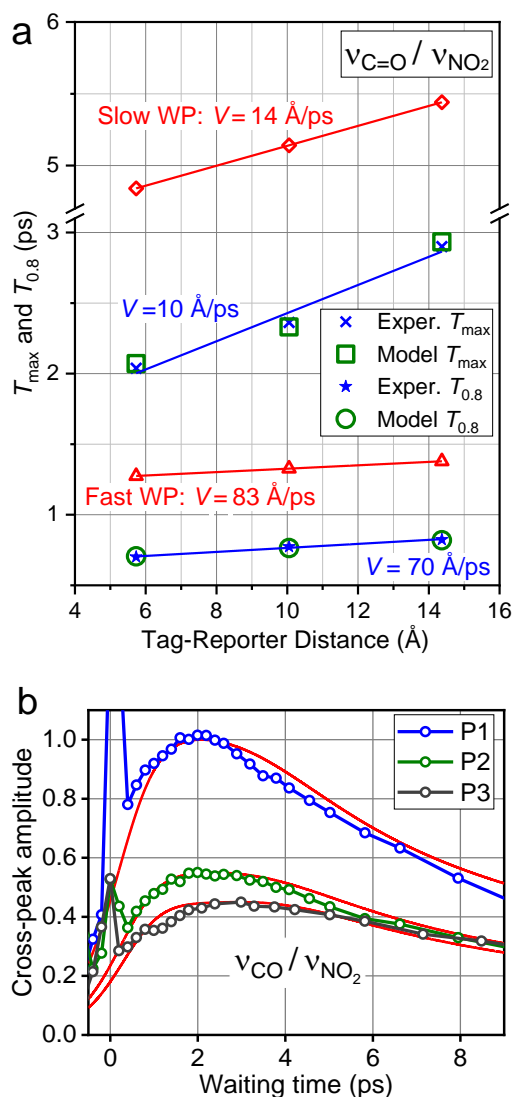


**Figure 3.9.** (a) Experimental (blue symbols) and modeled with two participating wavepackets (green symbols)  $T_{\max}$  and  $T_{0.8}$  values plotted as a function of tag-reporter distance in the P1-P3 compounds for the transport initiated by  $v_{C=O}$ .  $T_{\max}$  values for the individual wavepackets (WP), fast and slow, are shown with red symbols; their transport speeds are shown as inset. (b) Waiting-time dependences of the  $v_{C=O} / v_{NO_2}$  experimental cross-peak amplitude for P1 (blue), P2 (green), and P3 (gray). The modeled waiting-time traces, obtained by the summation of the fast and slow wavepackets, are shown with red lines.

40% of the overall trace intensity, suggesting that energy is arriving at the reporter site quickly during the experiments via a chain band which supports very fast speeds. In contrast, the  $\nu_{\text{NO}_2}$ -initiated traces show a rising portion encompassing more than an 80% of the cross-peak intensity which implies a reduced contribution from fast wavepackets to the overall energy transport, supporting the findings that  $\nu_{\text{NO}_2}$ -initiated energy transport lacks a very high-speed chain band. As is apparent from Figure 3.2a, the shape of the waiting time trace for  $\nu_{\text{C}=\text{O}}$  initiation depends on the chain length, supporting the expectation that several wavepackets contribute to the transport with the speeds ranging from 9.6 to 86 Å/ps (Table 3.2). The faster moving wavepackets affect mostly the rising portion of the waiting-time dependence, while the  $T_{\text{max}}$  value is mostly determined by the slower moving wavepackets.

To inspect the transport via faster moving wavepackets, a  $T_{0.8}$  value was evaluated for each waiting-time dependence as the time at which the curve rises to the 0.8 fraction level of its maximum. The  $T_{0.8}$  values are plotted as a function of the chain length in Figure 3.9a (blue stars). An extremely high speed, determined from  $T_{0.8}$  values, was found for the  $\nu_{\text{C}=\text{O}}$  initiation, amounting at  $69 \pm 5$  Å/ps, indicating strong contribution of the fast wavepackets.

### 3.4.5. Nature of the Coupling in Selected Chain Bands

Inspection of the normal modes of the chain states revealed that the modes dominated by the ring CC stretching motion, feature similar, moderately high  $\beta$  values. On the contrary, the bands dominated by the CH bending, especially in-plane bending (D, E, F, H), feature rather small  $\beta$  and narrow bands, including D, E, F, H, L, T and Q bands. Significant coupling between the Ph sites comes predominantly from the CC network of the chain, involving either in-plane CC ring stretching or in-plane or out-of-plane ring deformation (bending) motions.

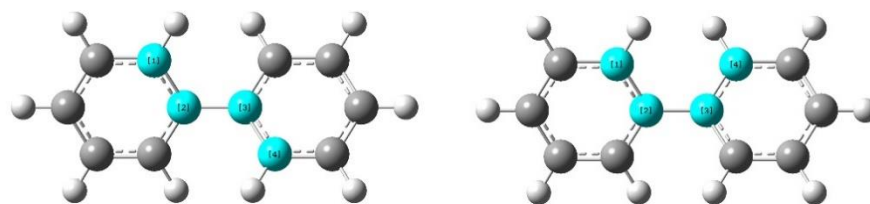


**Figure 3.10.** Structures used for calculating the coupling of nearest neighbor C=C stretching local modes. Carbon atoms assigned with normal atomic masses are highlighted in cyan.

For example, the coupling for bands K, J, I and G is facilitated by the nearest C=C groups on the neighboring rings,  $\text{HC}_a=\text{C}_a-\text{C}_b=\text{C}_b\text{H}$  in  $\text{Ph}_a\text{-Ph}_b$  of  $(\text{Ph})_2$ , which was computed at  $10.8\text{ cm}^{-1}$  (gauche) and  $11.6\text{ cm}^{-1}$  (antiperiplanar) conformations (Fig. 3.10). As a result, bands K, J, I, and G, feature similar  $|\beta|$  values of  $10.2\text{-}12.4\text{ cm}^{-1}$  (Table 3.1). Note that the chain structures with alternating torsion angles ( $+35^\circ, -35^\circ$ ) were used for the band calculations as the Bloch theorem of solid-state physics requires chain periodicity.<sup>146</sup> A more randomized distribution of torsion angle signs, which occurs in real samples is not expected to affect the nearest-neighbor interaction strength because of the local nature of the coupling.

### 3.4.6. Transport Initiated by $\nu_{\text{NO}_2}$

Both speeds,  $T_{\text{max}}$  and  $T_{0.8}$  based, for  $\nu_{\text{NO}_2}$  initiation are similar and much smaller than those for  $\nu_{\text{C}=\text{O}}$  initiation. Such small speed can be supported by rather narrow bands with  $\beta$  of  $2\text{-}3\text{ cm}^{-1}$ . Analysis of the IVR relaxation pathways for  $\nu_{\text{NO}_2}$  (Fig. 3.7b) identified many chain bands receiving energy and two groups can be formed based on the speed they support. The fast group contains in-plane band D (15.3% contribution and  $19.9\text{ \AA}/\text{ps}$  speed) and out-of-plane bands N (20.0%,  $39\text{ \AA}/\text{ps}$ ) and O (3.3%,  $21.6\text{ \AA}/\text{ps}$ ) (Fig. 3.7(b), Table 3.2), each supporting the speed that is much higher than observed. The slow group includes bands T (5.7%,  $3.2\text{ \AA}/\text{ps}$ ), C (2.5%,  $3.0\text{ \AA}/\text{ps}$ ), R (6.4%,  $6.9\text{ \AA}/\text{ps}$ ) and Q (3.4%,  $3.4\text{ \AA}/\text{ps}$ ). The rate-averaged transport speed for the bands of this group is  $4.5\text{ \AA}/\text{ps}$ , which is similar to the experimental speeds  $V(T_{\text{max}}) = 3.4 \pm 0.6\text{ \AA}/\text{ps}$  and  $V(T_{0.8}) = 5.3 \pm 0.6\text{ \AA}/\text{ps}$ .

It is surprising that although the overall contribution, of the fast group is about two-fold larger than that of the slow group, mostly the slow group transport is observed in the experiment. Several factors may contribute to this observation, including dominant role of the  $n_{\text{NO}_2}$  relaxation pathways into local  $\text{NO}_2$  modes,<sup>147</sup> longer lifetime of  $\nu_{\text{NO}_2}$  (Fig. 3.11), and possibly faster dephasing of out-of-plane chain band N.<sup>148</sup> The observed speed of ca.  $3.4\text{ \AA}/\text{ps}$  is close to that expected for directed

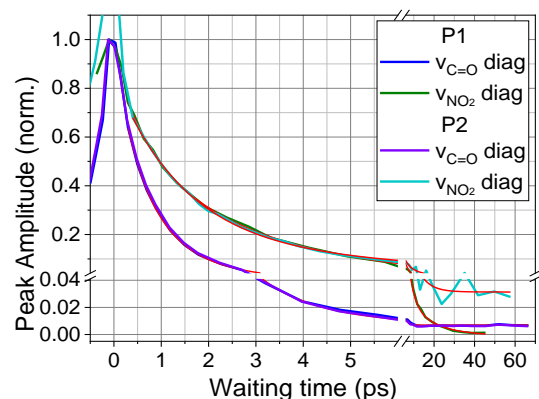


**Figure 3.11.** Waiting-time traces for P1 of the diagonal  $\nu_{\text{C}=\text{O}}$  amplitude (blue) and diagonal  $\nu_{\text{NO}_2}$  amplitude (green) and for P2 of the diagonal  $\nu_{\text{C}=\text{O}}$  amplitude (purple) and diagonal  $\nu_{\text{NO}_2}$  amplitude (cyan). All four peaks were fit with a triple exponential function (red lines).

diffusion regime<sup>149</sup> in *p*-phenylene chains; it is larger than previously reported values of 1.3-1.5 Å/ps<sup>76, 150</sup> for compounds lacking primary structure periodicity due to a larger unit cell size. Further discussion on energy transport efficiency is discussed in Section 3.4.8.

### ***3.4.7. Cross-peak Amplitude Decay with Distance***

For each tag used, the cross-peak amplitude decreases with the chain length increase. To eliminate the dependence on the sample concentration, the raw  $\nu_{\text{NO}_2}/\nu_{\text{C=O}}$  cross peak amplitude was normalized by the volume of the  $\nu_{\text{NO}_2}$  diagonal peak (integral over the diagonal peak). As the ratio of the extinction coefficients for  $\nu_{\text{C=O}}$  and  $\nu_{\text{NO}_2}$  modes ( $\epsilon_{\text{CO}}$ ,  $\epsilon_{\text{NO}_2}$ ) changes as a function of chain length, an additional correction factor of  $\epsilon_{\text{CO}}/\epsilon_{\text{NO}_2}$  was applied to the cross-peak amplitudes (Fig. 3.2a, 3.3a). A fit with an exponential function,  $\exp(-R/R_0)$ , resulted with the distance decay parameter,  $R_0$ , of  $9.5 \pm 1$  Å. The characteristic distance is smaller than that for alkane and PEG chains ( $\sim 15$  Å),<sup>151, 152</sup> which supports the assignment that the transport initiated by  $\nu_{\text{NO}_2}$  has a large contribution from directed diffusion mechanism.

The  $\nu_{\text{C=O}}/\nu_{\text{NO}_2}$  cross peak spectra did not show strong diagonal peaks, making it difficult to compensate for different experimental conditions. Note however, that for each chain length, the amplitude of the  $\nu_{\text{C=O}}/\nu_{\text{NO}_2}$  cross-peak is significantly larger than that of the  $\nu_{\text{NO}_2}/\nu_{\text{C=O}}$  cross peak, see color bar values in Figure 3.2. and 3.3. This result agrees with a much more efficient transport initiation found with  $\nu_{\text{C=O}}$  where a large number of fast chain bands are excited upon  $\nu_{\text{C=O}}$  relaxation.

**Table 3.3.** Band parameters,  $\omega_0$ ,  $\beta$  and  $\gamma$ , maximum speed supported,  $V_{\max}$ , band rate contribution,  $r_{\text{inj}}$ , to the  $\nu_{\text{NO}_2}$  tag relaxation, and percent of tag energy injected into each band,  $\eta_{\text{inj}}$ , in P4.

Tag	Relaxation daughters	$\omega_0$ , $\text{cm}^{-1}$	$\beta$ , $\text{cm}^{-1}$	$\gamma$ , $\text{cm}^{-1}$	$V_{\max}$ , $\text{\AA}/\text{ps}$	$r_{\text{inj}}$ , % <sup>a</sup>	$\eta_{\text{inj}}$ , %
VNO <sub>2</sub>	T	1307	1.7	0.3	3.2	5.7	4.5
	D	1051	-9.4	2.8	19.9	15.3	9.8
	C	1022	-1.2	0.4	3.0	2.5	1.6
	R	975	-3.7	0.6	6.9	6.4	3.8
	Q	862	1.6	-0.4	3.4	3.4	1.8
	O	754	-9.1	3.2	21.6	3.3	1.5
	N	554	-22.6	-2.2	39.0	20.0	6.7
	End-gr. modes					57	67

<sup>a</sup> rate cut-off was at 2%.

### 3.4.8. Harmonic Mixing of End-group and Chain-states

The coupling of  $\nu_{\text{C=O}}$  with the B-states was evaluated from the mixing amplitudes in the two coupled states resulted from the  $\nu_{\text{C=O}}$  and B-state interaction in compound P1, featuring only one B state (Fig, 3.12). Using the coupled state frequencies,  $\epsilon_{1,2}$  and mixing contributions of the site  $\nu_{\text{C=O}}$  and B states,  $C_1$ ,  $C_2$ , ( $C_1/C_2 = 0.67$ ) in the coupled states and assuming binary interaction, the interaction energy,  $\beta$ , was evaluated using equations 3.3 and 3.4, resulting in  $\beta = 60 \text{ cm}^{-1}$ . The coupling of the K-band states and  $\nu_{\text{C=O}}$  was evaluated similarly resulting in  $\beta \sim 20 \text{ cm}^{-1}$ .

$$\epsilon_{1,2} = \frac{E_2 + E_1}{2} \pm \frac{E_2 - E_1}{2} \sqrt{1 + \frac{4\beta^2}{(E_1 + E_1)^2}} \quad (3.3)$$

$$\left| \frac{C_1}{C_2} \right| = \frac{\beta}{E_1 - \epsilon_1} \quad (3.4)$$

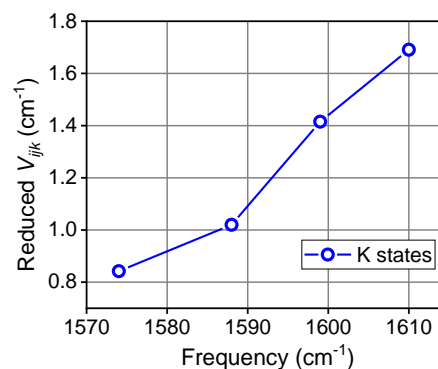


**Figure 3.12.** DFT-computed third-order reduced force constants,  $V_{ijk}$ , as a function of the B-state frequency. Indices  $i$  and  $j$  denote the  $\nu_{\text{C=O}}$  mode and each of K states, respectively. Index  $k$  is selected for the pathway with the highest rate of  $\nu_{\text{C=O}}$  relaxation populating the respective K mode.

### 3.4.9. Energy Injection Efficiency

It is interesting to compare the transport in  $(\text{Ph})_n$  chains with that via alkane chains, found to be promising heat conductors when stretched.<sup>153</sup> Transport via optical bands in alkane chains was found to occur ballistically with the  $T_{\text{max}}$ -based speeds of 8.0 and 14.4 Å/ps when initiated by  $\nu_{\text{C=O}}$  of the carboxylic acid and an azido end-group antisymmetric stretch, respectively (the  $T_{0.8}$ -based speeds were only marginally larger).<sup>85</sup> Alkane chains have a very broad  $\text{CH}_2$  rocking band centered at  $\sim 900 \text{ cm}^{-1}$ , featuring  $\beta$  of  $\sim 100 \text{ cm}^{-1}$  and supporting group velocity of  $\sim 65 \text{ Å/ps}$ .<sup>85</sup> However, such high speed has not been observed for alkane chains.

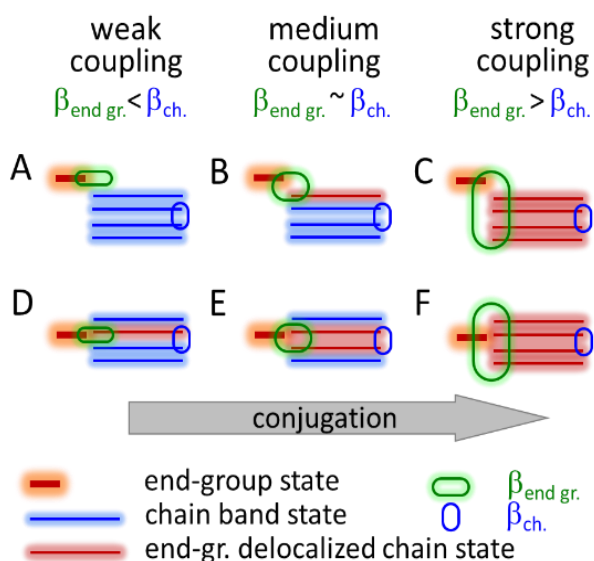


**Fig. 3.13.** Influence of the end-group-state location with respect to the chain band (a-c vs. d-f) and their coupling strength (green oval) on the end-group state delocalization.

simultaneously to generate a wavepacket?

It was determined that the localization of the end-group states has to be broken to excite a coherent wavepacket, similar to that for acoustic phonons.<sup>155</sup> Delocalization of the end-group and chain states is achieved if the two states are in resonance. The delocalization (mixing) extent depends on the relation between the energy gap and the coupling of the two site states. With smaller coupling, a more precise resonance is required for the state mixing, as illustrated in Fig. 3.12, where two-state delocalization is found in panels (d) and (b), but not (a). A complete delocalization involving 50-50

Here, it is shown that electronic conjugation and the unit cell size are the main differences for alkane and *p*-phenylene chains that define the energy injection and transport outcomes. Relaxation of an end-group localized tag mode occurs predominantly to local end-group modes, such that the spatial overlap between the parent and daughter modes ensures stronger anharmonic force constants, resulting in high relaxation efficiency. The locality of the relaxation can be seen in a weak dependence of the tag lifetime on the type of the moieties it is attached to.<sup>154</sup> If the relaxation is local to the end group, how can it populate multiple chain states of a band

wavefunction mixing is achieved if the coupling is much larger than the gap as shown in Figs. 3.13c and 3.13f with shared red color among the end group and chain states. Interaction of the neighboring monomers,  $\beta_{ch}$  (neglecting  $\gamma$  for clarity), defines the width of the band (Fig. 3.13). Depending on the value of  $\beta_{e.g.}$  compared to  $\beta_{ch}$ , no [Fig. 3.13, panel (a)], one [(d) and (b)], several (e), or all [(c) and (f)] chain states of the band are strongly mixed with the end-group state.

$\pi$  electrons facilitate stronger interaction among the vibrational modes of the end group and the chain. When an end-group with unsaturated bonds is attached to a conjugated moiety,  $\pi$  electrons of the two entities interact. This interaction does not lead to their strong conjugation in  $Pn$  compounds but is significant and strongly affects the vibrational coupling across the end-group connection. The conjugation is apparent from shortening the C–COOH bond length by  $\sim 0.03$  Å in  $Pn$ , compared to –COOH attached to saturated hydrocarbons.<sup>76</sup> The enhanced vibrational interaction,  $\beta_{e.g.}$ , results in a stronger mixing of the end-group states with the chains states (Fig. 3.13) and hence efficient tag relaxation into the chain states. We found a very strong coupling between an in-plane OCO bending mode ( $\delta_{OCO,i.p.}$ ) of the carboxylic acid end group, centered at  $\sim 650$   $\text{cm}^{-1}$ , and B-band states, featuring  $\beta_{e.g.} \sim 60\text{--}70$   $\text{cm}^{-1}$ , which is larger than  $\beta_{ch}$  of 41.5  $\text{cm}^{-1}$ . This coupling results in nearly complete mixing of the B states and the in-plane OCO bending local mode [Figs 3.13c and 3.13f]. States of several other bands are found to be mixed harmonically to the end-group states, but a much smaller degree. For example, the K-band states are coupled to the C=O stretching mode with  $\sim 20$   $\text{cm}^{-1}$ . Because of a larger energy gap of  $\sim 200$   $\text{cm}^{-1}$ , such strong coupling leads only to a weak local-state mixing, which nevertheless affects the IVR pathways significantly (Fig. 3.12). The resonances on a molecular level work analogously to mechanical resonances. When a platoon marching on a bridge gets into a resonance with the bridge's vibrational mode, energy is efficiently transferred to the bridge, resulting in high-amplitude oscillations and potentially its destruction. Without the resonance, no matter how hard the soldiers stomp on the bridge, the released energy is dissipated in the form of heat. On a molecular level, the resonance makes the end-group state a part of the chain states so that the end-group excitation excites a linear combination of the chain states, a wavepacket, instead of dispersing energy locally as heat.

Facilitated by a high density of chain states for  $(Ph)_n$ . When interactions among the end group and chain states are significantly smaller than among chain states, only a single chain state can be excited, requiring also a more precise frequency match. It was determined that  $\pi$ -electron interaction

(conjugation) greatly enhances the vibrational coupling between end-group and chain states. Under the condition  $\beta_{e.g.} \geq \beta_{ch.}$ , all states of the band have a chance to be excited with similar probabilities. This criterion is applicable even if the energy gap between the end group and chain states is significantly larger than  $\beta_{e.g.}$ , as for band K and  $\nu_{C=O}$ .

Thus, the advantage of *p*-phenylene vs alkane chains is in the presence of electronic conjugation, which facilitates the end-group–chain state coupling for multiple chain states. The higher density of chain states further enhances the state mixing. Interestingly, both end groups,  $-\text{COOH}$  and  $-\text{NO}_2$ , feature some extent of  $\pi$ -conjugation to the (Ph)*n* chain; nevertheless, they behave very differently for initiating wavepackets in the chain. The difference is in the number and location of their end-group states, resulting in relaxation into different chain bands and end-group modes; the latter pathways are dominant for  $\nu_{\text{NO}_2}$  initiation.

### 3.4.10. Energy Transport Efficiency

To quantify the rate of energy dissipation in the chain, we examined how the cross-peak amplitude depends on the chain length for the case of  $\nu_{\text{NO}_2}$  initiation (Fig. 3.14). A characteristic decay distance for the  $\nu_{\text{NO}_2}/\nu_{\text{C=O}}$  cross peak was found at  $R_0 = 9.5 \pm 1 \text{ \AA}$ . A resulting characteristic time for energy losses in the chain,  $\tau_d = R_0/V$ , exceeds 2 ps, providing an estimate of the dephasing times in the *p*-phenylene chains, a value similar to those reported for alkane and PEG chains.<sup>57, 83</sup> Using this dephasing time, the efficiency of the energy transport can be evaluated as  $\eta_{tr} = e^{-\frac{T_{tr}}{\tau_d}} = e^{-\frac{R}{V\tau_d}}$ , where the transport time,  $T_{tr} = \frac{R}{V}$  is defined by the transport speed,  $V$ . This estimation illustrates that the highest efficiency is achieved by the fastest chain bands where shorter travel.

Normalized  $\nu_{\text{NO}_2}/\nu_{\text{C=O}}$  cross-peak amplitude of as a function of the tag–reporter distance for compounds P1, P2, and P3. The fit with an exponential function (red

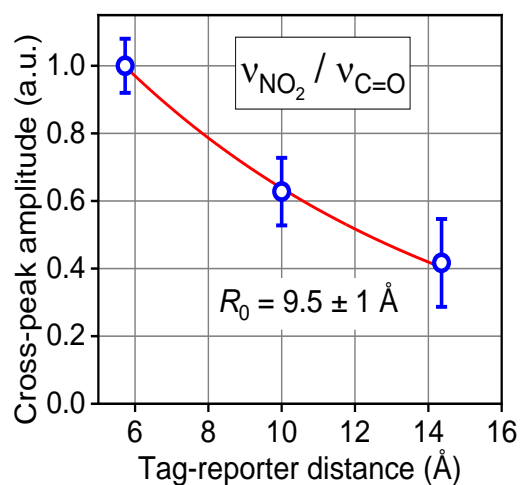


**Figure 3.14.** Normalized  $\nu_{\text{NO}_2}/\nu_{\text{C=O}}$  cross-peak amplitude of as a function of the tag-reporter distance for P1, P2 and P3. The fit with an exponential function (red line) result in a decay factor,  $R_0$ , of  $9.5 \pm 1 \text{ \AA}$ .

line) results in a decay factor,  $R_0$ , of  $9.5 \pm 1 \text{ \AA}$ . time leaves less opportunity for dephasing. Indeed, the transport time over three Ph units is rather short for fast chain bands, at 150 fs (band B) and 520 fs (band K), resulting in high transport efficiencies with  $\eta_{\text{tr}}(\text{B}, \text{Ph}_3) = 93\%$  and  $\eta_{\text{tr}}(\text{K}, \text{Ph}_3) = 77\%$ . The efficiency is significantly smaller for the bands featuring smaller transport speeds; it is only 12% for band T. The efficiencies for longer chains will become even more discriminatory among fast and slow bands with  $\eta_{\text{tr}}(\text{B}, \text{Ph}_{10}) = 78\%$  and  $\eta_{\text{tr}}(\text{T}, \text{Ph}_{10}) = 0.12\%$ . The overall efficiency of the energy delivery to the chain end is a product of the injection and transport efficiencies.

A comparison of the two transport initiation cases revealed that the overall mean efficiency calculated for the  $(\text{Ph})_3$  chain is significantly higher with  $\nu_{\text{C=O}}$  initiation at 42.3% vs 15% for  $\nu_{\text{NO}_2}$  initiation. The ratio of the energy delivery efficiencies for  $\nu_{\text{C=O}}$  vs  $\nu_{\text{NO}_2}$  initiation increases drastically for longer chains, calculated at 3.2 and 25 for  $\text{Ph}_{10}$  and  $\text{Ph}_{100}$  chains, respectively.

### 3.4.11. Computations and Experiments with Polythiophenes

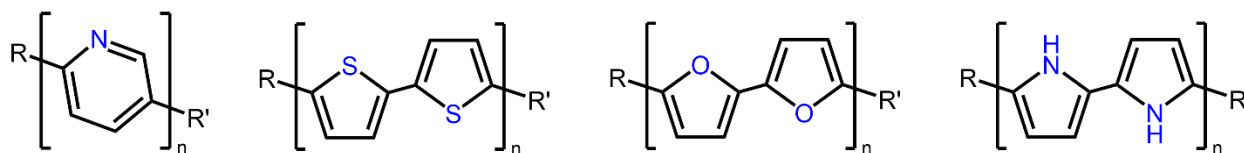


**Figure 3.15.** Structures of poly(2,5 pyridine), polythiophene, polyfuran and polypyrrole

Further studies of other conjugated molecular backbones would greatly improve the understanding of the effect conjugation has on vibrational energy transport. Polypyrrole, polythiophene, and polyfuran are among several examples of conjugated ring bridges. (Fig. 3.15).

One aromatic ring of great interest due to both its conductivity and optical properties is thiophene. Thiophenes present an advantage in terms of better solubility and access to longer chains. Polythiophene chains are also susceptible to changes in color and conductivity when exposed to different environmental stimuli such as solvent, temperature and applied potential. This makes polythiophenes attractive as potential sensors that could possibly provide a range of optical and electronic responses.

Preliminary experimental and theoretical studies were conducted on thiophene compounds with COOH and NO<sub>2</sub> end groups (Fig 3.16a). Polythiophene chain bands were computed for (Th)<sub>5</sub> using DFT methods to identify chain bands supporting the highest transport speed. We determined that various bands at high frequencies are capable of supporting high speeds (Fig. 3.16b). The maximum speed a chain band could support was calculated to be ~90 Å/ps (Fig. 3.16b, cyan line). RA 2DIR measurements of 5-nitro-2-thiophene carboxylic acid showed the presence of strong coupling

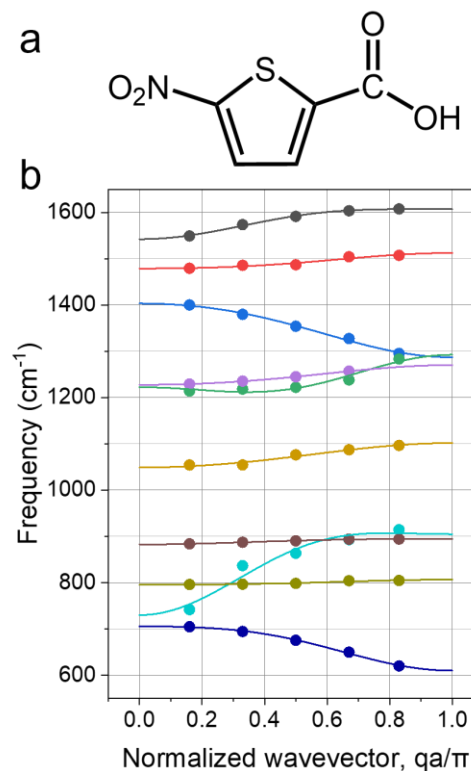


**Figure 3.16.** (a) 5-nitro-2-thiophene carboxylic acid (b) In-plane optical chain bands lower than 2000 cm<sup>-1</sup> DFT-computed for (Th)<sub>5</sub> chain.

between the two end group modes,  $\nu_{\text{asNO}_2}$  and  $\nu_{\text{C=O}}$ , preventing the evaluation of the transport time (Fig. 3.17).

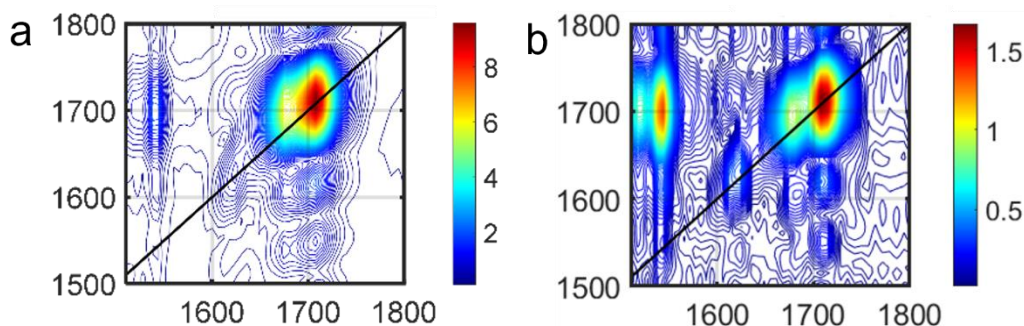


**Figure 3.17.** 2DIR magnitude spectra of 5-nitro-2-thiophene carboxylic acid showing  $1700\text{ cm}^{-1}$  diagonal region at (a) 1.2 ps and (b) 3.6 ps.

### 3.4.12. Novel Research Avenues

The speed of  $86\text{ \AA/ps} = 8.6\text{ km/s}$  is several folds larger than the speed of sound in common polymeric materials ( $\sim 2\text{ km/s}$ ). While some materials show even higher speeds of sound (e.g., the diamond at  $\sim 12\text{ km/s}$ ), the advantage of the present study is in finding a way of sending high-frequency quanta of energy rapidly to significant distances and with high spatial precision. As opposed to thermal quanta,<sup>153, 156, 157</sup> even an individual quantum of such energy is sufficient to accelerate some chemical reactions,<sup>158</sup> which could now be performed remotely using m-IR radiation. In this case, reactions can be activated in reactants under low temperature conditions, where high-energy quanta are delivered precisely to the degrees of freedom of the reaction coordinate. Star-like dendrimeric structures with the target at the center can be envisioned to deliver several quanta of energy to the target location.

One could also envision delivering energy to hard-to-reach places. For example, delivering energy to the middle of a lipid membrane, or across the membrane without increasing the temperature of the whole sample. The ability to send high-energy quanta across large distances could result in developing novel signaling strategies, resulting in new materials for heat management. The ballistic transport of high-energy quanta occurs regardless of the temperature gradient in the sample. Sending energy against thermal gradients in systems supporting electronic conjugation is an exciting prospect in developing devices involving both electron and energy transports.

The prospect in developing devices involving both electron and energy transports. Another avenue is to control the transport speed and efficiency by modifying the chain properties. As the extent of electronic conjugation is found to play a key role in the transport speed and efficiency, by altering the conjugation, the transport speed and efficiency can be modified. As both end groups,  $-\text{NO}_2$  and  $-\text{COOH}$ , are electron withdrawing through inductive and resonance mechanisms, the chain in  $P_n$  compounds is kept under undoped (electronically neutral) conditions with the intra-ring  $\pi$ -delocalization dominating over the inter-ring delocalization resulting in a small contribution from the quinoidal resonance structure. By changing the electronic doping extent, a stronger conjugated chain with a larger contribution from quinoidal resonant structure results (Fig. 3.18), featuring increased Ph–Ph coupling and faster and more efficient energy transport. The doping can be administered in multiple ways: either stationary via applying a potential to surface immobilized chains or transiently via electron injection from electronically excited, covalently attached chromophores.<sup>159, 160</sup> Our preliminary calculations show the widths of several bands increase significantly in electronically enriched chains.

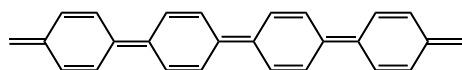


**Figure 3.18.** Quinoidal structure of polyphenylene.

Another area of interest is the application of electrochemistry and polyphenylene derivatives by attaching it to a gold layer and observing its vibrational energy transport. Gold nanorods (AuNRs) show high potential in electrochemical sensing owing to their excellent conductivity, electrocatalytic activity, and sensitivity.<sup>161, 162</sup> In a proposed electrochemical setup, AuNRs are chemically adsorbed to a polyphenylene derivative through the Au-S bond (Fig. 3.19). The polyphenylene would have  $\text{COOH}$  and  $\text{NO}_2$  end groups, allowing for m-IR excitation to study the vibrational energy transport. A potential would be applied to the electrochemical setup, resulting in electronically enriched chains. The fabrication of such gold-based electrochemical cells is discussed in Chapter 6.

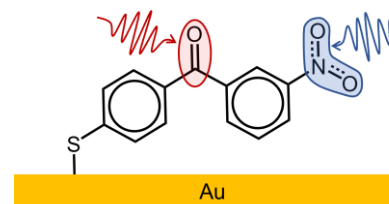


**Figure 3.19.** A polyphenylene derivative, with  $\text{COOH}$  and  $\text{NO}_2$  end groups, attached to a single AuNR, by Au-S bond

## Acknowledgements

The study was supported by grants from the National Science Foundation (CHE-1900568 and CHE-2201027).

## CHAPTER 4

# Tracking Energy Transfer across a Platinum Center

This chapter presents the results of using RA 2DIR spectroscopy to investigate energy transfer across metal centers in platinum complexes. The complexes had a triazole-terminated alkyne ligand consisting of either two or six carbons, a perfluorophenyl ligand, and two tri(*p*-tolyl) phosphine ligands. The study involved a comprehensive analysis of various cross and diagonal peaks, with a particular focus on coherent oscillation, energy transfer, and cooling parameters. These observables, combined with density functional theory computations of vibrational frequencies and anharmonic force constants to identify the distinct functional groups present in the compounds. Additionally, the study included computation of vibrational relaxation pathways and mode couplings, revealing two regimes of intramolecular energy redistribution. The first regime involves efficient energy transfer between ligands through high-frequency modes, but only if the modes involved are delocalized over both ligands and the energy transport pathways between them are recognized. The second regime involves redistribution via low-frequency delocalized modes, which does not lead to inter-ligand energy transport. Overall, the findings of this study contribute to a better understanding of energy transfer mechanisms in metal complexes, highlighting the importance of vibrational modes in governing inter-ligand energy transport. These insights could inform the design of new metal complexes for applications such as catalysis, energy storage, and electronic devices.

The work detailed in this chapter has been published in the following paper: Leong, T.X.; Collins, B.K.; Baksi, S.D.; Mackin, R.T.; Sribnyi, A.; Burin, A.L.; Gladysz, J.A. and Rubtsov, I.V. Tracking Energy Transfer across a Platinum Center. *J. Phys. Chem. A*. **2022**, 126, 4915-4930.

## 4.1. Introduction

For the past decade, compounds composed of long sp-hybridized carbon chains and transition-metal end groups have received substantial interest,<sup>163-172</sup> leading to extensive research on the synthesis of transition metal clusters containing alkynes and its derivatives.<sup>173-175</sup> These ligands offer versatility in coordination modes with the possibility of donating electrons serving as promising candidates for novel materials for molecular electronics.<sup>176-178</sup> Additionally, recent studies have indicated that these compounds could be useful as pharmaceuticals,<sup>179</sup> optical wires<sup>180</sup> and electronic reservoirs.<sup>181</sup>

Linear and rigid alkyne-based molecular wires feature strong covalent bonds with frequencies in the convenient region of ca. 2100 cm<sup>-1</sup>. As such they can serve as useful infrared (IR) reporters for studying structures via two-dimensional infrared (2DIR) spectroscopy.<sup>182</sup> Recent studies of ballistic transport of vibrational energy via oligomeric chains<sup>84, 183, 184</sup> revealed that electronic conjugation within the chain can lead to higher transport speeds and ballistic transport efficiency.<sup>185</sup> Alkyne-based molecular wires have not yet been tested as energy transporters. Here we report on energy relaxation and transfer in two square planar Pt complexes featuring alkynyl triazole ligands with alkyne moieties of different length, C<sub>2</sub> and C<sub>6</sub>, denoted as C2 and C6, respectively (Fig. 4.1). These contain F<sub>5</sub>Ph ligand opposite to C<sub>n</sub>-Tri ligand and two cis tri(*p*-tolyl)phosphine ligands.

Transition-metal complexes and organic compounds with polyyne moieties (ligands) are widely used as bridges in donor-bridge-acceptor (DBA) compounds, providing conjugation enhanced electronic coupling of the electron donor and acceptor.<sup>186</sup> Because of their unique properties of supporting conjugation and convenient vibrational frequency, such vibrationally excited bridges are attractive candidates for modulating electron transfer rates in DBA compounds.<sup>187-189</sup> Vibrational relaxation dynamics of excited alkyne bridges are important for the electron transfer studies but not well understood.

Vibrational relaxation and thermalization in molecules occur via intramolecular vibrational energy redistribution (IVR) process, which has been studied using a variety of experimental methods.<sup>57, 147, 190-192</sup> Energy transfer and thermalization in covalent networks<sup>79, 143, 193-195</sup> is better understood than the transfer across a metal center in a transition metal complex for which only a few studies were reported.<sup>196-199</sup> The coordination bonds at the metal center are often weak resulting in very inefficient energy transfer across the metal. For example, the lifetime of CO stretching modes in some metal carbonyls reaches 1 ns.<sup>200-204</sup> A similar situation is encountered when an organic compound is attached

to a metal or semiconductor surface. The surface binding energy is often small resulting in weak thermal conductivity through the interface.<sup>205-209</sup> In contrast to surfaces, transition metal complexes feature high-frequency vibrational modes on each side of the metal atom, which can potentially participate in the exchange of high-frequency quanta across the metal center. Understanding the role of energy transport involving high-frequency modes across the metal center is the objective of this study.

In this study, dual-frequency RA 2DIR spectroscopy<sup>70</sup> is used to interrogate intramolecular energy redistribution and energy transport in the C2 and C6 compounds. In this technique, a pair of short m-IR laser pulses excite a vibrational tag at one end of the molecule, while the third m-IR pulse is used to trace the excess energy arrival to the other end by probing the reporter mode. The amplitude of the 2DIR cross peak between the tag and reporter changes with the waiting time,  $T$ , yielding energy transport kinetics.<sup>70</sup>

As detailed below, multiple 2DIR cross peaks of C2 and C6 demonstrated coherent oscillations. Vibrational and vibronic coherences have long been observed in polyatomic molecules in the ground<sup>210, 211</sup> and excited<sup>212-216</sup> electronic states, respectively. In this study we used coherent oscillations to identify modes located at the same moiety, which appears useful when severe peak overlap occurs in the linear FTIR spectrum.

The chapter is structured as follows: we start with assigning peaks in the FTIR absorption spectra of the two compounds using DFT-based normal mode analysis. Then the RA 2DIR data are discussed, reporting on the energy transport from and towards  $\nu_{C=C}$ , as well as between different ligands. The experimental results highlighted include energy transfer times, cooling times, and frequencies of coherent oscillations observed for a range of various cross peaks. A computational section follows that clarifies the nature of energy transport pathways responsible for the observed RA 2DIR data. Special attention is given to identifying the requirements for efficient energy transfer across the Pt center.

## 4.2. Experimental Details

### 4.2.1. Experimental Method

A detailed accounting of the fully-automated 2DIR spectrometer is presented in Chapter 2.8. of this dissertation.

### 4.2.2. Sample Preparation

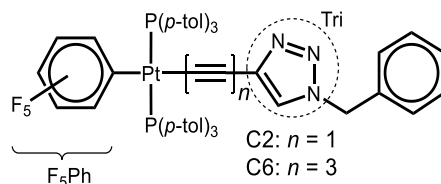


**Figure 4.1.** Structures of C2 ( $n=1$ ) and C6 ( $n=3$ ).

Compounds *trans*-( $C_6F_5$ )(*p*- $tol_3P$ ) $2Pt(C\equiv C)_nC=CHN(CH_2C_6H_5)N=N$  with  $n = 1$  and  $3$ , referred to as C2 and C6, were synthesized at Texas A&M University by students of Dr. John Gladysz. For FTIR and 2DIR measurements, ca. 15 mM  $CDCl_3$  solutions were used. The measurements were performed in a sample cell made of 1 mm-thick  $CaF_2$  windows and a 100  $\mu m$  Teflon spacer at room temperature,  $22 \pm 0.5$   $^\circ C$

### 4.2.3. DFT Calculations and Vibrational Relaxation Modeling

Geometry optimization, normal-mode analysis, and anharmonic force constant calculations were performed using the Gaussian 09 suite. A B3LYP functional and a 6-311G(d,p) basis set were used for all elements except platinum. LANL2DZ basis sets and effective core potential were used for platinum atoms. Vibrational relaxation pathways of the end-group states were computed using a theoretical approach developed by Burin and coworkers.<sup>74, 143</sup> The method uses DFT-computed anharmonic force constants of an isolated molecule to compute third-order relaxation pathways while the low frequency modes of the molecule serve as a bath.

## 4.3 Results

### 4.3.1. Linear FTIR Spectroscopy Measurements

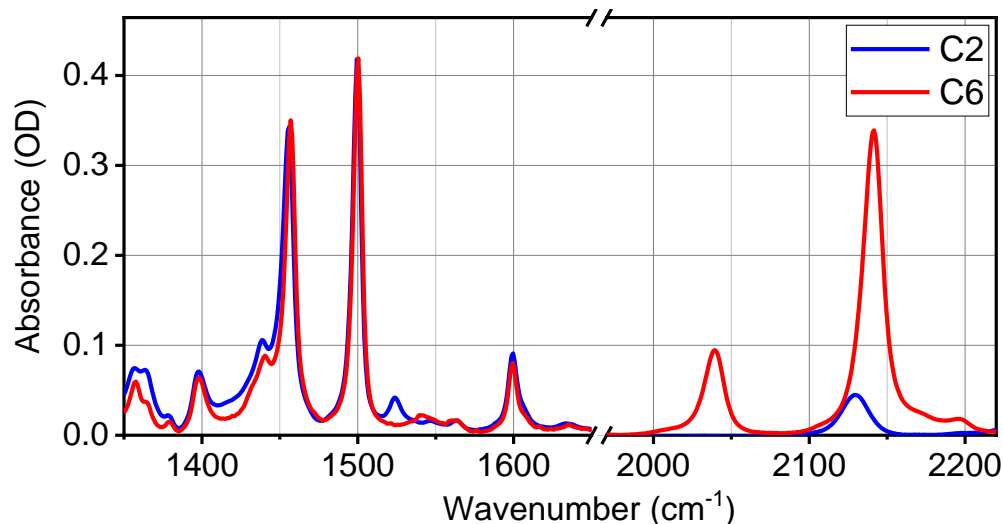


**Fig. 4.2.** Solvent-subtracted infrared absorption spectra of compounds C2 and C6 in  $\text{CDCl}_3$ . The spectrum of C6 was scaled by a factor of ca. 1.2 to match that of C2.

Linear absorption spectra of compounds C2 and C6 are very similar in the fingerprint region (Fig. 4.2). Alkyne stretching peaks in C2 and C6 are different: there is a single peak at  $2130\text{ cm}^{-1}$  for C2, while there are three peaks for C6, located at  $2040$ ,  $2140$ , and ca.  $2170\text{ cm}^{-1}$ , originating from coupling of three  $\text{C}\equiv\text{C}$  local modes. The strongest peak for C6, found at  $2140\text{ cm}^{-1}$ , is due to in-phase motions of all three  $\text{C}\equiv\text{C}$  groups; unless stated otherwise, 2DIR measurements for C6 were performed for this peak, referred to as  $\nu_{\text{C}\equiv\text{C}}$ .

The spectra of both compounds in the fingerprint region feature intense peaks at  $1460$  and  $1500\text{ cm}^{-1}$  and medium strength peaks at  $1600$ ,  $1435$ , and  $1400\text{ cm}^{-1}$ . The differences between C2 and C6 in the fingerprint region above  $1350\text{ cm}^{-1}$  are minor, involving a peak at  $1525\text{ cm}^{-1}$  for C2, while a similar peak in C6 is slightly weaker and observed at ca.  $1539\text{ cm}^{-1}$ , both referred to as a  $1530\text{ cm}^{-1}$  peak (see next section). Accurate peak assignment is paramount to understanding the results of the following 2DIR studies.

### 4.3.2. DFT-based Modeling of FTIR Spectra

To help assign peaks in the fingerprint region, we computed normal modes for both C2 and C6 compounds and constructed theoretical spectra by broadening the line spectra with a Lorentzian line shape of an area equal to the mode IR intensity. The computed line spectrum and theoretical (broadened) spectrum (orange line) for C6 are shown in Figure 4.3a. The amplitude of the lines in the line spectrum is equal to their computed IR intensities in km/mol, while the color of each bar reflects the location of the normal mode either on F<sub>5</sub>Ph (red), C<sub>n</sub>-triazole-CH<sub>2</sub>Ph (C<sub>n</sub>-TriPh, blue), or six tolyl (Tol, green) moieties.

The DFT-computed normal-mode frequencies for molecules in solution often appear higher than experimental values, mostly due to missing anharmonic corrections and solvent effects. As apparent from Figure 4.3a, uniform frequency corrections will not result in a

good match with the experimental spectrum. However, the experimental spectrum is simple enough to implement different corrections to modes localized at different functional groups. For example, the two strongest modes, computed at 1517 and 1473 cm<sup>-1</sup> (Fig. 4.3a), reside at the F<sub>5</sub>Ph moiety and clearly correspond to the two strongest experimental absorption peaks at 1500 and 1460 cm<sup>-1</sup>, requiring a correction factor,  $\kappa$ , of 0.9885 ( $v_{\text{corrected}} = \kappa v$ ). The same correction factor was applied to other modes of F<sub>5</sub>Ph. Corrections for tolyl groups were based on the peak at 1600 cm<sup>-1</sup>, which is characteristic for phenyl and Tol groups. Similar  $\kappa$  factor was applied to other modes located on Tol and C<sub>n</sub>-Tri moieties

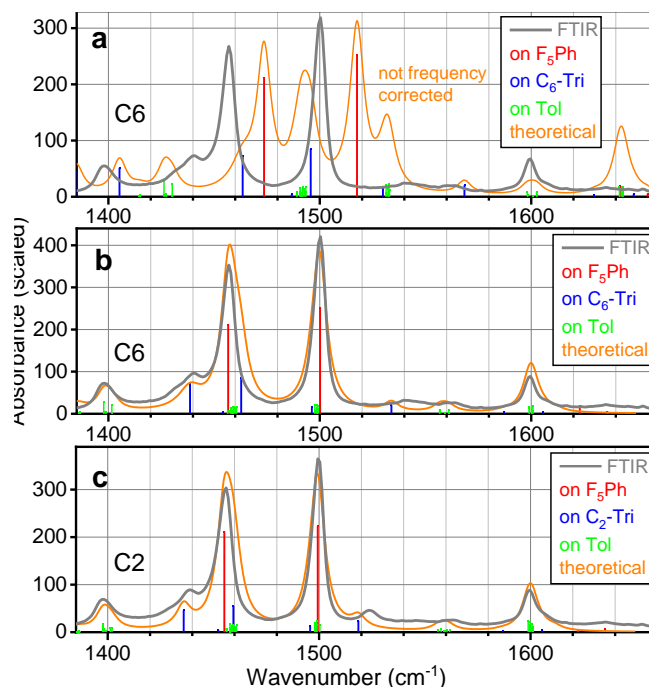


**Figure 4.3.** DFT-computed uncorrected line spectra for C6 (**a**) and frequency corrected line spectra for C6 (**b**) and C2 (**c**). The modes associated with F<sub>5</sub>Ph-, C<sub>n</sub>-Tri, and Tol moieties are shown with red, blue, and green, respectively. Experimental linear absorption spectra for C6 (**a,b**) and C2 (**c**) in CDCl<sub>3</sub> are shown with gray lines. Theoretical spectra of C2 (**c**) and C6 (**b**) obtained from applying Lorentzian line shape with a full width at half maximum of 8.1 cm<sup>-1</sup> are shown with orange lines. The Y-axes report the DFT-computed IR intensities (km/mole) for the line spectra. The experimental FTIR spectra in panels B and C (gray lines) were normalized to visually match the theoretical spectra.

(see Table 4.1 footnote). The resulting frequency-corrected theoretical spectra for C6 and C2 (Fig. 4.3 b,c) show a good match with amplitude-scaled experimental spectra. Note that no attempt was made to tweak the correction factors within each group of modes to achieve a better match with the experiment.

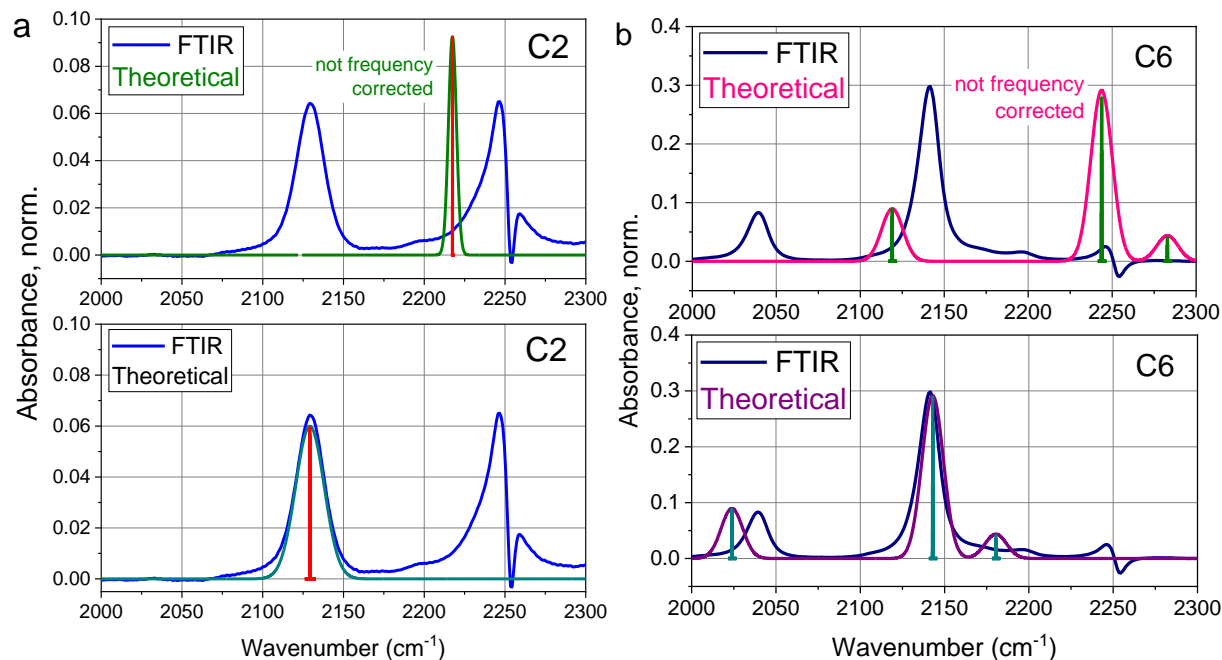


**Figure 4.4.** DFT-computed and experimental line spectra for the modes associated with the  $\nu_{C=C}$  motion. Experimental linear spectra for **(a)** C2, blue line and **(b)** C6, navy blue line.

**Table 4.1.** Main experimental absorption peaks and DFT computed, scaled normal modes of  $\nu_{C=C}$  for C2 and C6.

	Experimental Peak, $\text{cm}^{-1}$	Computed Peak, $\text{cm}^{-1}$	IR Intensity, $\text{km/mol}$
C2	2120	2217	75
C6	2040	2119	187
	2140	2243	609
	2170	2282	91

Frequency correction factors were 0.95 for C2 and 0.96 for C6.

DFT-computed modes for the  $\nu_{(C=C)}$  modes in C2 and C6 were calculated and compared to the experimental FTIR spectra. (Fig. 4.4) Frequency corrections were applied to the modes and it showed a good match with amplitude-scaled theoretical spectra. From the DFT-computed normal modes, the sum of all normal modes in a molecule is given by Eqn. 4.1, where x, y and z represent the translations of the molecule along the respective axes.

$$\sum_i^{All} (x_i^2 + y_i^2 + z_i^2) = 1 \quad (4.1)$$

The degrees of freedom for C2 and C6 were calculated to be 354 and 366 respectively. All vibrational modes of C2 and C6 were analyzed and grouped into specific functional groups. The total contribution of each group (F<sub>5</sub>Ph, Triazole, Toluy) were determined:

$$\sum_i^{F5Ph,Tol,Tri} (x_i^2 + y_i^2 + z_i^2) = \varkappa \quad (4.2)$$

The  $\varkappa$  value calculated for each function group for C2 and C6 is divided by the sum of all normal modes and multiplied by 100 to obtain the percent contribution of functional groups to the normal modes of C2 and C6.

$$\frac{\sum_i^{Group} (x_i^2 + y_i^2 + z_i^2)}{\sum_i^{All} (x_i^2 + y_i^2 + z_i^2)} \times 100\% = \% \text{ contribution of motion} \quad (4.3)$$

The modeling suggests that the peak at 1600 cm<sup>-1</sup> is mostly due to Tol motion. The peaks at 1500 and 1460 cm<sup>-1</sup> have dominant contributions from modes on F<sub>5</sub>Ph (see above). In addition, both peaks have significant (26-33%) contributions from Tol peaks and the peak at 1460 cm<sup>-1</sup> has a significant, 14% (20%) contribution from a single Tri mode for C2. The peak at ca. 1435 cm<sup>-1</sup> is assigned to a Tri motion. As expected, the peaks at ca. 1530 cm<sup>-1</sup> also belong to the alkyne-Tri moiety. The peak at 1400 cm<sup>-1</sup> is assigned to Tol moieties.

The Tol modes contributing to the peaks at 1500 and 1600 cm<sup>-1</sup> involve C-C stretching and C-H bending motions of the phenyl rings (Figure 4.4), while CH<sub>3</sub> bending modes of Tol moieties (Fig. 4.4(c)) contribute to the peak at 1460 cm<sup>-1</sup> (twelve modes). The peak assignment made for C2 and C6 was further corroborated by the results of RA 2DIR measurements (see below).

**Table 4.2.** Main experimental absorption peaks and DFT computed, scaled normal modes of C2 and C6.

	Experimental peak, $\text{cm}^{-1}$	Computed peak, <sup>a</sup> $\text{cm}^{-1}$	IR Intensity, $\text{km/mol}$	Mode description (number of modes)
C2	1600	1599-1601	98 (23) <sup>b</sup>	Tol (6)
		1606	4	Tri (1)
		1622	3	F <sub>3</sub> Ph (1)
	1530 <sup>c</sup>	1519	24	Tri (1)
	1500	1499	223	F <sub>3</sub> Ph (1)
		1498-1500	94 (22) <sup>b</sup>	Tol (6)
		1496	14	Tri (1)
	1460	1455	211	F <sub>3</sub> Ph (1)
		1456-1461	129 (18) <sup>b</sup>	CH <sub>3</sub> of Tol (12)
		1459	55	Tri (1)
1435	1436	46	Tri (1)	
C6	1600	1599-1601	88 (18) <sup>b</sup>	Tol (6)
		1605	5	Tri (1)
		1623	20	F <sub>3</sub> Ph (1)
	1530 <sup>c</sup>	1534	20	Tri (1)
	1500	1500	252	F <sub>3</sub> Ph (1)
		1498-1500	93 (22) <sup>b</sup>	Tol (6)
		1496	16	Tri (1)
	1460	1458	211	F <sub>3</sub> Ph (1)
		1456-1461	135 (17) <sup>b</sup>	CH <sub>3</sub> of Tol (12)
		1463	85	Tri (1)
1435	1434	73	Tri (1)	

<sup>a</sup> Frequency correction factors were 0.9885 for all F<sub>3</sub>Ph modes and 0.978 and 0.974 for all Tri and Tol modes below and above 1550  $\text{cm}^{-1}$ , respectively; <sup>b</sup> a sum of IR intensities of all modes in the range is given; the IR intensity of the mode with the largest IR intensity is given in parentheses; <sup>c</sup> actual experimental frequencies for the mode denoted as 1530  $\text{cm}^{-1}$  differ for C2 (1525  $\text{cm}^{-1}$ ) and C6 (1539  $\text{cm}^{-1}$ ).

The mode assignment is crucial for understanding the RA 2DIR data. Numerous cross peaks in 2DIR spectra were used to track the energy relaxation and transfer in the C2 and C6 compounds. The results are arranged into three groups involving energy transfer initiated by  $\nu_{\text{C}=\text{C}}$ , energy transfer towards  $\nu_{\text{C}=\text{C}}$ , and energy transfer initiated and detected by the modes in the fingerprint region.

### 4.3.3. Energy Transfer Initiated by $\nu_{C=C}$

The first group of RA 2DIR experiments involves  $\nu_{C=C}$  as a tag and a variety of reporters shown with boxes in Figure 4.5a. The waiting-time dynamics for these cross peaks were recorded, characterizing energy transport from the excited  $\nu_{C=C}$  tag towards various reporter modes throughout the molecule. One-dimensional waiting time traces of the cross-peak amplitude, constructed by integrating the cross-peak area within a respective box, are shown in Figure 4.5 b-f. The  $T_{\max}$  values, referred as the energy transport times, were obtained from the fits of the traces (see Experimental Details).<sup>217</sup> Table 4.3 summarizes the  $T_{\max}$  values for the transport initiated by the  $\nu_{C=C}$  tag, which vary greatly for different reporters.

Note that the  $\nu_{C=C}$  mode lifetimes were measured at  $0.85 \pm 0.1$  ps and  $1.9 \pm 0.1$  ps for C2 and C6, respectively (Fig. 4.6), which are much shorter than the measured  $T_{\max}$  values for each compound.

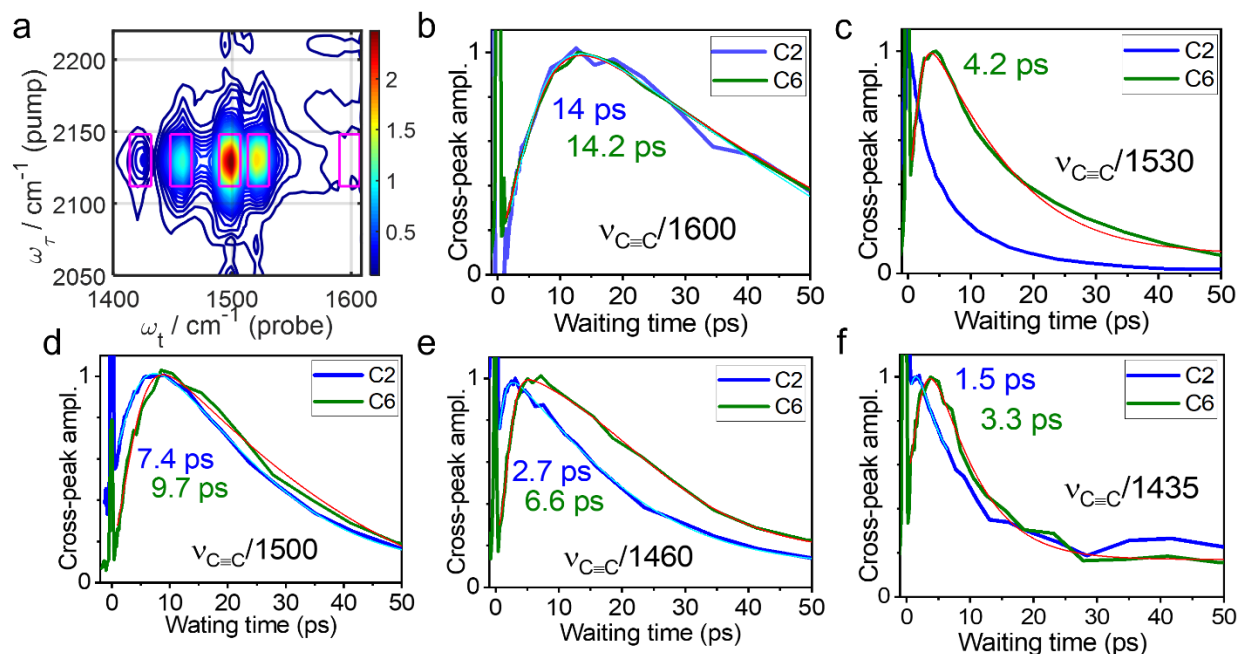


**Figure 4.5.** (a). 2DIR magnitude spectrum of C2 at  $T = 2.7$  ps. The magenta boxes show the integration windows for obtaining the waiting-time traces in panels b-f. (b-f). Waiting-time traces for indicated cross peaks for C2 (blue lines) and C6 (green lines). The traces were fitted with an asymmetric double sigmoidal function.  $T_{\max}$  values are shown in the graphs with matching colors.

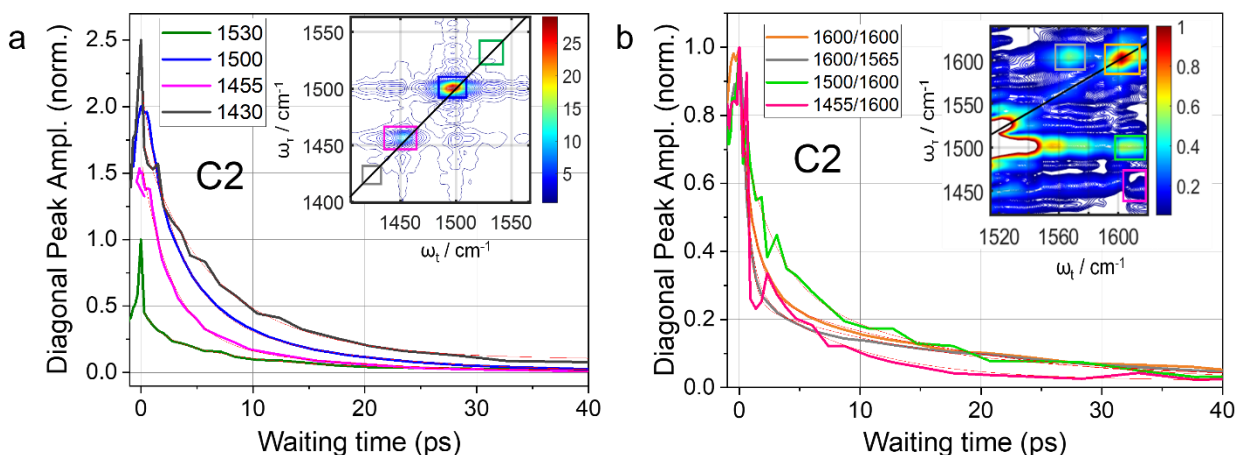


**Figure 4.6.** Scaled waiting-time traces for indicated diagonal and cross peaks for C2. **(a).** All peaks (1530, 1500, 1455 and 1430  $\text{cm}^{-1}$ ) were fitted globally with a double-exponential decay function (red lines). **(b).** Cross peaks in the fingerprint region for C2 were analyzed and fitted with a double-exponential decay function (red lines) The insets in A and B show 2DIR spectra measured at 3.5 ps with color-matching boxes indicating the cross-peak integration regions.

#### 4.3.4. Energy Transfer Towards $\nu_{C\equiv C}$

Relaxation pathways, resulting in energy transfer to remote moieties, are sensitive to the tag identity and location.<sup>184, 197</sup> Therefore, it is expected that reversing the tag and reporter would lead to different energy transfer dynamics, especially when high-frequency modes are involved in the pathways. Comparing the data for the reversed tag and reporter in each compound, the mechanism of energy transport can be assessed. In this section we describe experiments where various peaks in the fingerprint region served as tags initiating energy transport while the  $\nu_{C\equiv C}$  mode served as a reporter detecting energy arrival. Several cross peaks were measured (Fig. 4.7a) and their waiting-time dependences were constructed (Fig. 4.7 b-d).

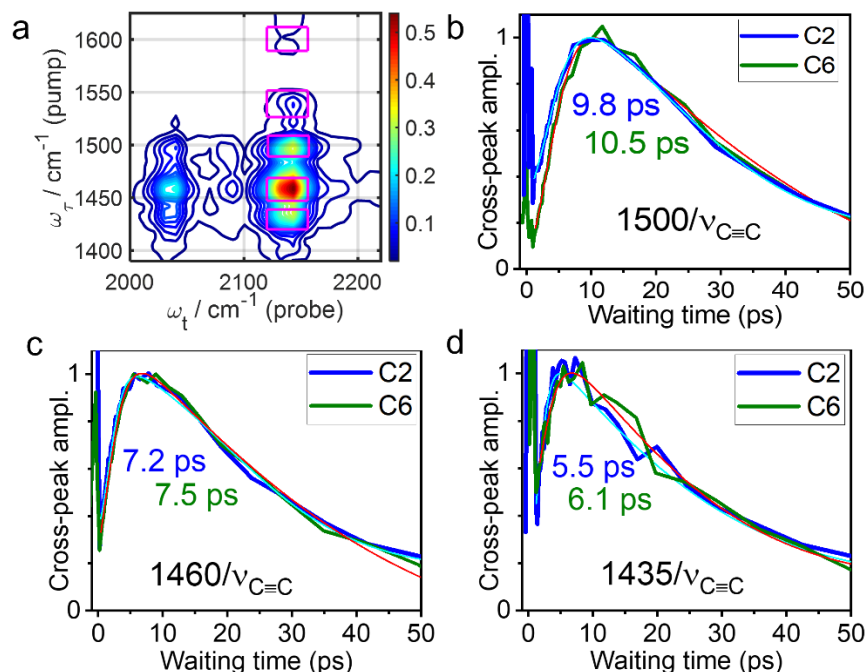


**Fig. 4.7 (a)** 2DIR magnitude spectrum of C6 at  $T = 2.0$  ps. The magenta boxes show the integration windows for obtaining the waiting-time traces in panels b-d. **(b-d)** Waiting-time traces for indicated cross peaks for C2 (blue lines) and C6 (green lines). The traces were fitted with an asymmetric double sigmoidal function (cyan lines for C2 and red lines for C6).  $T_{\max}$  values are shown in the graphs with matching colors.

As expected, the two cross peaks with modes at triazole ( $1530$  and  $1435$   $\text{cm}^{-1}$ ) feature the shortest  $T_{\max}$  values of ca. 5-6 ps (Fig. 4.7d, Table 4.3). The direct coupling between the  $1530$   $\text{cm}^{-1}$  mode and  $\nu_{C\equiv C}$  is strong in C2 resulting in the highest cross-peak intensity at  $T = 0$  (data not shown). The  $1600/\nu_{C\equiv C}$  cross peaks are too weak to record with confidence, as the excess energy escapes from the Tol moieties very slowly resulting in only a small amount arriving to the alkyne moiety region, see next section. Similarly, other Tol modes do not contribute much to the  $1500/\nu_{C\equiv C}$  and  $1460/\nu_{C\equiv C}$  cross peaks. The  $1500/\nu_{C\equiv C}$  cross peak (Fig. 4.7b) is dominated by the  $F_5\text{Ph}$  contribution, as the Tri contribution to the  $1500$   $\text{cm}^{-1}$  mode is small ( $<5\%$ ). The  $T_{\max}$  values for this cross peak represent energy transfer to the  $F_5\text{Ph}$  moiety. They are found to be only slightly larger (1-2 ps) than the  $T_{\max}$  values for the reverse direction,  $\nu_{C\equiv C}/1500$  (Tables 4.2,4.3). The  $T_{\max}$  values for the  $1460/\nu_{C\equiv C}$  cross peaks are smaller than those for  $1500/\nu_{C\equiv C}$ , explained by a stronger contribution of the Tri mode in the  $1460$   $\text{cm}^{-1}$  peak. Convolution of two cross peaks,  $1460(F_5\text{Ph})/\nu_{C\equiv C}$  and  $1460(\text{Tri})/\nu_{C\equiv C}$ , results in smaller measured  $T_{\max}$ .

**Table 4.3.**  $T_{\max}$  values from the waiting-time dependences of several cross-peaks of C2 and C6.

Cross peak	$T_{\max}$ (ps)		Reporter location <sup>a</sup>
	C2	C6	
1600 / $\nu_{\text{C}\equiv\text{C}}$	weak	weak	Tol
1530 / $\nu_{\text{C}\equiv\text{C}}$	NA*	$5 \pm 1.5$	Tri
1500 / $\nu_{\text{C}\equiv\text{C}}$	$9.8 \pm 0.2$	$10.5 \pm 0.3$	F <sub>5</sub> Ph, Tri, Tol
1460 / $\nu_{\text{C}\equiv\text{C}}$	$7.2 \pm 0.2$	$7.5 \pm 0.2$	F <sub>5</sub> Ph, Tri, Tol
1435 / $\nu_{\text{C}\equiv\text{C}}$	$5.5 \pm 0.5$	$6.1 \pm 0.5$	Tri

<sup>a</sup> reporters contributing the most to specific cross peak.

#### 4.3.5. Diagonal and Crosspeaks in the Fingerprint Region

Diagonal 2DIR peaks were measured for all the main peaks in both compounds and the waiting time traces were used to determine the lifetimes. Note that the diagonal 2DIR peaks for the absorption peaks with multiple overlapping contributions favor the strongest peak contributor as the diagonal peak contribution is proportional to the fourth power of their transition dipole, while the contribution to the linear absorption spectrum scales with the square of the transition dipole.<sup>218</sup>

The diagonal peaks at 1500 and 1460  $\text{cm}^{-1}$  have dominant contributions from modes of F<sub>5</sub>Ph. The waiting time traces for the two diagonal peaks are similar, as shown in Figure 4.8b for C6, and can be fitted with two exponential functions with a fast component of ca. 1.8-2.7 ps and a slow component of ca. 10 ps (see specific fit parameters in Table 4.4). The fast components are assigned to the lifetime of the two modes of F<sub>5</sub>Ph. Two Tri peaks at 1435 and 1530  $\text{cm}^{-1}$  in C6 feature the lifetime of ca. 3 ps, although the error bars are rather large at ca.  $\pm 1.5$  ps.

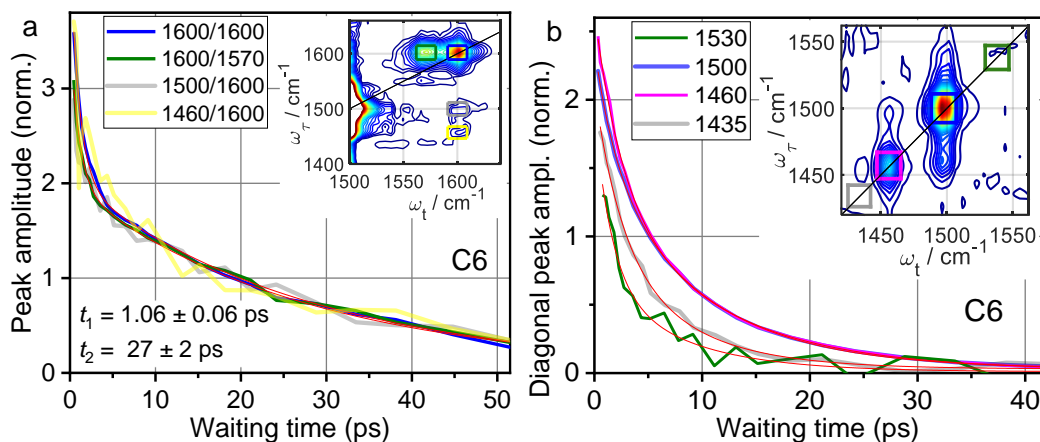


**Figure 4.8.** Scaled waiting-time traces for indicated diagonal and cross peaks for C6. **(a)** The 1600/1600 and 1600/1570 peaks were fitted globally with a double-exponential decay function (red lines) resulting in  $t_1 = 1.06 \pm 0.06$  ps and  $t_2 = 27 \pm 2$  ps and amplitudes of the fast component of 55% for 1600/1600 and 45% 1600/1570. **(b)** The results of individual fits of  $T$ -traces of diagonal peaks (red lines) are shown in Table 4. The insets in (a) and (b) show 2DIR spectra measured at 2.3 ps with color-matching boxes indicating the cross-peak integration regions.

The decay trace of the  $1600\text{ cm}^{-1}$  diagonal peak (1600/1600) is very characteristic with the fast component of  $1.06 \pm 0.06$  ps and slow component of  $27 \pm 2$  ps (Fig. 4.8b). The fast component is assigned to the lifetime of the Tol mode at  $1600\text{ cm}^{-1}$ . The slow component is slower than a typical cooling time of organic molecules to the solvent of ca. 15 ps<sup>219</sup> and has a surprisingly larger amplitude  $A_2 = 45\%$  (Table 4.4). The slow component is attributed to the relaxation-assisted (RA) effect: after relaxation of the  $1600\text{ cm}^{-1}$ , other modes within the Tol moiety became excited and many of these modes are strongly coupled to the reporter ( $1600\text{ cm}^{-1}$ ), resulting in a substantial amplitude of the 1600/1600 diagonal peak at larger waiting times. The strength of the coupling among the modes of Tol is facilitated by its compactness and electronic conjugation. The cooling time is likely affected by relative isolation of the Tol moieties separated from the rest of the molecule by three different bonds involving heavy atoms, C-P, P-Pt and Pt-C. The C-P-Pt-C bridge connecting Tol to  $\text{F}_5\text{Ph}$  and  $\text{C}_m\text{-Tri}$  features a small number of degrees of freedom and different low frequency modes, so that mode delocalization across the bridge is limited making the energy transport inefficient, trapping the excess energy at toluyls.

Two cross peaks involving  $1600\text{ cm}^{-1}$  peak as a reporter (probed mode) and peaks at 1500 and  $1460\text{ cm}^{-1}$  as tags (pumped modes) were also measured (Fig. 4.8b, yellow and gray lines). Note that the main contributors for both tags reside at the  $\text{F}_5\text{Ph}$  moiety. A rise of the amplitude is expected for a cross-peak between a tag at  $\text{F}_5\text{Ph}$  and a reporter at Tol at delays exceeding 10 ps due to the significant distance between the moieties. However, no rise was observed. Instead, the waiting time traces for

both cross peaks follow the trace of the 1600 diagonal peak (Fig. 4.8b) suggesting that both cross peaks originate fully from modes at the Tol moieties. Indeed, peaks at 1500 and 1460  $\text{cm}^{-1}$  bear significant contributions from the modes at Tol (Fig. 4.3, Table 1). The coupling of the Tol modes at 1500 and 1460  $\text{cm}^{-1}$  (tags) and the Tol mode at 1600  $\text{cm}^{-1}$  (reporter) is large, computed at ca.  $-3.8 \text{ cm}^{-1}$ , resulting in a significant cross peak amplitude at  $T = 0$ . Relaxation of these tags populates lower-frequency modes in Tol similar to relaxation of the 1600  $\text{cm}^{-1}$  tag, resulting in similar waiting time traces for three different Tol tags at 1600, 1500, and 1460  $\text{cm}^{-1}$ . Apparently, the mode proximity wins over the strength of the transition dipole of the tag.

Interestingly, there is a rather strong cross peak at 1600/1570. The Tol moiety features a mode computed at ca. 1570  $\text{cm}^{-1}$ , but it is over 10-fold weaker than that at 1600  $\text{cm}^{-1}$ . However, the 1600/1570 cross peak is strong at about a half of the diagonal peak at 1600  $\text{cm}^{-1}$ . The strength of the cross peak originates from a large off-diagonal 1600-1570 anharmonicity, computed at 7.4  $\text{cm}^{-1}$ , which is much larger than the diagonal anharmonicity of the mode at 1600  $\text{cm}^{-1}$ , computed at ca. 1  $\text{cm}^{-1}$ . The pair of diagonal and cross peaks can serve for identifying Tol moieties in 2DIR spectra. The waiting time trace of this cross peak follows the trace of the 1600 diagonal peak (Fig. 4.8b) and shows no coherent oscillations.

**Table 4.4.** Fit parameters for several diagonal peaks.

	Freq., $\text{cm}^{-1}$	$t_1$ , ps	$t_2$ , ps	Fast component contribution, <sup>a</sup> %	$t_{\text{mean}}$ , ps
C2	1600	$1.00 \pm 0.06$	$25 \pm 2$	56	
C2	1530	$1.6 \pm 0.4$	$8.5 \pm 0.8$		6.9
C2	1500	$1.65 \pm 0.15$	$9.4 \pm 0.4$	41	6.0
C2	1460	$1.3 \pm 0.1$	$8.1 \pm 0.5$	46	6.2
C2	1435	$3.4 \pm 1.5$	$14 \pm 5$	77	5.8
C6	1600	$1.06 \pm 0.06$	$27 \pm 2$	55	
C6	1530	$2.9 \pm 0.5$	$12 \pm 3$		6.1
C6	1500	$1.84 \pm 0.15$	$9.4 \pm 0.4$	33	6.9
C6	1460	$2.7 \pm 0.5$	$11.5 \pm 1.5$	47	7.4
C6	1435	$3.4 \pm 1.5$	$14 \pm 5$	88	4.7

<sup>a</sup> computed as  $A_1/(A_1+A_2) \times 100\%$ , where  $A_1$  and  $A_2$  are the amplitudes of the first and second exponential components,  $t_1$  and  $t_2$ .

Multiple cross peaks were observed in the fingerprint region (see Fig. 4.9a, inset) and their waiting time dependences were analyzed. Only one of these cross peaks shows a clear rise time, but

several cross peaks show coherent oscillations as a function of the waiting time. We first discuss the oscillations, then analyze the cross-peak decay times and then discuss the cross peak showing a rise.

#### 4.3.6. Cross-peak and Diagonal-peak Decay Times

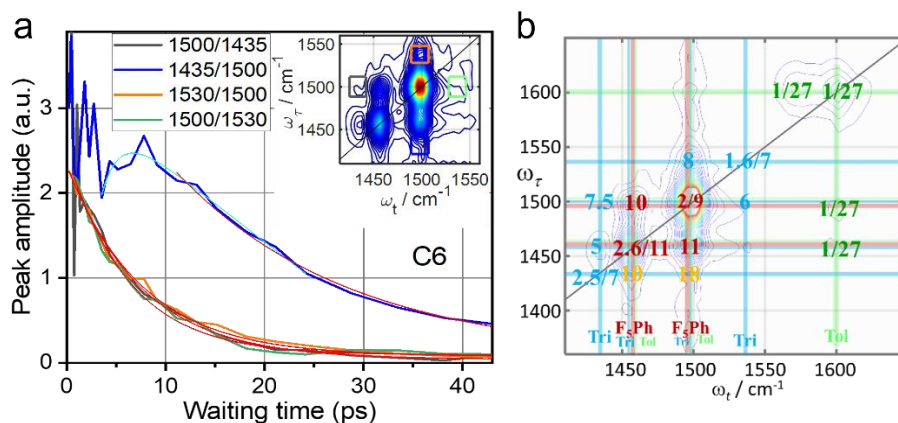


**Figure 4.9.** (a) Scaled waiting-time traces for indicated cross peaks for C6. The traces were fitted globally with an exponential decay function (red lines), see results in Table 4.6. The 1435/1500 cross peak was also fitted with an asymmetric double sigmoidal function (cyan, see Table 4.5). (b) Exponential decay times measured are summarized for each diagonal and cross peak, also reported in Tables 4-7. The vertical and horizontal lines are color coded to indicate FTIR contributions originated from different ligands, F<sub>5</sub>Ph (red), Tri (blue), and Tol (green).

**Slow Decay Components for Diagonal Peaks.** While the fast component of a diagonal peaks is attributed to the lifetime of the largest peak contributor, the slow decay component of the diagonal peak reflects its cooling time, observed via the mode coupling to low and medium frequency modes. Therefore, the slow decay components of diagonal peak traces for the modes residing at the same moiety should be similar. Indeed, both modes of the Tri moiety, 1435 and 1530 cm<sup>-1</sup>, feature similar cooling times of ca. 7 ps. The cooling times for the diagonal peaks at 1460 and 1500 cm<sup>-1</sup> are also similar at 10 ± 1 ps, as both peaks reside predominantly at F<sub>5</sub>Ph.

**Tol-Dominated Peaks.** The decay time for the diagonal peak at 1600 cm<sup>-1</sup>, representing Tol moieties, is exceptionally long at 27 ps. Interestingly, the decay times for two cross peaks with the reporter at 1600 cm<sup>-1</sup> (1500/1600 and 1460/1600) are also the same at ca. 27 ps (Fig. 4.9a), despite the fact that the strongest contributors to 1500 and 1460 cm<sup>-1</sup> peaks reside at F<sub>5</sub>Ph. This similarity indicates that all three cross peaks are dominated by the Tol/Tol type cross-peak contributions. In other words, for the 1500/1600 cross peak the Tol-localized modes are contributing as tags, not the strongest 1500 peak contributor of F<sub>5</sub>Ph. At the same time, the cross-peak contribution associated with the energy transfer between the F<sub>5</sub>Ph and Tol ligands, expected to feature a rise in the waiting

time dependence, is fully masked by a much stronger Tol/Tol type cross-peak contribution. Otherwise, either a cross-peak rise would be observed, or the decay time would be longer, affected by delayed energy arrival to the reporter site.

**Tri-Dominated Peaks.** The diagonal peaks of Tri modes at 1435 and 1530  $\text{cm}^{-1}$  feature the same cooling time of ca. 7 ps. The slow decay components are nearly the same for a range of cross peaks involving Tri modes, such as 1500/1435, 1469/1435, 1530/1500, and 1500/1530 (Fig. 4.9a, cyan color). This match suggests that these four cross peaks are dominated by local Tri modes while the Tri/ $\text{F}_5\text{Ph}$  and  $\text{F}_5\text{Ph}$ /Tri type cross peaks, involving energy transfer between the ligands, cannot compete, amplitude-wise with the local Tri/Tri type cross peaks.

**$\text{F}_5\text{Ph}$ -Dominated Peaks.** The diagonal peaks for the  $\text{F}_5\text{Ph}$ -residing modes at 1500 and 1460  $\text{cm}^{-1}$  show a characteristic cooling time of ca. 10 ps. Their cross peaks, 1500/1460 and 1460/1500 show similar cooling times of  $10 \pm 1$  ps, characteristic for cooling of the  $\text{F}_5\text{Ph}$  moiety.

**Cross-peaks at 1435/1500 and 1435/1460.** The cross peaks at 1435/1500 and 1435/1460 can have two contributions: one from spatially close Tri/Tri type modes, which may show coherent oscillations, and another of Tri/ $\text{F}_5\text{Ph}$  type, which is expected to show an amplitude rise with the waiting time. Only one cross peak in the fingerprint region is showing a rise time and a clear maximum; that is the 1435/1500 peak in C6 (4.9a). It shows small amplitude oscillations ( $\sim 10\%$ ) at early times, indicating a Tri/Tri contribution. The Tri/Tri type cross peak decays with ca. 7 ps, the cooling time of the Tri moiety. Because its contribution diminishes so rapidly, we can clearly see a cross-peak rise associated with 1435(Tri)/1500( $\text{F}_5\text{Ph}$ ) cross peak, which peaks at ca. 7-8 ps. This time is slightly shorter than  $T_{\text{max}}$  for the  $\nu_{\text{C}=\text{C}}$ /1500 cross peak of 9.7 ps, supporting the picture that excited  $\nu_{\text{C}=\text{C}}$  relaxes into the Tri modes, away from the  $\text{F}_5\text{Ph}$  ligand, resulting in a longer time. No rise for the 1435/1500 cross peak is found in C2, likely because the rising 1435(Tri)/1500( $\text{F}_5\text{Ph}$ ) peak contributor is expected to be earlier by 2-3 ps, which is then hidden by the decaying 1435(Tri)/1500(Tri) peak contribution. The 1435/1460 cross peak does not show a resolved maximum, likely due to its small amplitude compared to stronger Tri/Tri contribution as the Tri mode within the 1460  $\text{cm}^{-1}$  peak is much brighter than that within the 1500  $\text{cm}^{-1}$  peak. The exponential decay times measured for each diagonal and cross peak for C6 are summarized graphically in Fig. 4.9b.

Detailed assessment of the cooling times of different ligands (moieties) permits understanding the origin of the cross peaks and revealing different contributions to cross peaks with multiple overlapping modes. A significant difference in the effective cooling times for the modes at Tri,  $\text{F}_5\text{Ph}$

and Tol moieties was found; the cooling times are at ca. 7, 10, and 27 ps, respectively. To further understand the vibrational energy transport within these complex molecules, we computed relaxation pathways of various excited modes.

### 4.3.6. Coherent Oscillations in Cross-peaks

The presence of oscillations in a cross peak indicates that a coherent superposition of strongly coupled states is excited by a short m-IR pulse.<sup>210, 220, 221</sup> Therefore, coherent oscillations in 2DIR spectra can help identify modes that belong to the same moiety as their strong coupling requires significant spatial overlap. Several 2DIR cross peaks of C2 and C6 show coherent oscillations. These include the cross peaks between the two strongest peaks, 1500 and 1460  $\text{cm}^{-1}$  (1500/1460 and 1460/1500), as well as the cross peaks among the 1460 and 1435  $\text{cm}^{-1}$  peaks (1435/1460 and 1460/1435), Fig. 4.10. The period of oscillations,  $T_0$ , corresponds to the beating frequency as  $\Delta\nu$  (in  $\text{cm}^{-1}$ ) =  $1/(c T_0)$ , where  $c$  is the speed of light in vacuum. The computed beating frequencies,  $43 \pm 1 \text{ cm}^{-1}$  for 1500/1460 and 1460/1500 and  $21 \pm 1 \text{ cm}^{-1}$  for 1435/1460, are expected to match the energy gap between the involved states excited coherently – the two frequencies of the cross peak. Indeed, the frequency difference between the peaks at 1500 and 1460  $\text{cm}^{-1}$  for C6 is 43.2  $\text{cm}^{-1}$  (1500.1–1456.9  $\text{cm}^{-1}$ ), which matches well the oscillation frequency. The function used for fitting the data is described in Figure 4.10 caption, while the fit parameters are given in Table 4.5.

Note that the 1500 and 1460  $\text{cm}^{-1}$  peaks have dominant contributions from the F<sub>5</sub>Ph ligand. Their cross-peak oscillations are expected to be dominated by coherent excitation of the two F<sub>5</sub>Ph modes, but a smaller contribution from coherent excitation of the modes at Tri is also expected. Due to reduced coupling, it is less likely that the Tol modes will be excited coherently as the group of Tol modes at 1500  $\text{cm}^{-1}$  belong to the Ph ring motion, while those at 1460  $\text{cm}^{-1}$  are due to CH<sub>3</sub> bending.

The peak at 1435  $\text{cm}^{-1}$  belongs exclusively to Tri. Therefore, the oscillations of the 1435/1460 cross peak have to be due to coherent excitation of the modes at the Tri moiety. The presence of oscillations proves that both modes of the cross peak originate from the same moiety, Tri, permitting to identify a minor Tri contribution within the 1460  $\text{cm}^{-1}$  peak, predicted by the DFT-based peak assignment (Table 4.1). How strong is the contribution to the cross peak of the 1460  $\text{cm}^{-1}$  mode of F<sub>5</sub>Ph and the Tri mode of 1435  $\text{cm}^{-1}$ ? Such a cross peak is expected to be weak at waiting times close to zero. Indeed, the amplitude of the oscillations is significant,  $A_2/A_1 = 0.33$ , so the cross peak is

dominated by the Tri peaks, at least at small waiting times. Further in dept analysis on coherent oscillations and its functionality as structural reporters is presented in Chapter 5.

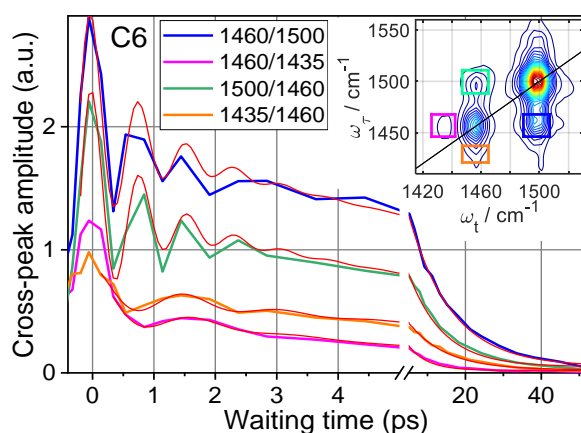


**Fig. 4.10.** Waiting-time dependence of the indicated cross peaks for C6. The inset shows 2DIR spectrum measured at 4.3 ps with color-matching boxes indicating the cross-peak integration regions. Thin red lines show fits of the traces with a function  $y = y_0 + A_1 \times \exp(-T/T_1) + A_2 \times \exp(-T/T_2) \times \cos(2\pi T/T_0 + \phi)$ . The fit resulted in the oscillation period,  $T_0$ , of  $0.78 \pm 0.02$  ps for both cross peaks involving 1460 and 1500  $\text{cm}^{-1}$  peak and of  $1.6 \pm 0.1$  ps for the peak at 1435/1460. The oscillation damping time,  $T_2$ , was  $0.8 \pm 0.1$  ps for 1460/1500 and 1500/1460 peaks and  $1.2 \pm 0.3$  ps for the peak at 1435/1460. The overall decay time,  $T_1$ , is about 10 ps for all three cross peaks. Complete list of fit parameters is given in Table 4.5.

**Table 4.5.** Fit parameters for several cross peaks (see Fig. 6 caption) for C6.

Cross peak	$T_1$ , ps	$T_2$ , ps	$T_0$ , ps	$\phi$	$A_2/A_1$	Oscillation freq., $\text{cm}^{-1}$
1460/1500	$11.3 \pm 0.7$	$0.79 \pm 0.1$	$0.78 \pm 0.02$	0.05	0.47	$43 \pm 1$
1500/1460	$9.8 \pm 0.8$	$0.79 \pm 0.1$	$0.78 \pm 0.02$	0.01	0.70	$43 \pm 1$
1435/1460	$9.8 \pm 0.7$	$1.3 \pm 0.4$	$1.6 \pm 0.1$	0.07	0.33	$21 \pm 1$
1460/1435	$5.1 \pm 0.3$	$0.9 \pm 0.2$	$1.7 \pm 0.2$	-0.05	0.51	$20 \pm 1$

**Table 4.6.** Exponential decay parameters for cross peaks for C6.

Cross peak	$t_1$ , ps	$T_{\max}$ , ps
1500/1435 <sup>&amp;</sup>	$7.5 \pm 0.4$	0
1435/1500 <sup>&amp;</sup>	$15.7 \pm 1$	7.0
1530/1500	$7.6 \pm 0.3$	0
1500/1530	$6.3 \pm 0.3$	0

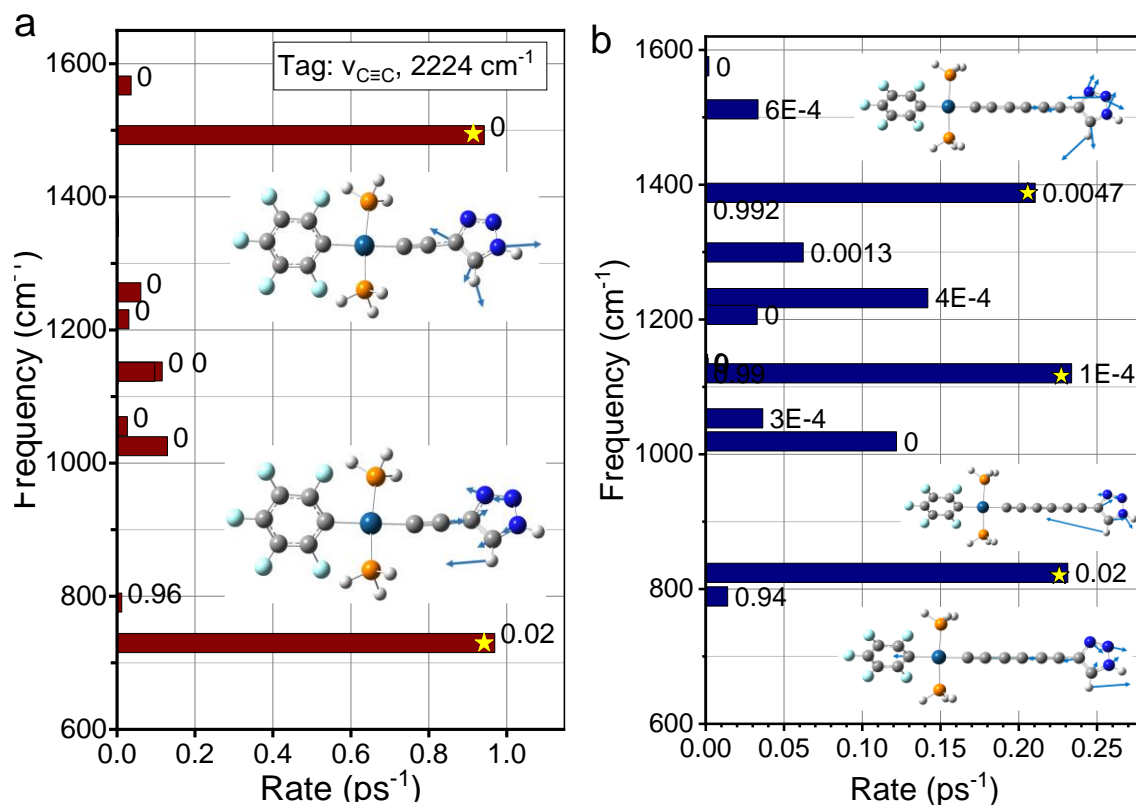
<sup>&</sup> coherent oscillations observed.

## 4.4. Discussion

### 4.4.1. Computing Vibrational Relaxation Pathways

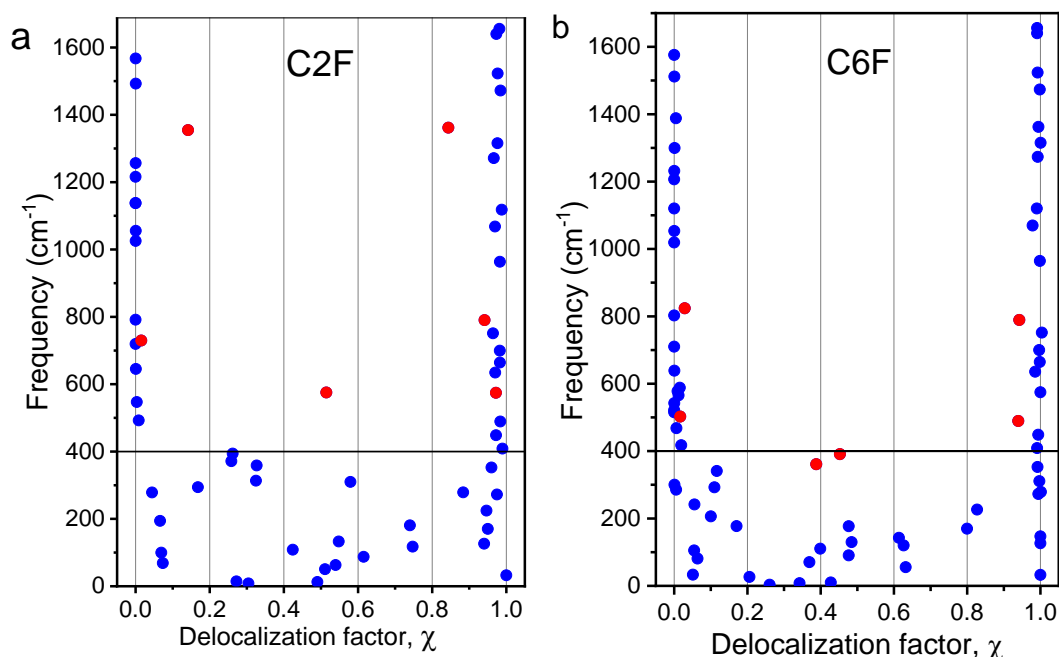
The whole molecules were too large to perform anharmonic DFT calculations, so such computations were performed on the fragments of the compounds where the Tol and CH<sub>2</sub>-C<sub>6</sub>H<sub>5</sub> groups were replaced by hydrogen atoms (labeled as C2F and C6F), as shown in Figures 4.11 a,b insets.

Figure 4.11a shows the dominant relaxation channels for the  $\nu_{C\equiv C}$  tag in C2F, presented as rate bars populating various daughter states. Each relaxation daughter mode is labeled with a  $\chi$  value, (Fig. 4.11a, right of bars) which represents the level of mode delocalization between the F<sub>5</sub>Ph and C<sub>n</sub>-Tri ligands across the Pt center (excluding motions at the PH<sub>3</sub> ligands). The modes with  $\chi \sim 1$  reside at the F<sub>5</sub>Ph ligand, while those with  $\chi \sim 0$  reside at the C<sub>2</sub>-Tri ligand. Clearly, the  $\nu_{C\equiv C}$  relaxation daughter modes are predominantly (99.5%) residing at the Tri ligand with  $\chi$  of 0 - 0.02. The two daughter modes populated the most are at 1492 and 729 cm<sup>-1</sup> (Fig. 4.11a, bars marked with stars). The  $\nu_{C\equiv C}$  relaxation pathways in the C6 compound are richer but similarly populate predominantly the modes of the Tri ligand with  $\chi < 0.01$  (Fig. 4.11 b). It is important to note that both compounds show negligible relaxation of the  $\nu_{C\equiv C}$  tag directly into the F<sub>5</sub>Ph localized modes.



**Figure 4.11.** Rates of dominant relaxation channels of  $\nu_{\text{C}\equiv\text{C}}$  computed for **(a)** C2F and **(b)** C6F. The displacements of the strongly contributing normal modes (labeled with stars) are shown as insets. Delocalization factors,  $\chi$ , are shown for each normal mode to the right of its rate bar. Note that  $\chi(\nu_{\text{C}\equiv\text{C}}) < 10^{-4}$ .

To illustrate the waiting time dependence on chain length, we performed a modeling in which the  $\nu_{\text{C}\equiv\text{C}}/\text{F}_5\text{Ph}$  cross-peak amplitude for C2 and C6 were plotted as a function of the waiting time (Figs 4.16a and 4.17a). Reasonable shapes of the waiting time dependences were obtained with the  $T_{\text{max}}$  values showing similar trends to the experimental values (7.4 ps in C2 and 9.7 ps in C6). Detailed analysis showed the presence of a very large number of relaxation pathways in the energy relaxation process, *vide infra*. To identify the pathways leading to energy crossing the Pt center, a detailed analysis of the mode couplings and delocalization was performed (Fig. 4.12 a,b).



**Figure 4.12.** Delocalization factor,  $\chi$ , for all normal modes below  $1650\text{ cm}^{-1}$  in **(a)** C2F and **(b)** C6F. Three pairs of significantly delocalized high-frequency modes are shown with red circles. Most high-frequency modes ( $>400\text{ cm}^{-1}$ ) are localized at either  $\text{F}_5\text{Ph}$  ( $\chi \sim 1$ ) or  $\text{C}_2\text{-Tri}$  ( $\chi \sim 0$ ) ligands. Low frequency modes ( $<400\text{ cm}^{-1}$ ) are mostly delocalized across the Pt center.

We found that despite some similarities of bond types in the  $\text{F}_5\text{Ph}$  or  $\text{C}_2\text{-Tri}$  ligands, most of their high-frequency modes are localized on either of the ligands. However, there are a few pairs of normal modes showing significant delocalization. To identify potential delocalization, the coupling strength among the local modes at  $\text{F}_5\text{Ph}$  and  $\text{C}_2\text{-Tri}$  were computed by varying the masses of the 11 atoms of  $\text{F}_5\text{Ph}$  in small increments and computing normal modes for each mass value using the Hessian matrix obtained via DFT normal-mode analysis. As a result of the mass change of the  $\text{F}_5\text{Ph}$  moiety, an avoided splitting is observed for the interacting modes which equals  $2\beta$ , where  $\beta$  is the interaction energy (Fig. 4.13). We found that the coupling of local modes across the Pt center does not exceed  $\sim 20\text{ cm}^{-1}$ , while typical couplings are less than  $2\text{ cm}^{-1}$ . Only two pairs of high-frequency modes ( $>400\text{ cm}^{-1}$ ) were found to be coupled strongly enough to result in mode delocalization at the actual atomic masses of  $\text{F}_5\text{Ph}$  ( $\chi = 1$ ). One pair involves partially delocalized modes at  $1355\text{ cm}^{-1}$  ( $\chi = 0.14$ ) and  $1362\text{ cm}^{-1}$  ( $\chi = 0.84$ ) with  $2\beta = 5\text{ cm}^{-1}$  (labeled with red circles in Fig. 4.12a). Another pair involves modes at  $730\text{ cm}^{-1}$  ( $\chi = 0.015$ ) and  $790\text{ cm}^{-1}$  ( $\chi = 0.94$ ) with  $2\beta = 17\text{ cm}^{-1}$  (Fig. 4.13). Relatively small couplings require rather precise match of the site frequencies to result in delocalization, limiting the number of delocalized modes. Interestingly, the low-frequency modes ( $<400\text{ cm}^{-1}$ ) are predominantly delocalized across the Pt center (Fig. 4.12).

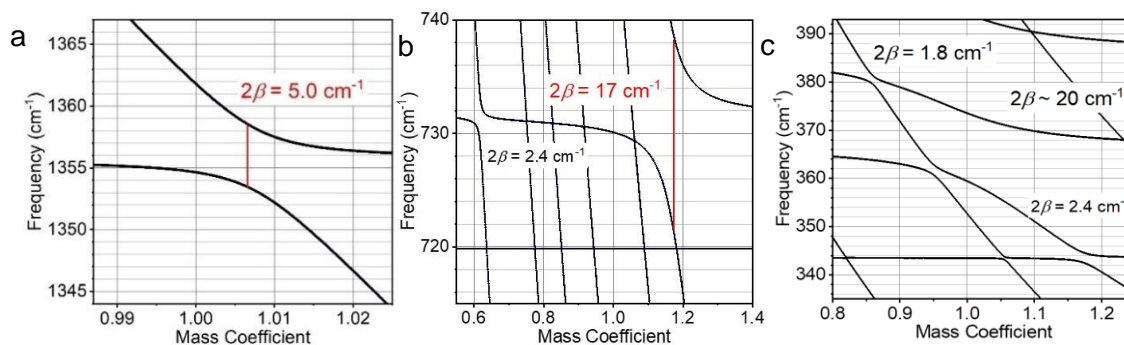


**Figure 4.13.** Mode frequency of delocalized pairs **(a)** 1354 and 1362  $\text{cm}^{-1}$ , **(b)** 729 and 790  $\text{cm}^{-1}$ , and **(c)** frequencies around 360  $\text{cm}^{-1}$  as a function of the mass scaling factor for the C and F atoms of the  $\text{F}_5\text{Ph}$  moiety. Vertical red lines show the frequency jump ( $2\beta$ ) of the observed modes.

#### 4.4.2. Electrical Dipole-dipole Coupling across Pt Center

The through-space electrical coupling of the modes across the Pt center was computed using a point dipole approach. The electrical dipole-dipole coupling was computed using Eq. 4.4:

$$U_{12} = -k \frac{\mu_1^{\text{tr}} \mu_2^{\text{tr}}}{R^3} \quad (4.4)$$

Here  $\mu_i^{\text{tr}}$  are the transition dipoles of the interacting modes,  $R$  is the distance between the oscillators, and  $k = 8.99 \cdot 10^9 \text{ C}^{-2}\text{Nm}^2$ . The transition dipole was calculated using the DFT-computed IR intensity by Eq. 4.5:<sup>222</sup>

$$A_a = \frac{N_A \pi (\mu_1^{\text{tr}})^2}{3c^2} \left( \frac{\partial \vec{\mu}}{\partial Q_a} \right)^2 \quad (4.5)$$

Here  $A_a$  is the IR intensity in  $\text{m/mol}$ ,  $N_A$  is Avogadro's number,  $c$  is the speed of light. The largest transition dipole moments of the pairs of coupled modes in C2 were found for the modes at 1362 and 1355  $\text{cm}^{-1}$ , at 0.04 and 0.09 D, respectively. The interaction energy computed for the distance,  $R$ , of 5.3 Å is ca. 0.13  $\text{cm}^{-1}$ . The largest IR intensity for C6 is found for the pair at 824 and 789  $\text{cm}^{-1}$ , where the transition dipoles are 0.1 and 0.084 D, respectively, resulting in interaction energy of 0.08  $\text{cm}^{-1}$  for  $R = 8 \text{ Å}$ . The interaction energies for other coupled pairs for both C2 and C6 are not exceeding 0.05  $\text{cm}^{-1}$ .

#### 4.4.3. Origin of Mode Coupling across the Pt Center

Two types of coupling mechanisms are possible: through-space electrical coupling and through-bond mechanical coupling. The modes of the two pairs feature IR intensities not exceeding 60  $\text{km/mol}$  and the effective distances well exceeding 4 Å (carbon-carbon distance across Pt is ca. 4.1

Å). For such weak modes and distances over 5.3 Å, the electrical dipole-dipole coupling is computed to be smaller than  $0.25 \text{ cm}^{-1}$  (see above). We found that the modes with the largest coupling strength ( $2\beta > 5.0 \text{ cm}^{-1}$ ) are coupled mechanically, involving a change of the C-Pt-C distances, as for modes of a coupled pair at 1350 and 1362  $\text{cm}^{-1}$  (Fig. 4.15 a,b). While the Pt atom is heavy and does not move much, both adjacent carbon atoms move in the Pt-C stretching fashion as in-phase and out-of-phase combinations for the modes of the pair. The energy gap of the local modes is larger than the coupling leading to only a partial mixing of the site states. The energy match is somewhat accidental, as the two ligands are different. At the same time, both ligands feature similar bond types, carbon-carbon with a bond order of 1.5, which facilitates the energy match and mixing of the local modes featuring Pt-C stretching motions. Another type of local motion that leads to strong coupling between the local modes of the two ligands involves C-Pt-C angle change (Fig. 4.14 c,d). Such motions are present in many local modes with 250-400  $\text{cm}^{-1}$  frequencies, ensuring delocalization of normal modes in this frequency region (Fig. 4.12 a). The lower frequency modes,  $<250 \text{ cm}^{-1}$ , are delocalized over the whole compound, as expected.

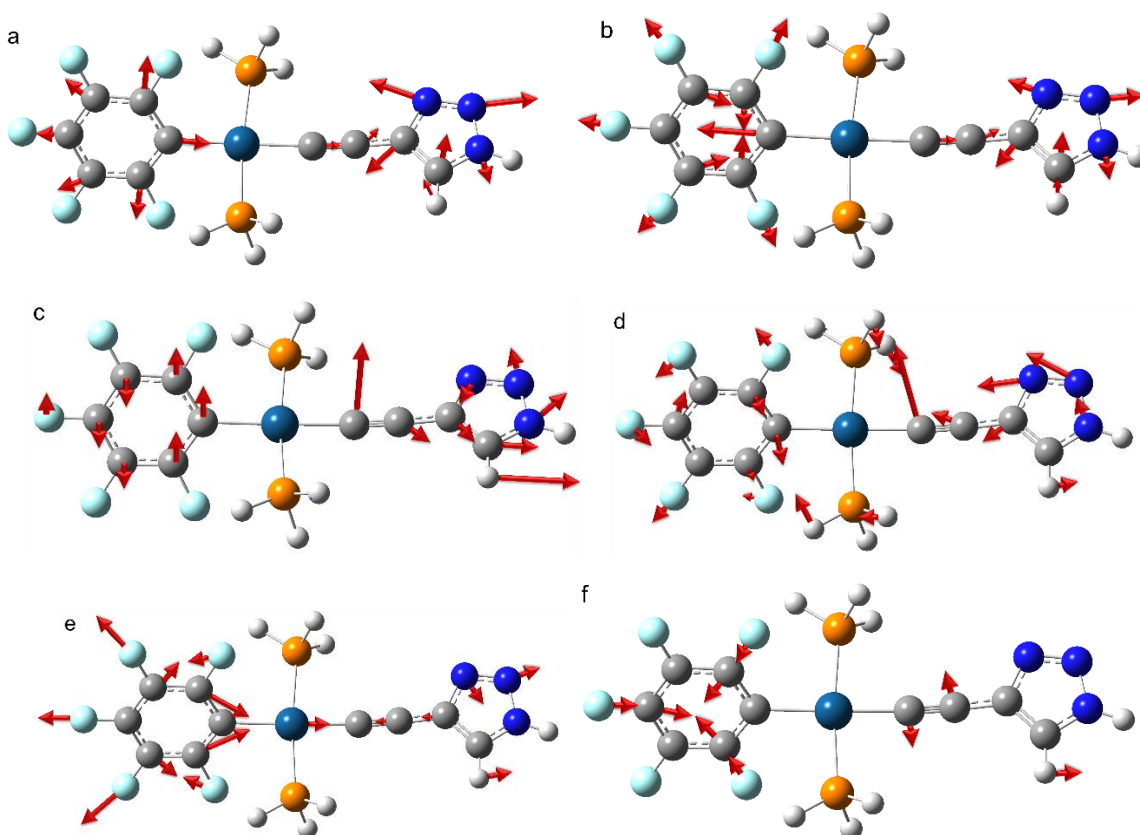


**Figure 4.14.** Displacements for normal modes at (a) 1355  $\text{cm}^{-1}$ , (b) 1362  $\text{cm}^{-1}$ , (c) 394  $\text{cm}^{-1}$ , (d) 359  $\text{cm}^{-1}$ , (e) 790  $\text{cm}^{-1}$ , and (f) 575.5  $\text{cm}^{-1}$ .

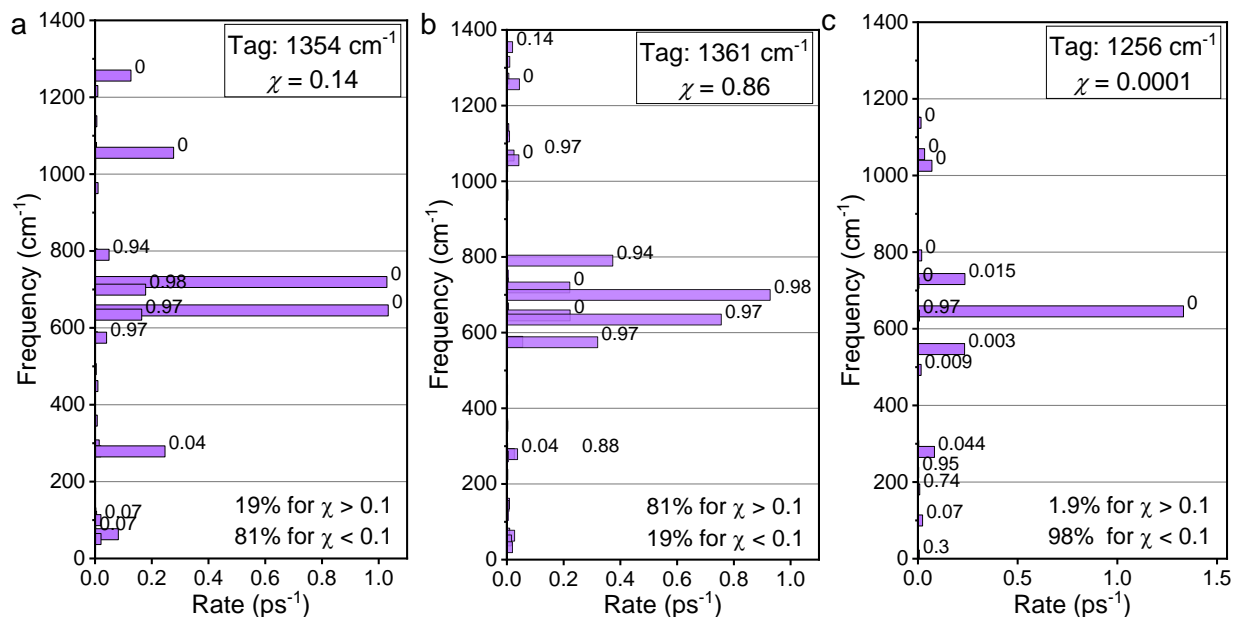


**Figure 4.15.** Rates of dominant relaxation channels in C2F for two delocalized modes **(a)** 1361 cm<sup>-1</sup> and **(b)** 1354 cm<sup>-1</sup> and one mode localized at C<sub>2</sub>-Tri ligand, **(c)** 1256 cm<sup>-1</sup>. The values on the right of each bar represent the mode delocalization factor,  $\chi$ .

Vibrational relaxation is governed by third-order force constants; to be significant they require spatial overlap of the parent and daughter modes. Figure 4.15 illustrates this statement presenting relaxation pathways of the three modes, two modes of the partially delocalized pair at 1361 and 1354 cm<sup>-1</sup> with a delocalization extent of 0.86 and 0.14, respectively, and a high-frequency mode at 1256 cm<sup>-1</sup> located at the C<sub>2</sub>-Tri ligand ( $\chi=0.001$ ). The mode at 1354 cm<sup>-1</sup> ( $\chi=0.14$ ) relaxes predominantly to modes within C<sub>2</sub>-Tri (81%) but also relaxes to modes localized at the F<sub>5</sub>Ph ligand (19%), thus providing a high-frequency (600-800 cm<sup>-1</sup>) pathway to F<sub>5</sub>Ph across the Pt center (Fig. 4.15a). The rate distribution vs. delocalization factor is bimodal with peaks at around  $\chi = 0$  and  $\chi = 1$  (Fig. 4.12). The relaxation pathways of the 1361 cm<sup>-1</sup> mode ( $\chi=0.86$ ) are complementary to those for 1354 cm<sup>-1</sup>; 19 rate percent of the pathways involve energy passage from F<sub>5</sub>Ph to C<sub>2</sub>-Tri (Fig. 4.15b inset).

The daughters of the 1256 cm<sup>-1</sup> mode ( $\chi=0.001$ ) relaxation located predominantly (>98 rate percent) at the same ligand as the parent mode (Fig. 4.15c). Therefore, to have sizable relaxation rates across the Pt center, the parent mode should be delocalized significantly across the center. If such a delocalized parent mode became excited, it relaxes into modes on both sides of the Pt center. At the same time if a mode is localized at C<sub>*n*</sub>-Tri, it predominantly relaxes into the modes at C<sub>*n*</sub>-Tri, resulting in negligible energy transfer across the Pt center (Fig. 4.15c). As the number of delocalized high-frequency modes is small, there is a small number of energy transfer pathways across the Pt center.

Most vibrational modes lower than  $400\text{ cm}^{-1}$  are delocalized (Fig. 4.12). A strong coupling of local modes of  $\text{F}_5\text{Ph}$  and  $\text{C}_2\text{-Tri}$  in the  $250\text{-}400\text{ cm}^{-1}$  region originates from local modes resulting in a change of the C-Pt-C angle (bending). The low-frequency modes ( $<250\text{ cm}^{-1}$ ) naturally involve motion of the whole molecule. The delocalized modes ( $<400\text{ cm}^{-1}$ ) feature a significant coupling to high-frequency modes on each side of the Pt center. If excited, they perturb the reporter at the  $\text{F}_5\text{Ph}$  moiety causing an increase of the  $\text{C}\equiv\text{C}$ /reporter cross peak amplitude. It is important to note that excitation of delocalized low-frequency modes does not lead to energy transfer across the Pt center, as the energy excess remains on both sides of the Pt center.

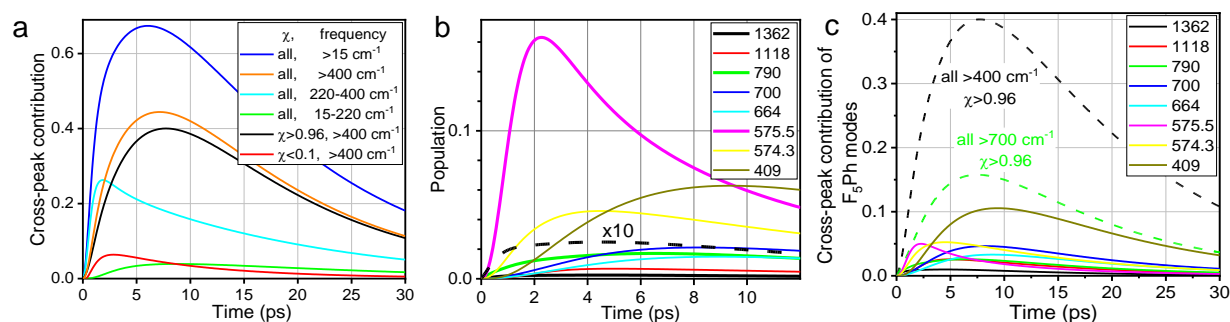


**Figure 4.16.** (a) Contributions of different groups of modes to the  $\nu_{\text{C}\equiv\text{C}}/1500(\text{F}_5\text{Ph})$  cross peak computed for C2F. The groups are formed based on the frequency ( $>15$ ,  $>400$ ,  $220\text{-}400$ , or  $15\text{-}220\text{ cm}^{-1}$ ) and delocalization factor,  $\chi$  (all,  $>0.96$ , or  $<0.1$ ). (b) Waiting-time population traces for high-frequency modes of  $\text{F}_5\text{Ph}$  ( $\chi > 0.96$ ) and the mode at  $575.5\text{ cm}^{-1}$  ( $\chi = 0.51$ ). 10-fold normalized population trace for 1362 mode is also shown by black dashed line. (c) Cross-peak contributions of the modes shown in panel B. The overall contributions of all  $\text{F}_5\text{Ph}$  modes ( $\chi > 0.96$ ) of frequencies  $>700\text{ cm}^{-1}$  (green) and  $>400\text{ cm}^{-1}$  (black) are shown with dashed lines.

The relaxation dynamics initiated by relaxation of the excited  $\nu_{\text{C}\equiv\text{C}}$  mode was computed and the excess populations of every mode (Fig. 4.16b) and their contributions to the  $\nu_{\text{C}\equiv\text{C}}/1500(\text{F}_5\text{Ph})$  cross-peak were extracted and analyzed (Fig. 4.16 a,c). The IVR process of  $\nu_{\text{C}\equiv\text{C}}$  populates every mode in the compound but to a different extent and at different times. The maximum computed for all modes higher than  $15\text{ cm}^{-1}$  is peaking at  $\sim 6.1\text{ ps}$  (Fig. 4.16a, blue line). To understand which modes are involved in transferring energy from the  $\text{C}_n\text{-Tri}$  ligand to  $\text{F}_5\text{Ph}$ , we analyzed contributions from different groups of modes to the cross-peak (Fig. 4.16a).

As expected, we found that the  $\nu_{\text{C}\equiv\text{C}}/1500(\text{F}_5\text{Ph})$  cross-peak is dominated by contributions of the modes at  $\text{F}_5\text{Ph}$  (those with high  $\chi$ , Fig. 4.16a, black) as they are well coupled to the reporter located at  $\text{F}_5\text{Ph}$ . The high-frequency modes,  $>400\text{ cm}^{-1}$ , are mostly localized at either ligand so they are easily sorted into the modes at  $\text{F}_5\text{Ph}$  (large  $\chi$ , black line) or  $\text{C}_2\text{-Tri}$  (small  $\chi$ , red line). The modes with  $\chi > 0.96$

contribute the most (black line) with a peak at 7.7 ps. High frequency modes with  $\chi < 0.1$  (red line) contribute much less, peaking at ca. 3 ps.

Many modes in the 220-400  $\text{cm}^{-1}$  window are delocalized over the two ligands due to the motion involving C-Pt-C angle change (Fig. 4.14 c,d); their contribution is shown in Fig. 4.16a, cyan. Interestingly, the contribution is significant but peaking at earlier delay times of  $\sim 2$  ps, thus shortening the  $T_{\text{max}}$  values for the  $\nu_{\text{C}=\text{C}}/\text{F}_5\text{Ph}$  cross-peaks. Low-frequency modes,  $< 220$   $\text{cm}^{-1}$  (Fig. 4.16a, green), are not contributing much to the cross peak, mostly because of their small coupling to the high-frequency reporter at  $\text{F}_5\text{Ph}$ .

Based on the match of the experimental  $T_{\text{max}}$  values for the  $\nu_{\text{C}=\text{C}}/1500(\text{F}_5\text{Ph})$  cross peak (7.4 ps) and the computed  $T_{\text{max}}$  (Fig. 4.16a), we conclude that the high-frequency modes at  $\text{F}_5\text{Ph}$  (high  $\chi$ ) determine the  $T_{\text{max}}$  values.

To understand the pathways populating the high-frequency modes at  $\text{F}_5\text{Ph}$  we analyzed the population dynamics of these modes. Figure 4.16b shows the high-frequency modes with  $\chi > 0.5$  having the highest populations. Importantly, the modes of  $\text{F}_5\text{Ph}$  that are populated the earliest and to the largest extent contribute the most to the energy transfer process from the  $\text{C}_2\text{-Tri}$  ligand to  $\text{F}_5\text{Ph}$ . We found that such modes involve those modes of the coupled pairs: 575.5, 790, and 1362  $\text{cm}^{-1}$  (Fig. 4.16b). The populations for the 790 and 1362  $\text{cm}^{-1}$  modes are rising with no delay, indicating that they are daughter modes of the  $\nu_{\text{C}=\text{C}}$  relaxation. However, their contributions are not very large, even though they carry larger energy. The mode at 575  $\text{cm}^{-1}$  (Fig. 4.16, magenta) belongs to a coupled pair involving mixing of the CCC bending at  $\text{C}_2\text{-Tri}$  and  $\text{F}_5\text{Ph}$  deformation motions (Fig. 4.14). It is not populated directly from  $\nu_{\text{C}=\text{C}}$ , as apparent from the presence of the induction period, but is still populated very rapidly leading to a maximum at  $\sim 2.3$  ps. Another mode of the pair, 574.3  $\text{cm}^{-1}$  ( $\chi = 0.972$ , Fig. 4.16b, yellow), follows the trace of the 575.5 mode with some lag, peaking at  $\sim 4.5$  ps. Figure 4.16c shows the largest high-frequency contributors to the cross peak. Note that because of a strong coupling among the modes of  $\text{F}_5\text{Ph}$ , the equilibration among them occurs within a few IVR steps (3-5 ps), so that many  $\text{F}_5\text{Ph}$  modes became populated after 3 ps. The large contribution of the mode at 409  $\text{cm}^{-1}$  ( $\chi = 0.9895$ ) reflects its lower frequency. Nevertheless, the overall contribution of the high-frequency modes ( $> 700$   $\text{cm}^{-1}$ ) is very significant (Fig. 4.16 c, green dashed line).

To summarize, the high-frequency modes of the mode pairs coupled across the Pt center provide pathways to transfer energy between the two ligands. The process should be treated as energy transport, not the IVR process into fully localized modes. The high-frequency modes,  $> 400$   $\text{cm}^{-1}$ , are

responsible for 66% of the cross-peak amplitude. The modes in the 220-400  $\text{cm}^{-1}$  region also contribute significantly, reaching ca. 40% in amplitude, but interestingly, the maximum is reached much earlier than  $T_{\text{max}}$  at 1.9 ps (Fig. 4.16a, cyan). The modes in this range are largely delocalized over the two ligands. This delocalization is caused by the similarity of the groups on each side of the Pt center resulting in similar frequencies of the Pt-C-C bending motion on each ligand. Therefore, the process of energy transfer between the ligands relies on the similarity of the groups at the two ligands in the vicinity of the Pt center and frequencies of their modes.

The computations of relaxation pathways of  $\nu_{\text{C}\equiv\text{C}}$  in C6F revealed a similar behavior to that for C2F: only high-frequency modes of strongly coupled pairs showed a significant energy transfer from C<sub>6</sub>-Tri to F<sub>5</sub>Ph (Fig. 4.17b); the populations of those modes and all high-frequency modes of F<sub>5</sub>Ph, however, reach much smaller values compared to those in C2F (Fig. 4.16b). As a result, the overall relative contribution of energy transfer pathways involving high-frequency modes in C6F (~35%, Fig. 4.17a) is half of that for C2F. Low-frequency modes, 15-220  $\text{cm}^{-1}$  (green) and especially 220-400  $\text{cm}^{-1}$  (cyan), show a much larger relative contribution to the cross peak in C6F. Spatial proximity of the centers of the two ligands dictates the outcome of the energy transport process, showing a similar connectivity observed previously for modes within a covalent network.<sup>150, 223</sup>

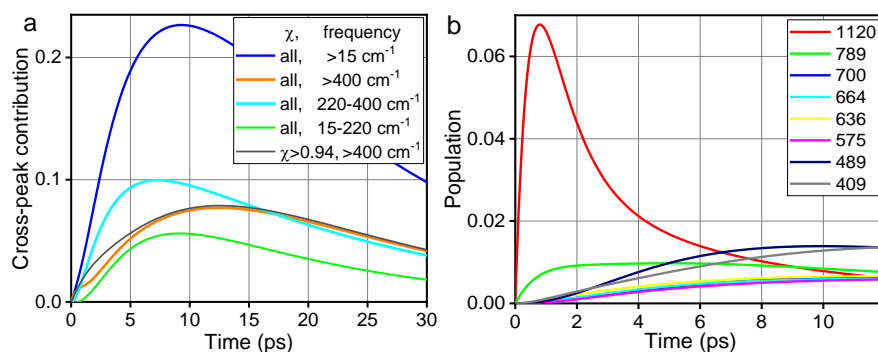


**Figure 4.17.** (a) Contributions of different groups of modes to the  $\nu_{\text{C}\equiv\text{C}}/1500(\text{F}_5\text{Ph})$  cross peak computed for C6F. The groups are formed based on the frequency (>15, >400, 220-400, or 15-220  $\text{cm}^{-1}$ ) and delocalization factor,  $\chi$  (all or >0.94). (b) Waiting-time population traces for high-frequency modes of F<sub>5</sub>Ph ( $\chi > 0.94$ ) contributing the most to the cross peak.

Detailed analysis of relaxation pathways of high-frequency modes enables us to identify specific modes involved in energy transfer across the molecule in C2F and C6F. The efficiency of the energy transfer across the Pt center was found to correlate with the delocalization extent of the parent mode across the center. A negligible energy transport efficiency from the C<sub>n</sub>-Tri to F<sub>5</sub>Ph moieties was found for the modes with the extent of delocalization at the F<sub>5</sub>Ph moiety smaller than 1%. The overall

cross-peak waiting time dynamics in C2F is dominated by the energy transfer via high-frequency modes ( $>400\text{ cm}^{-1}$ ), while low-frequency modes dominate for C6F.

The energy transfer time,  $T_{\max}$ , appears to be different when the tag and reporter are reversed (Tables 4.2, 4.3), indicating different contributions of high- and low-frequency energy transfer channels in the two cases. The transport channels associated with high-frequency modes are expected to alter with a change of the tag as the relaxation channels are tag specific and will not involve the same modes. Such changes are found for C2,  $T_{\max}(v_{C\equiv C}/1500) = 7.4\text{ ps}$  and  $T_{\max}(1500/v_{C\equiv C}) = 9.7\text{ ps}$ , indicating the importance of the high-frequency mode transport initiated more efficiently by  $v_{C\equiv C}$  compared to the  $1500\text{ cm}^{-1}$  mode initiation. Similar effect is observed for the  $v_{C\equiv C}/1460$  and  $1460/v_{C\equiv C}$  peaks, although the Tri contribution to the peak at  $1460\text{ cm}^{-1}$  makes quantitative assessment difficult. On the other hand, the similarity of the transport times for reversed tag and reporters likely points at a dominant contribution of the low-frequency modes in the thermalization process, as, for example, for the  $v_{C\equiv C} / 1500$  and  $1500 / v_{C\equiv C}$  cross peaks for C6 (9.7 and 11 ps, respectively).

Note that no strongly coupled high-frequency local modes of Tol and  $C_n$ -Tri or Tol and  $F_5Ph$  were found. Therefore, it is concluded that the thermalization to and from Tol moieties occurs via low-frequency modes.

#### 4.5. Conclusions

Rather large compounds, C2 and C6, were investigated with 2DIR and RA 2DIR spectroscopies, and waiting-time dependences of large numbers of cross and diagonal peaks were measured. Comprehensive analysis of their waiting-time traces enabled i) better assignment of peaks in FTIR spectrum to different functional groups, ii) finding delineating kinetic parameters for several functional groups, which include coherent oscillations of specific cross peaks, energy transfer and cooling parameters, iii) understanding of the mechanism of energy transfer between the ligands. DFT calculations, IVR modeling, and evaluation of mode couplings were used to understand the details of the energy transfer and relaxation pathways.

Due to the closeness of the alkyne bridge to the  $F_5Ph$  ligand and similarity of some bond types in them, a rather efficient energy transfer from  $v_{C\equiv C}$  to modes at  $F_5Ph$  was found. The requirements for energy transport across the Pt center at high-frequency modes have been formulated and illustrated. They involve coupling and delocalization of the local modes at two sides of the center. The

transport from  $\nu_{C\equiv C}$  to  $F_5Ph$  in C2 occurs predominantly via three mode pairs delocalized over both ligands, featuring frequencies of 1362/1354, 730/790, and 575.5/574.3  $cm^{-1}$ , and involving C-Pt-C stretching (1<sup>st</sup> two pairs) and bending (last pair) motions (Fig. 4.14). These motions on each ligand are coupled across the Pt center with the coupling strength of 5-20  $cm^{-1}$ , which is sufficient to cause significant delocalization and to provide efficient energy relaxation pathways between the ligands. The similarity of the bond types at the  $F_5Ph$  and  $C_n$ -Tri ligand helps the frequency match of their local states, thus causing delocalization. However, an accidental frequency match can lead to delocalization in the same way.

The modes associated with C-Pt-C bending motion (250-400  $cm^{-1}$ ) are also involved in energy transfer between the ligands, but their contribution is smaller than that of the high-frequency modes in C2. Low frequency modes (<250  $cm^{-1}$ ) are largely delocalized across the Pt center in C2 and C6. Population of such modes occurs as vibrational relaxation proceeds, reaching maximum at ca. 7-8 ps. When excited, such modes affect the reporter frequency wherever it is located in the molecule. As the low-frequency modes are delocalized, the excess energy is delocalized over the majority of the molecule and the process needs to be treated as an IVR but not as energy transfer from one ligand to another.

As typical lifetime of a high-frequency mode in compounds with more than ten atoms is 1 ps and a few IVR steps lead to dominant population of the low-frequency modes, the time window for energy transport in medium size compounds, such as C2 and C6, is limited to 2-4 ps. The observed  $T_{max}$  values for the  $\nu_{C\equiv C}$  / (modes at Tol) greatly exceed this limit; thus, low-frequency modes determine the  $T_{max}$  values for such cross-peak types. Note that for the  $\nu_{C\equiv C}$  /  $F_5Ph$  cross peaks, the low-frequency modes in the 250-400  $cm^{-1}$  region contribute significantly, while not for the  $\nu_{C\equiv C}$  / Tol cross peaks, where the delocalized modes <250  $cm^{-1}$  are contributing the most. A positive correlation between the tag-reporter distance and the  $T_{max}$  time is observed as expected, emphasizing the value of the RA 2DIR method for mode assignment. The distance correlation is clear in comparing the  $T_{max}$  values for C2 and C6.

## Acknowledgments

This work was supported by the National Science Foundation (NSF grant CHE-2201027 to I.V.R. and A.L.B.) The synthesis of C2 and C6 compounds was supported by the NSF grant CHE-1900549 to J.A.G.).

## CHAPTER 5

# Coherent Oscillations as Structural Reporters

In this chapter, the results of RA 2DIR studies on a platinum complex with a triazole-terminated alkyne ligand of six carbons, a perfluorophenyl ligand, and two tri(*p*-tolyl)phosphine ligands in deuterated chloroform are presented. We observed fully resolved vibrational state coherences, which were analyzed in detail to reveal a waiting time dependence of cross-peaks and diagonals in the fingerprint region (1300-1620  $\text{cm}^{-1}$ ). We concluded that the presence of cross-peak oscillations in the waiting time identifies strongly coupled states that are close in proximity, typically belonging to the same moiety. A pattern of cross-peak oscillations was recorded, and was determined to be useful to identify the moiety in complex linear and 2DIR spectra with multiple overlapping peaks. The requirements for oscillations were categorized, and it was determined that compact functional groups with many similar local modes (like perfluorophenyl) can result in the formation of normal modes featuring large cross anharmonicities, resulting in oscillations. Overall, the results highlight the rich information contained in fully exploring 2DIR spectra, demonstrating the potential of 2DIR spectroscopy as an analytical tool.

## 5.1. Introduction

In the previous chapter, it was mentioned that it is challenging to assign specific vibrational modes in C2 and C6 based on their FTIR peaks. The DFT-computed vibrational spectrum, which used the standard B3LYP functional, did not accurately predict the pattern of vibrational peaks, and different scaling factors were applied to match the calculations with the experimental results for modes residing at different moieties. To supplement and validate the assignment made by DFT modeling, relaxation-assisted 2DIR data was utilized to investigate the energy transport of vibrational energy within the molecule. One area of interest is the origin and importance of coherence oscillations, including the precise identification of peaks in complex FTIR spectra.

Research has been carried out on the waiting time oscillations of different metal carbonyls. In their study, Khalil et al. utilized 2DIR to observe oscillations of coherent quantum beats (QB) in the waiting-time dynamics of a  $\text{Rh}(\text{CO})_2\text{acac}$  system. They took into account coherence transfer and the phenomenon of quantum beats in their analysis.<sup>210</sup> It was determined that coherence transfer arose from the mutual interaction of the bright  $\text{C}\equiv\text{O}$  stretches with dark states. The signatures of vibrational coherence transfer are the anomalous frequency oscillations of specific but ordinary peaks, as seen in work by Kubarych and co-workers, where coherence transfer was observed in rephasing and non-rephasing spectra of three diiron hexacarbonyl organometallic complexes, including what appeared to be coherence transfer between bright and dark vibrational modes.<sup>224</sup> Oscillatory components in the pump-probe signal of N-H stretching vibrational modes of adenosine monomer in solution were demonstrated and were attributed to the coherent superpositions induced by the pump pulse result in quantum beats between the  $\nu(\text{NH}_2)_\text{S}$  and  $\nu(\text{NH}_2)_\text{A}$  normal modes.<sup>225</sup> Recently, a 2DIR measurements combined with pulse-shaping were used to study acetylacetonato dicarbonyl rhodium (RDC) to study the coherence and population transfer between carbonyl symmetric and asymmetric stretching modes.<sup>226</sup> The study pointed at weak contribution of coherence transfer to the oscillatory signals. Spectral shaping of the m-IR pulses was shown to effectively suppress the QB, making easier the extraction of structural and dynamical information.

In our study, coherent oscillations in the waiting-time were detected for cross peaks among multiple vibrational modes in the fingerprint region ( $1300\text{-}1600\text{ cm}^{-1}$ ) of C6. In this chapter, we explore QB oscillations as a structural reporter, potentially opening avenues for 2DIR as method to determine

the structure of a molecule. In addition to its potential use as a structural reporter, QB oscillations can be used to aid in the identification of peaks in complex FTIR spectra.

## 5.2. Experimental Details

### 5.2.1. Experimental Method

A detailed accounting of the fully-automated 2DIR spectrometer is presented in Chapter 2.8. of this dissertation.

### 5.2.2. Sample Preparation

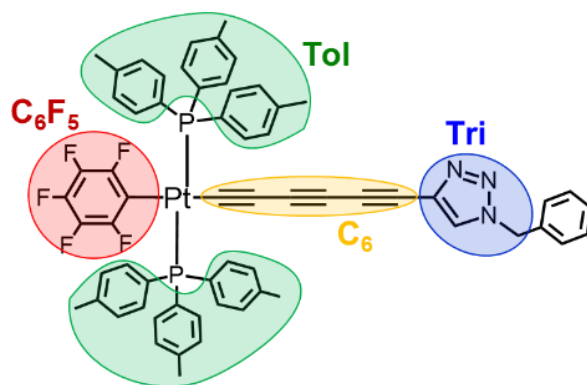


**Figure 5.1.** Structure of C6. Notation for the main functional groups is shown in colors that are used throughout the chapter.

Compounds *trans*-(C<sub>6</sub>F<sub>5</sub>)(*p*-tol<sub>3</sub>P)<sub>2</sub>Pt(C≡C)<sub>3</sub>C=CHN(CH<sub>2</sub>C<sub>6</sub>H<sub>5</sub>)N=N, referred to as C6, was synthesized by students of John Gladysz at Texas A&M University. For FTIR and 2DIR measurements, ca. 30 mM CDCl<sub>3</sub> solutions were used. The measurements were performed in a sample cell made of 1 mm-thick CaF<sub>2</sub> windows and a 100 μm Teflon spacer at room temperature, 22 ± 0.5 °C.

### 5.3. Results

#### 5.3.1. Linear FTIR Measurement

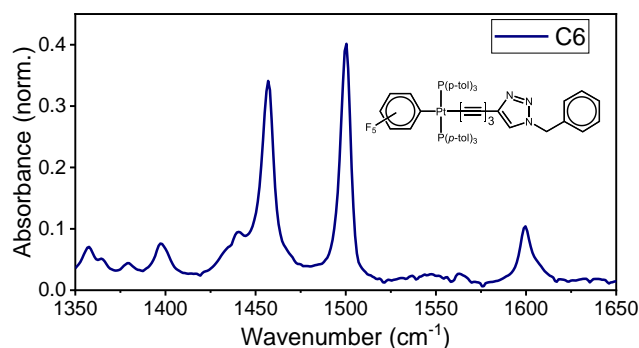


**Figure 5.2.** Solvent-subtracted infrared absorption spectra of C6 in  $\text{CDCl}_3$ .

The linear absorption spectra of C6 (Fig. 5.2) in the fingerprint region feature intense peaks at 1460 and 1500  $\text{cm}^{-1}$  and medium strength peaks at 1600, 1435, 1400  $\text{cm}^{-1}$  and 1355  $\text{cm}^{-1}$ .

#### 5.3.2. Multiple Oscillations in Cross Peaks in the Fingerprint Region

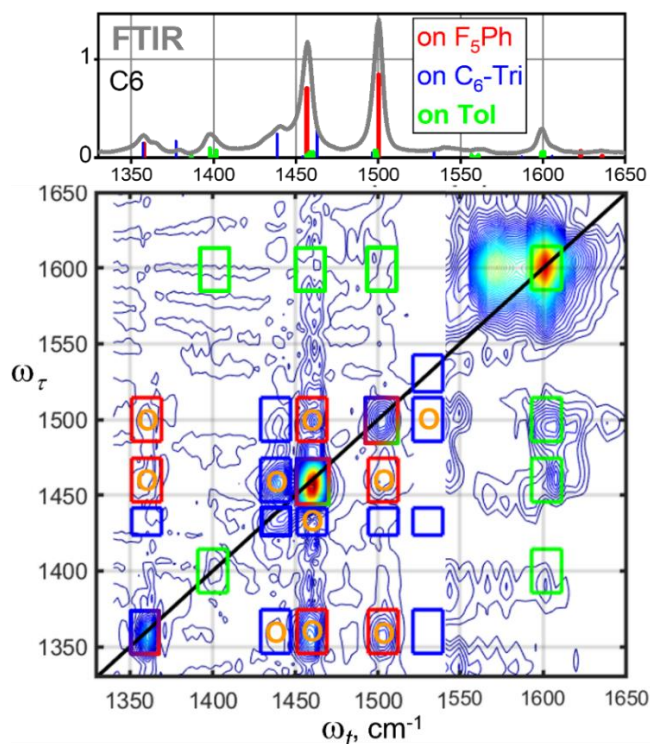


**Figure 5.3.** 2DIR spectrum of C6 measured at  $T = 0.6$  ps. The boxes indicate the integration area of various diagonals and cross peaks, where the color of the box indicates the main contributors for each peak in reference to colors in Figure 5.1. Cross-peaks that indicate the presence of oscillations are denoted by the letter “O”. The spectrum was combined from two parts with  $\omega_r$  smaller and larger than 1500  $\text{cm}^{-1}$ . The FTIR spectrum of C6 is attached as top panel.

The rephasing 2DIR measurements for C6 in  $\text{CDCl}_3$  were performed in the fingerprint region ( $1300\text{--}1650\text{ cm}^{-1}$ ) using 3-beam photon-echo 2DIR instrument. The magnitude rephasing 2DIR spectrum measured at  $T = 0.6\text{ ps}$  shown in Figure 5.3. Upon analysis of the waiting time dependences, many cross-peaks were found to show QB in the waiting time dependence (Fig. 5.3, denoted by “O”). Figure 5.4. shows the waiting time oscillations of various cross peaks. The traces were fitted with a two-exponential function augmented with an exponentially damped oscillatory component. (Eq. 5.1), shown with red lines in Figure 5.4, while the fit parameters are provided in Table 5.1.

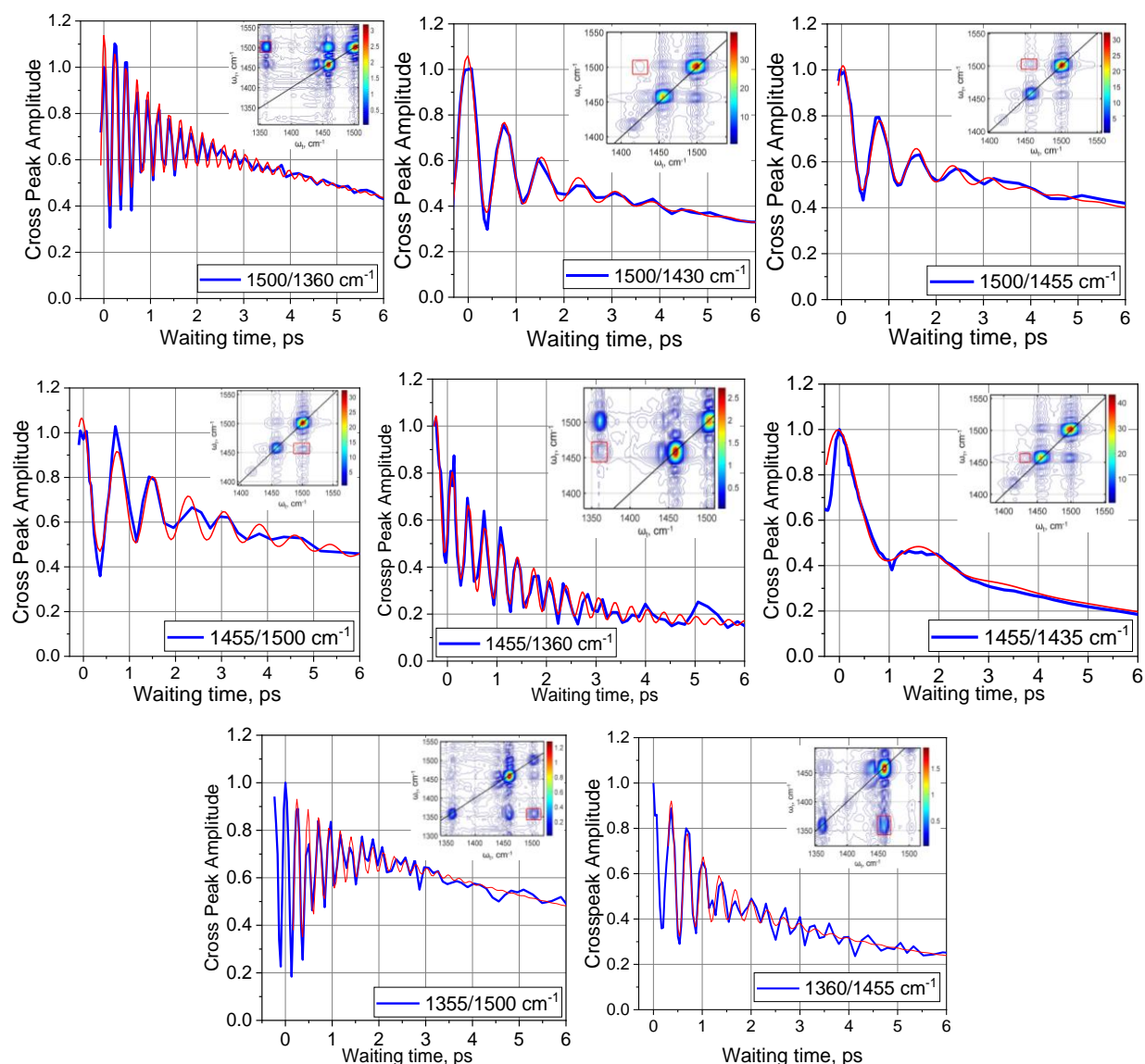


**Figure 5.4.** Waiting-time dependences of the indicated cross peaks for C6. The inset shows the 2DIR spectrum measured at 4.3 ps with red boxes indicating the cross-peak integration regions. Red lines show fits of the oscillations with Equation 5.1.

$$y(T) = y_0 + A_1 e^{-\frac{T}{T_1}} + A_2 e^{-\frac{T}{T_2}} + A_3 e^{-\frac{T}{T_3}} \cos\left(\frac{2\pi T}{T_0} + \varphi\pi\right) \quad (5.1)$$

**Table 5.1.** Fit Parameters for C6 Cross Peaks (Rephasing)

Cross peak	$T_1$ , ps	$T_2$ , ps	$T_0$ , ps	$\varphi$	$A_2/A_1$	Oscillation Freq., $\text{cm}^{-1}$	Dominant Contribution
1500/1360	$4.1 \pm 0.2$	$7.2 \pm 0.3$	$1.29 \pm 0.1$	$1.9 \pm 0.1$	$2.6 \pm 0.2$	142.8	F <sub>5</sub> Ph/F <sub>5</sub> Ph
1500/1435	$5.6 \pm 0.5$	$0.43 \pm 0.11$	$0.53 \pm 0.02$	$0.83 \pm 0.03$	$0.92 \pm 0.05$	63.1	F <sub>5</sub> Ph/Tri
1500/1455	$0.53 \pm 0.17$	$11.9 \pm 0.5$	$0.76 \pm 0.01$	$0.91 \pm 0.01$	$6.7 \pm 0.1$	43.7	F <sub>5</sub> Ph/Tri
1500/1545	$7.1 \pm 0.2$	$0.78 \pm 0.11$	$0.75 \pm 0.01$	$1.5 \pm 0.1$	$0.39 \pm 0.05$	44.3	F <sub>5</sub> Ph/Tri
1500/1355	$25.1 \pm 0.6$	$25.1 \pm 0.5$	$0.23 \pm 0.02$	$1.05 \pm 0.09$	$1.0 \pm 0.5$	141.0	F <sub>5</sub> Ph/Tri
1455/1500	$0.30 \pm 0.07$	$10.4 \pm 0.8$	$0.80 \pm 0.01$	$0.96 \pm 0.02$	$1.8 \pm 0.1$	41.6	Tri/F <sub>5</sub> Ph
1455/1435	$3.3 \pm 0.9$	$10.4 \pm 0.7$	$1.6 \pm 0.04$	$0.79 \pm 0.07$	$0.44 \pm 0.1$	20.2	Tri/Tri
1455/1360	$0.31 \pm 0.16$	$1.8 \pm 0.3$	$0.33 \pm 0.01$	$1.3 \pm 0.01$	$4.3 \pm 0.1$	101.6	Tri/Tri
1435/1360	$2.5 \pm 0.2$	$0.62 \pm 0.35$	$0.42 \pm 0.01$	$0.16 \pm 0.11$	$1.7 \pm 0.2$	78.7	Tri/Tri
1360/1455	$2.5 \pm 0.9$	$10.5 \pm 0.4$	$0.33 \pm 0.02$	$0.7 \pm 0.1$	$1.2 \pm 0.1$	101.2	Tri/Tri
1355/1500	$9.2 \pm 0.7$	$0.90 \pm 0.18$	$0.23 \pm 0.01$	$1.84 \pm 0.02$	$0.37 \pm 0.02$	144.0	Tri/F <sub>5</sub> Ph

The frequency of the oscillation between two modes can be determined by measuring the difference in frequency of the cross-peak. Additionally, from the fit parameters (Table 5.1), the oscillation frequency of all cross-peaks can also be calculated by:

$$\Delta\nu = \frac{1}{c(T_0)} \quad (5.2)$$

Where  $c$  is the speed of light, and  $T_0$  is the period of the oscillations. The accuracy of the oscillation frequency derived from the  $T_0$  value obtained by fitting the oscillations is high in comparison to the frequency difference between the two modes of the cross-peak.

### 5.3.3. Diagonal Peaks in the Fingerprint Region

Diagonal rephasing 2DIR peaks were measured for all the main peaks in C6, and the waiting time traces were used to determine the lifetimes. The descriptions of the diagonal peaks in the fingerprint region were previously discussed in Chapter 4.3.5. Analysis of the waiting time kinetics yielded a decay, with no waiting time oscillations present.

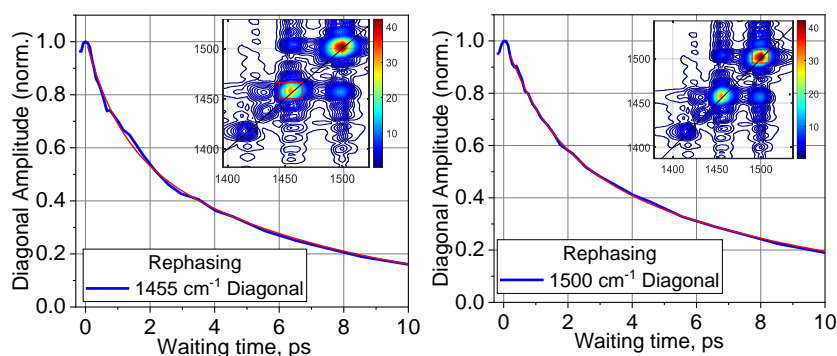


**Figure 5.5.** Scaled waiting-time traces for the (a)  $1455\text{ cm}^{-1}$  and (b)  $1500\text{ cm}^{-1}$  diagonal peaks for C6. The insets in both show rephasing 2DIR spectra measured at 1.6 ps, with the integration region indicated by the red box. The peaks were fitted globally with a double-exponential decay function (red lines) and the results of the fit are shown in Table 4.4.

### 5.3.4. Non-rephasing Measurements

Rephasing and non-rephasing measurements are two types of experiments performed in 2DIR spectroscopy. During the measurement, three wave vectors are used:  $k_1$ ,  $k_2$  and  $k_3$  giving rise to two signals, rephasing ( $k_R = -k_1 + k_2 + k_3$ ) and non-rephasing ( $k_{NR} = k_1 - k_2 + k_3$ ). Swapping the timing of  $k_1$  and  $k_2$  enables performing the rephasing and non-rephasing sequences using the same beam alignment and signal direction.

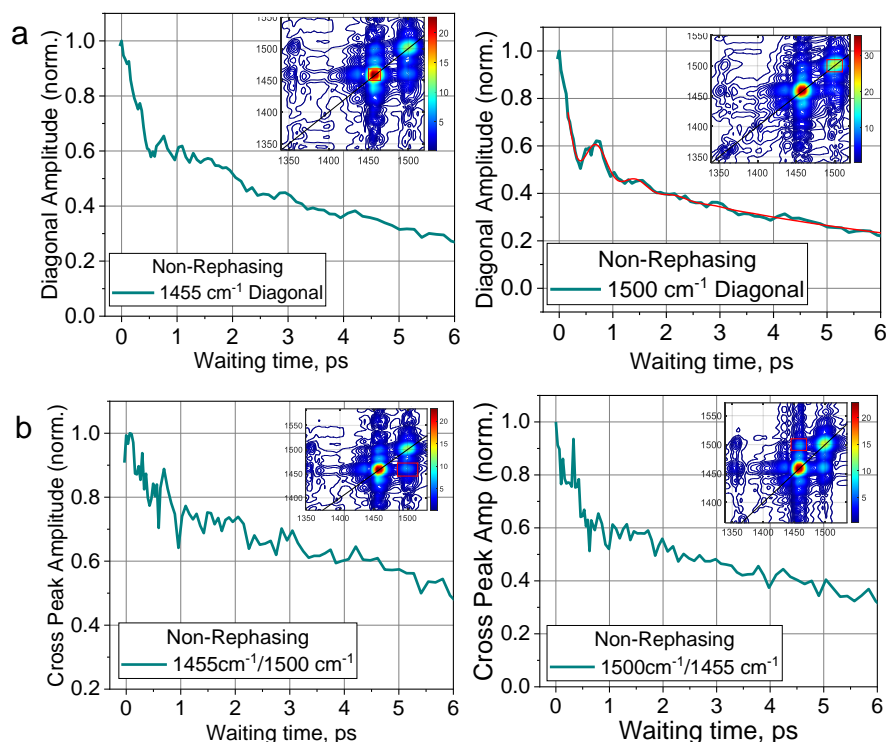


**Figure 5.6.** Scaled waiting-time traces for indicated non-rephasing **(a)** diagonal and **(b)** cross peaks for C6. The insets show 2DIR spectra measured at 1.6 ps, with the integration regions shown with the red box. The waiting time trace for the 1500 cm<sup>-1</sup> diagonal was fit with Eqn 5.1 (red line).

Non-rephasing diagonal 2DIR spectra were measured in the fingerprint region for C6 in CDCl<sub>3</sub>. The waiting time kinetics of the two strongest IR peaks at 1455 and 1500 cm<sup>-1</sup>, as well as both cross-peaks are shown in Fig. 5.6. Although there are no evident oscillations visible in the cross-peaks, the 1500 cm<sup>-1</sup> diagonal peak exhibits oscillation. Equation 5.1 was used to fit the 1500 cm<sup>-1</sup> diagonal (Figure 5.6b, right), and its period corresponds to that of the 1455/1500 cm<sup>-1</sup> and 1500/1455 cm<sup>-1</sup> cross-peaks obtained from the rephasing measurements.

## 5.4. Discussion

Nonlinear optical spectroscopies are powerful techniques for investigating the dynamics of condensed phase systems, including excitonic systems. Feynman diagrams have long been a crucial tool in simple representation of various 2DIR peak contributions and in calculating and interpreting the spectra.<sup>227</sup> Feynman diagrams offer a clear and succinct visual representation of the contributions of time-dependent perturbation theory to spectroscopic signals. To better understand the energy

transfer processes at play within C6, this section will delve into the specific Feynman pathways involved in these processes. Feynman diagrams are frequently employed to depict the time-dependent changes in the system's density matrix through the four-point correlation functions, which are referred to as Liouville pathways. By examining these pathways in detail, a deeper understanding of the complex dynamics at work in this system is gained.

### 5.4.1. Isolating Frequency Components

Fourier transformation (FT) was performed to see if other beat frequencies are involved. The oscillatory component was isolated by subtracting the non-oscillating portion of the fit with Eq. 5.1 from the data. The spectrum obtained for the 1500/1360  $\text{cm}^{-1}$  cross peak (Fig. 5.4, labeled) shows a single peak centered at  $143.0 \pm 0.4 \text{ cm}^{-1}$  (Fig. 5.7c, blue line) and the full width at half maximum of  $21 \pm 1 \text{ cm}^{-1}$ , revealed from its fit with a Lorentzian function (Fig. 5.7c, red line). The short damping time (0.97 ps) results in a rather broad FT peak ( $fwhm = 21 \text{ cm}^{-1}$ ).

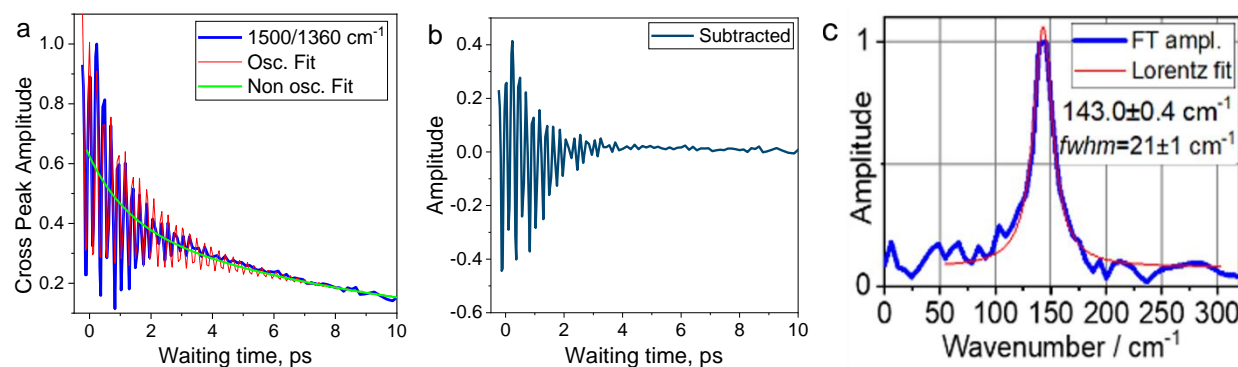
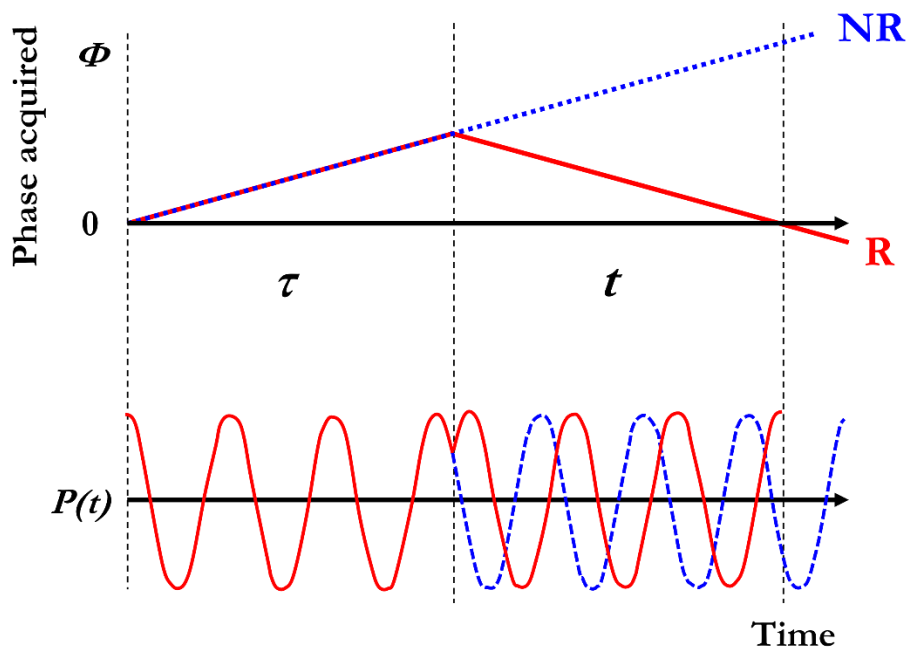


**Figure 5.7.** (a) Waiting-time dependence of the 1500/1360  $\text{cm}^{-1}$  rephasing cross-peak. The fit with Eq. 5.1 is shown with the red line, and the non-oscillations component of the fit is shown in green. (b) Waiting-time dependence of the same cross-peak, after the subtraction of the non-osc. fit from the data (c) Fourier transform of the oscillatory component shown in panel (b), fitted with a Lorentzian function (red line).

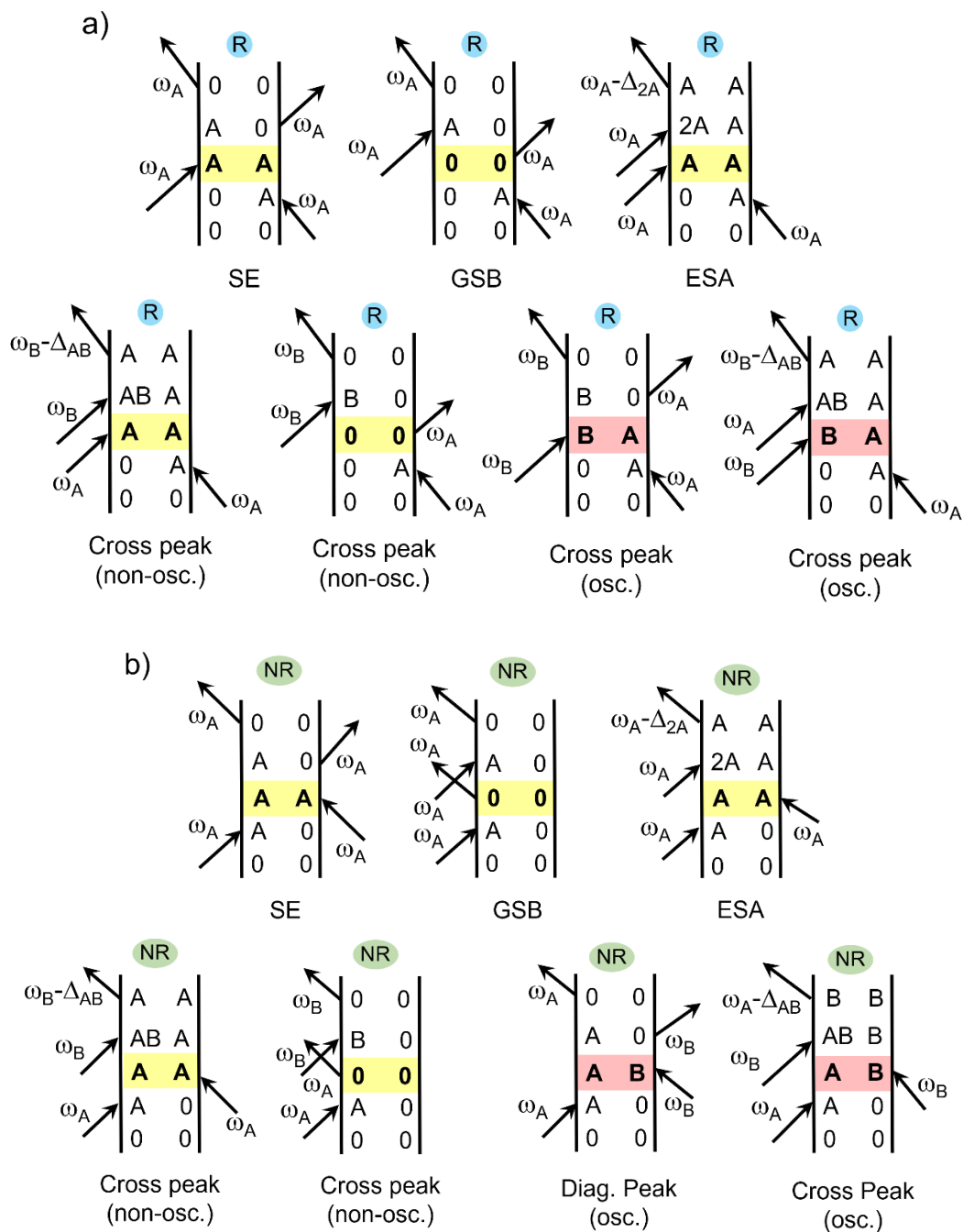
This Fourier transform approach was applied to all cross-peaks of C6 in the fingerprint region, and all the oscillatory waiting-time dependencies only revealed one peak. From this, we determined that the oscillations are dominated by a single frequency. It is interesting to note that in metal carbonyls such as  $\text{Fe}(\text{CO})_3$ , oscillations were recorded up to 12 ps,<sup>224</sup> and Fourier transforming the oscillations revealed several contributions, which was attributed to dark and bright vibrational modes present in metal carbonyls. However, short life- and dephasing times of the vibrational states of C6 result in a smaller time window the oscillations are visible, making it difficult to see multiple frequency contributions in the oscillations.

### 5.4.2. Rephasing vs. Non-rephasing Sequences

The difference between rephasing and non-rephasing measurements lies in the way the vibrational states of the molecules in the sample are accessed.



**Figure 5.8.** Phase of the signal as a function of time. Blue dotted line represents non-rephasing signal while the red line represents the rephasing signal.



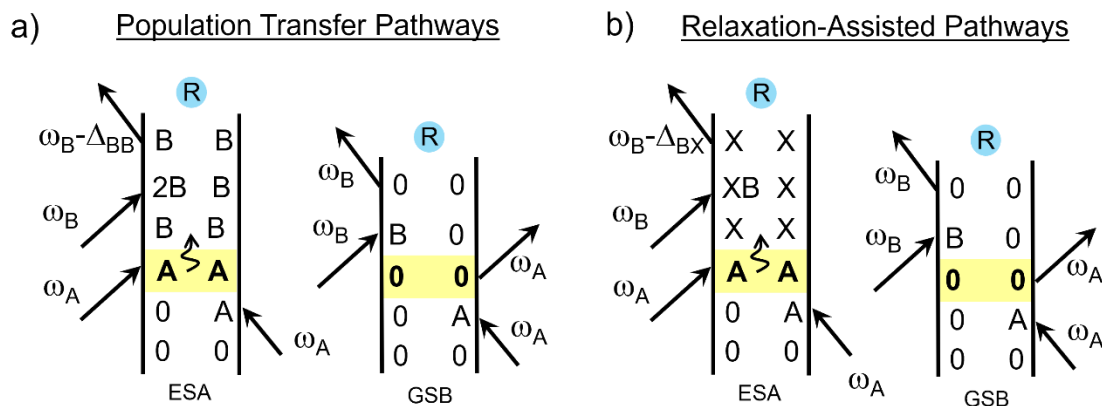
**Figure 5.9.** Double-sided Feynman diagrams associated with the (a) rephasing ( $k_R = -k_1 + k_2 + k_3$ ) and (b) the non-rephasing ( $k_{NR} = k_1 - k_2 + k_3$ ) 2DIR peaks. The pathways leading to a diagonal peak are categorized as ground state bleach (GSB), stimulated emission (SE), or excited state absorption (ESA). In the rephasing sequence, the cross-peaks showcase coherent oscillations, while in the non-rephasing sequence, the diagonal peaks demonstrate coherent oscillations. The yellow boxes represent population states during the waiting time, while the red boxes represent the presence of coherent states which oscillate during  $T$ .

Figure 5.9 depicts the Liouville pathways corresponding to (a) rephasing and (b) non-rephasing pulse sequences. The time goes upwards from the bottom and the arrows indicate field-matter interactions. The state of the density matrix after each interaction is indicated within the diagram.

### 5.4.3. *Origin of Coherent Oscillations*

There are numerous Feynman pathways that can contribute to 2DIR spectra features. Quantum beats observed during the waiting time are linked to fully coherent Liouville pathways, where a coherent state  $|A\rangle\langle B|$  or  $|B\rangle\langle A|$  is produced after interaction with the second pulse, resulting in oscillations during the waiting time (labeled as osc. in Fig. 5.9). Oscillations caused by QBs were present in many of the rephasing waiting-time traces. In addition to QB contribution, coherence transfer pathways can contribute to coherent oscillations. CT involves the transfer of a coherent superposition of two states,  $|A\rangle\langle B|$ , to another coherent superposition of states,  $|A\rangle\langle C|$ . This process provides valuable information about the coupling between different vibrational modes and can be used to investigate the dynamics of chemical reactions and energy transfer in complex molecular systems. Population transfer (PT), on the other hand, involves the transfer of the population of two states,  $|A\rangle\langle A|$ , to another state in the system,  $|B\rangle\langle B|$ , and does not induce waiting-time oscillations (see below).

The coupling between the quantum states creates an interference pattern, which causes the system to oscillate between the different states at a frequency determined by the energy difference between them. In RA 2DIR, both pump pulses are spectrally broad, resulting in the formation of new pathways capable of generation quantum beats (QB) and coherence transfer (CT). In this section, we focus on determining the importance of CT and QB pathways. After excitation from the ground state  $|0\rangle\langle 0|$  to an excited state  $|0\rangle\langle A|$  at  $\omega_A$ , a second interaction ( $\omega_B$ ) causes the system to be in a coherent superposition  $|B\rangle\langle A|$  (red boxes), resulting in the presence of QBs (Fig. 5.9a). In addition to the fully coherent QB cross-peak pathways, there are conventional pathways that do not oscillate, which exist alongside them. These pathways create a population state of either  $|A\rangle\langle A|$  or  $|0\rangle\langle 0|$  when the second pulse ( $\omega_A$ ) is applied, as shown in Figure 5.9a. The decay of the  $|A\rangle\langle A|$  state over time is determined by the lifetime of state A, which is approximately 1 ps for C6. As a result, the non-oscillating pathways depicted in Figure 5.9a have a significant effect only at short waiting times.



**Figure 5.10.** Double-sided rephasing Feynman diagrams associated with the labeled pathways: **(a)** population transfer and **(b)** relaxation-assisted. The yellow boxes represent a population state. Note that none of these diagrams exhibit oscillations during the waiting time.

However, they are replaced by other pathways that involve population transfer between modes A and B (Fig. 5.10a) and the population relaxation, where the population of state A is transferred into other modes in the molecule, denoted as X (Figure 5.10b). Here, the waiting time dependence,  $T$ , is dependent on the number of population transfers between various states  $|X\rangle\langle X|$ . We observed waiting times of up to  $\sim 15$  ps for  $\nu_{C=C}$ /toluyl cross-peaks in C6, so one would expect contributions from many  $|X\rangle\langle X|$  states at large  $T$ . The relaxation of state A results in the population of other modes that are strongly coupled to mode B and contribute to the A/B cross peak at longer  $T$  delays.

#### 5.4.4. Diagonal Peaks in the Fingerprint Region

In both rephasing and non-rephasing measurements, diagonal peaks are observed in 2DIR spectra, representing transitions from a vibrational state to itself. No oscillations were observed in the rephasing measurements of the 1455 and 1500 diagonal peaks (Fig. 5.4). This process can be described with Feynman diagrams (Fig 5.9a, SE, GSB and ESA). Here, the first pulse ( $\omega_A$ , pump pulse) promotes the molecule to a population state  $|A\rangle\langle A|$  (Fig 5.9a, yellow boxes). After a delay time  $\tau$ , a second pulse ( $\omega_A$ , probe pulse) is applied, which induces a transition from the populated to another higher energy state. The rephasing signal is obtained by detecting the emitted signal with the same phase as the pump pulse. Therefore, we can conclude that the absence of oscillations aligns with our expectation based on the Feynman diagrams.

Next, we focus on the non-rephasing measurements of the 1455 and 1500  $\text{cm}^{-1}$  diagonal peaks (Fig. 5.6 a). The first ( $\omega_A$ ) and second ( $\omega_B$ ) beam have to excite different transitions even though they come from the same OPA (close frequency values). Hence, oscillations should be observed in the waiting time trace of the diagonal peaks from non-rephasing measurements. The presence of weak oscillations can be seen in the 1500  $\text{cm}^{-1}$  diagonal peak for non-rephasing measurements (Fig. 5.6a, right). From this, we can infer that the Feynman diagram that represents the non-rephasing diagonals are shown in Fig. 5.9b (SE, GSB, ESA), where only transition from the initial state to a population state  $|A\rangle\langle A|$  or back to the ground state  $|0\rangle\langle 0|$  occurs.

Why are the oscillations in the diagonals in the non-rephasing measurements so weak? The significant discrepancy in intensity between the diagonal ( $\sim 25$ ) and the cross-peaks ( $\sim 7$ ) (Fig 5.6) resulting in oscillations with small contribution relative to non-oscillating peaks. Some of the oscillations are too weak to be detected atop of stronger non-oscillation signals and could potentially be lost in noise.

#### ***5.4.5. Suppressing Quantum Beat Oscillations***

The utilization of two ultrafast, broadband IR pump pulses in combination with an ultrafast probe pulse optimizes the experimental time and frequency resolution in 2DIR measurements, allowing one to measure the coherence time of the studied quantum system and introducing QB and CT pathways. In experiments where the PT states are the main pathways studied, it may be desirable to eliminate QB oscillations in 2DIR spectra.

We attempted to use our 3-beam photon echo setup to suppress QB oscillations. To achieve this, we focused the center of the pump pulse at  $\sim 1325 \text{ cm}^{-1}$  (Fig. 5.11a), and the probe pulse at 1425  $\text{cm}^{-1}$  (Fig. 5.11c), hoping to limit the QB oscillations of the cross peaks in the 1600/1500  $\text{cm}^{-1}$  area. Similarly, we conducted other measurements by focusing the center of the pump pulse at 1600  $\text{cm}^{-1}$  (Fig. 5.11b) and the probe pulse in the similar region of 1425  $\text{cm}^{-1}$  (Fig 5.11c) to suppress QB oscillations of the cross-peaks in the 1300/1500  $\text{cm}^{-1}$ . Although the 2DIR spectra (Fig. 5.12 a,b) showed reduced cross-peak intensity, QB oscillations were still present, albeit weaker and noisier.

We realized that while we could conduct experiments to minimize QB oscillations, it was not feasible for a three-beam photon echo spectrometer to fully eliminate them as the pulse spectra remained broad. Pulse shaping would be useful for suppressing QB oscillations fully.

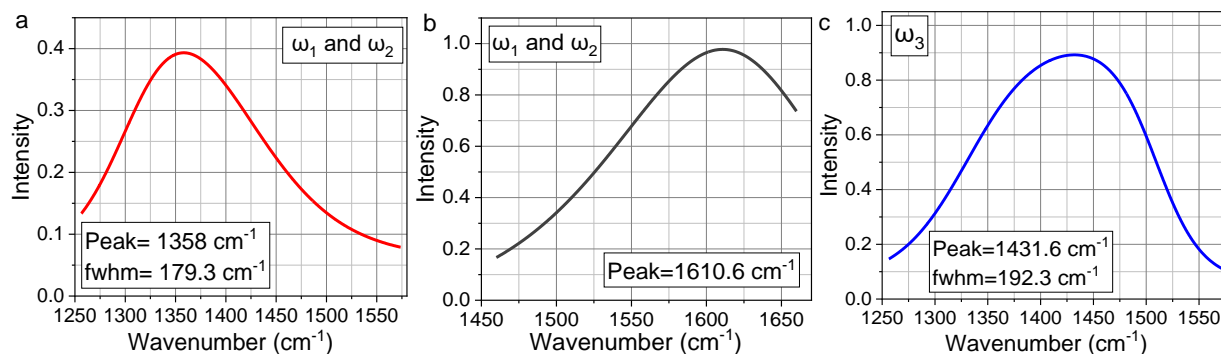


**Figure 5.11.** Beam profile of the (a,b) pump laser pulses used in 3-beam 2DIR instrument, centered at 1358 and 1610  $\text{cm}^{-1}$  in separate experiments, while the (c) probe laser pulse centered at 1431  $\text{cm}^{-1}$  is the same for both experiments.

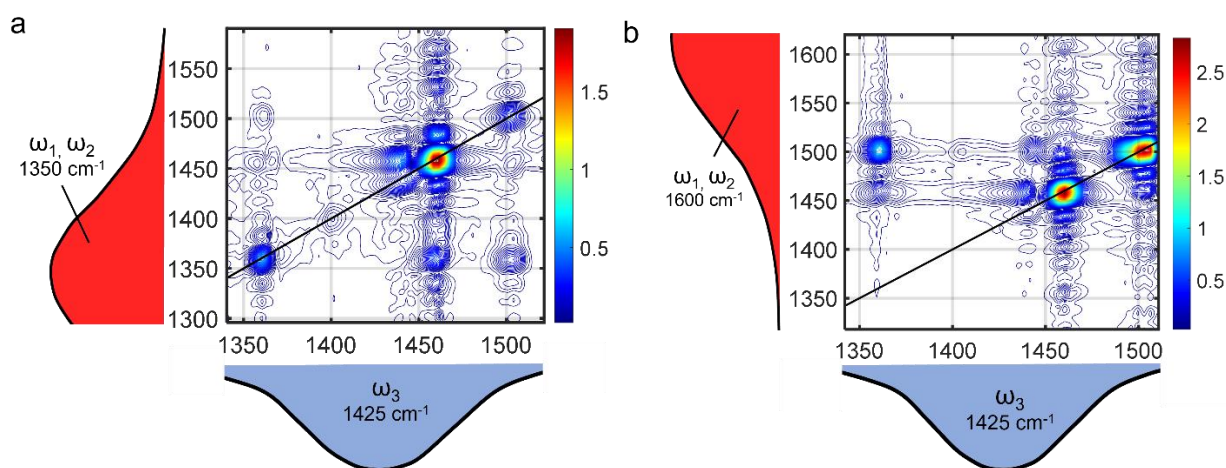


**Figure 5.12.** 2DIR magnitude spectrum of C6 at  $T = 1.38$  ps for (a) 1350/1450  $\text{cm}^{-1}$  pump/probe and (b) 1600/1450  $\text{cm}^{-1}$  pump/probe.

In contrast to CT, double-CT involves the transfer of vibrational coherence from one mode to another via a third mode and can be used to study the anharmonic coupling between the vibrational modes. The third interaction ( $\omega_B$ ) prepares a coherence involving a two-quanta state ( $|2B\rangle\langle B| \rightarrow |AB\rangle\langle B|$ ), and the overall diagram involves two CT steps. The pulse-shaping technique allows for the suppression of QB oscillations and limits the accessible pathways to just PT and conventional pathways. For QB (Fig. 5.9a, osc.) and double-CT

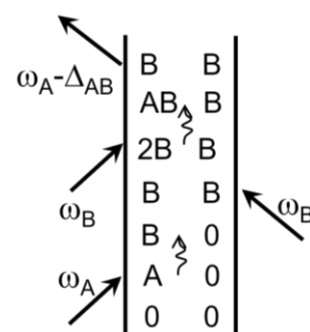


**Figure 5.13.** Feynman diagram for double-CT pathway.

pathways (Fig. 5.13), the first and second excitation must have different transitions (i.e.  $\omega_A$  and  $\omega_B$ ).

Pulse shaping is a technique used in the field of optics to manipulate the temporal profile of laser pulses. It involves modifying the intensity and phase of different frequency components of a laser pulse, in order to achieve a desired spectral shape.<sup>228</sup> The objective of the pulse-shaping experiments was to suppress QB oscillations and restrict the accessible energy pathways. Marroux et al. effectively reduced QB oscillations in 2DIR spectra of a rhodium dicarbonyl complex, acetylacetonato dicarbonyl rhodium (RDC), by implementing a pulse-shaping method.<sup>226</sup> In a separate study, Fayer and his colleagues employed a similar method to diminish QB oscillations in their analysis of center line slope changes in 2DIR spectra of a metal-organic framework.<sup>229</sup> Previous research has focused on metal carbonyls to investigate the feasibility of suppressing QB oscillations in C6 with the pulse-shaping method. Our laboratory implemented a similar pulse shaping method to address this issue. Junhan Zhou and Artem Sribnyi carried out the pulse-shaping experiments utilizing a home-built 2-Beam 2DIR instrument with a pulse shaper, and they were able to effectively eliminate QB in 2DIR spectra with the use of spectrally-narrow pulses.

## 5.5. Conclusion

In summary, the use of quantum beat oscillations (QBOs) in cross-peaks has the potential to identify strongly coupled states within the same functional group, allowing for effective identification of functional group peaks in complex linear and 2DIR spectra with multiple overlapping peaks. The presence of harmonic delocalization often results in strong off-diagonal anharmonicities, which can be observed in several structural motifs through an extended pattern of oscillatory 2DIR peaks.

## CHAPTER 6

# Nanofabrication of Gold Arrays

The latest advancements in nanofabrication techniques have opened up exciting possibilities for creating high-precision nanometer-size structures. By activating surface plasmons on the surfaces of metal nanostructures, we can trigger a localized surface plasmon resonance (LSPR), which amplifies optical spectroscopy techniques like surface enhanced infrared absorption (SEIRA) spectroscopy. The precise manufacturing has opened exciting possibilities for developing new and more sensitive detection methods for a range of applications. One of the promising applications of nanofabrication is the construction of ordered arrays of nanostructures. By fabricating such arrays, a thousand-fold enhancement in IR intensity extinction signals of molecular transitions of compounds in the vicinity of the metal surface can be achieved, making such arrays particularly useful for spectroscopic studies. In this chapter, a comprehensive description of the production of well-ordered gold nanoarrays using electron-beam lithography is provided. These arrays consist of nanorods of various lengths and widths, and we have characterized them using several techniques, including scanning electron microscopy, atomic force microscopy, and infrared spectroscopy. Moreover, we explore the possibilities of tuning the surface plasmon resonances of these structures across m-IR wavelengths by altering different parameters such as nanorod length, width, and spacing. Such fine-tuning enables us to customize the optical properties of these structures, making them ideal for various applications. The future prospects of these nanostructured arrays are promising. For example, they can be used to develop an electrochemical cell that can be utilized for molecular adsorption to modify electronic properties. This approach has the potential to revolutionize the development of nanoscale devices, including sensors, optical switches, and electronic devices.

## 6.1. Introduction

In recent years, the fabrication of periodic arrays of nanostructures has been of great interest due to their size-dependent properties<sup>230</sup>. These nanostructures have found potential applications as biosensors<sup>231-234</sup>, chemical sensors<sup>235-238</sup> and optical devices.<sup>239-243</sup> In recent years, the fabrication of periodic arrays of nanostructures has been of great interest due to their size-dependent properties<sup>230</sup>. These nanostructures have found potential applications as biosensors<sup>231-234</sup>, chemical sensors<sup>235-238</sup> and optical devices.<sup>239-243</sup> These nanostructures are also useful in the study of surface enhanced plasmon resonance.<sup>244</sup> A variety of techniques have been developed to fabricate arrays of nanoparticles. Among these techniques, electron beam lithography and optical lithography are capable of fabricating arrays of nanoparticles with excellent size, shape, and spacing control.

Recent advancements in the field of surface-enhanced infrared absorption (SEIRA) vibrational spectroscopy have led to significant progress in detecting and characterizing molecules at the nanoscale level. This technique relies on the interaction between molecules and locally enhanced near-fields, induced by plasmon resonances excited on the surface of gold nanostructures. Work by Mackin et al. has demonstrated that gold nanoantennas can effectively localize and amplify vibrational signals from nearby molecules. Specifically, when excited at the frequency of their plasmon resonance, gold nanoantennas generate enhanced near-fields that are closely localized to the metal surface. This effect dramatically enhances the sensitivity of SEIRA spectroscopy, enabling the detection nearby molecules with high precision and accuracy.<sup>245</sup>

To conduct a comprehensive examination of size-dependent properties, an optimal nanofabrication technique should possess certain characteristics. First, it should be applicable to a variety of materials and substrates, affordable, and offer flexibility in nanoparticle size, shape, and spacing parameters. Additionally, the fabrication method should enable parallel processing to increase productivity. While many standard lithographic techniques can create controlled nanostructures, photolithography is the most commonly used,<sup>246</sup> although it has limitations due to its diffraction-limited resolution of ca.  $\lambda/2$ . Hence, photolithography has not been widely adopted for nanofabrication of nanostructures.

As a result, it is challenging to produce high-quality nanoscale features using conventional photolithography. To address these limitations, various new nano-fabrication techniques have emerged, including electron-beam lithography,<sup>247</sup> focused-ion lithography,<sup>248</sup> dip-pen lithography,<sup>249</sup>

laser interference lithography,<sup>250</sup> nanosphere lithography<sup>251</sup> and nanoimprint lithography.<sup>252</sup> The ideal nanofabrication technique should be cost-effective, have high throughput, high resolution, and offer great flexibility to customize the size and shape of the nanostructures.

Electron Beam Lithography (EBL) is a relevant technique to the nanoscience community as it enables the production of precise structures at the nanoscale. The technique of EBL operates on the principle that some chemicals undergo changes in their properties when exposed to electrons, much like how photographic film responds to light. By precisely controlling the position of the electron beam using a computer, it is feasible to generate customized structures on a surface, which enables the direct transfer of the original digital image onto the target substrate. For incorporating EBL into a manufacturing process, it is crucial to achieve both precision and speed, in addition to maintaining control and yield throughout the nanofabrication processes. During the EBL process, the electron-beam resist coating is exposed by an electron-beam and the exposed resist is then developed and dissolved in a solvent. The resulting patterned resist serves as a temporary mask in subsequent deposition or etching procedures to create metallic nanostructures. Finally, in the lift-off process, the substrate is submerged in a solvent bath to remove both the remaining resist and any unwanted materials.

The initial motivation behind creating surfaces with precisely defined, periodic nanostructures was to enhance our understanding of the mechanisms responsible for surface-enhanced infrared absorption spectroscopy (SEIRA). The ability to induce localized surface plasmon resonance (LSPR) in the m-IR has led to the fabrication of an array of gold nanoantennas with a relatively long length on a CaF<sub>2</sub> substrate. By varying the rod length and aspect ratio (ratio of length to width), it was observed that the LSPR wavelength of optical antennae experiences a red shift as the rod length is increased. In addition to simple antenna structures, the electrochemical capabilities of gold were also explored by creating connected arrays, with each side joined to connectors where a potential could be applied. The array could be frequency-tuned to match the IR vibrational mode of the molecule under investigation, and electronically induced changes could be applied to the molecule by chemically adsorbing it to the gold array using a thiol-gold bond. This chapter provides a comprehensive account of the fabrication process for gold nanoarrays and the potential applications of these structures.

## 6.2. Experimental Details

### 6.2.1. Nanoarray Fabrication

Gandman *et al.* have previously reported on a fabrication methodology for gold on  $\text{CaF}_2$  windows.<sup>244</sup> Their research demonstrated that by using periodic arrays of gold, the near fields in close proximity to the gold surface can be enhanced, resulting in the amplification of vibrational signals emitted by nearby molecules at the frequency of their plasmon resonance. Building on this methodology, I present modifications and improvements that enable the fabrication of more complex structures.

In addition to simple gold nanostructures, the modified methodology also enables the fabrication of more complex structures, such as interconnected arrays and nanogaps. The fabrication of these structures requires additional steps, such as multiple layers of resist and selective deposition of gold, but the resulting structures offer enhanced sensitivity and tunability in SEIRA. The modified methodology presented in this work offers an improved and versatile approach for the fabrication of gold structures on calcium fluoride substrates. The resulting structures offer great potential for a wide range of applications in SEIRA and other areas of nanotechnology.

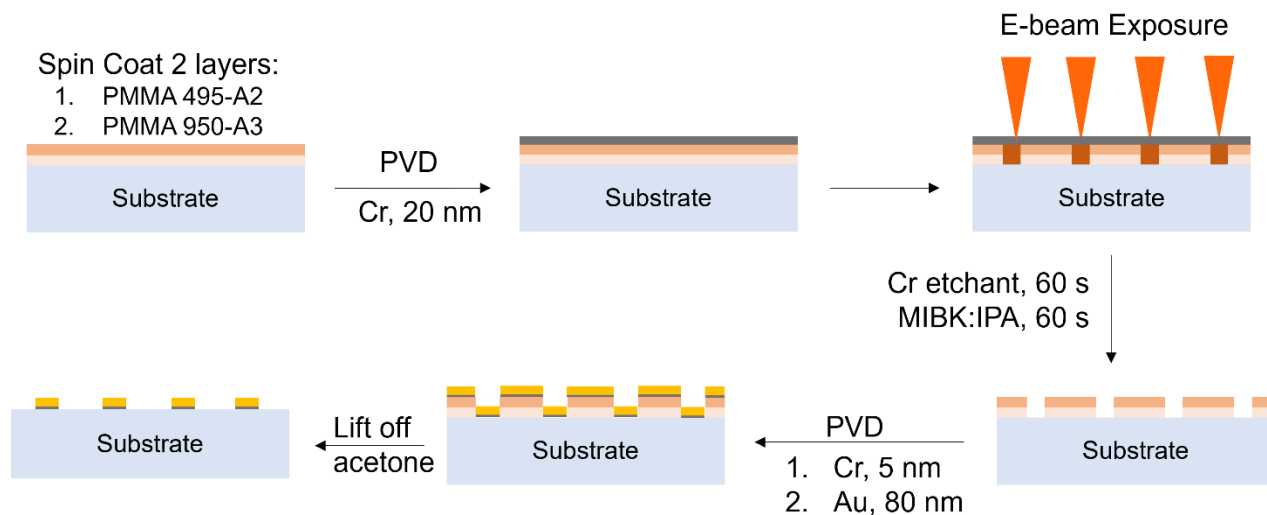


**Figure 6.1.** Schematic representation of the nanofabrication process sequence.

To prepare the samples for the experiment, a  $\text{CaF}_2$  wafer with a diameter of 1 in was used. Two layers of poly methyl methacrylate (PMMA, Microchem) were spin-coated onto the wafer at 3000 rpm for 60 seconds. The first layer applied was 495-A2, followed by 950-A3, and both were placed a hotplate at  $180^\circ\text{C}$  for one minute each, to increase adhesion to the substrate and remove any residual solvent. This process resulted in a  $\sim 320$  nm thick layer of PMMA resist. The double resist layer approach was implemented to reduce undercutting resist in thicker deposited materials. To verify the PMMA thickness, AFM (Bruker Dimension XR) imaging was performed, and the cross section was analyzed (Fig. 6.2). A 20 nm-thick layer of chromium was deposited on top of the PMMA resist layer using an electron-beam physical vapor deposition (EBPVD) system (Angstrom Engineering). Chromium served as

an anti-charging layer to prevent electron buildup on the  $\text{CaF}_2$  substrate during electron beam exposure. Electron Beam Lithography (EBL) was performed using a 50 kV acceleration voltage system (Raith Voyager System). The column was operated in high-mid current mode with a  $50\ \mu\text{m}$  aperture size. To calibrate exposure, cylindrical test structures were imaged to correct astigmatism and ensure proper beam focusing. The e-beam current was measured using a Faraday cup on the sample holder and was determined to be  $\sim 6200$  pA. Based on this measurement, the dwell time and speed were calculated with a fixed e-beam exposure area step size of  $0.02\ \mu\text{m}$  and line size of  $0.0005\ \mu\text{m}$ . A base dose of  $750\ \mu\text{C}/\text{cm}^2$  was set for  $\sim 320$  nm of PMMA resist, and a  $500 \times 500\ \mu\text{m}^2$  writefield was used. The plasmonic arrays were patterned with a single unit cell dimension of  $2.95 \times 2.2\ \mu\text{m}^2$ , and the single bar dimensions were  $1.95 \times 0.26 \times 0.08\ \mu\text{m}^3$  (Fig. 6.3) This precise and

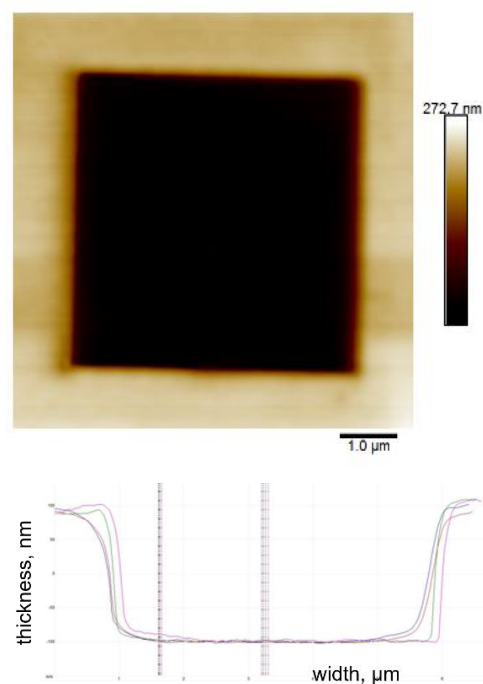


**Figure 6.2.** (a) AFM amplitude image of the cross section of PMMA resist and  $\text{CaF}_2$  substrate. (b) The resulting cross section of the PMMA.

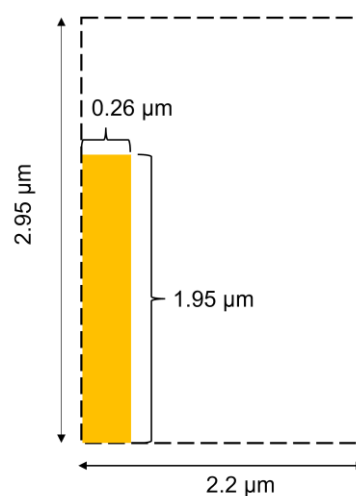


**Figure 6.3.** Size of the array unit cell (1)

careful calibration and design of the EBL process allowed for the fabrication of high-quality and uniform nanostructures.

After the e-beam exposure, the next step involved removing the chromium layer using a chromium etchant solution. To dissolve the exposed PMMA layer, a solution of methyl isobutyl ketone and 2-propanol (MIBK:IPA 1:3, Microchem) was used. The development process was stopped by dipping the wafer in isopropanol for 20 seconds, all of which was carried out at room temperature. Next, a chromium adhesion layer of 5 nm thickness was deposited onto the sample by EBPVD, followed by deposition of an 80 nm layer of gold. Finally, a lift-off process was carried out in acetone for 5 minutes at room temperature, and the wafer was then rinsed in isopropyl for 30 seconds. Optical microscopy was used to examine the final product, which showed a uniform array. However, some stitching errors were observed between individual writefields (Fig. 6.4). To fix this issue, further writes were conducted using a writefield of size  $499.4 \times 498.55 \mu\text{m}^2$  representing whole number of unit cells in each direction and ensuring equal spacing of unit cells between adjacent writefields.

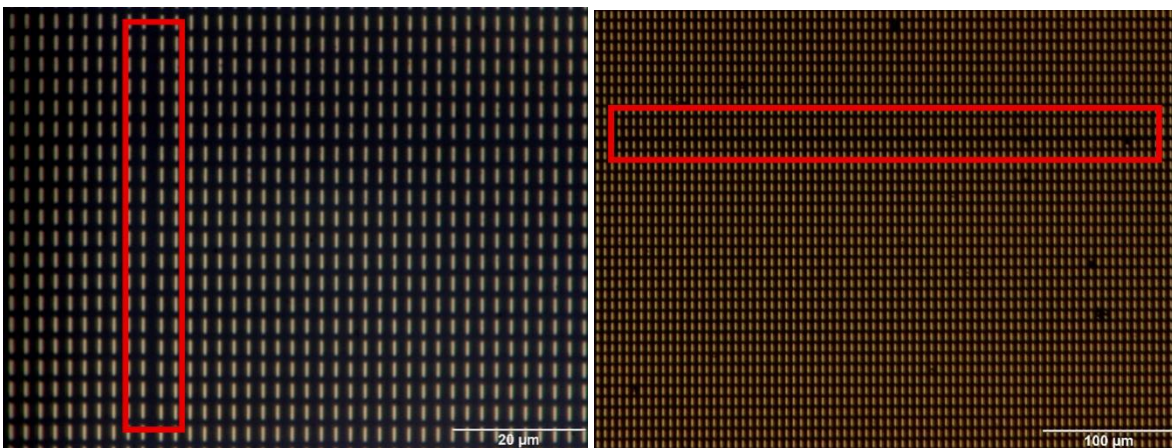


**Figure 6.4.** Optical microscopy images of the stitching error (red boxes) between two writefields, when unit cell spacing is not taken into consideration.

## 6.3. Results and Discussion

### 6.3.1. Linear Spectroscopy of Gold Arrays

Infrared gold antennas localize enhanced near fields close to the metal surface, when excited at the frequency of their plasmon resonance, and amplify vibrational signals from the nearby molecules.<sup>244</sup> In particular, FTIR spectroscopy of gold nanoarrays can reveal information about the localized surface plasmon resonances (LSPRs) of the nanoparticles. Nanoplasmonic applications often require the use of highly sensitive noble metals, and among them, silver (Ag) is particularly sensitive. Nonetheless, in wet environments like aqueous and organic solvents, Ag tends to oxidize, which can result in inadequate adhesion between Ag and dielectrics.<sup>253</sup> This limitation makes Ag less suitable for biosensing applications. As a result, gold has become a more popular alternative due to its chemical stability and high conductivity. In the case of gold nanoarrays, the LSPRs are particularly strong due to the unique electronic properties of gold. The FTIR spectra of these nanoarrays can be used to probe the plasmonic response of the nanoparticles, which can provide information about the relative size of the individual nanoparticles within the array.

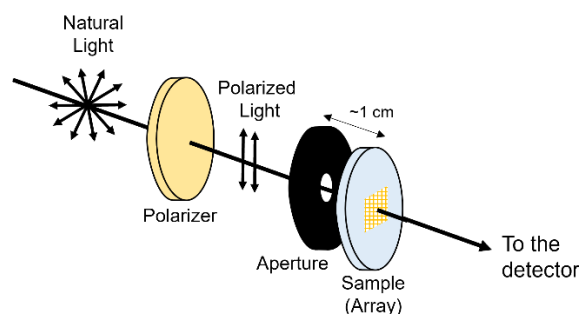


**Figure 6.5.** Optical setup for FTIR measurement with nanoarrays. A wire grid polarizer selects the polarization of mid-IR radiating parallel (or perpendicular) to the direction of the individual bars of the array. Because of the small size of the nanoarray, an aperture is used to eliminate the radiation passing around the array. The aperture should be placed close to the array, typically within 1 cm distance.

Modifications were made to the FTIR instrument for measuring extinction spectra of plasmonic array samples (Fig. 6.5). A gold wire-grid polarizer was placed before the sample to allow for selection of IR radiation which is either parallel or perpendicular to the long axis of the antennas. A series of infrared spectroscopy measurements were conducted on the gold nanoarrays at parallel polarization. If the array is placed so that the radiating is parallel to the bars, an IR peak would be observed corresponding to LSPR of the array. FTIR measurements on a gold array with individual

bars measuring  $1.95 \times 0.26 \mu\text{m}^2$ , displayed a peak at  $1868 \text{ cm}^{-1}$  and had a maximum absorbance of 0.73 OD (Fig. 6.6) (the packing distance also affects the central frequency).

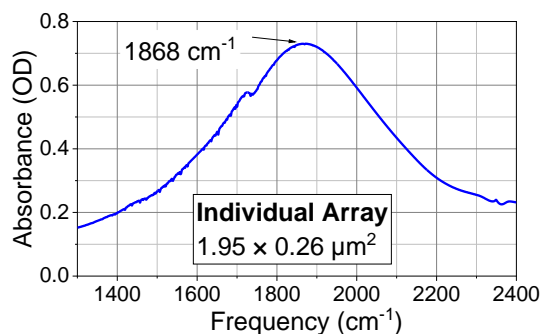


**Figure 6.6.** Linear spectrum of the plasmonic antenna array, where an individual array was  $1.95 \times 0.26 \mu\text{m}^2$  (see Fig. 6.3)

### ***6.3.2. Electron Scattering in the Resist Layer Affects PMMA Dose***

When writing features in a thick resist layer, the dose of exposure to the e-beam needs to be appropriate. A common challenge is dose insufficiency, which occurs when the electron beam resolution approaches the focal spot size. Thus, a loss of resolution during patterning originates from electron scattering due to the proximity effect. The proximity effect is the phenomenon that occurs when the electrons penetrate solid materials, such as the PMMA resist, and their interaction results in scatterings. The electrons interact with the resist and create secondary electrons that can cause exposure in unintended areas. This effect results in a dose distribution that is broader than expected, leading to a reduction in resolution and feature fidelity.

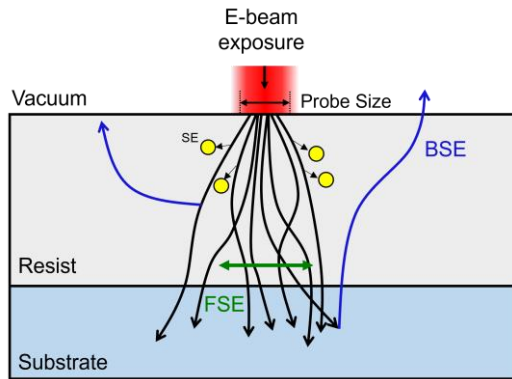


**Figure 6.7.** A representation of the interactions of an electron beam with a resist layer on a substrate. The scattering of electrons causes unintentional exposure of resist (proximity effect)

During electron-solid interaction, there are two types of electron scatterings that occur: small angle scattering (forward scattering, FSE) and large angle scattering (backscattering, BSE). The FSE (Fig. 6.7, green arrow) broadens the initial beam diameter, while the BSE (Fig. 6.7, blue arrow) causes the proximity effect. The scattered electrons from both types of scattering create secondary electrons (SE, Fig. 6.7, yellow circles). Although both types of scatterings contribute to the proximity effect, the range of BSE is much larger than that of FSE, making BSE more significant in this effect. As a result, nearby features

can scatter electrons that alter the dose the pattern receives, leading to broadening or distortion of the intended feature.

The proximity effect can result in a narrow line between two large and exposed areas receiving so many scattered electrons that it can be developed away in a positive resist. To mitigate this effect, several process parameters can be optimized. For example, a high acceleration voltage can be used in the electron beam lithography tool to reduce the broadening effect caused by scattering. The resist type also plays a critical role in determining the proximity effect. Using resists that exhibit a lower sensitivity to secondary electron scattering, such as hydrogen silsesquioxane (HSQ), can reduce the proximity effect and improve the resolution of the pattern.

To achieve optimal results in exposure, it is essential to determine the required specifications for the resist layer and the dose necessary to clear it. To determine the clearing dose for the resist layer, a 320 nm layer of PMMA was spin-coated onto a calcium wafer, followed by a 20 nm layer of chromium. The original array pattern was used for this experiment, where the dimension of individual bars was set to  $1.95 \times 0.26 \mu\text{m}^2$ . A total of 30 writefields measuring  $500 \times 500 \mu\text{m}^2$  were patterned, using doses ranging from 300 to  $1550 \mu\text{C}/\text{cm}^2$ . The e-beam system employed in this study exposed the individual writefield patterns multiple times by gradually increasing the dose in small steps. This approach allowed for precise control over the dose applied to each writefield, resulting in an accurate determination of the clearing dose for the resist layer.

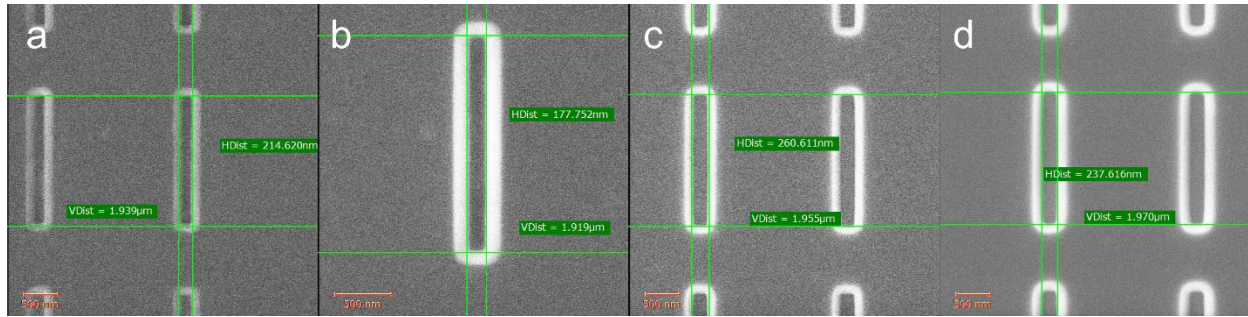


**Figure 6.8.** SEM images of nanoarrays exposed at (A)  $300 \mu\text{C}/\text{cm}^2$  (B)  $500 \mu\text{C}/\text{cm}^2$  (C)  $650 \mu\text{C}/\text{cm}^2$  and (D)  $1550 \mu\text{C}/\text{cm}^2$ .

After exposure, the PMMA is immersed in a Cr etchant for 30 seconds and a PMMA developer solution (MIBK:IPA 1:3) for 60 seconds, which results in the development of the desired nanostructures. To prevent further development of the PMMA layer, it is then rinsed in IPA for 30 seconds. After development is complete, a 20 nm layer of Cr was deposited on top of the developed PMMA by EBPVD, and the resulting structures were imaged using scanning electron microscopy (SEM). Figure 6.8 displays SEM images of the nanoarray obtained at different exposure doses. The SEM images in Figure 6.8 show the effects of varying doses on the patterned structures.

In Scanning Electron Microscopy (SEM), contrast in images is generated by detecting and measuring the intensity of the secondary electrons, backscattered electrons, or both, that are emitted from the sample surface as a result of interaction with the electron beam. In this chapter, SE imaging is used as it provides higher resolution and greater sensitivity to surface features than BSE imaging. Topographic contrast in Scanning Electron Microscopy (SEM) refers to the variation in brightness and darkness of the sample surface features due to differences in height or depth. This contrast is generated by detecting and measuring the intensity of the secondary electrons or backscattered electrons emitted from the sample surface. SEs are sensitive to the topography and roughness of the sample, and are emitted preferentially from the raised areas of the sample. Hence, in SEM images, the brighter areas correspond to the higher elevations on the sample while the darker areas correspond to the lower elevations. If one SEM image has higher contrast around the edges, it suggests that the surface of the nanostructure has steeper edges or sharper features.

At the lowest dose of  $300 \mu\text{C}/\text{cm}^2$  (Fig. 6.8(a)), the bar had a dimension of  $1.94 \times 0.21 \mu\text{m}^2$ , which was smaller than the preset design. As seen from the low contrast in the image, it suggests that the nanostructure has a more gradual transition between surfaces. The most likely explanation is that the resist was not completely cleared, possibly due to the low dose used. At the clearing dose of 500

$\mu\text{C}/\text{cm}^2$  (Fig. 6.8(b)), the bar had a dimension of  $1.92 \times 0.17 \mu\text{m}^2$ . At the optimal clearing dose of  $650 \mu\text{C}/\text{cm}^2$ , the bar had the exact dimensions as in the preset pattern, i.e.,  $1.95 \times 0.26 \mu\text{m}^2$ . However, at a high dose of  $1550 \mu\text{C}/\text{cm}^2$ , the bar had a dimension of  $1.97 \times 0.24 \mu\text{m}^2$ , and the edges of the bar appeared rounded. This deformation could be attributed to undesired exposure in the surrounding regions at high dose due to the proximity effect. Therefore, it is crucial to determine the optimal dose for EBL patterning to achieve high-quality patterns with precise resolution and minimal deformation.

In this experiment, as the dose increased, the residual thickness of the resist in the regions exposed the e-beam decreased until the clearing dose was reached, which is the lowest dose that entirely removes the resist while maintaining the precise patterning parameters of the array. For a 320 nm PMMA resist layer, the clearing dose was determined to be  $D_c = 650 \mu\text{C}/\text{cm}^2$ . It's worth noting that at higher e-beam doses, deformation in the arrays becomes more apparent, as shown in Figure 6.9, underscoring the importance of finding the optimal dose for successful patterning.

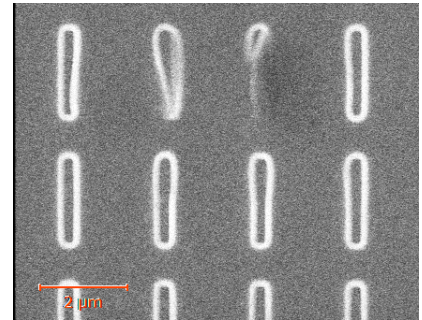


**Figure 6.9.** SEM image of deformed arrays due to high dose ( $1330 \mu\text{C}/\text{cm}^2$ )

### 6.3.3. Tuning Frequency Selectivity of Antennas

The central frequency of localized surface plasmon resonance (LSPR) is influenced by various parameters, such as the shape, size, and dielectric environment of the nanoparticles. In the case of gold nanoantennas, tuning the LSPR can be achieved by adjusting the length of individual bars, resulting in a monotonic dependence on their length. This property makes them desirable for designing optical antennas with high resonant efficiency and frequency selectivity in the infrared region. As the length of each individual antenna is increased, the peak of the IR extinction spectrum undergoes a red shift.

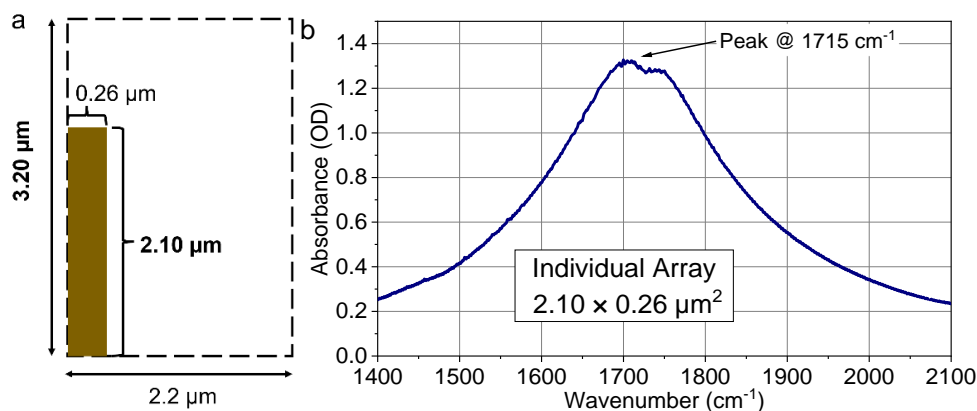


**Figure 6.10.** (a) Size of the nanoarray unit cell, designed to have its m-IR peak in the carbonyl region. The edited lengths are marked in bold. (b) Linear FTIR extinction of the plasmonic antenna array manufactured to the dimensions in panel (a).

Several nanoarrays were manufactured. The array having the unit cell of  $1.95 \times 0.26 \mu\text{m}^2$  and bar dimensions of  $1.95 \times 0.26 \mu\text{m}^2$  featured an IR peak at  $1868 \text{ cm}^{-1}$ , which is suitable for studying molecules with vibrational frequency at  $\sim 1868 \text{ cm}^{-1}$ . However, to achieve a better signal enhancement of a molecule with a carbonyl moiety, it is ideal to have an array with an m-IR peak at  $1700\text{--}1750 \text{ cm}^{-1}$ . Therefore, the lengths of each antenna and the unit cell were increased from  $1.95$  to  $2.10 \mu\text{m}$  and from  $2.95$  to  $3.20 \mu\text{m}$ , respectively, while the widths were kept the same (Fig. 6.10(a)). FTIR measurements displayed an IR peak at  $1715 \text{ cm}^{-1}$  with  $\sim 1.3$  OD (Fig. 6.10(b)). Note that the slight dip at  $1730 \text{ cm}^{-1}$  is due to PMMA absorbance.

The process for fabricating the gold nanoarrays was identical to the process described in 6.2.1. A  $10 \times 10$  matrix of  $500 \times 500 \mu\text{m}$  writefields was patterned using an EBL tool, resulting in a  $5 \times 5$  mm array. Prior to the final deposition of gold, a  $20 \text{ nm}$  Cr layer was deposited, and the PMMA mask was imaged with SEM. The SEM images indicated no stitching errors between the writefields, and the dimensions of each nanoantenna were measured to be  $2.10 \times 0.258 \mu\text{m}^2$  (Fig. 6.11(a)).

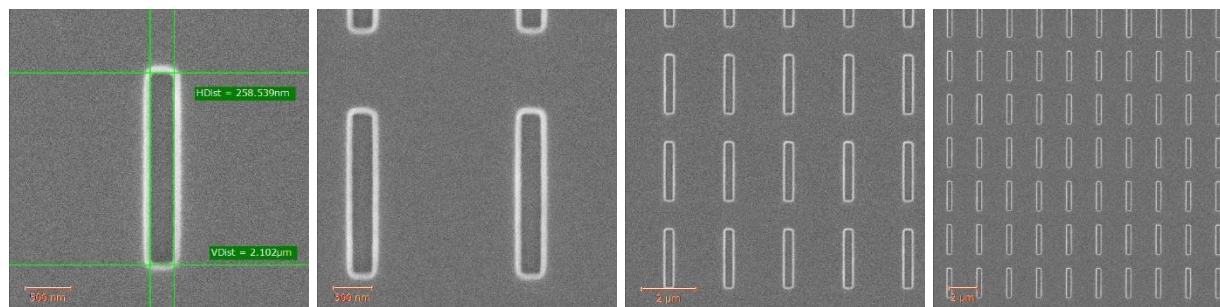


**Figure 6.11.** SEM images of antennas fabricated on a  $\text{CaF}_2$  substrate. The size of an individual array is  $2.10 \times 0.26 \mu\text{m}^2$

### 6.3.4. Design and Fabrication of Nanoarrays for Electrochemical Measurements

Recent advancements in the development of electrochemical cell chips based on functionalized nanometals<sup>254</sup> have raised interest in the fabrication of nanopatterned surfaces capable of rapid electrochemical scanning of a range of compounds simultaneously. Plasmonic nano-arrays have emerged as a valuable tool for electrochemical research due to their remarkable optical sensitivity and promising conductivity.<sup>255, 256</sup> In the past, signals obtained from electrochemistry were limited to representing the average electrochemical process of the bulk samples, even though the electrochemical process occurs at the electrode surface. As a result, plasmonic sensors are now being used more frequently as electrodes photoanodes to uncover individual electrochemical reactions.<sup>257</sup> The integration of SPR/LSPR phenomenon with electrochemistry, through the use of plasmonic nano-arrays as working electrodes, has the potential to provide a highly effective approach for leveraging both optical and electrochemical properties during redox reactions. Li *et al.* have introduced a new spectro-electrochemical technique with optical detection in the visible range in which biosensors were created using a hybrid structure of nanohole arrays and gold nanoparticles.<sup>258, 259</sup> The working electrode was NanoLCA (nanocup). The researchers found that electrochemical-enhanced optical LSPR measurements had a better signal-to-noise ratio and lower detection limits compared to conventional electrochemical detection.

One promising direction for advancing the field of electrochemical cells is the development of gold-based electrochemical cells on glass substrates. This innovative approach would involve depositing a thin layer of gold onto a glass substrate, followed by the formation of a self-assembled monolayer (SAM) of molecules on the gold surface. The SAM is functionalized with specific ligands or probes that can selectively bind to the target molecules of interest. As a result, we have designed a gold-based electrochemical cell, designed to tune the electronic properties of the attached molecule to possibly alter the chain properties and thus affect vibrational energy transfer through the molecule.

The difference between the electrochemical array and the standard array are the connections between the individual bars, “wires”, as well as two terminals on the side as a way to apply potential. Every alternate row is connected to the same terminals on the side (Fig. 6.12(a)).

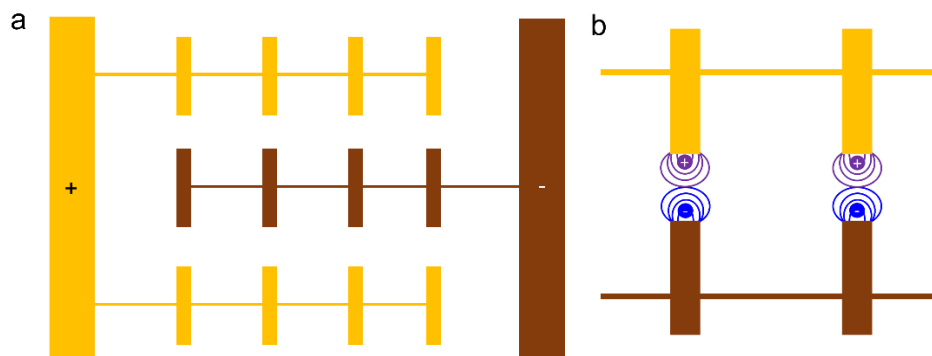


**Figure 6.12** (a) Simplified setup of the connected arrays, where orange represents the bars connected to the positively charged terminal and brown represents the bars connected to the negatively charged terminal. (b) The LSPR field expected from the setup, purple cloud represents a positive charge while blue represents a negative charge.

The electrochemical cell has been fabricated on a glass substrate the same process as above. However, additional steps were conducted before the first PMMA coating. To form the terminals on the side, UV lithography was used. One layer of S1813 (Microchem), a positive photoresist, was spin-coated on the surface of a  $\text{CaF}_2$  wafer at 500 rpm for 5 s followed by 4000 rpm for 60 s, resulting in a 1.2  $\mu\text{m}$  thick layer of photoresist. The wafer was placed on a hotplate at 100  $^\circ\text{C}$  for 3 min. The wafer was loaded into a photolithography tool (Suss MJB4), with a photomask placed above it. The photomask consisted of the terminal design and four alignment markers and was printed on a transparency sheet (Fig. 6.13). The mask selectively allows light through the wafer and the pattern is consequently recreated on the photoresist. The wafer was exposed to UV light (365-405 nm). Following exposure, the wafer was placed in AZ300 developer (Microchem) for 30s, where the exposed S1813 is dissolved. 5 nm of Cr and 80 nm of Au were then deposited using

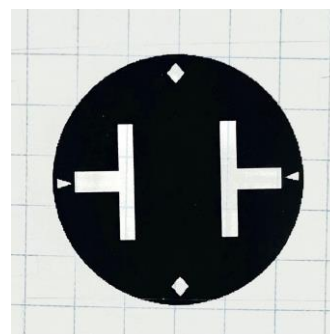


**Figure 6.13.** Photomask printed on a transparency, used for photolithography with a positive resist. The terminals are the T-bars on the side and four alignment markers are equally spaced around the circumference of design.

EBPVD. The final lift-off was done in acetone for 1 min at room temperature. The sequence of the whole process is depicted in Figure 6.14. After the terminals are printed using UV lithography, the process outlined in the preceding section was followed. While EBL can also be employed for printing the terminals, it has a low throughput, and printing large structures can be time-consuming, even with the use of high currents.

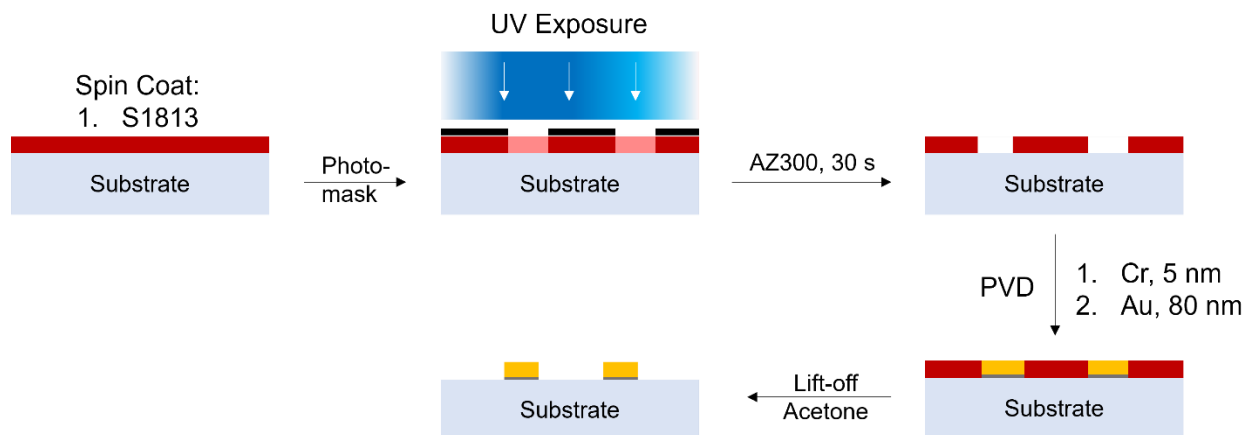


**Figure 6.14.** Schematic representation of the UV lithography process sequence used to fabricate the side terminals.

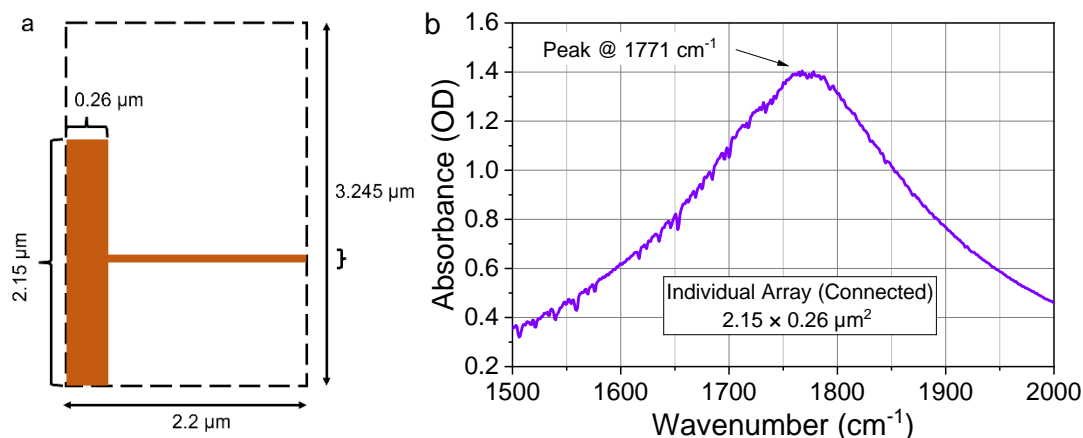


**Fig. 6.15 (a)** Size of the array unit cell of the electrochemical fabrication. **(b)** Linear spectrum of the plasmonic antenna array of electrochemical cell.

With the aim to adjust the conjugation properties of poly(*p*-phenylene) chains, as discussed in Chapter 3, an electrochemical cell was devised and made. Note that the presence of thin, bar-connecting wires affected the central frequency of the plasmon resonance, resulting in a peak at 1771  $\text{cm}^{-1}$  (Fig. 6.15b), instead of expected  $\sim 1642 \text{ cm}^{-1}$  for the array of the same dimensions without connecting wires. To tune the LSPR frequency to the carbonyl frequency region, the lengths of the bars and the length of the unit cell were increased by 10% from 1.95 to 2.15  $\mu\text{m}$ , resulting in the observed LSPR peak at 1771  $\text{cm}^{-1}$  (Fig. 6.15b). This modification resulted in an appropriate length for the nanoarray, where the FTIR peak was observed at 1771  $\text{cm}^{-1}$  (as depicted in Fig. 6.15b).

Imaging the completed array on SEM is challenging due to the exposed  $\text{CaF}_2$  substrate which contributes to charge buildup. To obtain images of the connected array, SEM imaging was performed

after EBL write and before final gold deposition. Prior to imaging, a 20 nm layer of Cr was deposited onto the PMMA mask surface using EBPVD. The resulting SEM images (Fig. 6.16) confirmed that the dimensions of each bar were  $2.15 \times 0.26 \mu\text{m}^2$ , and the wires between the bars were visible. Furthermore, the images demonstrated that every alternate row of nanobars was connected.

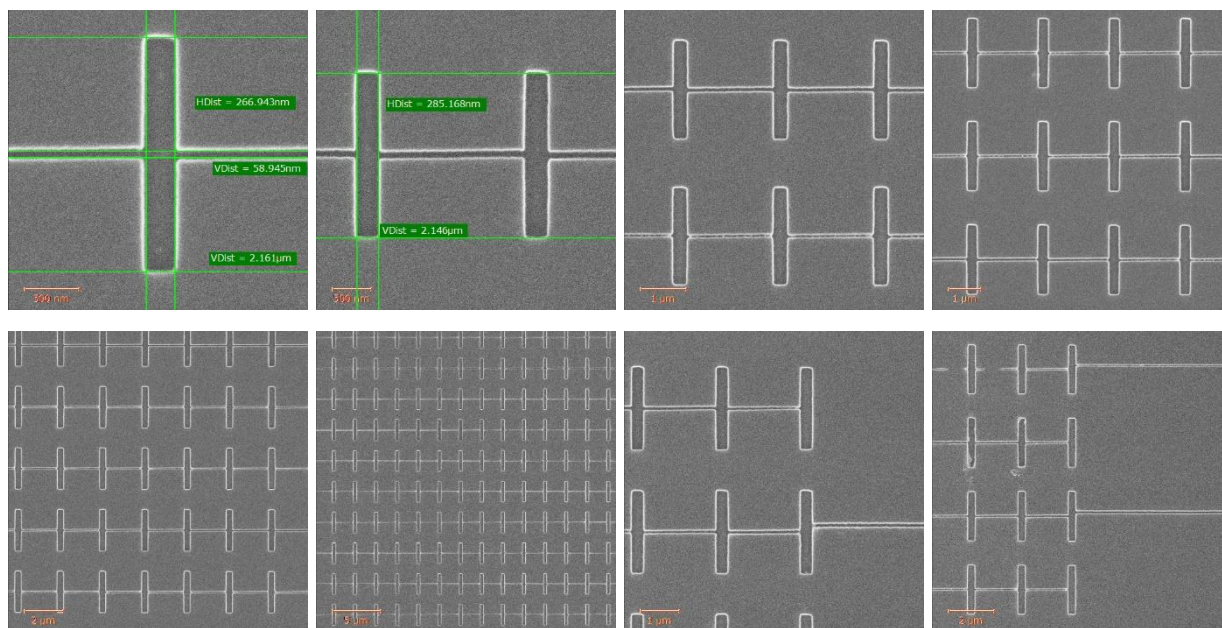


**Figure 6.16.** SEM images of connected antennas pattern in PMMA mask on a  $\text{CaF}_2$  substrate. The size of an individual array is  $2.15 \times 0.26 \mu\text{m}^2$  and the width of the connecting wires are  $\sim 50 \text{ nm}$  thick.

The use of both a schematic diagram and an actual image enhances the clarity and comprehensibility of the experimental setup, allowing for easy interpretation of the data and providing a clear visual representation of the results. Figure 6.17 depicts the cartoon scheme and actual array on a  $\text{CaF}_2$  wafer of 1" in diameter.

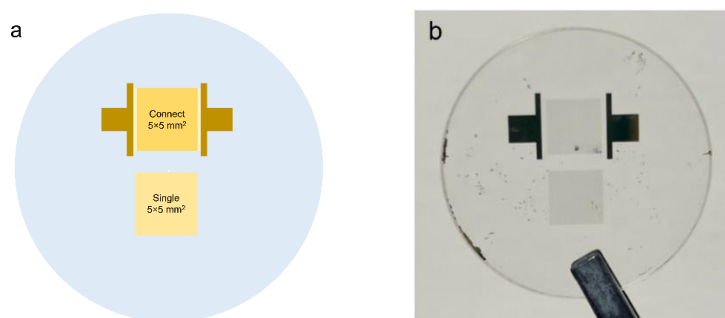


**Figure 6.17.** (a) Schematic representation of a single array and a connected array positioned on the same a  $\text{CaF}_2$  wafer., providing a clear idea of the geometry and size of the structures. The diagram is made to scale, providing a realistic sense of the dimensions of the arrays. (b) Actual image of the fabricated arrays on a 1"  $\text{CaF}_2$  wafer providing a visual verification of the successful fabrication of the intended structures.

## 6.4. Conclusion

Fabrication of site-specific nanostructures of desired shape, structure, and composition is probably the most desirable goal pursued actively by the nanotechnology community. To fabricate periodic, nanoscale patterns on arbitrary substrates, various nanofabrication technologies have been developed. Here, gold-based nanostructures with controllable size were fabricated using EBL, EBPVD and photolithography. This approach is a rapid and straightforward method for creating large-area ( $5 \times 5 \text{ mm}^2$ ) plasmonic Au patterns with the ability to control LSPR in the m-IR range. With the superior structural stability and strong peak in the m-IR region, these nanostructures are designed as a platform for electrochemical reactions with m-IR detection. Beyond SERIA spectroscopy, these results would be highly useful in many areas of nanoscience and nanotechnology, including biosensing, cathode electrodes of light-emitting diodes (LED) and organic dye solar cells.

# Summary

Vibrational energy transport is a crucial phenomenon not only in the macroscopic world but also in the microscopic realm of nanostructures and biomolecules. In this thesis, we utilized femtosecond infrared spectroscopy coupled with computational methods to study the transport of vibrational energy through conjugated oligomers and complex metal compounds. Additionally, we thoroughly discuss the fabrication of gold nanoarrays and their various applications.

The primary objective of the first study on poly(*p*-phenylene) chains was to investigate the impact of electronically conjugated chains on vibrational energy transport. The study revealed that electronically conjugated chains are exceptionally efficient at transporting vibrational energy, with transport speeds of up to  $\sim 67$  Å/ps with C=O excitation, in contrast to  $\sim 14$  Å/ps in alkanes. The primary distinction between poly(*p*-phenylene) chains and alkane chains is the degree of conjugation, which indicates the advantage of using conjugated systems for rapid energy transfer. The high speed observed in the study was attributed to efficient energy injection into the chain, leading to the formation of wavepackets that freely propagated through the chain. These findings shed light on previously unknown questions about the effect of conjugation on energy transfer pathways and provide an explanation for the various energy relaxation pathways involved in different tag excitations.

Motivated by the findings of the conjugated oligomer study, we conducted a new experiment to investigate the vibrational energy transport properties of large and complex molecules ( $\sim 1200$  amu) containing a metal center. Initially, we aimed to study energy transport across an alkyne bridge but overlap of strongly coupled modes on each side of the molecule presented a challenge. Consequently, we shifted our focus to energy transport across the Pt bridge, with the goal of understanding the rules of energy relaxation and transfer across metal centers in such compounds. To this end, we performed comprehensive analyses of waiting-time dynamics for numerous cross and diagonal peaks, which focused on parameters such as coherent oscillation, energy transfer, and cooling, with a particular interest in coherent oscillations that were further studied in detail later. Through computations of vibrational relaxation pathways, we identified two regimes of intra-molecular vibrational relaxation (IVR) in the molecule, which allowed us to successfully characterize energy transport across the Pt center. Furthermore, we discovered characteristic 2DIR features of several functional groups, which could potentially be used to identify these groups using 2DIR spectroscopy, making it a promising analytical tool.

To build upon our understanding of vibrational energy transport across Pt centers, we sought to explore the potential of using 2DIR spectroscopy as an analytical tool for identifying functional groups in complex structures. During our analysis of the previously mentioned large Pt compound, we made an interesting observation: oscillatory patterns were present in the majority of the cross-peaks within the fingerprint region. The novelty of this observation lies in the fact that there is no prior literature documenting the oscillations of non-metal carbonyl groups. The presence of quantum beat (QB) oscillations in the 2DIR spectra indicated a superposition of two strongly coupled modes that were excited by a m-IR pump. By using QB oscillations in cross-peaks, we were able to identify strongly coupled states that typically belong to the same functional group, thus identifying the peaks of such functional groups in complex linear and 2DIR spectra that contained multiple overlapping peaks.

With the growing interest in nanofabricated functional devices, the final chapter of this thesis presents a method used to precisely fabricate gold plasmonic arrays on CaF<sub>2</sub> wafers at the nanometer scale. The frequency tuning of the array was achieved by changing the length of individual nanorods to have an absorbance peak in the IR vibrational mode region of the molecule of interest. Various functionalities of these nanostructures were explored, including their A new type of nanoarrays suitable for combined electrochemical and m-IR measurements were designed and manufactured. In these arrays, the individual bars were connected to electrical terminals on both sides. Each alternate row was linked to an opposite charge - either positive or negative. Potential applications of the arrays to affect the electronic properties of molecules chemisorbed on gold surface are discussed. In addition to their role as signal enhancers in spectroscopic measurements such as surface-enhanced infrared absorption (SEIRA) spectroscopy, these nanostructures have potential applications as biosensors, chemical sensors, and photovoltaic devices.

With the results presented in this thesis it is finally possible to answer all four questions raised in Chapter 1:

- Does the conjugation of oligomeric chains dictate the maximum speed each chain band can support?

The maximum speed of each chain band in energy transport is indeed dictated by the conjugation of oligomeric chains. This is because the vibrational energy transport through oligomeric chains is sensitive to the degree of conjugation of the chain type. Conjugated oligomeric chains have been shown to have chain bands that can support a high maximum

speed, as indicated by large  $\beta$  values. In comparison, alkane chains (which are non-conjugated) possess several broad chain bands, but the transport speed is significantly slower than in conjugated chains (14 vs. 67 Å/ps). It is important to note that the overall energy transport speed is largely determined by which chain bands contribute, meaning that even if there are many broad chain bands, if none contribute to the energy transport, the energy transport speed would still be slow.

- How does the end group type affect the efficiency of energy injection into the chain?

To address this question, we can examine the significant contrast in energy transport rates observed in poly(*p*-phenylene) when NO<sub>2</sub> (5.3 Å/ps) or COOH (67 Å/ps) is excited. It is clear that COOH initiation is much more effective than NO<sub>2</sub> initiation. The efficient relaxation of the end-group localized tag mode occurs when the parent and daughter modes overlap, leading to high relaxation effectiveness. If the end-group remains localized after excitation, it results in inefficient energy injection, meaning that the localization must be disrupted to excite a coherent wavepacket. End-group delocalization is only possible when the end-group and chain-state are in resonance. In the case of poly(*p*-phenylenes), COOH-chain bands are strongly coupled to broad chain states, resulting in greater mixing of the end-group state with the chain states, leading to highly effective tag relaxation.

- Under the conditions of directed diffusion, does a transition occur between the regimes of ballistic and diffusive transport in large complex molecules with metal centers?

The immediate relaxation and high transport speed between the alkyne bridge and the triazole ring suggest that energy transport in that system is ballistic. However, once the initial energy relaxation occurs, diffusive transport takes over. As described in Chapter 1, ballistic energy transport requires highly periodic, delocalized molecular structures. Upon examining C2 and C6, it becomes apparent that the 6-carbon alkyne bridge in C6 is the only noticeably periodic component. Experimental data indicates that after energy relaxation into the triazole ring following alkyne excitation, the energy either relaxes into the terminal phenyl or returns to the alkyne bridge and crosses the Pt center towards the fluorinated phenyl or tolyl groups. This is evidenced by the long energy transport times between both moieties. All this occurs under the diffusive energy transport process.

- What are the requirements for efficient energy transfer between ligands of a transition metal complex?

In C2 and C6, the Pt center is located between the alkyne bridge, and the fluorinated phenyl and toluyl groups. For efficient energy transfer across a metal center, the two local modes at the two sides of the metal center must be delocalized and coupled. We noticed that the  $F_5Ph$  modes and  $C_6Tri$  modes were similar, resulting in an accidental frequency match. We also determined that the transport from  $\nu_{C=C}$  to  $F_5Ph$  in C2 occurs predominantly via three high-frequency mode pairs delocalized over both ligands. Additionally, the motions on each side of the ligand were coupled to the Pt center, with sufficient coupling strength to cause significant delocalization, providing energy relaxation pathways between the ligands.

To conclude, this thesis has presented experimental and theoretical investigations that have improved our comprehension of vibrational energy transport in oligomeric chains and metal complexes. Several open questions have successfully been resolved, leading to a clearer understanding of the topic at hand. Additionally, the nanofabrication techniques discussed in this thesis offer a framework for creating more intricate structures, which will facilitate further SEIRA studies in the future.

# Bibliography

- (1) Leitner, D. M.; Pandey, H. D.; Reid, K. M. Energy Transport across Interfaces in Biomolecular Systems. *The Journal of Physical Chemistry B* **2019**, *123* (45), 9507-9524. DOI: 10.1021/acs.jpcc.9b07086.
- (2) Leitner, D. M. Energy Flow in Proteins. *Annual Review of Physical Chemistry* **2008**, *59* (1), 233-259. DOI: 10.1146/annurev.physchem.59.032607.093606.
- (3) Nagy, A. M.; Raicu, V.; Miller, R. J. D. Nonlinear optical studies of heme protein dynamics: Implications for proteins as hybrid states of matter. *Biochimica et Biophysica Acta (BBA) - Proteins and Proteomics* **2005**, *1749* (2), 148-172.
- (4) Schoenlein, R. W.; Peteanu, L. A.; Mathies, R. A.; Shank, C. V. The First Step in Vision: Femtosecond Isomerization of Rhodopsin. *Science* **1991**, *254* (5030), 412-415. DOI: doi:10.1126/science.1925597.
- (5) Fang, C.; Frontiera, R. R.; Tran, R.; Mathies, R. A. Mapping GFP structure evolution during proton transfer with femtosecond Raman spectroscopy. *Nature* **2009**, *462* (7270), 200-204. DOI: 10.1038/nature08527.
- (6) Botan, V.; Backus, E. H. G.; Pfister, R.; Moretto, A.; Crisma, M.; Toniolo, C.; Nguyen, P. H.; Stock, G.; Hamm, P. Energy transport in peptide helices. *Proceedings of the National Academy of Sciences* **2007**, *104* (31), 12749-12754. DOI: doi:10.1073/pnas.0701762104.
- (7) Lian, T.; Locke, B.; Kholodenko, Y.; Hochstrasser, R. M. Energy Flow from Solute to Solvent Probed by Femtosecond IR Spectroscopy: Malachite Green and Heme Protein Solutions. *The Journal of Physical Chemistry* **1994**, *98* (45), 11648-11656. DOI: 10.1021/j100096a005.
- (8) Fayer, M. D. FAST PROTEIN DYNAMICS PROBED WITH INFRARED VIBRATIONAL ECHO EXPERIMENTS. *Annual Review of Physical Chemistry* **2001**, *52* (1), 315-356. DOI: 10.1146/annurev.physchem.52.1.315.
- (9) Barends, T. R. M.; Foucar, L.; Ardevol, A.; Nass, K.; Aquila, A.; Botha, S.; Doak, R. B.; Falahati, K.; Hartmann, E.; Hilpert, M.; et al. Direct observation of ultrafast collective motions in CO myoglobin upon ligand dissociation. *Science* **2015**, *350* (6259), 445-450. DOI: doi:10.1126/science.aac5492.
- (10) Yang, M.; Skinner, J. L. Signatures of coherent vibrational energy transfer in IR and Raman line shapes for liquid water. *Physical Chemistry Chemical Physics* **2010**, *12* (4), 982-991, 10.1039/B918314K. DOI: 10.1039/B918314K.
- (11) Xiang, B.; Ribeiro, R. F.; Du, M.; Chen, L.; Yang, Z.; Wang, J.; Yuen-Zhou, J.; Xiong, W. Intermolecular vibrational energy transfer enabled by microcavity strong light-matter coupling. *Science* **2020**, *368* (6491), 665-667. DOI: doi:10.1126/science.aba3544.

- (12) Quéméner, G.; Balakrishnan, N.; Krems, R. V. Vibrational energy transfer in ultracold molecule-molecule collisions. *Physical Review A* **2008**, *77* (3), 030704. DOI: 10.1103/PhysRevA.77.030704.
- (13) Kim, S.; Shin, J.; Park, S.; Pak, Y.; Lim, M. Vibrational Energy Transfer Dynamics of HCO<sub>2</sub>CH<sub>3</sub> in CH<sub>3</sub>CN Solution. *Bulletin of the Korean Chemical Society* **2017**, *38* (7), 693-695.
- (14) Bakker, H. J.; Planken, P. C. M.; Legendijk, A. Role of solvent on vibrational energy transfer in solution. *Nature* **1990**, *347* (6295), 745-747. DOI: 10.1038/347745a0.
- (15) Pein, B. C.; Sun, Y.; Dlott, D. D. Unidirectional Vibrational Energy Flow in Nitrobenzene. *The Journal of Physical Chemistry A* **2013**, *117* (29), 6066-6072. DOI: 10.1021/jp3127863.
- (16) Fujisaki, H.; Yagi, K.; Kikuchi, H.; Takami, T.; Stock, G. Vibrational energy transport in acetylbenzonitrile described by an ab initio-based quantum tier model. *Chemical Physics* **2017**, *482*, 86-92.
- (17) Segal, D.; Agarwalla, B. K. Vibrational Heat Transport in Molecular Junctions. *Annual Review of Physical Chemistry* **2016**, *67* (1), 185-209. DOI: 10.1146/annurev-physchem-040215-112103.
- (18) Joachim, C.; Ratner, M. A. Molecular electronics: Some views on transport junctions and beyond. *Proceedings of the National Academy of Sciences* **2005**, *102* (25), 8801-8808. DOI: doi:10.1073/pnas.0500075102.
- (19) Scheer, E.; Reineker, P. Focus on Molecular Electronics. *New Journal of Physics* **2008**, *10* (6), 065004. DOI: 10.1088/1367-2630/10/6/065004.
- (20) Kaneko, S.; Murai, D.; Marqués-González, S.; Nakamura, H.; Komoto, Y.; Fujii, S.; Nishino, T.; Ikeda, K.; Tsukagoshi, K.; Kiguchi, M. Site-Selection in Single-Molecule Junction for Highly Reproducible Molecular Electronics. *Journal of the American Chemical Society* **2016**, *138* (4), 1294-1300. DOI: 10.1021/jacs.5b11559.
- (21) Stapleton, J. J.; Harder, P.; Daniel, T. A.; Reinard, M. D.; Yao, Y.; Price, D. W.; Tour, J. M.; Allara, D. L. Self-Assembled Oligo(phenylene-ethynylene) Molecular Electronic Switch Monolayers on Gold: Structures and Chemical Stability. *Langmuir* **2003**, *19* (20), 8245-8255. DOI: 10.1021/la035172z.
- (22) Sancho-García, J. C.; Brédas, J.-L.; Beljonne, D.; Cornil, J.; Martínez-Álvarez, R.; Hanack, M.; Poulsen, L.; Gierschner, J.; Mack, H.-G.; Egelhaaf, H.-J.; et al. Design of  $\pi$ -Conjugated Organic Materials for One-Dimensional Energy Transport in Nanochannels. *The Journal of Physical Chemistry B* **2005**, *109* (11), 4872-4880. DOI: 10.1021/jp045364i.
- (23) Sneyd, A. J.; Fukui, T.; Paleček, D.; Prodhon, S.; Wagner, I.; Zhang, Y.; Sung, J.; Collins, S. M.; Slater, T. J. A.; Andaji-Garmaroudi, Z.; et al. Efficient energy transport in an organic semiconductor mediated by transient exciton delocalization. *Science Advances* **2021**, *7* (32), eabh4232. DOI: doi:10.1126/sciadv.abh4232.
- (24) Wang, Q. H.; Bellisario, D. O.; Drahushuk, L. W.; Jain, R. M.; Kruss, S.; Landry, M. P.; Mahajan, S. G.; Shimizu, S. F. E.; Ulissi, Z. W.; Strano, M. S. Low Dimensional Carbon Materials for

Applications in Mass and Energy Transport. *Chemistry of Materials* **2014**, *26* (1), 172-183. DOI: 10.1021/cm402895e.

(25) Li, D.; Gao, J.; Cheng, P.; He, J.; Yin, Y.; Hu, Y.; Chen, L.; Cheng, Y.; Zhao, J. 2D Boron Sheets: Structure, Growth, and Electronic and Thermal Transport Properties. *Advanced Functional Materials* **2020**, *30* (8), 1904349.

(26) Sakakibara, K.; Chithra, P.; Das, B.; Mori, T.; Akada, M.; Labuta, J.; Tsuruoka, T.; Maji, S.; Furumi, S.; Shrestha, L. K.; et al. Aligned 1-D Nanorods of a  $\pi$ -Gelator Exhibit Molecular Orientation and Excitation Energy Transport Different from Entangled Fiber Networks. *Journal of the American Chemical Society* **2014**, *136* (24), 8548-8551. DOI: 10.1021/ja504014k.

(27) Dijkstra, A. G.; Beige, A. Efficient long-distance energy transport in molecular systems through adiabatic passage. *The Journal of Chemical Physics* **2019**, *151* (3), 034114. DOI: 10.1063/1.5100210.

(28) Reifsnnyder, A.; Nawwar, M.; Doan-Nguyen, V.; McComb, D. W. Exploring Vibrational Spectroscopy of Quantum Materials in the Scanning Transmission Electron Microscope. *Microscopy and Microanalysis* **2022**, *28* (S1), 1678-1680. DOI: 10.1017/S1431927622006687 From Cambridge University Press Cambridge Core.

(29) Solis, D., Jr.; Willingham, B.; Nauert, S. L.; Slaughter, L. S.; Olson, J.; Swanglap, P.; Paul, A.; Chang, W.-S.; Link, S. Electromagnetic Energy Transport in Nanoparticle Chains via Dark Plasmon Modes. *Nano Letters* **2012**, *12* (3), 1349-1353. DOI: 10.1021/nl2039327.

(30) Wittmann, B.; Wenzel, F. A.; Wiesneth, S.; Haedler, A. T.; Drechsler, M.; Kreger, K.; Köhler, J.; Meijer, E. W.; Schmidt, H.-W.; Hildner, R. Enhancing Long-Range Energy Transport in Supramolecular Architectures by Tailoring Coherence Properties. *Journal of the American Chemical Society* **2020**, *142* (18), 8323-8330. DOI: 10.1021/jacs.0c01392.

(31) Hurley, D. H.; El-Azab, A.; Bryan, M. S.; Cooper, M. W. D.; Dennett, C. A.; Gofryk, K.; He, L.; Khafizov, M.; Lander, G. H.; Manley, M. E.; et al. Thermal Energy Transport in Oxide Nuclear Fuel. *Chemical Reviews* **2022**, *122* (3), 3711-3762. DOI: 10.1021/acs.chemrev.1c00262.

(32) Rose, G. D.; Fleming, P. J.; Banavar, J. R.; Maritan, A. A backbone-based theory of protein folding. *Proceedings of the National Academy of Sciences* **2006**, *103* (45), 16623-16633. DOI: doi:10.1073/pnas.0606843103.

(33) Fujisaki, H.; Straub, J. E. Vibrational energy relaxation in proteins. *Proceedings of the National Academy of Sciences* **2005**, *102* (19), 6726-6731. DOI: doi:10.1073/pnas.0409083102.

(34) Yaliraki, S. N.; Roitberg, A. E.; Gonzalez, C.; Mujica, V.; Ratner, M. A. The injecting energy at molecule/metal interfaces: Implications for conductance of molecular junctions from an ab initio molecular description. *The Journal of Chemical Physics* **1999**, *111* (15), 6997-7002. DOI: 10.1063/1.480096.

(35) Lu, J.-Q.; Wu, J.; Chen, H.; Duan, W.; Gu, B.-L.; Kawazoe, Y. Electronic transport mechanism of a molecular electronic device: structural effects and terminal atoms. *Physics Letters A* **2004**, *323* (1), 154-158.

- (36) Fox, M. A. Fundamentals in the Design of Molecular Electronic Devices: Long-Range Charge Carrier Transport and Electronic Coupling. *Accounts of Chemical Research* **1999**, *32* (3), 201-207. DOI: 10.1021/ar9600953.
- (37) Ren, J.; Hänggi, P.; Li, B. Berry-Phase-Induced Heat Pumping and Its Impact on the Fluctuation Theorem. *Physical Review Letters* **2010**, *104* (17), 170601. DOI: 10.1103/PhysRevLett.104.170601.
- (38) Majumdar, S.; Sierra-Suarez, J. A.; Schiffrès, S. N.; Ong, W.-L.; Higgs, C. F., III; McGaughey, A. J. H.; Malen, J. A. Vibrational Mismatch of Metal Leads Controls Thermal Conductance of Self-Assembled Monolayer Junctions. *Nano Letters* **2015**, *15* (5), 2985-2991. DOI: 10.1021/nl504844d.
- (39) Galperin, M.; Saito, K.; Balatsky, A. V.; Nitzan, A. Cooling mechanisms in molecular conduction junctions. *Physical Review B* **2009**, *80* (11), 115427. DOI: 10.1103/PhysRevB.80.115427.
- (40) Yavatkar, R.; Tirumala, M. Platform wide innovations to overcome thermal challenges. *Microelectronics Journal* **2008**, *39* (7), 930-941.
- (41) Moore, A. L.; Shi, L. Emerging challenges and materials for thermal management of electronics. *Materials Today* **2014**, *17* (4), 163-174.
- (42) Cahill, D. G.; Ford, W. K.; Goodson, K. E.; Mahan, G. D.; Majumdar, A.; Maris, H. J.; Merlin, R.; Phillpot, S. R. Nanoscale thermal transport. *Journal of Applied Physics* **2003**, *93* (2), 793-818. DOI: 10.1063/1.1524305.
- (43) Han, X. X.; Rodriguez, R. S.; Haynes, C. L.; Ozaki, Y.; Zhao, B. Surface-enhanced Raman spectroscopy. *Nature Reviews Methods Primers* **2022**, *1* (1), 87. DOI: 10.1038/s43586-021-00083-6.
- (44) Fang, Y.; Seong, N.-H.; Dlott, D. D. Measurement of the Distribution of Site Enhancements in Surface-Enhanced Raman Scattering. *Science* **2008**, *321* (5887), 388-392. DOI: doi:10.1126/science.1159499.
- (45) Wang, Z.; Carter, J. A.; Lagutchev, A.; Koh, Y. K.; Seong, N.-H.; Cahill, D. G.; Dlott, D. D. Ultrafast Flash Thermal Conductance of Molecular Chains. *Science* **2007**, *317* (5839), 787-790. DOI: doi:10.1126/science.1145220.
- (46) Minnich, A. J.; Johnson, J. A.; Schmidt, A. J.; Esfarjani, K.; Dresselhaus, M. S.; Nelson, K. A.; Chen, G. Thermal Conductivity Spectroscopy Technique to Measure Phonon Mean Free Paths. *Physical Review Letters* **2011**, *107* (9), 095901. DOI: 10.1103/PhysRevLett.107.095901.
- (47) Siemens, M. E.; Li, Q.; Yang, R.; Nelson, K. A.; Anderson, E. H.; Murnane, M. M.; Kapteyn, H. C. Quasi-ballistic thermal transport from nanoscale interfaces observed using ultrafast coherent soft X-ray beams. *Nature Materials* **2010**, *9* (1), 26-30. DOI: 10.1038/nmat2568.
- (48) Maire, J.; Anufriev, R.; Nomura, M. Ballistic thermal transport in silicon nanowires. *Scientific Reports* **2017**, *7* (1), 41794. DOI: 10.1038/srep41794.

- (49) Kasyanenko, V. M.; Lin, Z.; Rubtsov, G. I.; Donahue, J. P.; Rubtsov, I. V. Energy transport via coordination bonds. *The Journal of Chemical Physics* **2009**, *131* (15), 154508. DOI: 10.1063/1.3246862.
- (50) Hsu, C.-P. The Electronic Couplings in Electron Transfer and Excitation Energy Transfer. *Accounts of Chemical Research* **2009**, *42* (4), 509-518. DOI: 10.1021/ar800153f.
- (51) Fückel, B.; Köhn, A.; Harding, M. E.; Diezemann, G.; Hinze, G.; Basché, T.; Gauss, J. Theoretical investigation of electronic excitation energy transfer in bichromophoric assemblies. *The Journal of Chemical Physics* **2008**, *128* (7), 074505. DOI: 10.1063/1.2829531.
- (52) Métivier, R.; Nolde, F.; Müllen, K.; Basché, T. Electronic Excitation Energy Transfer between Two Single Molecules Embedded in a Polymer Host. *Physical Review Letters* **2007**, *98* (4), 047802. DOI: 10.1103/PhysRevLett.98.047802.
- (53) Vayá, I.; Gustavsson, T.; Douki, T.; Berlin, Y.; Markovitsi, D. Electronic Excitation Energy Transfer between Nucleobases of Natural DNA. *Journal of the American Chemical Society* **2012**, *134* (28), 11366-11368. DOI: 10.1021/ja304328g.
- (54) Carter, J. A.; Wang, Z.; Fujiwara, H.; Dlott, D. D. Ultrafast Excitation of Molecular Adsorbates on Flash-Heated Gold Surfaces. *The Journal of Physical Chemistry A* **2009**, *113* (44), 12105-12114. DOI: 10.1021/jp906082u.
- (55) Narasimhan, T. N. Fourier's heat conduction equation: History, influence, and connections. *Proceedings of the Indian Academy of Sciences - Earth and Planetary Sciences* **1999**, *108* (3), 117-148. DOI: 10.1007/BF02842327.
- (56) Chen, G. Thermal conductivity and ballistic-phonon transport in the cross-plane direction of superlattices. *Physical Review B* **1998**, *57* (23).
- (57) Rubtsov, I. V.; Burin, A. L. Ballistic and diffusive vibrational energy transport in molecules. *J. Chem. Phys.* **2019**, *150* (2), 020901(020901-020918).
- (58) Hamm, P.; Zanni, M. *Concepts and methods of 2D infrared spectroscopy*; Cambridge University Press 2011.
- (59) Leitner, D. M. Heat Transport in Molecules and Reaction Kinetics: The Role of Quantum Energy Flow and Localization. In *Geometric Structures of Phase Space in Multidimensional Chaos*, Advances in Chemical Physics, 2005; pp 205-256.
- (60) T Elsaesser, a.; Kaiser, W. Vibrational and Vibronic Relaxation of Large Polyatomic Molecules in Liquids. *Annual Review of Physical Chemistry* **1991**, *42* (1), 83-107. DOI: 10.1146/annurev.pc.42.100191.000503.
- (61) Grondin, J.; Lassègues, J.-C.; Cavagnat, D.; Buffeteau, T.; Johansson, P.; Holomb, R. Revisited vibrational assignments of imidazolium-based ionic liquids. *Journal of Raman Spectroscopy* **2011**, *42* (4), 733-743.

- (62) Käß, G.; Schröder, C.; Schwarzer, D. Intramolecular vibrational redistribution and energy relaxation in solution: A molecular dynamics approach. *Physical Chemistry Chemical Physics* **2002**, *4* (2), 271-278, 10.1039/B107256K. DOI: 10.1039/B107256K.
- (63) Deniz, E.; Valiño-Borau, L.; Löffler, J. G.; Eberl, K. B.; Gulzar, A.; Wolf, S.; Durkin, P. M.; Kaml, R.; Budisa, N.; Stock, G.; et al. Through bonds or contacts? Mapping protein vibrational energy transfer using non-canonical amino acids. *Nature Communications* **2021**, *12* (1), 3284. DOI: 10.1038/s41467-021-23591-1.
- (64) Backus, E. H. G.; Nguyen, P. H.; Botan, V.; Moretto, A.; Crisma, M.; Toniolo, C.; Zerbe, O.; Stock, G.; Hamm, P. Structural Flexibility of a Helical Peptide Regulates Vibrational Energy Transport Properties. *The Journal of Physical Chemistry B* **2008**, *112* (48), 15487-15492. DOI: 10.1021/jp806403p.
- (65) Ree, J.; Kim, Y. H.; Shin, H. K. Intramolecular vibrational energy redistribution in nucleobases: Excitation of NH stretching vibrations in adenine–uracil + H<sub>2</sub>O. *The Journal of Chemical Physics* **2022**, *156* (20), 204305. DOI: 10.1063/5.0087289.
- (66) Liu, Y.; Guchhait, B.; Siebert, T.; Fingerhut, B. P.; Elsaesser, T. Molecular couplings and energy exchange between DNA and water mapped by femtosecond infrared spectroscopy of backbone vibrations. *Structural Dynamics* **2017**, *4* (4), 044015. DOI: 10.1063/1.4980075.
- (67) Kaiser, A.; Jayee, B.; Yao, Y.; Ma, X.; Wester, R.; Hase, W. L. Time-Dependent Perspective for the Intramolecular Couplings of the N–H Stretches of Protonated Tryptophan. *The Journal of Physical Chemistry A* **2020**, *124* (20), 4062-4067. DOI: 10.1021/acs.jpca.0c01611.
- (68) Nesbitt, D. J.; Field, R. W. Vibrational Energy Flow in Highly Excited Molecules: Role of Intramolecular Vibrational Redistribution. *The Journal of Physical Chemistry* **1996**, *100* (31), 12735-12756. DOI: 10.1021/jp960698w.
- (69) Karmakar, S.; Keshavamurthy, S. Intramolecular vibrational energy redistribution and the quantum ergodicity transition: a phase space perspective. *Physical Chemistry Chemical Physics* **2020**, *22* (20), 11139-11173, 10.1039/D0CP01413C. DOI: 10.1039/D0CP01413C.
- (70) Kurochkin, D. V.; Naraharisetty, S. R.; Rubtsov, I. V. A relaxation-assisted 2D IR spectroscopy method. *Proc. Natl. Acad. Sci. U.S.A.* **2007**, *104* (36), 14209-14214, Research Support, Non-U.S. Gov't. DOI: 10.1073/pnas.0700560104.
- (71) Leong, T. X.; Collins, B. K.; Dey Baksi, S.; Mackin, R. T.; Sribnyi, A.; Burin, A. L.; Gladysz, J. A.; Rubtsov, I. V. Tracking Energy Transfer across a Platinum Center. *The Journal of Physical Chemistry A* **2022**, *126* (30), 4915-4930. DOI: 10.1021/acs.jpca.2c02017.
- (72) Naraharisetty, S. R. G.; Kasyanenko, V. M.; Rubtsov, I. V. Bond connectivity measured via relaxation-assisted two-dimensional infrared spectroscopy. *The Journal of Chemical Physics* **2008**, *128* (10), 104502. DOI: 10.1063/1.2842071.

- (73) Kasyanenko, V. M.; Tesar, S. L.; Rubtsov, G. I.; Burin, A. L.; Rubtsov, I. V. Structure Dependent Energy Transport: Relaxation-Assisted 2DIR Measurements and Theoretical Studies. *The Journal of Physical Chemistry B* **2011**, *115* (38), 11063-11073. DOI: 10.1021/jp2066315.
- (74) Tesar, S. L.; Kasyanenko, V. M.; Rubtsov, I. V.; Rubtsov, G. I.; Burin, A. L. Theoretical Study of Internal Vibrational Relaxation and Energy Transport in Polyatomic Molecules. *The Journal of Physical Chemistry A* **2013**, *117* (2), 315-323. DOI: 10.1021/jp309481u.
- (75) Rubtsova, N. I.; Nyby, C. M.; Zhang, H.; Zhang, B.; Zhou, X.; Jayawickramarajah, J.; Burin, A. L.; Rubtsov, I. V. Room-temperature ballistic energy transport in molecules with repeating units. *The Journal of Chemical Physics* **2015**, *142* (21), 212412. DOI: 10.1063/1.4916326.
- (76) Rubtsova, N. I.; Qasim, L., N.; Kurnosov, A. A.; Burin, A. L.; Rubtsov, I. V. Ballistic energy transport in oligomers. *Acc. Chem. Res.* **2015**, *48*, 2547-2555. DOI: 10.1021/acs.accounts.5b00299.
- (77) Kim, G.-H.; Lee, D.; Shanker, A.; Shao, L.; Kwon, M. S.; Gidley, D.; Kim, J.; Pipe, K. P. High thermal conductivity in amorphous polymer blends by engineered interchain interactions. *Nature Materials* **2015**, *14* (3), 295-300. DOI: 10.1038/nmat4141.
- (78) Jiji, L. M. *Heat Conduction*; Springer Berlin, Heidelberg, 2009.
- (79) Tesar, S. L.; Kasyanenko, V. M.; Rubtsov, I. V.; Rubtsov, G. I.; Burin, A. L. Theoretical study of internal vibrational relaxation and energy transport in polyatomic molecules. *J. Phys. Chem. A* **2013**, *117* (2), 315-323. DOI: 10.1021/jp309481u.
- (80) Majumdar, A. Microscale Heat Conduction in Dielectric Thin Films. *Journal of Heat Transfer* **1993**, *115* (1).
- (81) Schwarzer, D.; Kutne, P.; Schröder, C.; Troe, J. Intramolecular vibrational energy redistribution in bridged azuleneanthracene compounds: Ballistic energy transport through molecular chains. *Journal of Chemical Physics* **2004**, *121* (4).
- (82) Lin, Z.; Rubtsova, N. I.; Kireev, V. V.; Rubtsov, I. V. Ballistic energy transport in PEG oligomers. In *Series in Chemical Physics*, Chergui, M., Taylor, A., Eds.; Springer: 2012; p in press.
- (83) Qasim, L. N.; Kurnosov, A.; Yue, Y.; Lin, Z.; Burin, A. L.; Rubtsov, I. V. Energy Transport in PEG Oligomers: Contributions of Different Optical Bands. *Journal of Physical Chemistry C* **2016**, *120* (47), 26663-26677. DOI: 10.1021/acs.jpcc.6b09389.
- (84) Rubtsova, N. I.; Rubtsov, I. V. Ballistic energy transport via perfluoroalkane linkers. *Chem. Phys.* **2013**, *422*, 16-21. DOI: 10.1016/j.chemphys.2013.01.026.
- (85) Yue, Y.; Qasim, L., N.; Kurnosov, A. A.; Rubtsova, N. I.; Mackin, R. T.; Zhang, H.; Zhang, B.; Zhou, X.; Jayawickramarajah, J.; Burin, A. L.; et al. Band-Selective Ballistic Energy Transport in Alkane Oligomers: Towards Controlling the Transport Speed. *Journal of Physical Chemistry B* **2015**, *119* (21), 6448-6456. DOI: 10.1021/acs.jpcc.5b03658.

- (86) Wang, H.; Kundu, J.; Halas, N. J. Plasmonic Nanoshell Arrays Combine Surface-Enhanced Vibrational Spectroscopies on a Single Substrate. *Angewandte Chemie International Edition* **2007**, *46* (47), 9040-9044.
- (87) Bochterle, J.; Neubrech, F.; Nagao, T.; Pucci, A. Angstrom-Scale Distance Dependence of Antenna-Enhanced Vibrational Signals. *ACS Nano* **2012**, *6* (12), 10917-10923. DOI: 10.1021/nn304341c.
- (88) Enders, D.; Pucci, A. Surface enhanced infrared absorption of octadecanethiol on wet-chemically prepared Au nanoparticle films. *Applied Physics Letters* **2006**, *88* (18), 184104. DOI: 10.1063/1.2201880.
- (89) Neubrech, F.; Beck, S.; Glaser, T.; Hentschel, M.; Giessen, H.; Pucci, A. Spatial Extent of Plasmonic Enhancement of Vibrational Signals in the Infrared. *ACS Nano* **2014**, *8* (6), 6250-6258. DOI: 10.1021/nn5017204.
- (90) Neubrech, F.; Huck, C.; Weber, K.; Pucci, A.; Giessen, H. Surface-Enhanced Infrared Spectroscopy Using Resonant Nanoantennas. *Chemical Reviews* **2017**, *117* (7), 5110-5145. DOI: 10.1021/acs.chemrev.6b00743.
- (91) Neubrech, F.; Pucci, A.; Cornelius, T. W.; Karim, S.; García-Etxarri, A.; Aizpurua, J. Resonant Plasmonic and Vibrational Coupling in a Tailored Nanoantenna for Infrared Detection. *Physical Review Letters* **2008**, *101* (15), 157403. DOI: 10.1103/PhysRevLett.101.157403.
- (92) Adato, R.; Altug, H. In-situ ultra-sensitive infrared absorption spectroscopy of biomolecule interactions in real time with plasmonic nanoantennas. *Nature Communications* **2013**, *4* (1), 2154. DOI: 10.1038/ncomms3154.
- (93) Homola, J. Surface Plasmon Resonance Sensors for Detection of Chemical and Biological Species. *Chemical Reviews* **2008**, *108* (2), 462-493. DOI: 10.1021/cr068107d.
- (94) Mayer, K. M.; Hafner, J. H. Localized Surface Plasmon Resonance Sensors. *Chemical Reviews* **2011**, *111* (6), 3828-3857. DOI: 10.1021/cr100313v.
- (95) Robelek, R. Surface plasmon resonance sensors in cell biology: basics and application. *Bioanalytical Reviews* **2009**, *1* (1), 57-72. DOI: 10.1007/s12566-009-0005-y.
- (96) Jung, L. S.; Campbell, C. T.; Chinowsky, T. M.; Mar, M. N.; Yee, S. S. Quantitative Interpretation of the Response of Surface Plasmon Resonance Sensors to Adsorbed Films. *Langmuir* **1998**, *14* (19), 5636-5648. DOI: 10.1021/la971228b.
- (97) Gauvreau, B.; Hassani, A.; Fehri, M. F.; Kabashin, A.; Skorobogatiy, M. Photonic bandgap fiber-based Surface Plasmon Resonance sensors. *Opt. Express* **2007**, *15* (18), 11413-11426. DOI: 10.1364/OE.15.011413.
- (98) Bolduc, O. R.; Masson, J.-F. Advances in Surface Plasmon Resonance Sensing with Nanoparticles and Thin Films: Nanomaterials, Surface Chemistry, and Hybrid Plasmonic Techniques. *Analytical Chemistry* **2011**, *83* (21), 8057-8062. DOI: 10.1021/ac2012976.

- (99) Zheng, Y. B.; Yang, Y.-W.; Jensen, L.; Fang, L.; Juluri, B. K.; Flood, A. H.; Weiss, P. S.; Stoddart, J. F.; Huang, T. J. Active Molecular Plasmonics: Controlling Plasmon Resonances with Molecular Switches. *Nano Letters* **2009**, *9* (2), 819-825. DOI: 10.1021/nl803539g.
- (100) Kang, T.; Hong, S.; Choi, I.; Sung, J. J.; Kim, Y.; Hahn, J.-S.; Yi, J. Reversible pH-Driven Conformational Switching of Tethered Superoxide Dismutase with Gold Nanoparticle Enhanced Surface Plasmon Resonance Spectroscopy. *Journal of the American Chemical Society* **2006**, *128* (39), 12870-12878. DOI: 10.1021/ja0632198.
- (101) Grakoui, A.; Bromley, S. K.; Sumen, C.; Davis, M. M.; Shaw, A. S.; Allen, P. M.; Dustin, M. L. The Immunological Synapse: A Molecular Machine Controlling T Cell Activation. *Science* **1999**, *285* (5425), 221-227. DOI: doi:10.1126/science.285.5425.221.
- (102) Lee, S. A.; Link, S. Chemical Interface Damping of Surface Plasmon Resonances. *Accounts of Chemical Research* **2021**, *54* (8), 1950-1960. DOI: 10.1021/acs.accounts.0c00872.
- (103) Hou, W.; Cronin, S. B. A Review of Surface Plasmon Resonance-Enhanced Photocatalysis. *Advanced Functional Materials* **2013**, *23* (13), 1612-1619.
- (104) Rhodes, C.; Franzen, S.; Maria, J.-P.; Losego, M.; Leonard, D. N.; Laughlin, B.; Duscher, G.; Weibel, S. Surface plasmon resonance in conducting metal oxides. *Journal of Applied Physics* **2006**, *100* (5), 054905. DOI: 10.1063/1.2222070.
- (105) Haes, A. J.; Duyne, R. P. V. Preliminary studies and potential applications of localized surface plasmon resonance spectroscopy in medical diagnostics. *Expert Review of Molecular Diagnostics* **2004**, *4* (4), 527-537. DOI: 10.1586/14737159.4.4.527.
- (106) Sciacca, B.; François, A.; Klingler-Hoffmann, M.; Brazzatti, J.; Penno, M.; Hoffmann, P.; Monro, T. M. Radiative-surface plasmon resonance for the detection of apolipoprotein E in medical diagnostics applications. *Nanomedicine: Nanotechnology, Biology and Medicine* **2013**, *9* (4), 550-557.
- (107) Masson, J.-F. Surface Plasmon Resonance Clinical Biosensors for Medical Diagnostics. *ACS Sensors* **2017**, *2* (1), 16-30. DOI: 10.1021/acssensors.6b00763.
- (108) Mariani, S.; Minunni, M. Surface plasmon resonance applications in clinical analysis. *Analytical and Bioanalytical Chemistry* **2014**, *406* (9), 2303-2323. DOI: 10.1007/s00216-014-7647-5.
- (109) Olaru, A.; Bala, C.; Jaffrezic-Renault, N.; Aboul-Encin, H. Y. Surface Plasmon Resonance (SPR) Biosensors in Pharmaceutical Analysis. *Critical Reviews in Analytical Chemistry* **2015**, *45* (2), 97-105. DOI: 10.1080/10408347.2014.881250.
- (110) Rich, R. L.; Myszka, D. G. Advances in surface plasmon resonance biosensor analysis. *Current Opinion in Biotechnology* **2000**, *11* (1), 54-61.
- (111) Homola, J. Present and future of surface plasmon resonance biosensors. *Analytical and Bioanalytical Chemistry* **2003**, *377* (3), 528-539. DOI: 10.1007/s00216-003-2101-0.

- (112) Myszka, D. G.; Rich, R. L. Implementing surface plasmon resonance biosensors in drug discovery. *Pharmaceutical Science & Technology Today* **2000**, *3* (9), 310-317.
- (113) Osawa, M.; Kuramitsu, M.; Hatta, A.; Suëtaka, W.; Seki, H. Electromagnetic effect in enhanced infrared absorption of adsorbed molecules on thin metal films. *Surface Science Letters* **1986**, *175* (3), L787-L793.
- (114) Osawa, M.; Ikeda, M. Surface-enhanced infrared absorption of p-nitrobenzoic acid deposited on silver island films: contributions of electromagnetic and chemical mechanisms. *The Journal of Physical Chemistry* **1991**, *95* (24), 9914-9919. DOI: 10.1021/j100177a056.
- (115) Dregely, D.; Neubrech, F.; Duan, H.; Vogelgesang, R.; Giessen, H. Vibrational near-field mapping of planar and buried three-dimensional plasmonic nanostructures. *Nature Communications* **2013**, *4* (1), 2237. DOI: 10.1038/ncomms3237.
- (116) Daniel, M.-C.; Astruc, D. Gold Nanoparticles: Assembly, Supramolecular Chemistry, Quantum-Size-Related Properties, and Applications toward Biology, Catalysis, and Nanotechnology. *Chemical Reviews* **2004**, *104* (1), 293-346. DOI: 10.1021/cr030698+.
- (117) Xia, Y.; Halas, N. J. Shape-Controlled Synthesis and Surface Plasmonic Properties of Metallic Nanostructures. *MRS Bulletin* **2005**, *30* (5), 338-348. DOI: 10.1557/mrs2005.96.
- (118) Haes, A. J.; Haynes, C. L.; McFarland, A. D.; Schatz, G. C.; Van Duyne, R. P.; Zou, S. Plasmonic Materials for Surface-Enhanced Sensing and Spectroscopy. *MRS Bulletin* **2005**, *30* (5), 368-375. DOI: 10.1557/mrs2005.100.
- (119) Frontmatter. In *Absorption and Scattering of Light by Small Particles*, 1998; pp i-xiv.
- (120) Kumbhar, A. S.; Kinnan, M. K.; Chumanov, G. Multipole Plasmon Resonances of Submicron Silver Particles. *Journal of the American Chemical Society* **2005**, *127* (36), 12444-12445. DOI: 10.1021/ja053242d.
- (121) Millstone, J. E.; Park, S.; Shuford, K. L.; Qin, L.; Schatz, G. C.; Mirkin, C. A. Observation of a Quadrupole Plasmon Mode for a Colloidal Solution of Gold Nanoprisms. *Journal of the American Chemical Society* **2005**, *127* (15), 5312-5313. DOI: 10.1021/ja043245a.
- (122) Shuford, K. L.; Ratner, M. A.; Schatz, G. C. Multipolar excitation in triangular nanoprisms. *The Journal of Chemical Physics* **2005**, *123* (11), 114713. DOI: 10.1063/1.2046633.
- (123) Kelly, K. L.; Coronado, E.; Zhao, L. L.; Schatz, G. C. The Optical Properties of Metal Nanoparticles: The Influence of Size, Shape, and Dielectric Environment. *The Journal of Physical Chemistry B* **2003**, *107* (3), 668-677. DOI: 10.1021/jp026731y.
- (124) Krenn, J. R.; Schider, G.; Rechberger, W.; Lamprecht, B.; Leitner, A.; Aussenegg, F. R.; Weeber, J. C. Design of multipolar plasmon excitations in silver nanoparticles. *Applied Physics Letters* **2000**, *77* (21), 3379-3381. DOI: 10.1063/1.1327615.

- (125) Jain, P. K.; Lee, K. S.; El-Sayed, I. H.; El-Sayed, M. A. Calculated Absorption and Scattering Properties of Gold Nanoparticles of Different Size, Shape, and Composition: Applications in Biological Imaging and Biomedicine. *The Journal of Physical Chemistry B* **2006**, *110* (14), 7238-7248. DOI: 10.1021/jp057170o.
- (126) Murphy, C. J.; Sau, T. K.; Gole, A. M.; Orendorff, C. J.; Gao, J.; Gou, L.; Hunyadi, S. E.; Li, T. Anisotropic Metal Nanoparticles: Synthesis, Assembly, and Optical Applications. *The Journal of Physical Chemistry B* **2005**, *109* (29), 13857-13870. DOI: 10.1021/jp0516846.
- (127) Sun, Y.; Xia, Y. Shape-Controlled Synthesis of Gold and Silver Nanoparticles. *Science* **2002**, *298* (5601), 2176-2179. DOI: doi:10.1126/science.1077229.
- (128) Dirac, P. A. M. The quantum theory of the emission and absorption of radiation. *Proceedings of the Royal Society A* **1927**, *114* (767).
- (129) Spence, D. E.; Kean, P. N.; Sibbett, W. 60-fsec pulse generation from a self-mode-locked Ti:sapphire laser. *Opt. Lett.* **1991**, *16* (1), 42-44. DOI: 10.1364/OL.16.000042.
- (130) Verma, P. K.; Kundu, A.; Poretz, M. S.; Dhoonmoon, C.; Chegwidan, O. S.; Londergan, C. H.; Cho, M. The Bend+Libration Combination Band Is an Intrinsic, Collective, and Strongly Solute-Dependent Reporter on the Hydrogen Bonding Network of Liquid Water. *The Journal of Physical Chemistry B* **2018**, *122* (9), 2587-2599. DOI: 10.1021/acs.jpcc.7b09641.
- (131) Hamm, P.; Lim, M.; Hochstrasser, R. M. Structure of the Amide I Band of Peptides Measured by Femtosecond Nonlinear-Infrared Spectroscopy. *The Journal of Physical Chemistry B* **1998**, *102* (31), 6123-6138. DOI: 10.1021/jp9813286.
- (132) Asplund, M. C.; Zanni, M. T.; Hochstrasser, R. M. Two-dimensional infrared spectroscopy of peptides by phase-controlled femtosecond vibrational photon echoes. *Proceedings of the National Academy of Sciences* **2000**, *97* (15), 8219-8224. DOI: doi:10.1073/pnas.140227997.
- (133) Rubtsova, N. I.; Lin, Z.; Mackin, R. T.; Rubtsov, I. V. How Intramolecular Vibrational Energy Transport Changes with Rigidity and Polarity of the Environment? . *High Energy Chemistry* **2020**, *54* (6), 427-435
- (134) Leger, J. D.; Nyby, C. M.; Varner, C.; Tang, J.; Rubtsova, N. I.; Yue, Y.; Kireev, V. V.; Burtsev, V. D.; Qasim, L. N.; Rubtsov, G. I.; et al. Fully automated dual-frequency three-pulse-echo 2DIR spectrometer accessing spectral range from 800 to 4000 wavenumbers. *Review of Scientific Instruments* **2014**, *85* (8), 083109. DOI: 10.1063/1.4892480.
- (135) Nyby, C. M.; Leger, J. D.; Tang, J.; Varner, C.; Kireev, V. V.; Rubtsov, I. V. Mid-IR beam direction stabilization scheme for vibrational spectroscopy, including dual-frequency 2DIR. *Opt. Express* **2014**, *22* (6), 6801-6809. DOI: 10.1364/OE.22.006801.
- (136) Nyby, C. M.; Leger, J. D.; Tang, J.; Varner, C.; Kireev, V. V.; Rubtsov, I. V. Mid-IR beam direction stabilization scheme for vibrational spectroscopy, including dual-frequency 2DIR. *Opt. Express* **2014**, *22* (6), 6801-6809. DOI: 10.1364/OE.22.006801.

- (137) Qasim, L. N.; Atuk, E. B.; Maksymov, A. O.; Jayawickramarajah, J.; Burin, A. L.; Rubtsov, I. V. Ballistic Transport of Vibrational Energy through an Amide Group Bridging Alkyl Chains. *Journal of Physical Chemistry C* **2019**, *123*, 3381-3392. DOI: 10.1021/acs.jpcc.8b11570.
- (138) Rubtsova, N. I.; Kurnosov, A. A.; Burin, A. L.; Rubtsov, I. V. Temperature dependence of the ballistic energy transport in perfluoroalkanes. *J. Phys. Chem. B* **2014**, *118* (28), 8381-8387.
- (139) Lin, Z.; Zhang, N.; Jayawickramarajah, J.; Rubtsov, I. V. Ballistic energy transport along PEG chains: distance dependence of the transport efficiency. *Physical Chemistry Chemical Physics* **2012**, *14* (30), 10445-10454. DOI: 10.1039/c2cp40187h.
- (140) Robert T. Mackin, T. X. L., Natalia I. Rubtsova, Alexander L. Burin, and Igor V. Rubtsov. Low-Temperature Vibrational Energy Transport via PEG Chains. *Journal of Physical Chemistry Letters* **2020**, *11*, 4578-4583.
- (141) Skotheim, T. A.; Elsenbaumer, R. L.; Reynolds, J. R. *Handbook of Conducting Polymers Marcel*; 1998.
- (142) Gustafsson, G.; Cao, Y.; Treacy, G. M.; Klavetter, F.; Colaneri, N.; Heeger, A. J. Flexible light-emitting diodes made from soluble conducting polymers. *Nature* **1992**, *357* (6378), 477-479. DOI: 10.1038/357477a0.
- (143) Burin, A. L.; Tesar, S. L.; Kasyanenko, V. M.; Rubtsov, I. V.; Rubtsov, G. I. Semiclassical model for vibrational dynamics of polyatomic molecules: Investigation of Internal Vibrational Relaxation. *J. Phys. Chem. C* **2010**, *114* (48), 20510-20517.
- (144) Zerbi, G. Z. a. G. Lattice dynamics and vibrational spectra of undoped and doped polyparaphenylene. *The Journal of Chemical Physics* **1985**, *82* (31).
- (145) Fayer, M. D. *Elements of quantum mechanics*; 2001.
- (146) Fayer, M. D. *Elements of quantum mechanics*; Oxford University Press, 2001.
- (147) Pein, B. C.; Dlott, D. D. Modifying Vibrational Energy Flow in Aromatic Molecules: Effects of Ortho Substitution. *J. Phys. Chem. A* **2014**, *118* (6), 965-973. DOI: 10.1021/jp4120546.
- (148) Boulatov, A.; Burin, A. L. Crucial effect of transverse vibrations on the transport through polymer chains. *The Journal of chemical physics* **2020**, *153* (13), 134102. DOI: 10.1063/5.0018591.
- (149) Kurnosov, A. A.; Rubtsov, I. V.; Burin, A. L. Fast transport and relaxation of vibrational energy in polymer chains. *J. Chem. Phys.* **2015**, *142* (1), 011101.
- (150) Naraharisetty, S. G.; Kasyanenko, V. M.; Rubtsov, I. V. Bond connectivity measured via relaxation-assisted two-dimensional infrared spectroscopy. *J. Chem. Phys.* **2008**, *128*, 104502.
- (151) Yue, Y.; Qasim, L. N.; Kurnosov, A. A.; Rubtsova, N. I.; Mackin, R. T.; Zhang, H.; Zhang, B.; Zhou, X.; Jayawickramarajah, J.; Burin, A. L.; et al. Band-selective ballistic energy transport in alkane oligomers: toward controlling the transport speed. *J. Phys. Chem. B* **2015**, *119* (21), 6448-6456. DOI: 10.1021/acs.jpcc.5b03658.

- (152) Lin, Z.; Zhang, N.; Jayawickramarajah, J.; Rubtsov, I. V. Ballistic energy transport along PEG chains: distance dependence of the transport efficiency. *Phys. Chem. Chem. Phys.* **2012**, *14* (30), 10445-10454. DOI: 10.1039/c2cp40187h.
- (153) Shen, S.; Henry, A.; Tong, J.; Zheng, R.; Chen, G. Polyethylene nanofibres with very high thermal conductivities. *Nature Nanotechnology* **2010**, *5* (4), 251-255. DOI: 10.1038/nnano.2010.27.
- (154) Gruebele, M.; Wolynes, P. G. Vibrational Energy Flow and Chemical Reactions. *Accounts of Chemical Research* **2004**, *37* (4), 261-267. DOI: 10.1021/ar030230t.
- (155) Wei, X.; Luo, T. A phonon wave packet study of thermal energy transport across functionalized hard-soft interfaces. *Journal of Applied Physics* **2019**, *126* (1), 015301. DOI: 10.1063/1.5095775.
- (156) Xu, Y.; Wang, X.; Zhou, J.; Song, B.; Jiang, Z.; Lee, E. M. Y.; Huberman, S.; Gleason, K. K.; Chen, G. Molecular engineered conjugated polymer with high thermal conductivity. *Science Advances* **2018**, *4* (3), eaar3031. DOI: doi:10.1126/sciadv.aar3031.
- (157) Segal, D.; Nitzan, A.; Hänggi, P. Thermal conductance through molecular wires. *The Journal of Chemical Physics* **2003**, *119* (13), 6840-6855. DOI: 10.1063/1.1603211.
- (158) Nguyen, S. S.; Prescher, J. A. Developing bioorthogonal probes to span a spectrum of reactivities. *Nature Reviews Chemistry* **2020**, *4* (9), 476-489. DOI: 10.1038/s41570-020-0205-0.
- (159) Hoven, C. V.; Yang, R.; Garcia, A.; Crockett, V.; Heeger, A. J.; Bazan, G. C.; Nguyen, T.-Q. Electron injection into organic semiconductor devices from high work function cathodes. *Proceedings of the National Academy of Sciences* **2008**, *105* (35), 12730-12735. DOI: doi:10.1073/pnas.0806494105.
- (160) Watson, D. F.; Meyer, G. J. ELECTRON INJECTION AT DYE-SENSITIZED SEMICONDUCTOR ELECTRODES. *Annual Review of Physical Chemistry* **2005**, *56* (1), 119-156. DOI: 10.1146/annurev.physchem.56.092503.141142.
- (161) Gonçalves, J. M.; Kumar, A.; da Silva, M. I.; Toma, H. E.; Martins, P. R.; Araki, K.; Bertotti, M.; Angnes, L. Nanoporous Gold-Based Materials for Electrochemical Energy Storage and Conversion. *Energy Technology* **2021**, *9* (5), 2000927.
- (162) Alagiri, M.; Rameshkumar, P.; Pandikumar, A. Gold nanorod-based electrochemical sensing of small biomolecules: A review. *Microchimica Acta* **2017**, *184* (9), 3069-3092. DOI: 10.1007/s00604-017-2418-6.
- (163) Dembinski, R.; Bartik, T.; Bartik, B.; Jaeger, M.; Gladysz, J. A. Toward Metal-Capped One-Dimensional Carbon Allotropes: Wirelike C<sub>6</sub>-C<sub>20</sub> Polyyne-diyl Chains That Span Two Redox-Active ( $\eta^5$ -C<sub>5</sub>Me<sub>5</sub>)Re(NO)(PPh<sub>3</sub>) Endgroups. *J Am Chem Soc* **2000**, *122* (5), 810-822. DOI: 10.1021/ja992747z.
- (164) Zheng, Q.; Bohling, J. C.; Peters, T. B.; Frisch, A. C.; Hampel, F.; Gladysz, J. A. A Synthetic Breakthrough into an Unanticipated Stability Regime: A Series of Isolable Complexes in which C<sub>6</sub>,

C8, C10, C12, C16, C20, C24, and C28 Polyynediyl Chains Span Two Platinum Atoms. *Chem. Eur. J.* **2006**, *12* (25), 6486-6505.

(165) Gauthier, S.; Weisbach, N.; Bhuvanesh, N.; Gladysz, J. A. "Click" Chemistry in Metal Coordination Spheres: Copper(I)-Catalyzed 3+2 Cycloadditions of Benzyl Azide and Platinum Polyynyl Complexes  $\text{trans}-(\text{C}_6\text{F}_5)(\text{p-tol}_3\text{P})_2\text{Pt}(\text{C}\equiv\text{C})_n\text{H}$  ( $n = 2-6$ ). *Organometallics* **2009**, *28* (19), 5597-5599. DOI: 10.1021/om900680q.

(166) Zheng, Q.; Schneider, J. F.; Amini, H.; Hampel, F.; Gladysz, J. A. Wire like diplatinum, triplatinum, and tetraplatinum complexes featuring  $\text{X}[\text{PtC}\equiv\text{CC}\equiv\text{CC}\equiv\text{CC}\equiv\text{C}]_m\text{PtX}$  segments; iterative syntheses and functionalization for measurements of single molecule properties. *Dalton Trans.* **2019**, *48* (17), 5800-5816, 10.1039/C9DT00870E. DOI: 10.1039/C9DT00870E.

(167) Weisbach, N.; Kuhn, H.; Amini, H.; Ehnbohm, A.; Hampel, F.; Reibenspies, J. H.; Hall, M. B.; Gladysz, J. A. Triisopropylsilyl (TIPS) Alkynes as Building Blocks for Syntheses of Platinum Triisopropylsilylpolyynyl and Diplatinum Polyynediyl Complexes. *Organometallics* **2019**, *38* (17), 3294-3310. DOI: 10.1021/acs.organomet.9b00368.

(168) Amini, H.; Baranová, Z.; Weisbach, N.; Gauthier, S.; Bhuvanesh, N.; Reibenspies, J. H.; Gladysz, J. A. Syntheses, Structures, and Spectroscopic Properties of 1,10-Phenanthroline-Based Macrocycles Threaded by PtC8Pt, PtC12Pt, and PtC16Pt Axles: Metal-Capped Rotaxanes as Insulated Molecular Wires. *Chem. Eur. J.* **2019**, *25* (69), 15896-15914.

(169) Amini, H.; Weisbach, N.; Gauthier, S.; Kuhn, H.; Bhuvanesh, N.; Hampel, F.; Reibenspies, J. H.; Gladysz, J. A. Trapping of Terminal Platinapolyynes by Copper(I) Catalyzed Click Cycloadditions; Probes of Labile Intermediates in Syntheses of Complexes with Extended sp Carbon Chains, and Crystallographic Studies. *Chem. Eur. J.* **2021**, *27* (49), 12619-12634.

(170) Bruce, M. I.; Zaitseva, N. N.; Nicholson, B. K.; Skelton, B. W.; White, A. H. Syntheses and molecular structures of some compounds containing many-atom chains end-capped by tricobalt carbonyl clusters. *J. Organomet. Chem.* **2008**, *693* (17), 2887-2897, Journal Article. DOI: DOI:10.1016/j.jorganchem.2008.06.007.

(171) Cao, Z.; Xi, B.; Jodoin, D. S.; Zhang, L.; Cummings, S. P.; Gao, Y.; Tyler, S. F.; Fanwick, P. E.; Crutchley, R. J.; Ren, T. Diruthenium-Polyyn-diyl-Diruthenium Wires: Electronic Coupling in the Long Distance Regime. *J Am Chem Soc* **2014**, *136* (34), 12174-12183. DOI: 10.1021/ja507107t.

(172) Bruce, M. I.; Cole, M. L.; Ellis, B. G.; Gaudio, M.; Nicholson, B. K.; Parker, C. R.; Skelton, B. W.; White, A. H. The series of carbon-chain complexes  $\{\text{Ru}(\text{dppe})\text{Cp}^*\}_2\{\mu\text{-(CC)}_x\}$  ( $x=4-8, 11$ ): Synthesis, structures, properties and some reactions. *Polyhedron* **2015**, *86*, 43-56.

(173) Sappa, E.; Tiripicchio, A.; Braunstein, P. Alkyne-substituted homo- and heterometallic carbonyl clusters of the iron, cobalt and nickel triads. *Chem. Rev* **1983**, *83* (3), 203-239.

(174) Conole, G. The bonding modes adopted by organo-fragments on metal cluster surfaces. *Mater. Chem. Phys* **1991**, *29* (1-4), 307-322.

- (175) Falloon, S. B.; Szafert, S.; Arif, A. M.; Gladysz, J. A. Attaching Metal-Capped sp Carbon Chains to Metal Clusters: Synthesis, Structure, and Reactivity of Rhenium/Triosmium Complexes of Formula  $[(\eta^5\text{-C}_5\text{Me}_5)\text{Re}(\text{NO})(\text{PPh}_3)(\text{CC})_n\text{Os}_3(\text{CO})_y(\text{X})_z]_m^+$ , Including Carbon Geometries More Distorted than Planar Tetracoordinate. *Chem. Eur. J.* **1998**, *4* (6), 1033-1042.
- (176) Sánchez-Cabrera, G.; Zuno-Cruz, F. J.; Rosales-Hoz, M. J. Reactivity of Alkyne-Substituted Transition Metal Clusters: An Overview. *J. Clust. Sci.* **2014**, *25*, 51–82.
- (177) Zhang, S.; Ocheje, M. U.; Huang, L.; Galuska, L.; Cao, Z.; Luo, S.; Cheng, Y.-H.; Ehlenberg, D.; Goodman, R. B.; Zhou, D.; et al. The Critical Role of Electron-Donating Thiophene Groups on the Mechanical and Thermal Properties of Donor–Acceptor Semiconducting Polymers. *Advanced Electronic Materials* **2019**, *5* (5).
- (178) Akita, M.; Tanaka, Y. Carbon-rich organometallics: Application to molecular electronics. *Coord. Chem. Rev.* **2022**, *461*, 214501.
- (179) Gasser, G.; Ott, I.; Metzler-Nolte, N. Organometallic Anticancer Compounds. *J. Med. Chem.* **2011**, *54* (1), 3-25.
- (180) Yau, S. H.; Ashenfelter, B. A.; Desiredy, A.; Ashwell, A. P.; Varnavski, O.; Schatz, G. C.; Bigioni, T. P.; Goodson, T. Optical Properties and Structural Relationships of the Silver Nanoclusters  $\text{Ag}_{32}(\text{SG})_{19}$  and  $\text{Ag}_{15}(\text{SG})_{11}$ . *J. Phys. Chem. C* **2017**, *121* (2), 1349–1361.
- (181) Li, F.; Carpenter, S. H.; Higgins, R. F.; Hitt, M. G.; Brennessel, W. W.; Ferrier, M. G.; Cary, S. K.; Lezama-Pacheco, J. S.; Wright, J. T.; Stein, B. W.; et al. Polyoxovanadate–Alkoxide Clusters as a Redox Reservoir for Iron. *Inorg. Chem.* **2017**, *56*, 7065–7080.
- (182) Zheng, M. L.; Zheng, D. C.; Wang, J. Non-Native Side Chain IR Probe in Peptides: Ab Initio Computation and 1D and 2D IR Spectral Simulation. *J. Phys. Chem. B* **2010**, *114*, 2327–2336.
- (183) Lin, Z.; Rubtsov, I. V. Constant-speed vibrational signaling along polyethyleneglycol chain up to 60-Å distance. *Proc. Natl. Acad. Sci. U.S.A.* **2012**, *109* (5), 1413-1418. DOI: 10.1073/pnas.1116289109.
- (184) Yue, Y.; Qasim, L. N.; Kurnosov, A. A.; Rubtsova, N. I.; Mackin, R. T.; Zhang, H.; Zhang, B.; Zhou, X.; Jayawickramarajah, J.; Burin, A. L.; et al. Band-selective ballistic energy transport in alkane oligomers: toward controlling the transport speed. *J. Phys. Chem. B* **2015**, *119* (21), 6448-6456. DOI: 10.1021/acs.jpcc.5b03658.
- (185) Leong, T. X.; Qasim, L. N.; Mackin, R. T.; Du, Y.; Jr., R. A. P.; Rubtsov, I. V. Unidirectional coherent energy transport via conjugated oligo(p-phenylene) chains. *J. Chem. Phys.* **2021**, *154* (13), 134304. DOI: 10.1063/5.0046932.
- (186) Albinsson, B.; Eng, M. P.; Pettersson, K.; Winters, M. U. Electron and energy transfer in donor–acceptor systems with conjugated molecular bridges. *Physical Chemistry Chemical Physics* **2007**, *9* (44), 5847-5864, 10.1039/B706122F. DOI: 10.1039/B706122F.

- (187) Lin, Z.; Lawrence, C. M.; Xiao, D.; Kireev, V. V.; Skourtis, S. S.; Sessler, J. L.; Beratan, D. N.; Rubtsov, I. V. Modulating unimolecular charge transfer by exciting bridge vibrations. *J. Am. Chem. Soc.* **2009**, *131* (50), 18060-18062, Research Support, Non-U.S. Support, U.S. Gov't, Non-P.H.S. DOI: 10.1021/ja907041t.
- (188) Delor, M.; Scattergood, P. A.; Sazanovich, I. V.; Parker, A. W.; Greetham, G. M.; Meijer, A. J.; Towrie, M.; Weinstein, J. A. Toward control of electron transfer in donor-acceptor molecules by bond-specific infrared excitation. *Science* **2014**, *346* (6216), 1492-1495, Research Support, Non-U.S. Gov't. DOI: 10.1126/science.1259995.
- (189) Yue, Y.; Grusenmeyer, T.; Ma, Z.; Zhang, P.; Schmechl, R. H.; Beratan, D. N.; Rubtsov, I. V. Electron transfer rate modulation in a compact Re(i) donor-acceptor complex. *Dalton Trans.* **2015**, *44*, 8609-8616. DOI: 10.1039/c4dt02145b.
- (190) Fujii, N.; Mizuno, M.; Ishikawa, H.; Mizutani, Y. Observing Vibrational Energy Flow in a Protein with the Spatial Resolution of a Single Amino Acid Residue. *J. Phys. Chem. Lett.* **2014**, *5* (18), 3269-3273. DOI: 10.1021/jz501882h.
- (191) Chergui, M. Ultrafast Photophysics of Transition Metal Complexes. *Acc. Chem. Res.* **2015**, *48* (3), 801-808. DOI: 10.1021/ar500358q.
- (192) Mizuno, M.; Mizutani, Y. Role of atomic contacts in vibrational energy transfer in myoglobin. *Biophys. Rev.* **2020**, *12* (2), 511-518. DOI: 10.1007/s12551-020-00681-w PubMed.
- (193) Schmitz, A. J.; Pandey, H. D.; Chalyavi, F.; Shi, T.; Fenlon, E. E.; Brewer, S. H.; Leitner, D. M.; Tucker, M. J. Tuning Molecular Vibrational Energy Flow within an Aromatic Scaffold via Anharmonic Coupling. *J. Phys. Chem. A* **2019**, *123* (49), 10571-10581. DOI: 10.1021/acs.jpca.9b08010.
- (194) Rubtsova, N. I.; Rubtsov, I. V. Vibrational energy transport in molecules studied by relaxation-assisted two-dimensional infrared spectroscopy. *Ann. Rev. Phys. Chem.* **2015**, *66*, 717-738.
- (195) Backus, E. H. G.; Bloem, R.; Pfister, R.; Moretto, A.; Crisma, M.; Toniolo, C.; Hamm, P. Dynamical Transition in a Small Helical Peptide and Its Implication for Vibrational Energy Transport. *J. Phys. Chem. B* **2009**, *113*, 13405-13409.
- (196) Yang, X.; Keane, T.; Delor, M.; Meijer, A. J. H. M.; Weinstein, J.; Bittner, E. R. Identifying electron transfer coordinates in donor-bridge-acceptor systems using mode projection analysis. *Nature Communications* **2017**, *8* (1), 14554. DOI: 10.1038/ncomms14554.
- (197) Kasyanenko, V. M.; Lin, Z.; Rubtsov, G. I.; Donahue, J. P.; Rubtsov, I. V. Energy transport via coordination bonds. *J. Chem. Phys.* **2009**, *131*, 154508.
- (198) Sazanovich, I. V.; Best, J.; Scattergood, P. A.; Towrie, M.; Tikhomirov, S. A.; Bouganov, O. V.; Meijer, A. J. H. M.; Weinstein, J. A. Ultrafast photoinduced charge transport in Pt(ii) donor-acceptor assembly bearing naphthalimide electron acceptor and phenothiazine electron donor. *Physical Chemistry Chemical Physics* **2014**, *16* (47), 25775-25788, 10.1039/C4CP03995E. DOI: 10.1039/C4CP03995E.

- (199) Fedoseeva, M.; Delor, M.; Parker, S. C.; Sazanovich, I. V.; Towrie, M.; Parker, A. W.; Weinstein, J. A. Vibrational energy transfer dynamics in ruthenium polypyridine transition metal complexes. *Physical Chemistry Chemical Physics* **2015**, *17* (3), 1688-1696, 10.1039/C4CP04166F. DOI: 10.1039/C4CP04166F.
- (200) Heilweil, E. J.; Cavanagh, R. R.; Stephenson, J. C. CO( $v=1$ ) population lifetimes of metal-carbonyl cluster compounds in dilute CHCl<sub>3</sub> solution. *The Journal of Chemical Physics* **1988**, *89* (1), 230-239. DOI: 10.1063/1.455510.
- (201) Crum, V. F.; Kiefer, L. M.; Kubarych, K. J. Ultrafast vibrational dynamics of a solute correlates with dynamics of the solvent. *The Journal of Chemical Physics* **2021**, *155* (13), 134502. DOI: 10.1063/5.0061770.
- (202) Eckert, P. A.; Kubarych, K. J. Solvent Quality Controls Macromolecular Structural Dynamics of a Dendrimeric Hydrogenase Model. *The Journal of Physical Chemistry B* **2018**, *122* (50), 12154-12163. DOI: 10.1021/acs.jpcc.8b07259.
- (203) Kiefer, L. M.; Kubarych, K. J. Two-dimensional infrared spectroscopy of coordination complexes: From solvent dynamics to photocatalysis. *Coordination Chemistry Reviews* **2018**, *372*, 153-178.
- (204) Kiefer, L. M.; Kubarych, K. J. Solvent-Dependent Dynamics of a Series of Rhenium Photoactivated Catalysts Measured with Ultrafast 2DIR. *The Journal of Physical Chemistry A* **2015**, *119* (6), 959-965. DOI: 10.1021/jp511686p.
- (205) Segal, D.; Agarwalla, B. K. Vibrational Heat Transport in Molecular Junctions. *Ann. Rev. Phys. Chem.* **2016**, *67* (1), 185-209. DOI: 10.1146/annurev-physchem-040215-112103.
- (206) Galperin, M.; Ratner, M.; Nitzan, A. Molecular transport junctions: vibrational effects. *J. Phys. Condensed Matter* **2007**, *19*, 103201.
- (207) Leitner, D. M.; Pandey, H. D.; Reid, K. M. Energy Transport across Interfaces in Biomolecular Systems. *J. Phys. Chem. B* **2019**, *123* (45), 9507-9524. DOI: 10.1021/acs.jpcc.9b07086.
- (208) Pandey, H. D.; Leitner, D. M. Influence of thermalization on thermal conduction through molecular junctions: Computational study of PEG oligomers. *J. Chem. Phys.* **2017**, *147* (8), 084701. DOI: 10.1063/1.4999411.
- (209) Chen, R.; Sharony, I.; Nitzan, A. Local Atomic Heat Currents and Classical Interference in Single-Molecule Heat Conduction. *J. Phys. Chem. Lett.* **2020**, *11* (11), 4261-4268. DOI: 10.1021/acs.jpclett.0c00471.
- (210) Khalil, M.; Demirdoven, N.; Tokmakoff, A. Vibrational coherence transfer characterized with Fourier-transform 2D IR spectroscopy. *J. Chem. Phys.* **2004**, *121* (1), 362-373.
- (211) Chesnoy, J.; Mokhtari, A. Resonant impulsive-stimulated Raman scattering on malachite green. *Phys. Rev. A* **1988**, *38*, 3566-3576.

- (212) Rubtsov, I. V.; Yoshihara, K. Oscillatory Fluorescence Decay of an Electron Donor-Acceptor Complex. *J. Phys. Chem. A* **1997**, *101*, 6138-6140.
- (213) Rosca, F.; Kumar, A. T. N.; Ye, X.; Sjodin, T.; Demidov, A. A.; Champion, P. M. Investigations of Coherent Vibrational Oscillations in Myoglobin. *J. Phys. Chem. A* **2000**, *104*, 4280-4290.
- (214) Arpin, P. C.; Turner, D. B.; McClure, S. D.; Jumper, C. C.; Mirkovic, T.; Challa, J. R.; Lee, J.; Teng, C. Y.; Green, B. R.; Wilk, K. E.; et al. Spectroscopic Studies of Cryptophyte Light Harvesting Proteins: Vibrations and Coherent Oscillations. *The Journal of Physical Chemistry B* **2015**, *119* (31), 10025–10034.
- (215) Rubtsov, I. V.; Yoshihara, K. Vibrational Coherence in Electron Donor-Acceptor Complexes. *J. Phys. Chem. A* **1999**, *103*, 10202-10212.
- (216) Grant, C. D.; Schwartzberg, A. M.; Norman, T. J.; Zhang, J. Z. Ultrafast Electronic Relaxation and Coherent Vibrational Oscillation of Strongly Coupled Gold Nanoparticle Aggregates. *J. Am. Chem. Soc.* **2003**, *125* (2), 549–553.
- (217) Rubtsova, N. I.; Qasim, L., N.; Kurnosov, A. A.; Burin, A. L.; Rubtsov, I. V. Ballistic energy transport in oligomers. *Acc. Chem. Res.* **2015**, *48*, 2547-2555. DOI: 10.1021/acs.accounts.5b00299.
- (218) Dunkelberger, E. B.; Grechko, M.; Zanni, M. T. Transition Dipoles from 1D and 2D Infrared Spectroscopy Help Reveal the Secondary Structures of Proteins: Application to Amyloids. *The Journal of Physical Chemistry B* **2015**, *119* (44), 14065-14075. DOI: 10.1021/acs.jpcc.5b07706.
- (219) Rubtsova, N. I.; Lin, Z.; Mackin, R. T.; Rubtsov, I. V. How Intramolecular Vibrational Energy Transport Changes with Rigidity and Polarity of the Environment? *High Energy Chem.* **2020**, *54* (6), 427–435.
- (220) Nee, M. J.; Baiz, C. R.; Anna, J. M.; McCanne, R.; Kubarych, K. J. Multilevel vibrational coherence transfer and wavepacket dynamics probed with multidimensional IR spectroscopy. *J. Chem. Phys.* **2008**, *129* (8), 084503/084501-084503/084511.
- (221) Eckert, P. A.; Kubarych, K. J. Vibrational coherence transfer illuminates dark modes in models of the FeFe hydrogenase active site. *J. Chem. Phys.* **2019**, *151* (5), 054307. DOI: 10.1063/1.5111016.
- (222) Dybal, J.; Krimm, S. Dipole derivatives and infrared intensities of the ester group. An ab initio and force field study of methyl acetate. *J. Mol. Struct.* **1988**, *189*, 383-392.
- (223) Müller-Werkmeister, H. M.; Li, Y.-L.; Lerch, E.-B. W.; Bigourd, D.; Bredenbeck, J. Ultrafast Hopping from Band to Band: Assigning Infrared Spectra based on Vibrational Energy Transfer. *Angew. Chem. Int. Ed.* **2013**, *52* (24), 6214-6217. DOI: doi:10.1002/anie.201209916.
- (224) Eckert, P. A.; Kubarych, K. J. Vibrational coherence transfer illuminates dark modes in models of the FeFe hydrogenase active site. *The Journal of Chemical Physics* **2019**, *151* (5), 054307. DOI: 10.1063/1.5111016.

- (225) Greve, C.; Preketes, N. K.; Costard, R.; Koeppe, B.; Fidder, H.; Nibbering, E. T. J.; Temps, F.; Mukamel, S.; Elsaesser, T. N–H Stretching Modes of Adenosine Monomer in Solution Studied by Ultrafast Nonlinear Infrared Spectroscopy and Ab Initio Calculations. *The Journal of Physical Chemistry A* **2012**, *116* (29), 7636-7644. DOI: 10.1021/jp303864m.
- (226) Marroux, H. J. B.; Orr-Ewing, A. J. Distinguishing Population and Coherence Transfer Pathways in a Metal Dicarbonyl Complex Using Pulse-Shaped Two-Dimensional Infrared Spectroscopy. *The Journal of Physical Chemistry B* **2016**, *120* (17), 4125-4130. DOI: 10.1021/acs.jpcc.6b02979.
- (227) Rose, P. A.; Krich, J. J. Automatic Feynman diagram generation for nonlinear optical spectroscopies and application to fifth-order spectroscopy with pulse overlaps. *The Journal of Chemical Physics* **2021**, *154* (3), 034109. DOI: 10.1063/5.0024105.
- (228) Weiner, A. M. Ultrafast optical pulse shaping: A tutorial review. *Optics Communications* **2011**, *284* (15), 3669-3692.
- (229) Nishida, J.; Tamimi, A.; Fei, H.; Pullen, S.; Ott, S.; Cohen, S. M.; Fayer, M. D. Structural dynamics inside a functionalized metal–organic framework probed by ultrafast 2D IR spectroscopy. *Proceedings of the National Academy of Sciences* **2014**, *111* (52), 18442-18447. DOI: doi:10.1073/pnas.1422194112.
- (230) Tan, B. J. Y.; Sow, C. H.; Koh, T. S.; Chin, K. C.; Wee, A. T. S.; Ong, C. K. Fabrication of Size-Tunable Gold Nanoparticles Array with Nanosphere Lithography, Reactive Ion Etching, and Thermal Annealing. *The Journal of Physical Chemistry B* **2005**, *109* (22), 11100-11109. DOI: 10.1021/jp045172n.
- (231) Wongkaew, N.; Simsek, M.; Griesche, C.; Baeumner, A. J. Functional Nanomaterials and Nanostructures Enhancing Electrochemical Biosensors and Lab-on-a-Chip Performances: Recent Progress, Applications, and Future Perspective. *Chemical Reviews* **2019**, *119* (1), 120-194. DOI: 10.1021/acs.chemrev.8b00172.
- (232) Gizem, K.; Nuray Beköz, Ü.; Selcan, K. Nanostructures in Biosensors: Development and Applications. In *Biosignal Processing*, Vahid, A., Selcan, K. Eds.; IntechOpen, 2022; p Ch. 12.
- (233) Solanki, P. R.; Kaushik, A.; Agrawal, V. V.; Malhotra, B. D. Nanostructured metal oxide-based biosensors. *NPG Asia Materials* **2011**, *3* (1), 17-24. DOI: 10.1038/asiamat.2010.137.
- (234) Roy, S.; Gao, Z. Nanostructure-based electrical biosensors. *Nano Today* **2009**, *4* (4), 318-334.
- (235) Stewart, M. E.; Anderton, C. R.; Thompson, L. B.; Maria, J.; Gray, S. K.; Rogers, J. A.; Nuzzo, R. G. Nanostructured Plasmonic Sensors. *Chemical Reviews* **2008**, *108* (2), 494-521. DOI: 10.1021/cr068126n.
- (236) Huang, X.-J.; Choi, Y.-K. Chemical sensors based on nanostructured materials. *Sensors and Actuators B: Chemical* **2007**, *122* (2), 659-671.
- (237) Hahn, Y.-B.; Ahmad, R.; Tripathy, N. Chemical and biological sensors based on metal oxide nanostructures. *Chemical Communications* **2012**, *48* (84), 10369-10385, 10.1039/C2CC34706G. DOI: 10.1039/C2CC34706G.

- (238) Zhang, B.; Gao, P.-X. Metal Oxide Nanoarrays for Chemical Sensing: A Review of Fabrication Methods, Sensing Modes, and Their Inter-correlations. *Frontiers in Materials* **2019**, *6*, Review. DOI: 10.3389/fmats.2019.00055.
- (239) Nguyen, H. P. T.; Arafin, S.; Piao, J.; Cuong, T. V. Nanostructured Optoelectronics: Materials and Devices. *Journal of Nanomaterials* **2016**, *2016*, 2051908. DOI: 10.1155/2016/2051908.
- (240) Wang, W.; Qi, L. Light Management with Patterned Micro- and Nanostructure Arrays for Photocatalysis, Photovoltaics, and Optoelectronic and Optical Devices. *Advanced Functional Materials* **2019**, *29* (25), 1807275.
- (241) Madhukar, A.; Lu, S.; Konkar, A.; Zhang, Y.; Ho, M.; Hughes, S. M.; Alivisatos, A. P. Integrated Semiconductor Nanocrystal and Epitaxial Nanostructure Systems: Structural and Optical Behavior. *Nano Letters* **2005**, *5* (3), 479-482. DOI: 10.1021/nl047947+.
- (242) Yermakov, O.; Schneidewind, H.; Hübner, U.; Wieduwilt, T.; Zeisberger, M.; Bogdanov, A.; Kivshar, Y.; Schmidt, M. A. Nanostructure-Empowered Efficient Coupling of Light into Optical Fibers at Extraordinarily Large Angles. *ACS Photonics* **2020**, *7* (10), 2834-2841. DOI: 10.1021/acsp Photonics.0c01078.
- (243) Anttu, N.; Heurlin, M.; Borgström, M. T.; Pistol, M.-E.; Xu, H. Q.; Samuelson, L. Optical Far-Field Method with Subwavelength Accuracy for the Determination of Nanostructure Dimensions in Large-Area Samples. *Nano Letters* **2013**, *13* (6), 2662-2667. DOI: 10.1021/nl400811q.
- (244) Gandman, A.; Mackin, R. T.; Cohn, B.; Rubtsov, I. V.; Chuntunov, L. Radiative Enhancement of Linear and Third-Order Vibrational Excitations by an Array of Infrared Plasmonic Antennas. *ACS Nano* **2018**, *12* (5), 4521-4528. DOI: 10.1021/acsnano.8b00845.
- (245) Mackin, R. T.; Cohn, B.; Gandman, A.; Leger, J. D.; Chuntunov, L.; Rubtsov, I. V. Surface-enhanced dual-frequency two-dimensional vibrational spectroscopy of thin layers at an interface. *J. Phys. Chem. C* **2018**, *122* (20), 11015-11023. DOI: 10.1021/acs.jpcc.8b02436.
- (246) Wu, C.-Y.; Hsieh, H.; Lee, Y.-C. Contact Photolithography at Sub-Micrometer Scale Using a Soft Photomask. *Micromachines* **2019**, *10* (8), 547.
- (247) Tseng, A. A.; Kuan, C.; Chen, C. D.; Ma, K. J. Electron beam lithography in nanoscale fabrication: recent development. *IEEE Transactions on Electronics Packaging Manufacturing* **2003**, *26* (2), 141-149. DOI: 10.1109/TEPM.2003.817714.
- (248) Bischoff, L. Application of mass-separated focused ion beams in nano-technology. *Nuclear Instruments and Methods in Physics Research Section B: Beam Interactions with Materials and Atoms* **2008**, *266* (8), 1846-1851.
- (249) Huang, L.; Braunschweig, A. B.; Shim, W.; Qin, L.; Lim, J. K.; Hurst, S. J.; Huo, F.; Xue, C.; Jang, J.-W.; Mirkin, C. A. Matrix-Assisted Dip-Pen Nanolithography and Polymer Pen Lithography. *Small* **2010**, *6* (10), 1077-1081.

- (250) Seo, J.-H.; Park, J. H.; Kim, S.-I.; Park, B. J.; Ma, Z.; Choi, J.; Ju, B.-K. Nanopatterning by Laser Interference Lithography: Applications to Optical Devices. *Journal for Nanoscience and Nanotechnology* **2014**, *14* (2).
- (251) Colson, P.; Henrist, C.; Cloots, R. Nanosphere lithography: a powerful method for the controlled manufacturing of nanomaterials. *J. Nanomaterials* **2013**, *2013*, Article 21. DOI: 10.1155/2013/948510.
- (252) Zankovych, S.; Hoffmann, T.; Seekamp, J.; Bruch, J. U.; Torres, C. M. S. Nanoimprint lithography: challenges and prospects. *Nanotechnology* **2001**, *12* (2), 91. DOI: 10.1088/0957-4484/12/2/303.
- (253) Bhalla, N.; Jamshaid, A.; Leung, M. H. M.; Ishizu, N.; Shen, A. Q. Electrical Contact of Metals at the Nanoscale Overcomes the Oxidative Susceptibility of Silver-Based Nanobiosensors. *ACS Applied Nano Materials* **2019**, *2* (4), 2064-2075. DOI: 10.1021/acsnm.9b00066.
- (254) El-Said, W. A.; Yoon, J.; Lee, S.-N.; Choi, J.-W. Electrochemical Cell Chips Based on Functionalized Nanometals. *Frontiers in Chemistry* **2021**, *9*, Mini Review. DOI: 10.3389/fchem.2021.671922.
- (255) Khan, I.; Qurashi, A. Sonochemical-Assisted In Situ Electrochemical Synthesis of Ag/ $\alpha$ -Fe<sub>2</sub>O<sub>3</sub>/TiO<sub>2</sub> Nanoarrays to Harness Energy from Photoelectrochemical Water Splitting. *ACS Sustainable Chemistry & Engineering* **2018**, *6* (9), 11235-11245. DOI: 10.1021/acssuschemeng.7b02848.
- (256) Peng, Z.; Zhang, J.; Liu, P.; Claverie, J.; Siaj, M. One-Dimensional CdS/Carbon/Au Plasmonic Nanoarray Photoanodes via In Situ Reduction–Graphitization Approach toward Efficient Solar Hydrogen Evolution. *ACS Applied Materials & Interfaces* **2021**, *13* (29), 34658-34670. DOI: 10.1021/acami.1c04006.
- (257) Jiang, J.; Wang, X.; Li, S.; Ding, F.; Li, N.; Meng, S.; Li, R.; Qi, J.; Liu, Q.; Liu, G. L. Plasmonic nano-arrays for ultrasensitive bio-sensing. *Nanophotonics* **2018**, *7* (9), 1517-1531. DOI: doi:10.1515/nanoph-2018-0023 (accessed 2023-04-02).
- (258) Li, N.; Zhang, D.; Zhang, Q.; Lu, Y.; Jiang, J.; Liu, G. L.; Liu, Q. Combining localized surface plasmon resonance with anodic stripping voltammetry for heavy metal ion detection. *Sensors and Actuators B: Chemical* **2016**, *231*, 349-356.
- (259) Li, N.; Lu, Y.; Li, S.; Zhang, Q.; Wu, J.; Jiang, J.; Liu, G. L.; Liu, Q. Monitoring the electrochemical responses of neurotransmitters through localized surface plasmon resonance using nanohole array. *Biosensors and Bioelectronics* **2017**, *93*, 241-249.